Toward a Wholly Organic, Immunomodulatory Neuroelectronic Interface

Lars M. Crawford

A dissertation

submitted in partial fulfillment of the

requirements for the degree of

Doctor of Philosophy

University of Washington

2021

Reading Committee:

Buddy Ratner, Chair

Steve Perlmutter

Marta Scatena

Christine Luscombe

Program Authorized to Offer Degree:

Department of Bioengineering

University of Washington

Abstract

Toward a Wholly Organic, Immunomodulatory Neuroelectronic Interface

Lars M. Crawford

Chair of the Supervisory Committee:

Buddy Ratner

Department of Bioengineering

The neuroelectronic interface is a fascinating and powerful tool for enabling direct electrochemical interaction with the central and peripheral nervous systems as a means to alleviate symptoms of debilitating neurological conditions. As the name implies, successful design and implementation of such systems requires a unique combination of neurobiological knowhow and engineering execution. A long and fruitful history of neuroscience investigation coupled with the more recent rise of microfabrication techniques and high-powered digital computing systems places the present engineering endeavors in a position to contribute significantly and meaningfully to solutions for these severest of conditions. Indeed, devices of this nature are already commercially available and more still are in development. However, interfacing robustly with this most delicate of human tissues, the brain, still presents a major

challenge to the long-term success of these devices as a result of the prolific and neuroinflammatory response to implanted materials which is still not fully understood. This complex and dynamic reaction is driven not only by the implantation procedure, but also by the materials chosen for the device itself. A primary research thrust in this space thus involves the design and optimization of materials which may not only limit the severity of this immune reaction but also actively modulate it toward more pro-regenerative outcomes. Central to this effort is the integration of material classes which enable control over multiple properties of the device simultaneously including microarchitecture, mechanical compliance, electrochemical activity, and delivery of biomolecular cues. The preliminary work and proposed future exploration presented herein aim to contribute to the neuroelectronic interface design toolbox new methods for synthesizing soft electronic materials and new understanding into the mechanisms behind the neuroinflammatory response. The ultimate goal of this venture is therefore to enable and promote the creation of a wholly organic, immunomodulatory neuroelectronic interface which may be translated into a robust medical device to improve the lives of those suffering from life-long neurological conditions.

I would like to acknowledge my family, Martha, Fred and Clay, for being so incredibly supportive and pushing me to achieve this once-in-a-lifetime milestone to show that I can work hard and conquer difficult problems. Another big and special thanks to my peers and friends in the Ratner lab who made the journey fun and interesting <3

Table of Contents

List of Figures

List of Tables

CHAPTER 1 – Introduction to the Problem Space

Tens of millions of people worldwide suffer from neurological diseases and injuries such as spinal cord injury, stroke, Parkinson's, epilepsy, and multiple sclerosis among others[1,2]. Brain-computer interfaces (BCIs) provide an opportunity to bypass faulty neuronal circuitry to return bodily function or interact with and/or control external devices[3–6]. BCIs are designed to record neural signals and decode information content to drive a computer cursor, a robot arm, electrical stimulation of muscles, or another actuator. Alternatively, they can be used to inject current into regions of the brain to bypass or disrupt faulty circuitry to alleviate symptoms of disease such as tremor or seizures. The most invasive methods of interfacing electrically with the central nervous system (CNS) via BCI, i.e. those involving surgical opening of the skull, enable placement of electrodes directly onto the surface of the brain or to penetrate the brain parenchyma. Both of these methods currently provide higher resolution signals of brain activity than non-invasive methods which record brain signals from outside the skull non-invasively. This improvement in resolution of the recorded signal allows for analysis of neuronal activity on the level of individual cells.

An array of electrode contacts fabricated on a planar substrate in 2-dimensions or along the length of a shank-like substrate also enables the formation of a neuroelectronic interface which may communicate with many individual cells or sets of cells which provides more degrees of freedom for a control signal and therefore may enable better BCI performance. Both designs have benefitted from the application of microelectronic manufacturing methods, such as various lithographic and micromachining techniques, which have been a key enabler in the development of multi-channel, high density neural electrode arrays. To date, penetrating microelectrode arrays (MEA) which utilize the shank-like geometry provide the highest degree of specificity in recording and stimulation of individual neurons and associated neural circuitry[7,8]. However, penetration into the brain parenchyma explicitly induces tissue damage which results in an immune response that may range from moderate to severe depending on the degree of implant-induced tissue damage

and material properties of the electrode. For example, classical penetrating MEAs have typically been fabricated from silicon and/or metallic materials that present a major mechanical mismatch with neural tissue. This has the tendency to cause continued tissue damage beyond the initial implantation as a result of normal brain micromotions during respiration and metabolism[9]. Both the initial implantation and this prolonged damage have the propensity to induce a chronic form of neuroinflammation, known as gliosis[10].

In the context of neural electrode implantation and recording, gliosis is an adverse phenomenon with a dynamic time-course of events and is known to be a primary failure mode for intracortical MEAs[11]. This neuroinflammatory response is driven by a pair of immune cells of myeloid origin, microglia and macrophages[12]. Microglia are resident immune effector cells in the brain which, in the absence of injury, are in a ramified or resting state and engage in tissue homeostasis. Macrophages are a peripherally derived immune effector cells which are not present in the healthy brain but are involved in the immune response across many tissue types. Upon injury to the brain, microglia enter an activated inflammatory state while macrophages enter the brain parenchyma via ruptured vasculature or via extravasation through vessel walls in response to damage-associated signals released during implantation-induced cell death. Throughout this process, these immune effector cells migrate toward the implant and release a host of neurotoxic chemicals in an effort to break down and phagocytose the implant which has a tendency to kill nearby neurons. Unsuccessful attempts at breakdown or phagocytosis of the device leads to the recruitment of astrocytes, another resident immune support cell type in the brain, which progressively encapsulate the device in a thick cellular sheath[13].

While this process is particularly pronounced for penetrating MEAs which explicitly damage brain parenchyma, 2-dimensional arrays on the brain surface, also known as electrocorticography (ECoG) arrays, have also been found to be subject to gliosis as a result of the surgical operation and ‘foreignness’ of the material in the neural tissue environment[14]. In this case, gradual cellular growth typically occurs between the neural tissue and array. The formation

of this cellular sheath, known as a glial scar, increases electrode impedance and may displace and/or kill nearby neurons, leading to the reduced functionality or failure of the BCI[10,15–20]. Ultimately, this results in diminished quality of care for patients who may require lifelong BCI intervention for treatment and hinders neuroscience research into long-term neuronal dynamics (e.g. learning, plasticity)[21].

As such, there are several research thrusts which aim to design high-performance, high-density electrode arrays which mitigate gliosis to enable BCI to serve as a long-term treatment modality for some of the most debilitating, life-long neurological injuries and diseases. Key design factors that have been identified to limit gliosis severity include: modifying the mechanical properties of the electrode to be similar to that of brain tissue by modifying the material composition of the device; minimizing the extent of implantation-induced damage, particularly vascular damage, by minimizing the footprint of the device and using methods for precision implantation; and incorporating coatings and mechanisms for release of bioactive molecules which actively modulate the inflammatory reactivity of relevant immune effector cells[22].

Hydrogels[23] and electrically active organic species[24] are two classes of materials which have found widespread application in the electrode design toolbox for their ability to improve electrode properties in an attempt to mitigate the negative effects of gliosis on long-term BCI performance[14]. Hydrogels are a class of water-soluble or hydrophilic polymers which have demonstrated an ability to dampen the neuroinflammatory response and improve electrode recording outcomes[25]. More specifically, hydrogel coatings, such as poly(2-hydroxyethyl methacrylate) (PHEMA)[23], on the surface of electrodes lessen tissue strain induced by the mechanical mismatch between hard silicon/metallic electrodes and nervous tissue with Young's modulus >10Gpa versus ~10kPa, respectively[26]. These studies demonstrate that the reduction in mechanical tissue strain scales with hydrogel thickness. However, thicker hydrogels also have the potential to displace neuronal cell bodies away from electrode recording sites, thus reducing signal quality, and do little to actively modulate the neuroinflammatory response beyond serving

as sink for pro-inflammatory cytokines. Coatings composed of organic conductors, including conductive polymers such as the highly studied poly(3,4-ethylenedioxy thiophene) (PEDOT)[27], carbon nanotubes (CNT)[28], and graphene (GR)[29], have been demonstrated improve the electrical connection between the electrode and neurons. However, when implemented in isolation, these improvements are still overshadowed by the thickness and density of the glial scar which may still limit the formation of an effective electrical interface over extended implant durations.

Conductive hydrogels are another class of materials which have been applied to neural electrodes because they combine the best features of both components: the tunable mechanical and swelling properties of hydrogels and the highly conductive nature of organic conductors[30]. Many research efforts involve the coating of conductive hydrogels onto the surface of classical electrode arrays to reduce the mechanical mismatch at the device-tissue interface while retaining high signal quality for recording and/or stimulating purposes[22]. Coating of classical electrode arrays with conductive hydrogels typically involves a 2-step process in which the hydrogel is coated onto the array first and then conductive polymers are grown from the electrode contact surface throughout the hydrogel matrix in a subsequent step via controlled electrochemical polymerization[31].

Conductive hydrogel coatings have demonstrated major improvements over non-coated classical electrode arrays and thus provided evidence for the positive impact these materials have on limiting the negative effects of gliosis. However, the size of the electrode footprint (i.e. cross-sectional area) is still a major issue for the damage it causes upon implantation which is made worse with a thicker hydrogel coating. Furthermore, the stiff substrate beneath the gel coating still may cause tissue damage over prolonged periods of brain micromotion and thus cause BCI failure over clinically relevant time frames (i.e. years to decades). This has led to more recent developments which involve new nanofabrication methods that allow for the shrinking of device dimensions down to the single micrometer range while still enabling high channel count. Particularly impressive in this regard is the recent work published by the lab of Dr. Chong Xie at

Rice University who utilized lithographic nanofabrication techniques to produce ultra-flexible, high density penetrating MEAs with electrode traces in the nanometer range and an overall device thickness as low as 1μm[32,33]. The substrate for these devices was SU-8 which has relatively stiff mechanical properties (~4GPa) though the ultra-thin form factor of these devices still enabled them to be highly flexible. Furthermore, a pinhole feature was designed on the end of these electrode arrays which provided a catch point for a micromanipulator (<10μm diameter) to engage for automated implantation.

This automated delivery method enabled both the targeted delivery of electrodes and removal of individual surgical operator error which can cause significant variation in tissue damage during manual implantation. These ultra-flexible arrays have also demonstrated success in recording action potentials from single cells for up to 8 weeks of implantation in rat brain, which is also very exciting for the field of neural engineering. More recently, the founding of the company Neuralink has integrated several of these developments in the production of a high channel count penetrating microelectrode array with sub-micron features and an automated, robotic implantation mechanism with aims to develop a commercially available BCI for human use in the near term[34]. However, as with the Xie electrodes, the electrodes developed by Neuralink are still composed of relatively stiff materials and have yet to demonstrate success in humans for prolonged implantation durations.

A more general shift in the field of neural engineering has been toward modifying the substrate material onto which electrode traces and contacts are fabricated toward more flexible and/or elastic materials such as parylene-C (~2GPa), polyimide (PI; ~1GPa), poly(dimethyl siloxane) (PDMS; ~1MPa) and most recently perfluoropoly(ether)-dimethacrylate (PFPEDMA; ~30kPa). These modifications also coincide with replacement of the metallic electrical components such as gold or platinum with softer organic composite materials such as conductive hydrogels. Some noteworthy attempts at fabrication of penetrating electrodes out of softer, wholly organic components include an agarose/CNT composite[35] and carbon fibers[36]. The agarose

electrode had a maximum conductivity of 131±1 S/cm and stiffness of 220±120 MPa when hydrated and demonstrated good biocompatibility when implanted into rat cortex. However, it was ~100μm in diameter, comprised of only a single channel, and no neural recordings were conducted. The carbon fiber electrode was much smaller, <10μm in diameter, with PEDOT deposited on the tip to improve recording properties. This electrode also demonstrated good integration with neural tissue and recording of action potentials out to 5 weeks but was also only composed of a single channel with a stiffness of ~4GPa.

There have been other successes with flexible penetrating arrays such as those made from CNT fiber electrodes which are small (<20μm in diameter) and highly flexible but these electrodes required a large, stiff, rapidly dissolving polymer-based shuttle for implantation[37]. These electrodes have demonstrated success at recording single action potentials but still elicited a neuroinflammatory response as the shuttle significantly increases the cross-sectional area of the electrodes at the time of implantation. These results illustrate the difficulty in designing penetrating microelectrodes out of wholly organic components which satisfy the design criteria discussed above. Namely that soft materials are incapable of penetrating the brain surface unless made large enough, stiff enough, or encapsulated with a large/stiff material which ultimately increases the device footprint and thus induces larger disruptions to the tissue upon implantation.

From a 2-dimensional array perspective, there have been great strides in developing stimulating and recording devices out of these soft materials. For example, the 'electronic dura'[38] from the lab of Dr. Stéphanie Lacour at EPFL that was fabricated on flexible PDMS with gold electrode traces, or the much smaller, highly conformable micro-ECoG (μECoG) array composed of gold electrodes on 2μm thick parylene-C substrate by Malliaras lab[39]. However, approaches like this which use metallic traces and contacts require sophisticated strain engineering techniques, such as microcracking or wavy electrode traces, to ensure the stability of the electrical pathway under strain. An ideal approach would involve the design of substrate, insulation, and conductive materials which are all soft, flexible, and capable of fabrication via precise

photolithographic or patterning techniques. This would enable the production of soft, high channel count intracortical MEAs with features that enable precision implantation such as those used by the Xie lab and Neuralink.

A promising approach in the space of wholly organic electrodes is the work recently published from the lab of Dr. Zhenan Bao at Stanford which involves the fabrication of an electrode array with conductive hydrogel traces and contacts on a soft, highly elastic PFPEDMA substrate[40]. These electrode arrays were highly conductive, extremely soft and elastic, and were successfully applied as a neural stimulatory interface for the sciatic nerve in mice. They were also able to fabricate the electrode traces and contacts as small as 5μm which has the potential to enable high-channel count, high-density arrays. However, their studies so far have only investigated relatively low channel count planar arrays in peripheral nerve stimulation, but the results are nonetheless exciting for the advancement of the field of soft neuroelectronics comprised of wholly organic components.

While these results are exciting in terms of the advancements they've made, the novelty of their methods required many of the steps in the fabrication process to be completed manually, making them complex and time intensive. Furthermore, while small and highly flexible, these devices did not incorporate features to actively mitigate implant-induced inflammatory reactivity. This is particularly important for the stiffer materials such as those used in the Xie and Neuralink electrode arrays as it has been found that immune cells can sense the stiffness of the substrate which they interface with and modulate their response accordingly[41]. Therefore, it is unknown how these stiff materials, even in their flexible form factor and associated precision implantation methods, will impact the long-term stability of the electrode-tissue interface. It should also be noted that, while there have been significant advances in each of these areas, none have yet demonstrated robust neural electrode function *in vivo* for clinically relevant time scales. As such, there is still a need to design new methods which may enable the fabrication of soft, high density electrode arrays which may limit implant-induced gliosis over chronic time scales.

Beyond application to neural electrodes, hydrogels constructed into tissue engineered scaffolds have served as an ideal model for studying the impact of different material properties on the neuroimmune response to implanted materials[42]. As with the electrode design process described above, the field of tissue engineering has identified a set of features which might be engineered into the scaffold design to modulate the tissue response upon implantation. These include: material properties such as mechanical, topographical, biochemical, and electrical cues; the delivery of bioactive entities such as cells and growth factors; biodegradability; and radical scavenging ability[43]. Much of the work in this space to date has utilized hydrogel scaffolds as vehicles for the delivery of bioactive molecules, such as surface bound or eluting neurotrophins[44] and anti-inflammatory drugs[45], and cells, such as stem cells[46] and Schwann cells[47], directly into nervous tissue. These biological entities have demonstrated improvements in the tissue response by inhibiting or stimulating specific neuroinflammatory or neuroprotective signaling pathways, respectively, or by modulating the overall cytokine milieu toward a more pro-healing environment. However, these treatments alone have not yet demonstrated satisfactory remission or attenuation of gliosis as their effects are typically transient in nature.

Previous work has also demonstrated that CNS tissue does infiltrate implanted microporous hydrogel scaffolds[48]. However, the fabrication methods of these materials, and indeed most porous hydrogels, are limited in that the porogens used do not provide a high degree of specificity or control in pore size or structure[49]. Conversely, the Ratner lab has developed well established protocols for fabricating hydrogels with precise porous microstructure, known as sphere-templated scaffolds (STS)[50]. Beyond tight control of porosity, the STS fabrication methodology enables control over other important material properties including: tuning of mechanical compliance over a broad range; covalent immobilization of bioactive molecules onto the material surface; seeding and culturing of cells of various lineages within the porous network; and incorporation of biodegradable crosslinkers to enable material degradation. As such, there

exists the capability to engineer a wide array of STS-based materials which may be optimized for specific tissue engineering applications.

STS with tightly controlled microporosity have demonstrated an ability to alter the local structural environment of immune cells, primarily macrophages[51], upon implantation. Modulation of macrophage phenotypic expression with STS *in vivo* has been shown to reduce fibrotic scar formation and stimulate regeneration of healthy tissue, including blood vessels, in and around the porous network[52]. The most prominent shift toward healthy vascular and tissue growth occurs when pores are 35-40μm[51,52]. These studies have also demonstrated that cells polarized to both pro-inflammatory (M1) and pro-regenerative (M2) phenotypes are found within the implant pores. Indeed, a large proportion of these cells co-stain for M1 and M2 markers, signifying the complex set of activation states that are necessary to provide optimal tissue regeneration and ingrowth into the material.

Additionally, preliminary studies of STS implantation in CNS tissue have shown a reduction in glial scar formation measured by astrocytic expression of glial fibrillary acidic protein (GFAP), along with the ingrowth of neurons and blood vessels[53]. The best results in this regard were found with a pore size of 40um, which is similar to previous results in peripheral tissues, and a material stiffness around 10kPa, which was expected given the close match to brain mechanical properties. Furthermore, studies from other groups continue to provide evidence that neural tissue regeneration can be improved by modulating macrophage and microglial activation, both of which have been implicated in a spectrum of pro- and anti-inflammatory phenotypes[54]. However, despite these engineering successes, the neuroinflammatory processes which drive gliosis and result in the formation of the glial scar are still not fully understood. Taken together, the impact STS have demonstrated on neural regeneration and the limited nature of our understanding of gliosis motivate further investigation into the effect of various STS properties on macrophage and microglial activation and the generalization and application of this knowledge to neural electrode design.

In the end, long-term performance reliability of neural microelectrodes remains an outstanding issue in the field[25]. This necessitates further investigation to both deepen our understanding of the processes underlying gliosis and to develop relevant and encompassing methods to overcome them over clinically relevant time frames. Given the biological complexity of these processes, it is likely that an equally sophisticated set of methodologies and material properties will need to be integrated and expressed over a range of time scales to effectively mitigate gliosis.

The work presented in this dissertation seeks to expand the neural electrode design toolbox in two distinct ways: 1) by developing new, facile methods for the synthesis of soft, conductive materials with broad applicability to various high throughput fabrication techniques; and 2) by deepening our understanding into the processes of property-dependent neuroimmune modulation of precision porous tissue engineered scaffolds. The following chapters are aimed at responding and contributing to the needs described above for new synthesis methods for soft electronic devices and in the determination of optimal material properties for neuroimmune modulation. Chapter 2 will present the development of a novel photochemical polymerization method for conductive hydrogel synthesis, characterization of the resulting materials, and discussion of its application to a soft, wholly organic neural electrode. Chapter 3 will present *in vitro* cell culture studies which investigate the property-dependent effects of neural tissue engineered scaffolds on the inflammatory reactivity of immune cells of myeloid origin using STS as a culture model. Chapter 4 will present the *in vivo* implantation of *in vitro*-optimized STS into the brains of rats to determine their impact on gliosis. Lastly, Chapter 5 will present the future prospects of integrating the findings presented in Chapters 2-4 into a high channel count stand-alone conductive hydrogel neural electrode. The ultimate goal of this work is therefore to contribute to the design of a truly robust wholly organic, immunomodulatory neuroelectronic interface that may be translated into a high-performance medical device for long-term use.

CHAPTER 2 – Development and Characterization of a Novel, One-Pot, Photochemical Polymerization Method for Conductive Hydrogel Synthesis

2.1 Background

The properties of conductive hydrogels make them well suited for application to devices intended to interface with the human nervous system given their highly tunable mechanical and electrical properties. The wide array of hydrogel polymers and conductive components provide an immense space to work within to engineer materials with highly specialized properties. Of all the conductive components available for production of conductive hydrogels, conductive polymers are a particularly interesting subset because their organic, monomer-based nature makes them highly amenable to chemical modifications and unique synthesis methods[55]. That is, conductive polymers can be incorporated into materials as pre-formed polymers, akin to other conductive nanoparticle formulations, but their monomeric constituents and diverse polymerization mechanisms also provide another degree of freedom in how they can be manipulated or incorporated into materials. For example, they can be polymerized from their monomeric constituents via oxidative chemical polymerization *in situ* throughout a pre-formed hydrogel network in the formation of an interpenetrating network (IPN)[56] or grown electrochemically from the surface of an electrode[57]. Furthermore, the need for a dopant or counterion to impart conductivity to the polymer provides an additional avenue for material design in terms of they grow through a material or their degree of electroactivity.

A brief overview of conducting polymers pertinent to this dissertation are discussed here, but the reader is referred to Bakhshi (1995)[58] for a more in-depth, historic review of the fundamentals behind these interesting materials. As alluded to above, conductive polymers are organic, polymeric materials that contain a π-conjugated backbone, i.e. comprised of carbon atoms which are all sp^2 hybridized. This produces a linear molecule that has alternating single and double bonds which enables a delocalization of electrons along the molecule's backbone as

a result of overlapping p-orbitals. The interaction of these molecular orbitals causes a change in the energy state of the electrons that results in a higher energy state of the highest occupied molecular orbital (HOMO) and a lower energy state for the lowest unoccupied molecular orbital (LUMO). This electronic structure ultimately results in a reduction of the band gap that is proportional to the effective conjugation length of the polymer. The band gap and energy levels of the HOMO and LUMO of conducting polymers are affected by the presence of electron donating or withdrawing groups and the physical structure of the polymer (e.g. twists/coils vs. linearity). The excitement and delocalization of the electrons from the HOMO to the LUMO requires an input of energy equivalent to the band gap of the conductive polymer. This effectively creates a conduction band with two charge carriers in the form of an excited electron in the upper molecular orbital and an electron hole in the lower molecular orbital. However, without this input of energy the conjugated backbone of the polymer is not conductive as the delocalization of electrons is limited due to the 1-dimensional nature of the molecule.

In order to overcome this energy gap, the backbone of the conductive polymer can be reduced or oxidized to impart an electron into the LUMO or extract an electron (i.e. form an electron hole) in the HOMO, respectively. Initial, low levels of reduction/oxidation result in an uncoupled charge carrying defect known as a soliton which is relatively unstable[59]. As such, ionic dopant molecules are introduced to help stabilize the charge along the polymer backbone; cationic dopants stabilize electrons within reduced conductive polymers (i.e. n-type doping) while anionic dopants stabilize electron holes within oxidized conductive polymers (i.e. p-type doping) (Kaur 2015). In the case of a soliton, however, this electrostatic stabilization induced by the dopant also limits mobility of the charge and thus the conductivity of the polymer as whole. As the degree of reduction/oxidation and doping increases, the electronic structure of the backbone shifts from a poorly conducting, uncoupled soliton to a coupled defect known as a polaron. Further increases in doping lead to the formation of bipolarons which ultimately generate a stable conduction band

that enable these stabilized charge defects to travel along the polymer backbone and hop between adjacent chains in the presence of an electric field[60]. The mechanisms of doping and charge conduction discussed here are important to consider when engineering conductive polymers for specific applications, such as with the conductive hydrogel materials developed and characterized throughout this dissertation.

Among the wide array of conductive polymers available today, poly(3,4-ethyelene dioxythiophene) (PEDOT) was chosen for the design of the conductive hydrogel materials explored here for several reasons[61]. Firstly, the chemical modification of the thiophene ring of the EDOT monomer with the ethylene dioxy unit serves as both an electron donating group to decrease the band gap of the polymer and also improve the regioregularity (i.e. intermonomer bond structure) of the polymer during polymerization. Together these provide control over the polymerization of EDOT and provide the potential for a high degree of electrical activity in the resulting polymer. Secondly, PEDOT has been widely studied in the context of implanted electrode devices and has demonstrated a high degree of biocompatibility[62–64]. Thirdly, the polyanion poly(styrene sulfonate) (PSS) has also been widely studied as a successful dopant molecule for PEDOT.

The work by the Bao lab discussed above illustrates an ideal approach for applying conductive polymers in the fabrication of soft neuroelectronic devices. Their first principles approach involved designing each component of the device to be soft, highly elastic, and processable via well-established lithographic patterning techniques. The insulator they designed, PFPEDMA, had a high dielectric constant, was extremely elastic, and was easily polymerizable via photopolymerization. The organic conductor they used was a commercially available form of PSS-doped PEDOT (PEDOT:PSS). Integration of PEDOT:PSS involved custom processing with an anionic liquid plasticizer, which significantly increased the conductivity and elasticity of the PEDOT:PSS films when deposited on a PDMS substrate. However, a wash step was required to

remove the highly toxic ionic liquid prior to completing the process which, while simple, adds another layer of complexity to the fabrication process.

Beyond the methods that Bao et al. implemented, a plethora of other conductive hydrogel fabrication techniques have been introduced in the literature specifically designed for bioengineering applications[65]. These methods utilize polymers that are of natural origin, such as chitosan[66], hyaluronic acid[67], laminin[68], etc., or synthetic, bioinert polymers such as PHEMA[69], poly(ethylene glycol) dimethacrylate/diacrylate (PEGDMA/PEGDA)[31], and poly(vinyl alcohol) (PVA)[70] among others. Furthermore, a variety of mechanism for incorporating the conductive components have been developed. These range from the addition of conductive nanomaterials, such as CNT or GR, to the pre-gel mixture before polymerization[71]; incorporating crosslinking components, such as glutaraldehyde[72], that link the conductive components to the polymer chains *in situ* during gelation; or *in situ* electrochemical or oxidative chemical polymerization of conductive monomers throughout the network of a preformed hydrogel[56]. A wide range of conductive monomers have also been used[73], the most prominent including pyrrole (Py), aniline (ANI), and EDOT. In all cases, these methods produce an interpenetrating or composite network of hydrogel and organic conductive components in the formation of a conductive hydrogel. However, each of these methods are not amenable as stand-alone materials for application to the fabrication of neural microelectrodes given the particular steps necessary in their synthesis and/or their inability to be precisely patterned via standard lithographic techniques.

The work presented here seeks to develop a new method of conductive hydrogel synthesis which makes use of the mechanisms behind successful approaches like that of Bao's and others to help streamline the soft electrode fabrication process. This novel synthesis method involves the photochemical polymerization of hydrogel and conductive polymer components alongside each other from their respective commercially available monomeric constituents. This so called one-pot synthesis reaction has the potential to simultaneously improve ease of

conductive hydrogel fabrication and provide a greater degree of control over final gel properties by tuning the initial pre-gel conditions over a wide range. Others have successfully designed conductive hydrogel solutions which may be photopolymerizable by adding dried commercially available organic conductors, such as PEDOT:PSS powders, into pre-gel mixtures[74–76]. However, the dark black color of these powders produces a significant limitation on the amount that may be added to the pre-gel solution to impart conductivity to the gel without compromising polymerization efficiency to ensure gelation occurs.

Presented below are the results and discussion around the development of this novel photochemical polymerization method, a systematic investigation into major factors impacting the photochemical polymerization mechanism and resulting gel properties, and application of the method in the fabrication and characterization of stand-alone conductive hydrogel electrode prototypes.

2.2 Methods

2.2.1 Materials

All materials were purchased from Sigma-Aldrich (St. Louis, MO) unless otherwise stated. Chemical structures of the relevant molecules are visualized below and exact compositions for each gel are listed in tables throughout this dissertation. For the fabrication of monomer-based hydrogel systems, the gels consisted of monomers of 2-hydroxyethyl methacrylate (HEMA; Polysciences, Warrington, PA), glycerol methacrylate (GMA; Polysciences), methacrylic acid (MAA), acrylic acid (AA), 2-acrylamido-2-methylpropane sulfonic acid (AMPS), and/or styrene sulfonate (SS), and crosslinked with tetraethyleneglycol dimethacrylate (TEGDMA; Polysciences).

For macromolecular hydrogel systems, the base hydrogel polymer used was poly(vinyl alcohol) (PVA, 16kDa average Mw) which was chemically modified with methacrylate (MA) crosslinking moieties using 2-isocyanatoethyl methacrylate (ICEMA) and with anionic dopant moieties using the amino acid taurine (Tau) via previously established methods[30]. PVA macromers used were modified to contain 10 MA groups and 20 Tau groups on average per PVA chain (referred to as either PVA-MA-Tau or simply PVA).

Conductive elements included the monomer 3,4-ethylene dioxythiophene (EDOT) and subsequent polymer PEDOT, with polycounterion and dopant poly(styrene sulfonate) (PSS), carboxylated multiwalled carbon nanotubes (CNT) and graphene (GR; gift from collaborator) with Pluronic F127 (PEG:PPG:PEG, 101:56:101) as a surfactant. Polymerization initiator species used were Irgacure 651 (2,2-dimethoxy-1,2-diphenylethanone) and Irgacure 2959 (2-hydroxy-4′-(2-hydroxyethoxy)-2-methylpropiophenone) for photopolymerization of vinyl groups and ammonium persulfate (APS) for oxidative polymerization of EDOT to PEDOT.

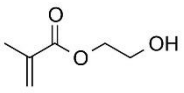
HEMA

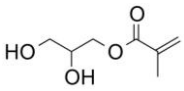
GMA

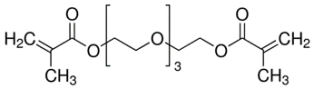
TEGDMA

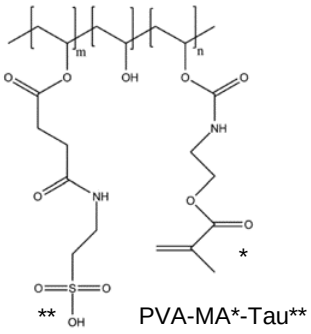
PVA-MA*-Tau**

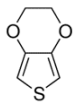
EDOT

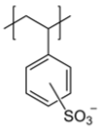
PSS

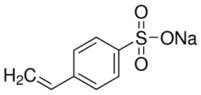
SS

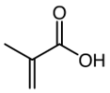
MAA

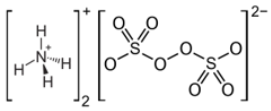
APS

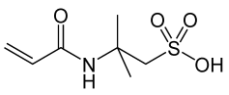
AMPS

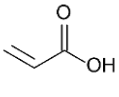
AA

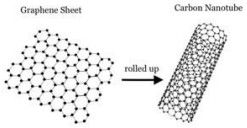

GR CNT

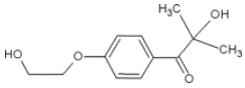
Irgacure 2959

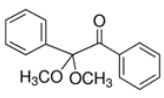
Irgacure 651

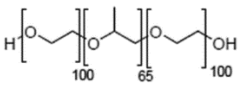
Pluronic F127

Solvents tested included DI water, ethanol, methanol, isopropanol, acetonitrile, poly(ethylene glycol) (PEG200), dimethysulfoxide (DMSO), ethylene glycol (EG), and glycerol (Gly).

2.2.2 Two-Pot Conductive Hydrogel Fabrication - Step 1: Hydrogel Synthesis

HEMA was chosen as the sole monomer component for the hydrogel system in these studies for several reasons including: 1) its high degree of biocompatibility; 2) its hydrolytic stability to enable long-term implantation; and 3) its ability to be tailored to possess similar mechanical and hydration properties to living tissues[69]. TEGDMA and Irgacure 651 were chosen as standard crosslinker and photopolymerization initiator species, respectively. In addition to EDOT, CNT and GR were chosen for their excellent electrical properties and ease of incorporation[73]. Aqueous suspensions of CNT or GR (4mg/mL) were prepared by using Pluronic F127 (12.5mg/mg) as a surfactant and incorporated into the prepolymer solution for encapsulation within the PHEMA matrix upon polymerization (~0.4% final weight fraction CNT/GR). The pregel solution contained approximately 50% HEMA monomer (v/v), 2.5% TEGDMA (v/v; 50:1 monomer:crosslinker ratio), 0.25wt% Irgacure 651 (420:1 monomer:initiator ratio), and 50% DI water (v/v) or aqueous suspension of CNT/GR+Pluronic F127. Pregel solutions were filled between 2 glass slides separated with a 1mm Teflon spacer to produce gel sheets or into glass capillary tubes with an 800μm inner diameter to produce gel rods and then photopolymerized under a broad-spectrum UV light from a high-intensity mercury lamp with an average intensity of 12mW/cm^2 for 12 minutes. Gels were gently removed from the glass slides/tubes and washed thoroughly in DI water to remove unreacted species. Gel sheets were then punched into discs of 5mm diameter thickness and rods were cut into 3cm long segments in preparation for interpenetrating network formation and subsequent characterization.

2.2.3 Two-Pot Conductive Hydrogel Fabrication - Step 2: Interpenetrating Network (IPN) Formation

A panel of conductive hydrogels were formed via a two-step method involving *in situ* polymerization of PEDOT:PSS (1:1.5 weight ratio) in the presence of HEMA hydrogels to produce an IPN of the conductive polymer complex PEDOT:PSS throughout the gel network following previously established methods[56]. This process is visualized in Figure 1. Briefly, an aqueous solution containing 10% PSS (w/v) and 6.5% EDOT (w/v) was stirred vigorously on a stir plate in an air-tight container to which DI water-equilibrated discs and rods were added and set to incubate with mild stirring. After 72 hours, 13.5% APS (w/v) was added to initiate the oxidative polymerization of EDOT and the solution was bubbled with nitrogen gas and left to polymerize for 1 week with mild stirring during which the solution turned from opaque white to blue and then to black. After 1 week the gels were removed from the vessel, gently wiped to remove excess PEDOT:PSS, and then thoroughly washed in DI water to remove unreacted species. After washing, rods were equilibrated in PBS (pH 7.4) in preparation for electrochemical analysis while discs remained equilibrated in DI water for swelling, mechanical, and morphological analysis.

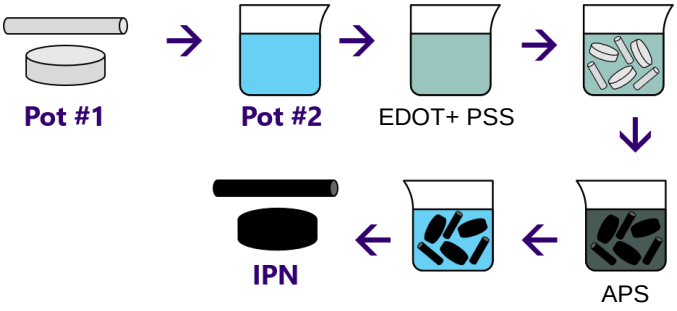

Figure 1: Schematic of two-pot conductive hydrogel synthesis process. Gels are fabricated in the first step (pot #1) and then an IPN is formed via *in situ* polymerization of the conductive polymer in the second step (pot #2) followed by a wash step to remove unreacted species.

Sphere-Templated Scaffold (STS) Fabrication

The STS fabrication process has been described in depth elsewhere[52,53]. Briefly, monodisperse, uncrosslinked poly(methyl-methacrylate) (PMMA) microbeads of select diameter are placed into a mold with a specified geometry (e.g. between glass slides with Teflon spacer, within a glass capillary tube, etc.), ultrasonicated to ensure close packing, then heated to sinter the beads together. Sinter temperature and time can be modified to control bead interconnect

diameter. The mold is filled with a pre-gel solution of choice, polymerized, and refluxed in an organic solvent to clear the sintered PMMA beads, leaving a crosslinked hydrogel scaffold with a well-defined porous network. Porous sheets produced between glass slides were also subsequently punched with a biopsy punch to produce uniform discs or with a needle to produce porous rods for comparison to rods produced via the glass capillary tube molding method.

2.2.4 One-Pot Conductive Hydrogel Fabrication

To enable greater control over conductive hydrogel fabrication parameters, e.g. gel microarchitecture, a novel one-step synthesis procedure was developed which incorporates all hydrogel and conductive precursors and initiators in a layered selection of solvents into a single reaction vessel. This one-pot parallelized photochemical polymerization process is visualized in Figure 2. Controls for each of the chemical compositions tested were fabricated following identical procedures with the exclusion of EDOT from the pre-gel mixture.

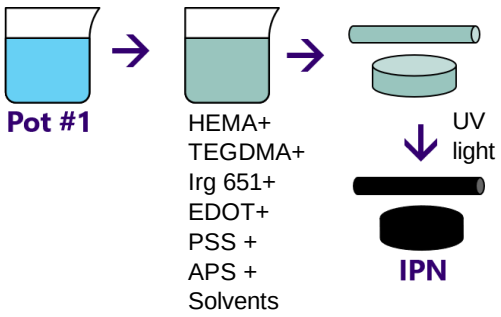

Figure 2: Schematic of one-pot conductive polymer synthesis process. Gels are fabricated in a single vessel (pot #1) by mixing all necessary components to enable polymerization of hydrogel and conductive polymer components in parallel to form an IPN in a single step.

To date, this method has been tested in a variety of methacrylate-based monomer systems and a methacrylate-based macromer system with PVA-MA-Tau. In all cases, PEDOT served as the primary conductive component. Slight differences in the fabrication process and equipment used for the systems occurred as these studies were conducted across two different lab spaces: the lab of Dr. Laura Poole-Warren at the University of New South Wales (UNSW) in Australia, and the lab of Dr. Buddy Ratner at the University of Washington (UW) in Seattle, WA.

In general, pre-gel solutions were mixed within a single vessel with the hydrogel component, crosslinker, photoinitiator, conductive monomer, dopant component, oxidative initiator, and cosolvent. The monomeric systems investigated via the one-pot method used 2.5% (v/v) TEGDMA as crosslinker, 0.25% (w/v) Irgacure 651 as photoinitiator, and 5.7% (w/v) APS as oxidative initiator. The macromeric system investigated via the one-pot method used 8% (w/v) PVA-MA-Tau (10x methacrylate groups/PVA chain; 20x taurine groups/PVA chain), which equates to 0.75% (w/v) MA as crosslinker and 1.25% (w/v) Tau as dopant per chain, 0.1% (w/v) Irgacure 2959 as photoinitiator, and 5.7% (w/v) APS as oxidative initiator. EDOT was used as the sole organic conductive component for these systems. Values for other components within these systems were varied according to the specific compositions tested. The reader is directed to the tables in the results sections below for the nomenclature and exact chemical composition of the gels tested.

Gels fabricated at UNSW were made by filling a known volume, i.e. 70-80µL, of pre-gel solution into 10mm diameter silicone molds covered with glass coverslips or into 800µm inner-diameter glass capillary tubes and photopolymerized under a UV spot lamp. The control gels for the monomer system were exposed to 70mW/cm^2 UV light for 3 minutes while controls for the macromer system were exposed to 30mW/cm^2 UV light for 3 minutes as it was found that these parameters produced stable mechanical and swelling values for each system, respectively. The conductive counterparts to these systems containing EDOT in the pre-gel mixture were exposed to the same intensity UV light as their respective controls but for 12 minutes as gelation did not occur until this duration, indicating a reduction in methacrylate polymerization efficiency when all components reacted simultaneously in parallel. Conversely, gels fabricated at UW were photopolymerized under a broad-spectrum UV light from a high-intensity mercury lamp with an average intensity of 4mW/cm^2 for 12-40 minutes depending on the pre-gel composition.

During UV exposure, all systems containing EDOT and APS experienced gelation of the hydrogel component and apparent polymerization of EDOT into PEDOT as the gels turned from translucent to light blue to dark blue to black over the course of the UV exposure duration. After gelation had occurred, gels were kept in their molds, wrapped in parafilm, and stored at 4C for 1 week in the dark. After 1 week, gels were removed from their molds, washed in DI water for 1 hour in an attempt to quickly remove unreacted monomers to prevent contamination of measurement devices for measurements on Day 0. Gels prepared for measurement on Days 1 and 7 were subsequently washed/incubated in PBS (pH 7.4) prior to analysis.

2.2.5 Morphological Analysis

To analyze the micro-scale morphological features of each system, gels equilibrated in DI water were cut in half with a sharp razor, frozen at -80C and then lyophilized (freeze dried) until completely dry. Dehydrated gels were then sputter coated with a thin layer of metal (Au/Pd) and imaged using a scanning electron microscope (SEM) at various magnifications. SEM images taken at UNSW used a Hitachi S3400 (Hitachi High-Tech Corporation, Japan) while those taken at UW used a SNE-3200M (SEC Co., Ltd., South Korea).

2.2.6 Swelling Study

The effect of material composition on bulk hydration properties was assessed with block (i.e. non-porous) gel discs. A swelling study was carried out by measuring the weights of gels swollen in solvent and after lyophilization to calculate the swelling ratio via the following equation:

$$Swelling\ (\%) = (W_s - W_d)/W_d \times 100 \quad (1)$$

Here W_s refers to the weight of the gel in the solvent swollen state while W_d refers to the weight of the gel in the dehydrated state to calculate swelling ratio as a percent of the solvent

component absorbed into the gel with respect to the total mass of the polymer component. Swelling values equal to 100% indicate that the swollen gel contains the same mass of solvent as that of the polymer component in the swollen state.

The dry mass fraction of PEDOT:PSS incorporated during the *in situ* post-polymerization step was also calculated with the following equation:

$$PEDOT{:}PSS\ (wt\%) = (W_0 - W_{IPN})/W_{IPN} \times 100 \quad (2)$$

Here W_0 refers to the dry weight of the gel before IPN formation and W_{IPN} refers to the dry weight of the gel after IPN formation.

Lastly, the expected dry mass of several gel systems was calculated with the following equation:

$$W_{d*} = C \times V \quad (3)$$

Here W_{d*} refers to the expected weight of the gel in the dehydrated state, *C* refers the concentration of polymeric components in the gel (w/v) and *V* refers to the volume used in the fabrication of the gel.

2.2.7 Mechanical Compression

The effect of material composition on bulk mechanical properties was assessed with monolithic gel discs. The compression moduli of gels was measured via a compression testing with a TA|Electroforce 5500 (TA Instruments, Inc., Delaware) at UNSW or an Instron 5543 (Instron, Inc. Massachusetts) system at UW with a compression rate of 0.1mm/min to emulate previous studies investigating the compression modulus of brain tissue[77]. Compression modulus was obtained by calculating the slope of the linear region of the stress vs. strain curve around 10-15% compressive strain.

Raman Spectroscopy

PEDOT vibrational modes were measured via Raman spectroscopy using a Renishaw Raman Microscope with a 50x objective and 784nm laser at 0.5% power and scanned between 1170 and 1640 cm^{-1} wavenumbers. Exposure time was set to 30s with a total of 3 integrated scans/sample. Raw spectra were processed with Renishaw's WiRE 3.4 software by first subtracting the background signal with a linear background subtractor, smoothed, and then a peak picking function was run to isolate peaks. The wavenumber of the PEDOT peak centered between 1400-1450 cm^{-1} were compared between samples.

2.2.8 Conductivity

The effect of material composition on bulk conductivity was assessed with monolithic gel discs and a 2400 Keithley source meter (Keithley Instruments, LLC, Ohio). Gel discs hydrated in PBS (pH 7.4) were gently sandwiched between two metal plates which were connected to the source meter and a 100mV DC voltage was passed between them. Output current was recorded to determine ohmic resistance via R = I/V and then the material bulk resistivity was calculated via the following equation:

$$\rho = \frac{RA}{d} \qquad (4)$$

Here, ρ refers to the calculated resistivity of the material, d is the thickness of the material, R is the resistance determined from the input voltage and current measurement, A is the cross-sectional area of the gel disc. Conductivity, σ, was then calculated as $\sigma = 1/\rho$.

2.2.9 Electrochemical Characterization

Electrochemical characterization of materials was carried out with a potentiostat connected to electrodes in a 3-electrode cell containing PBS (pH 7.4) as the supporting electrolyte, a platinum mesh or wire as counter electrode, and a silver/silver-chloride (Ag/AgCl) reference electrode. Rod-shaped gel blocks 800µm in diameter were cut into 3cm long segments and equilibrated in PBS (pH 7.4) before being insulated with a 200µm thick layer of shrink-wrapped polyolefin such that one end of the insulation was flush with the end of the gel with the other end of the gel exposed from the insulation by ~1mm for connection to the potentiostat. Insulated gel rods were gently connected to the potentiostat via their exposed end with a flat alligator clip and served as the working electrode in the electrochemical cell. A 2mm diameter gold electrode or 1mm diameter platinum electrode served as working electrode controls. The potentiostats used were an eDAQ Electrochemical Impedance Analyzer z100, (eDAQ, New South Wales, Australia) at UNSW and a Metrohm Autolab PGSTAT204 (Metrohm AG, Switzerland) at UW.

Electrical impedance spectroscopy was carried out across 5-7 orders of magnitude with 5-10 points per decade and a sinusoidal potential at 50mV root-mean squared. Impedance at 1kHz was compared across gels for statistical analysis as this is a relevant frequency at which neuronal signals operate[78]. Cyclic voltammetry was carried out with a 50mV/s scan rate and cathodal chare storage capacity (CSC_C) calculated by taking the time integral of the cathodal (negative) current from a single scan cycle and then normalizing to electrode geometric surface area[78].

2.2.10 Statistics

For comparison of two-pot conductive hydrogels, paired T-tests were used to determine if statistically significant differences existed between samples of the same type before and after

PEDOT inclusion (e.g. H50 vs H50-E) with α = 0.05. Comparisons with p-values less than 0.05 were designated statistically significant and marked with an asterisk (*). One-way ANOVA was used to compare across sample types followed by repeated T-tests with a Bonferroni correction (α / # of comparisons) to account for multiple comparisons. Comparisons with p-values less than this corrected value were designated statistically significant and marked with a hash (#) or double hash (##) to designate specific comparisons. All experiments were run in triplicate with at least 3 gels per experimental repeat and data are reported as mean ± standard deviation.

2.3 Results and Discussion

2.3.1 Two-Pot Conductive Hydrogel Electrodes

2.3.1.1 Fabrication of Hydrogel Materials

The initial conception of the final device architecture of a wholly organic, immunomodulatory conductive hydrogel electrode involved applying the STS fabrication method to produce a porous penetrating microelectrode composed of a soft, conductive hydrogel material. Figure 3a depicts an example STS rod produced via the needle-punch method which has an ideal porous structure expressed on its surface and throughout its interior but varies greatly in shaft diameter. Conversely, Figure 3b depicts a rod produced by the capillary tube molding method which has highly uniform shaft diameter and good internal porous structure but moderate surface porosity. The two approaches yield devices with opposing properties: rods with highly uniform diameter will likely be easier to handle and penetrate the brain surface without bending or breaking while rods with highly uniform porous structure will

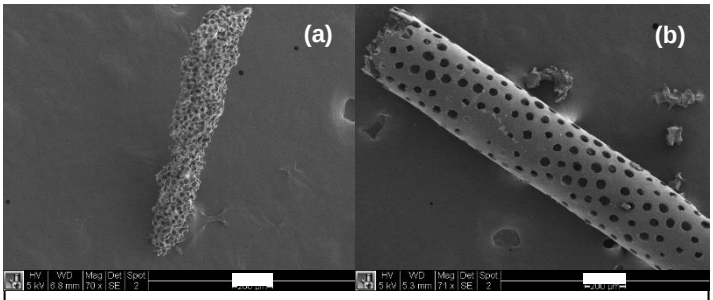

Figure 3: STS rods fabricated via the needle-punch (a) and capillary tube mold (b) methods (bars = 200μm).

likely enable a greater degree of immunomodulation to reduce scaring and improve regeneration across the tissue-implant interface.

This proof-of-concept validates that conductive hydrogel penetrating microelectrodes may be fabricated with a porous architecture. However, the assessment of this design by various scientific review panels indicates that this would be unlikely to perform well as a recording device given the large cross-sectional area required to adequately express the porous microstructure and the single-channel nature of the design. As such, the design thinking around the conductive hydrogels presented herein has pivoted toward designing materials that might be more readily applied to fabrication methods that enable small features and high channel count. That said, future innovations in 3D printing methods may allow for the production of penetrating electrodes which express some degree of porous microstructure while also integrating multiple recording channels such that this proof-of-concept design still holds merit for incorporation into the electrode design toolbox.

Furthermore, the use of rod-shaped hydrogels produced via these methods still provide a useful model for investigating how tuning various input parameters (i.e. pre-gel composition, pore size, etc.) impact material properties in the context of neural microelectrodes and tissue engineering. Therefore, the rod form-factor was used to characterize the electrochemical properties of non-porous conductive hydrogel electrode prototypes throughout this dissertation. Additionally, microporous shafts have been used to characterize the *in vivo* tissue response to various material properties and will be applied and discussed subsequently in Chapter 4.

First attempts at producing conductive hydrogel materials involved application of a two-pot fabrication method adapted from Naficy, et al.[56] Table 1 provides information regarding the nomenclature and composition of the gels tested in the following studies. Non-porous PHEMA gels were first fabricated as sheets or rods and then run through a secondary reaction to polymerize the conductive polymer complex PEDOT:PSS *in situ* throughout the gel network in

the production of an interpenetrating network (IPN) of polymer chains. Figure 4a shows hydrogel discs pre/post-IPN formation (top/bottom) in preparation for hydration and mechanical characterization. CNT and GR were incorporated into the pre-gel mixture in an attempt to improve gel conductivity. It should be noted that PHEMA alone is optically translucent but becomes black once organic conductive components are incorporated. That is, CNT and GR incorporation produced dark pre-gel solutions and gels prior to IPN formation due the dark black color of these nanomaterials, while the post-polymerization of PEDOT further darkened all gels. These differences are clearly observed between the gels in Figure 4a.

Table 1 Two-Pot HEMA-based Hydrogel Nomenclature and Composition

Gel Name	HEMA Monomer Concentration [%, v/v]	Organic Conductor
H50	50	-
H50-C	50	CNT[a)]
H50-G	50	GR[b)]
H50-E	50	PEDOT:PSS[c)]
H50-CE	50	CNT + PEDOT:PSS
H50-GE	50	GR + PEDOT:PSS

[a)] carbon nanotubes; [b)] graphene; [c)] poly(3,4-ethylenedioxy thiophene):poly(styrene sulfonate)

Figure 4b shows H50 rods prepared for electrochemical characterization pre/post-IPN formation (right vs. left groups) with shrink-wrap polyolefin insulation (left samples in each group). The circular tip of the lower end of each gel was exposed to control for electrode geometric surface area and a small section of shaft was exposed on the upper end to gently connect to a potentiostat via a flat alligator clip. Figures 4c and 4d depict a high magnification view of the tips of pre-IPN (Fig 4c) and post-IPN (Fig. 4d) gel rods which shows the gels flush with the polyolefin insulation, providing a degree of control over the geometric surface area of the electrode.

The geometric surface area (GSA) was estimated using the inner diameter of glass capillary tubes used to fabricate the gels (800µm diameter) at $GSA = \pi(0.04cm)^2 = 0.005cm^2$ as a first approximation. This GSA was used as a normalization factor when reporting results from electrochemical measurements, as is standardly done in the literature for planar electrodes. However, the 3-dimensionality of the conductive components within these conductive hydrogel electrodes suggests that perhaps a volumetric normalization factor might be more apt, discussed in detail below.

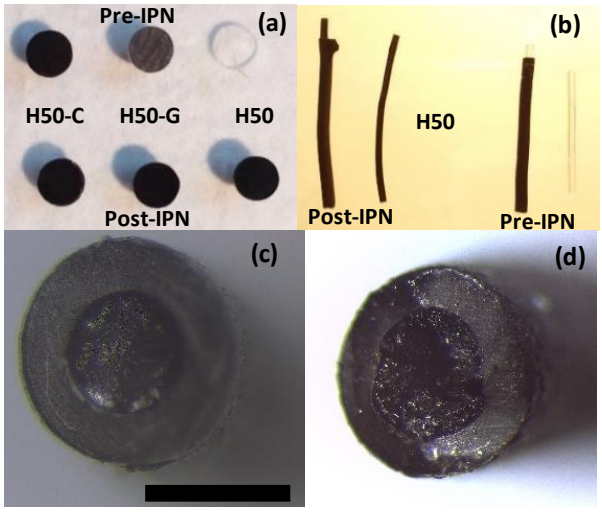

Figure 4: (a) Hydrogel discs pre/post-PEDOT IPN (top/bottom). (b) H50 rods pre/post-PEDOT IPN (right/left), left insulated. High resolution optical microscopy images of (a) pre-IPN and (b) post-IPN hydrogel rod tips insulated with polyolefin. Gel rod in (c) is dark due to shading but contains no organic conductors. Black bar in (c) is 1mm.

It is also worth mentioning here that attempts to fabricate conductive hydrogels with precise porous microstructure via the integration of the 2-step conductive hydrogel and STS fabrication methodologies produced unsatisfactory results. Figure 5 illustrates how the lack of

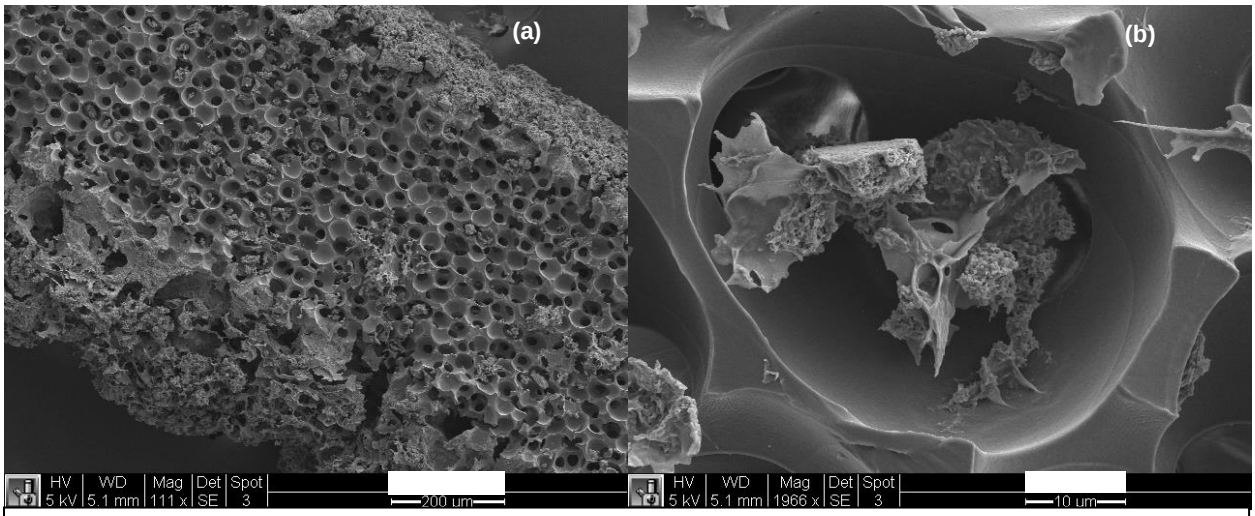

Figure 5: Low (a) and high (b) magnification SEM images of STS run through the two-pot conductive hydrogel synthesis process, providing little control over PEDOT:PSS particle localization. Bars are 200µm (a) and 10µm (b).

control over the localization of PEDOT:PSS formation during *in situ* polymerization produces porous networks filled with PEDOT:PSS particles. While these gels are highly conductive, this is a non-ideal result as these pores are designed to serve as a priming cue for immune cells to modulate their degree of inflammation. As such, it is expected that PEDOT:PSS-filled pores would inhibit this immunomodulatory priming signal, or introduce undesirable variation across samples, and thus result in poorer tissue integration *in vivo*. This provides a clear demonstration of the need for materials and synthesis methods which provide greater control over the device architecture while retaining a high degree of tunability over other material properties such as electrical activity. The development of such a novel synthesis method is discussed in detail in the next section.

2.3.1.2 Swelling Study

Characterization of hydrogel swelling before and after treatments provides information into changes in the interaction of the matrix with the solvent (e.g. hydrophilicity) and relative mobility of the crosslinked chains (i.e. matrix free volume)[79]. Incorporation of CNT or GR produced statistically significant increases in hydrogel swelling properties as seen in Figure 6 (blue bars), indicating that either the matrix has become more hydrophilic or there is an increase in matrix free volume. It is most likely that the sharp change in hydrogel opacity caused by the inclusion of CNT or GR into the pre-gel mixture had a significant, negative impact on photopolymerization efficiency. Considering all samples were UV irradiated for the same duration (12 mins), this reduction in polymerization efficiency would result in an attenuation of monomer conversion and thus an overall reduction in polymer chain formation and crosslinking for CNT and GR hydrogels. Subsequent wash procedures would remove unreacted monomer, thus leaving larger free volume within the hydrogel matrix for absorption of water molecules.

Interestingly, the degree of hydrogel opacity observed in Figure 4a for H50-C and H50-G correlates with changes in swelling ratio. That is, H50-C samples were more opaque than H50-G samples while also demonstrating swelling properties further from H50 which supports the notion of reduced matrix density as a result of reduced photopolymerization efficiency in more opaque samples. On the other hand, IPN formation does not have a statistically significant impact on swelling ratio between samples of the same type (orange vs blue bars) with swelling ratio values of 64.4 ± 2.4%, 89.9 ± 3.9%, and 74.6 ± 1.8% for H50, H50-C, and H50-G, respectively, and 67.5 ± 2.2%, 85.9 ± 5.2%, and 76.1 ± 4.3%. Given that PEDOT:PSS particles are forming among the PHEMA chains and thus reducing the free volume of the matrix, these data suggest that the PEDOT:PSS may increase the bulk hydrophilicity of the hydrogel proportional to the amount of PEDOT:PSS incorporated such that its overall capacity of the gel to swell is not significantly affected. PSS is highly hydrophilic and is used frequently as a dopant to make water-soluble PEDOT[80]. Conversely, the PEDOT:PSS particles may only have minor interactions with the solvent but do not significantly interact with the PHEMA matrix such that the overall swelling properties of the gel are still dominated by the hydrogel component.

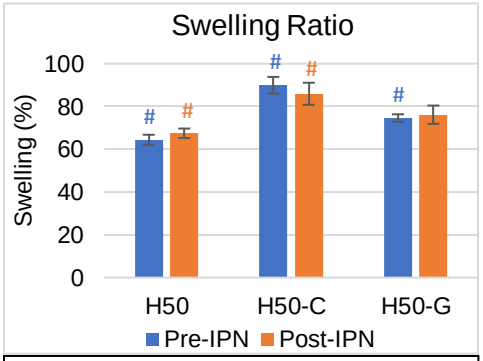

Figure 6: Hydrogel swelling ratio pre/post-PEDOT IPN formation.

Figure 7 provides a quantitative measure of the amount of PEDOT:PSS that was formed throughout the hydrogel matrices for each of the 3 gel compositions tested. The weight percent of PEDOT:PSS measured in these gels was 5.3 ± 1.6%, 8.6 ± 2.7%, and 7.5 ± 2.0% for H50-E, H50-CE, and H50-GE, respectively. The differences between the samples were not statistically significant, but the trends are consistent with the swelling observations. That is, the H50-C

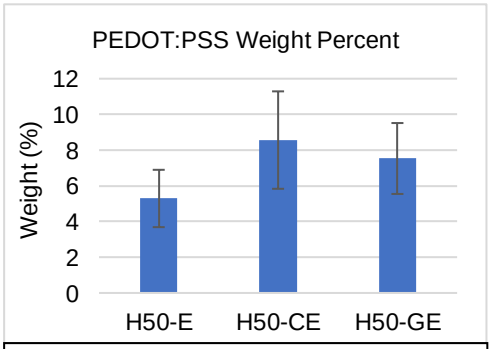

Figure 7: Degree of PEDOT:PSS (wt%) incorporated into gels post-IPN.

samples which produced the highest swelling ratio also enabled the highest degree of PEDOT:PSS formation, possibly due to the increased matrix free volume allowing for larger or a greater number of PEDOT:PSS particles. The degree of variability between the samples is large, potentially due to the resolution of the measurement technique or intrinsic variability in the synthesis procedure and makes it difficult to conclude the fine-grained impact that IPN formation has on gel hydration properties with the compositions tested. However, we may conclude with some confidence that the impact is relatively minor and that a high degree of control over the hydration properties of conductive hydrogels is retained when produced via this 2-step synthesis procedure.

2.3.1.3 Mechanical Compression

Characterization of hydrogel mechanical properties is important as mechanical compliance is one of the primary motivating factors for using this class of materials to robustly interface with delicate nervous tissue[25]. The goal is to develop a hydrogel that has a compression modulus approaching healthy brain tissue (~10 kPa)[26] while also retaining good control over material properties (i.e. electrical activity) of the final device. Figure 8 demonstrates that current synthesis parameters produce pre-IPN gels with compression moduli on the order of 100's of kPa at 1,302 ± 73 kPa, 764 ± 133 kPa, and 1227 ± 22 kPa for H50, H50-C, and H50-G, respectively (blue bars). Notably, the changes in compression modulus across these samples is inversely proportional to changes in their swelling properties which provides further evidence that there was a reduction in hydrogel matrix density for H50-C and

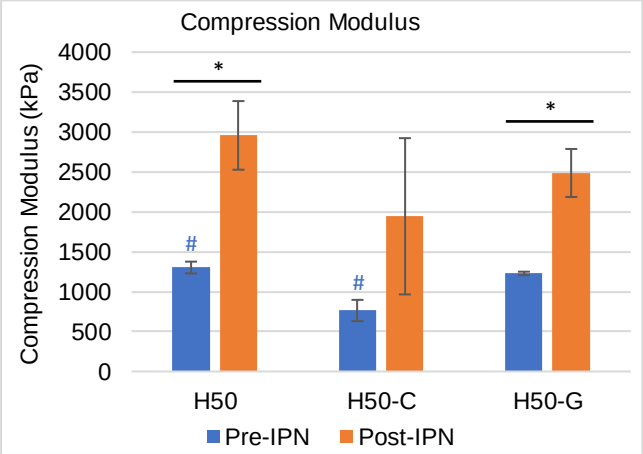

Figure 8: Hydrogel compression modulus pre/post-PEDOT IPN (blue/orange).

H50-G compared to H50. Conversely, while IPN formation does not appear to have a significant impact on swelling, it does have a statistically significant impact on compression modulus at 2956 ± 429 kPa, 1943 ± 978 kPa, and 2486 ± 300 kPa for H50-E, H50-CE, and H50-GE, respectively (orange bars).

PEDOT:PSS is known to have relatively stiff mechanical properties due to the conjugated PEDOT backbone[81]. It is likely that PEDOT:PSS chains physically contact the PHEMA matrix upon compression to impart rigidity to the overall polymer network, thus increasing the bulk hydrogel compression modulus. The large variation in compression modulus for H50-CE samples is likely due to variations in HEMA polymerization within H50-C gels which produces variable matrix free volume that is thus propagated to variability in PEDOT:PSS particle size within the matrix. It is also interesting to note that the degree of variation within sample types is proportional across each mode of measurement discussed thus far. For example, a similar degree of variation in swelling ratio of H50-C samples is observed in the mechanical properties and amount of PEDOT:PSS within the gel. In any case, these data demonstrate that a modification of synthesis parameters is needed to produce conductive hydrogels with moduli closer to that of brain tissue. Some possible modifications include a reduction in concentration of the hydrogel component in the pre-gel solution, a reduction in crosslinker density, and/or alterations to the structural interactions of PEDOT and other polymer chains.

2.3.1.4 Electrical Impedance Spectroscopy

The electrochemical properties of hydrogel rods have been investigated as a proof-of-concept that these materials may serve as stand-alone (i.e. excluding a stiff silicon or metallic substrate) conductive hydrogel electrodes. Electrical impedance was measured to investigate the charge transfer characteristics of the pre- and post-IPN gels. In general, low impedance values are desirable for neuronal recording applications to detect extracellular neuronal signals that

occur within the microvolt range[78]. Figure 9a demonstrates representative impedance spectra of these gels across a wide range of excitation frequencies. Modest reductions in impedance were observed across all frequencies for H50-C and H50-G gels compared to H50 gels (solid lines) which may be due to the incorporation of CNT and GR improving the electrical activity of the gels. However, the differences between H50, H50-C and H50-G are roughly proportional to the differences observed in the swelling ratio between these gels, suggesting that the overall density of the gel matrix likely contributes to the gels' impedance.

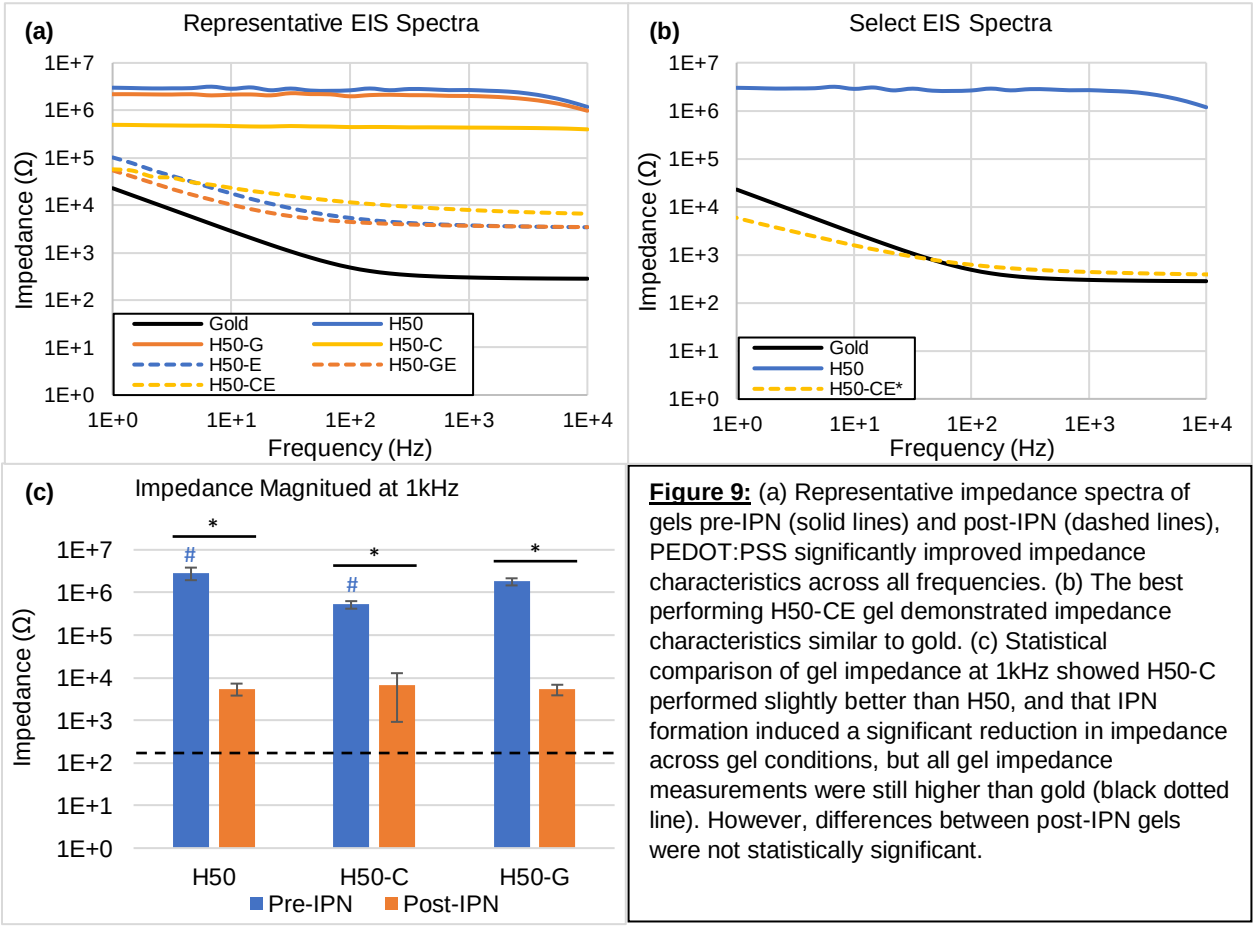

Figure 9: (a) Representative impedance spectra of gels pre-IPN (solid lines) and post-IPN (dashed lines), PEDOT:PSS significantly improved impedance characteristics across all frequencies. (b) The best performing H50-CE gel demonstrated impedance characteristics similar to gold. (c) Statistical comparison of gel impedance at 1kHz showed H50-C performed slightly better than H50, and that IPN formation induced a significant reduction in impedance across gel conditions, but all gel impedance measurements were still higher than gold (black dotted line). However, differences between post-IPN gels were not statistically significant.

A less dense polymer network may enable a greater degree of ionic conductivity within the gels in the presence of an externally applied voltage which would act to reduce the magnitude of the measured impedance. That the impedance characteristics of these gels are frequency-independent also suggests that the system is behaving like an ideal resistor with little to no

capacitive current. If this were the case, then gel density may be serving as a kind of ideal resistance parameter.

Figure 9a also demonstrates that incorporation of PEDOT:PSS into H50-E, H50-CE, and H50-GE gels (dashed lines) enabled a more drastic reduction in impedance over a broad range of frequencies. However, the differences in impedance observed between the groups was greatly diminished with all IPN groups producing similar spectra. This suggests that PEDOT:PSS became the primary charge carrier and that minor differences in ionic conductivity induced by the density of the hydrogel matrix were overwhelmed by the addition of a connected pathway of highly electrically active PEDOT:PSS particles. This provides further evidence that the differences observed between H50, H50-C, and H50-G are primarily due to differences in gel density as no significant synergistic effects of the CNT, GR and PEDOT:PSS were observed on average.

However, Figure 9b depicts an extreme outlier from the H50-CE group, H50-CE*, which produced an impedance spectrum in the same order of magnitude of the gold control electrode. It may be that the H50-C system, though highly variable, was actually quite near an electrical percolation threshold such that the CNT and PEDOT:PSS were able to act synergistically in this single gel to provide a highly efficient path for electrical current to flow. Or perhaps this gel was significantly less dense than other H50-C gels, thus enabling larger PEDOT:PSS particle formation, or some combination of the two. Unfortunately, however, this result was not reproducible across several experimental repeats. The incorporation of a higher weight percent of CNT or GR may act to improve the reproducibility of results like these. However, adding significantly more CNT or GR to the pre-gel mixture does not reliably produce gels that can be physically manipulated due to the significant reduction in polymerization efficiency. This presents a trade-off between conductivity and gel formation that ultimately places a physical limit on the total amount of black, carbon-based nanomaterial that can be included into the pre-gel solution for photochemically polymerized gels.

Lastly, to provide a more rigorous statistical analysis of impedance across these gels, Figure 9c compares the impedance measured at 1kHz between gels as this is a relevant frequency for recording neural circuit activity[78]. As discussed above, incorporation of CNT, but not GR, produced a statistically significant, order of magnitude reduction in the impedance compared to H50 at 2.9 ± 0.9MΩ, 0.5 ± 0.1E6Ω, and 1.8 ± 3.4MΩ for H50, H50-C, and H50-G, respectively (blue bars). Interestingly, the variation in impedance for H50-C gels was not as large as observed for other measurements, though large variation for H50-CE gels was readily observable. IPN formation produced a statistically significant reduction in impedance for all gels compared to their pre-IPN controls, reduced by 3 orders of magnitude down to the single kOhm range at 5.5 ± 1.7kΩ, 6.8 ± 5.9kΩ, and 5.3 ± Ω for H50, H50-C, and H50-G (orange bars). However, these values are still two orders of magnitude larger than gold (300 Ω). There was no statistically significant difference between post-IPN gels (orange bars), again indicating that PEDOT:PSS became the primary charge carrier regardless of the pre-IPN gel conditions.

2.3.1.5 Cyclic Voltammetry

The measurement of an electrode's current density in response to the application of a potential cycle allows for a measure of its ability to pass and store charge[78]. The cathodal charge storage capacity (CSC_C) of an electrode is a useful value to quantify as it correlates with the magnitude of the voltage transient delivered during a stimulation pulse. A high CSC_C is desirable for neural stimulation applications to enable sufficient charge delivery to excite neurons while remaining within voltage ranges that limit tissue damage and electrode corrosion[78]. Figure 10 demonstrates that the trends seen across previous characterization techniques hold similarly for CSC_C for the conductive hydrogel electrodes tested here. Figure 10a presents representative cyclic voltammograms (CV) for each of the pre-IPN gel groups in which an increase in overall current density and charge storage capacity, visualized by the open shape of the CV curve, was observed for H50-C and H50-G gels compared to H50.

Figure 10b presents CV curves for the respective post-IPN gels which demonstrated an increase in current density by up to 3 orders of magnitude. The open area of these curves was also much wider which is also indicative of a proportional increase in charge storage over the pre-IPN control gels. Here again, as for the impedance spectra, the impact of PEDOT:PSS far outweighed the contributions of CNT or GR within the gels. However, Figure 10c demonstrates the CV curve for the outlier gel, H50-CE*, also produced a much greater increase in current density and charge storage capacity compared to the other post-IPN gels.

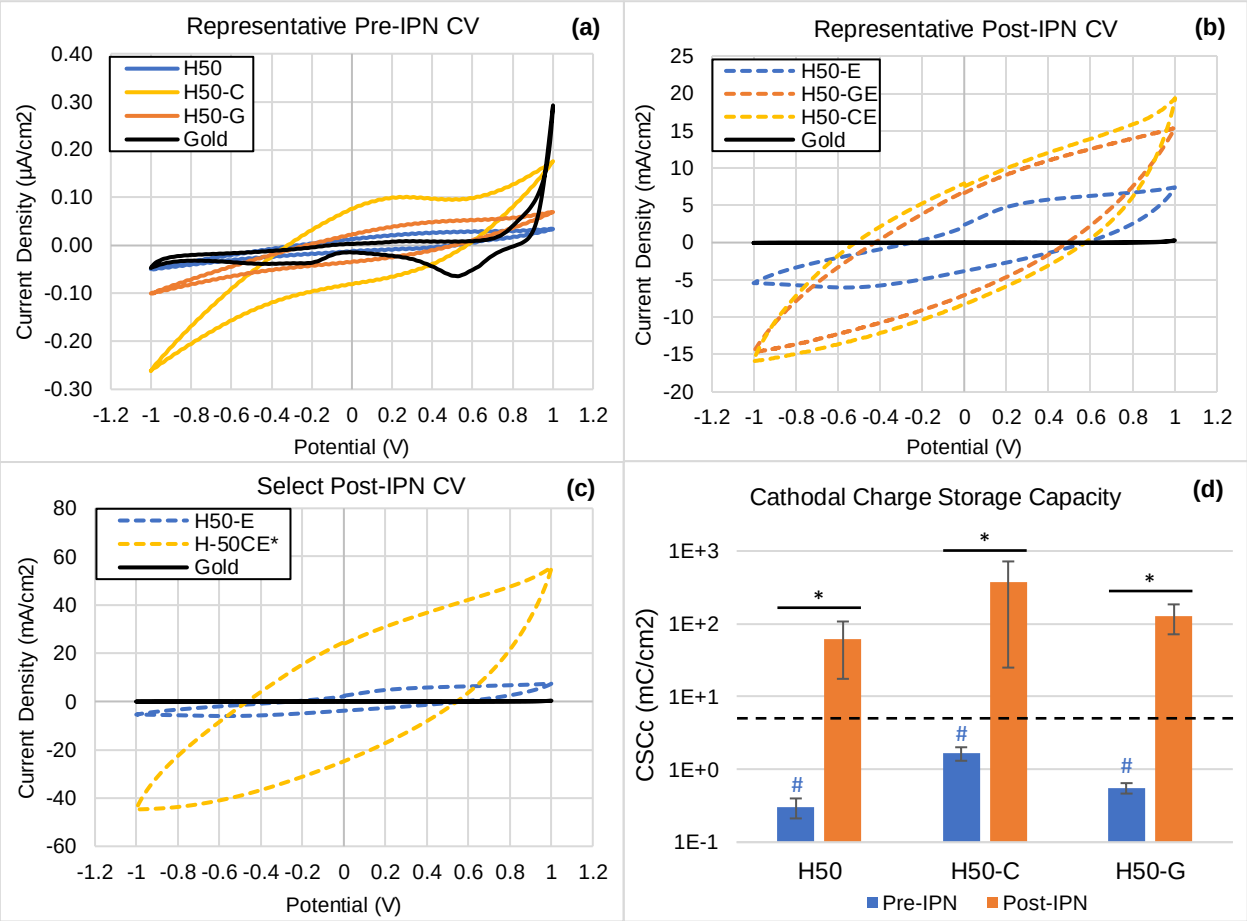

Figure 10: Representative CV scans of pre-IPN gels (a) and post-IPN gels (b) demonstrating IPN formation significantly increased current density and charge storage (open area of curves). Note the 3 order of magnitude difference in scale of the y-axis between (a) and (b). Representative CV scan of best performing H50-CE gel (c) demonstrated a drastic increase in current density and charge storage. (d) Statistical comparison of gel cathodal charge storage capacity (CSC_C) demonstrates moderate but significant differences between pre-IPN gels with a much larger, statistically significant increase in CSC_C post-IPN. Post-IPN gels also significantly outperformed gold (black dotted line). However, differences between post-IPN gels were not statistically significant.

It is also worth noting that while gold is an excellent conductor with a very low impedance across a broad range of frequencies, the conductive hydrogel materials presented here far outperform it in terms of current density and charge storage capacity. That said, the normalization factor used here was the 2D geometric surface area introduced above which may not be sufficient to capture the differences in charge transfer between a planar metallic electrode and a 3D polymeric electrode. Future experiments designed to deepen the investigation into the impact of gel dimensions (e.g. volume, length, cross-sectional area, etc.) on electrochemical properties is warranted to elucidate these differences.

Lastly, for statistical comparison across groups, Figure 10d demonstrates that incorporation of CNT in H50-C gels produced a statistically significant increase in CSC_C as compared to H50 alone, as did incorporation of GR in H50-G gels though to a lesser degree at 0.31 ± 0.1mC/cm^2, 1.66 ± 0.3mC/cm^2, 0.56 ± 0.1mC/cm^2 for H50, H50-C, and H50-G, respectively (blue bars). A dramatic increase in CSC_C was observed upon IPN formation (orange bars) exceeding that of gold, though differences between groups were not statistically significant at 62.5 ± 45.0mC/cm^2, 372.0 ± 347.0mC/cm^2, 128.3 ± 56.5mC/cm^2 for H50-E, H50-CE, and H50-GE, respectively. Another factor that may be impacting the electrochemical properties of these materials is the presence of a Pluronic F127 monolayer that may remain on the CNT/GR particles after washing. While Pluronic F127 serves as an excellent surfactant to produce aqueous suspensions of CNT/GR, it may also be inhibiting these particles from interacting electrically with one another and PEDOT:PSS chains, thus reducing their ability to pass current. PSS has also been explored as a surfactant for CNT/GR and preliminary results indicate that it produces good aqueous CNT/GR suspensions and thus may also improve the interaction of PEDOT:PSS chains upon IPN formation.

2.3.1.6 Conclusion

The materials produced and characterized in the studies discussed above have properties which are desirable in application to neural electrodes, particularly their electrochemical properties. However, the relatively large increase in mechanical properties of the conductive hydrogels produced by the two-pot synthesis method and the inapplicability of the method to the fabrication of precision porous scaffolds indicate that the need for softer electronic materials and facile synthesis methods remains. The following section will discuss the development of a one-pot conductive hydrogel synthesis method aimed at resolving these issues.

2.3.2 One-Pot Conductive Hydrogel Electrodes

2.3.2.1 Fabrication of Hydrogel Materials

As discussed above, there is a need for new methods for the synthesis of conductive hydrogels that can be produced with arbitrarily complex architecture, provide good control over tuning final gel properties, and can be applied to high throughput manufacturing techniques for the fabrication of high-channel count microelectrode arrays. The novel synthesis procedure presented here aims to provide a platform for addressing these needs simultaneously by integrating all the necessary components into a single vessel for reaction in parallel. At first glance, this synthesis procedure utilizes the same basic principles as the 2-pot conductive hydrogel synthesis procedure described above: photopolymerization of a methacrylate-based hydrogel system alongside *in situ* oxidative chemical polymerization of conductive monomers. However, the reaction of these components in parallel within a single vessel appears to incur a set of chemical interactions which may be engineered to produce beneficial or synergistic outcomes. The following sections introduce this one-pot synthesis method, characterize the resultant materials, and discuss the nature of these chemical interactions and their implications in optimizing the method and its applicability to neural electrode design.

The first notable result of this one-step conductive hydrogel synthesis methodology involves its successful application to the STS fabrication process. The integration of all components in a layered set of solvents enables the system to be solution processable and easily drawn into the void space of the sintered PMMA bead network for photopolymerization. Figure 11 shows the results of this process in the production of an STS sheet imaged with SEM at two

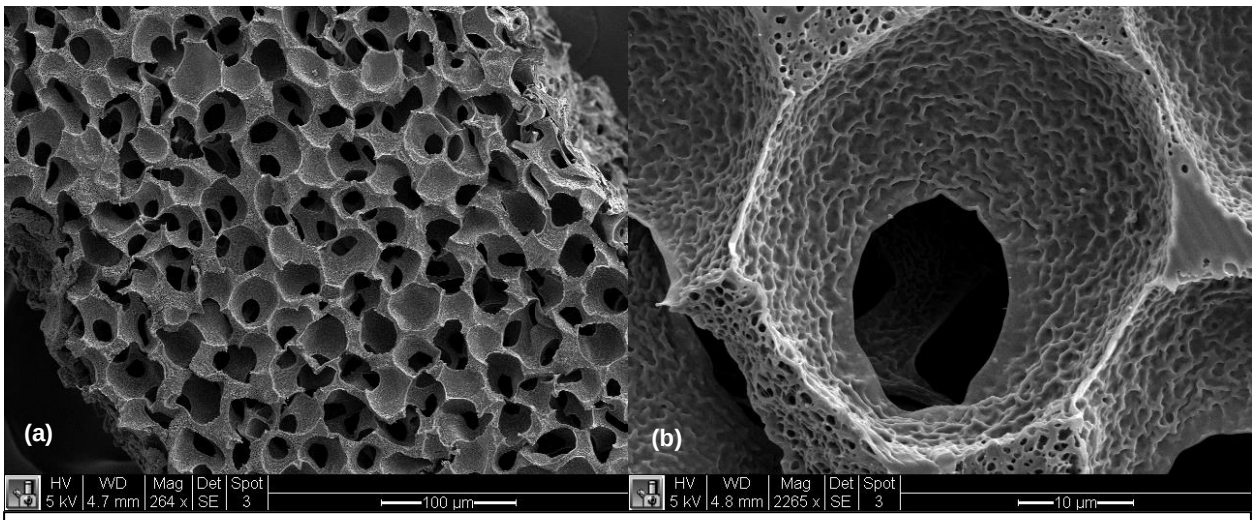

Figure 11: Application of one-pot conductive hydrogel synthesis method to the STS fabrication process. (a) Low magnification SEM image of STS cross section demonstrating no adverse PEDOT particle growth within pores. (b) High magnification SEM image of STS pore demonstrating microstructure and micropore formation on the order of 1µm throughout the material.

different magnifications. At lower magnifications, a cross section of the precision porous network can be seen to be adequately expressed without the uncontrolled growth of PEDOT particles. The high magnification image depicts the cross section of a single pore with a roughened inner surface and much smaller pores on the scale of 1µm dotted throughout the gel. Some of the side reactions mentioned above may be producing gaseous by-products which could be inducing the creation of these structures. These microstructural artifacts may be beneficial for cell adhesion/migration or nutrient diffusion when implanted *in vivo* and thus may serve as a design feature that can be utilized productively. Lastly, the STS fabrication process provides a useful

model for demonstrating the capability of the one-pot system to produce gels with arbitrarily complex geometries.

Another notable aspect of this synthesis methodology involves the consequence of integrating two radically different polymerization initiation and growth mechanisms into a single vessel, enabling what appears to be the rapid photochemical polymerization of PEDOT. Figure 12 displays the results of this photochemical polymerization process for a HEMA-based

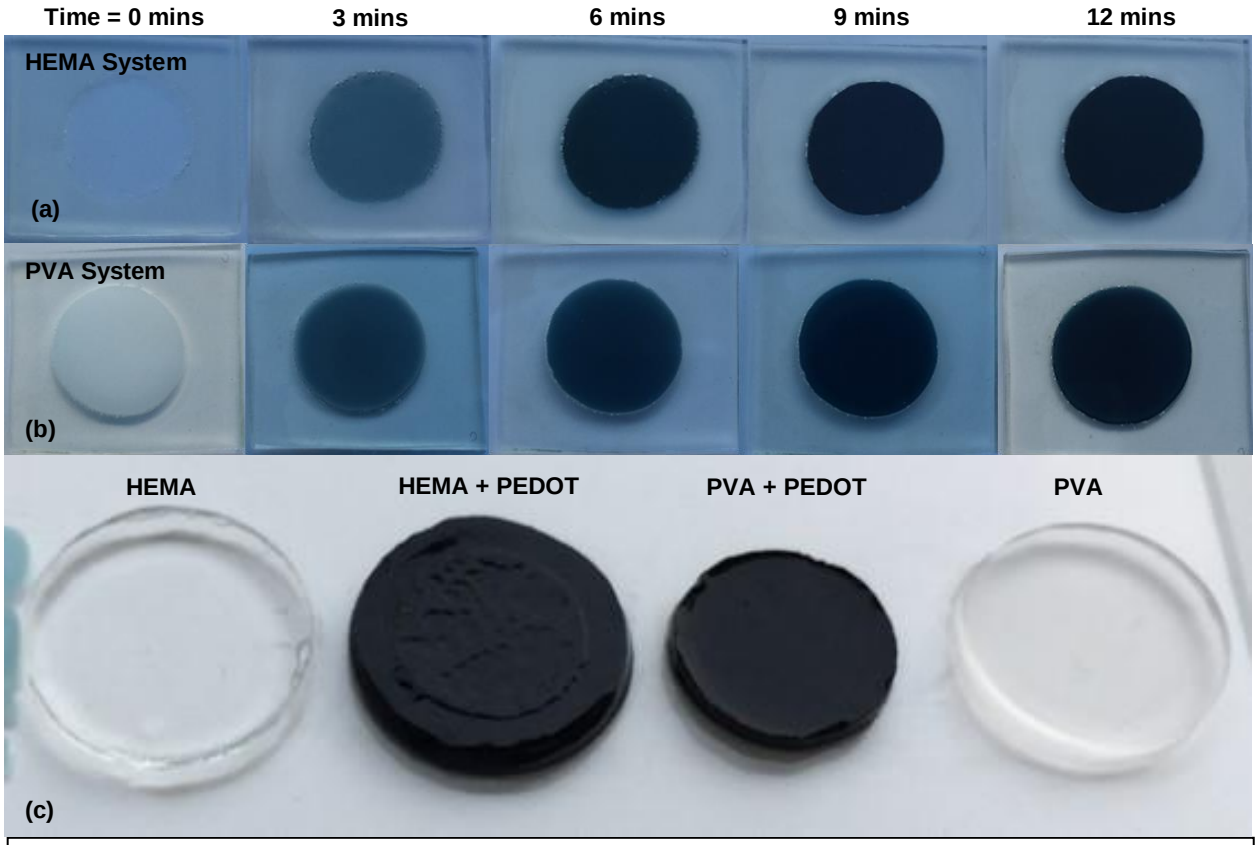

Figure 12: Time series of photochemical polymerization of HEMA-based gels (a) and PVA-based gels (b). The one-pot conductive hydrogel synthesis method enables rapid photochemical polymerization of PEDOT alongside the hydrogel component, but also increases gelation time from 3 minutes to 12 minutes. (c) Discs of all four gel systems at their PBS swelling equilibrium.

monomeric gel system (Fig. 12a) and a PVA-based macromeric gel system (Fig 12b) exposed to UV radiation for 12 minutes, visualized at 3-minute intervals. Figure 12c depicts discs of gels produced via the one-pot synthesis method at their swelling equilibrium in PBS (pH 7.4). Details

of the chemical composition and deeper characterization of these HEMA- and PVA-based materials are presented in the following section.

It is worth noting that the PEDOT-containing HEMA system was highly soluble and thus was transparent while the PEDOT-containing PVA system exhibited a slight degree of precipitation and thus was an opaque white color prior to polymerization. However, both systems transitioned from light blue to dark blue to black over the course of the 12-minute irradiation period which is classically indicative of PEDOT polymerization. Interestingly, PEDOT chemical polymerization with an oxidative initiator such as APS typically requires hours to days to produce high polymer yields. Additionally, incorporation of EDOT and APS into the pre-gel solution caused a significant decrease in the photopolymerization efficiency of the hydrogel component. This was observed clearly in the gelation time required for the non-conductive vs. conductive systems with an extension of time to gelation from 3 to 12 minutes for gels lacking and including EDOT, respectively.

Taken together, these observations suggest that there is an interaction occurring between the polymerization mechanisms, perhaps at the level of the photo- and oxidative initiators, that caused an increase in EDOT polymerization and a decrease in methacrylate polymerization. Photoinitiators as a chemical class are designed to have optical absorbance peaks at specific frequencies. When exposed to light at or around those frequencies, the species dissociate to form molecular free radicals that may initiate a polymerization cascade, typically involving initial attack of a vinyl (double bond-containing) monomer (e.g. various acrylates and methacrylates). This initial vinyl activation then rapidly propagates across other vinyl groups to form long polymer chains[82].

Conversely, in oxidative chemical polymerization the initiator species dissociates (most often spontaneously in an aqueous solution) to produce a molecular radical that instead oxidizes another chemical species, such as a conductive monomer, via the removal of an electron[83]. This

stabilizes the initiator, often in the production of an anion, while leaving the conductive monomer as a cationic radical that then reacts with another oxidized cationic radical with the release of protons to form a neutral dimer. A major difference between these mechanisms involves the lack of radical propagation in the oxidative polymerization case. That is, to produce oligomers or polymers via oxidative polymerization, the dimer species must be oxidized by another oxidative initiator as all species from the previous reaction step end up as stable ions or neutral species. This imposes drastic differences between the two reaction mechanisms on both the overall rate of the polymerization reaction and the ratio of monomer to initiator species necessary to effectively produce a high yield of long polymer chains.

In the one-pot system presented here, production of free radicals via photoinitiation may be acting upon the persulfate species to increase the rate of oxidation of EDOT monomer species to accelerate PEDOT polymerization while consuming photoinitiator species and thus slowing methacrylate polymerization in the process. Interestingly, the mechanism of methacrylate polymerization and crosslinking was very different between the monomeric HEMA and macromeric PVA systems in terms of vinyl density, crosslinking density, and size and concentrations of monomeric/macromolecular units, but analogous effects on polymerization dynamics were observed across both systems. That said, the resulting gel properties were quite different, as detailed in the next section.

Qualitative experiments were also run using the HEMA system by excluding various species from the pre-gel mixture to observe the effect on the resulting gel. Exclusion of the oxidative initiator APS enabled rapid gel formation via photopolymerization but the resulting gel was a white, opaque color, indicating that micelles or a precipitate formed during the reaction and that PEDOT was not formed. Conversely, when the photoinitiator Irgacure 651 was excluded, the gel was no longer photopolymerizable but did produce a light bluish gel with weak mechanical properties after several days in ambient conditions on a benchtop. This suggests that

polymerization of both hydrogel and conductive polymer components occurred but with poor efficiency. This was perhaps expected as APS is also known to serve as an initiator of free radical polymerization with heat as an energy source[84]. Furthermore, a mixture of EDOT and Irgacure 651 alone did not produce any significant changes when exposed to UV light or extended periods in ambient conditions, indicating that the molecular free radicals formed by the photoinitiator are insufficient at initiating EDOT polymerization alone.

Solvent selection was also investigated in a set of qualitative experiments to determine the best cosolvent with water. Solvents tested included methanol, ethanol, isopropanol, ethylene glycol (EG), dimethyl sulfoxide (DMSO), acetonitrile, and low molecular weight poly(ethylene glycol) (PEG200). Methanol, ethanol, and isopropanol appear to preform equally well out of all the solvents tested by most easily producing a uniform solution with all components entirely miscible. EG and DMSO were not able to produce uniform solutions, both producing some degree of precipitation. This still enabled gel formation and thus could still be applied in this methodology, but also added an additional dimension that would need to be designed/optimized over (precipitate/micellular size and structure, etc.) and thus was excluded for experimentation in these studies. Future work examining the impact of controlled precipitation in this one-pot system with purposeful design of limited solubility solvents is warranted as this factor may also play a significant role in the final gel properties.

Acetonitrile also produced nicely uniform solutions but is not an orthogonal solvent for PMMA such that it could not be readily applied to the STS fabrication process and thus was also ultimately excluded. Lastly, PEG200 produced a uniform solution and performed well until washed at which point the gels swelled an enormous amount due to the low water content of the pre-gel solution compared to the combined hydrophilicity of PHEMA and PEG200 chains. After about an hour the gels began to deswell, likely as a result of the diffusion of PEG chains out of the gel, but

the gels were deformed and a large portion of PEDOT also left the gel. Therefore, PEG200 was also excluded.

Similar results were observed when utilizing these solvents for the PVA system except that ethanol seemed to preform slightly better than the other alcohols to produce a uniform solution when heated to 80C. Therefore, ethanol was chosen for the synthesis of PVA gels in these studies. Methanol was chosen as the cosolvent for the HEMA system for consistency considering all initial tests with the HEMA system utilized methanol as the cosolvent. While this investigation provided information on a selection of solvents to use for these systems, the search was not exhaustive so there may be other solvent combinations that would outperform those tested here, especially in the context of other conductive hydrogel systems.

Interestingly, others have developed methods for photopolymerization or photochemical polymerization of conductive polymers. However, to the best of my knowledge, each of these mechanisms investigated has specific requirements (or combination thereof) that limit their generalized application such as: relying on the specific excitation of electrons in the monomer molecule along with a suitable electron acceptor[85]; only working within a very narrow range of highly toxic oxidants which are subsequently impossible to remove from the resulting polymer[86]; require many day reaction durations[86]; are prepared in solution but only generate thin films of polymer on the edges of the reaction vessel[87]; or require unique monomeric species whose initiation and polymerization mechanism are also highly unique and specialized[88]. Furthermore, as far as can be determined upon an in depth but by no means exhaustive literature review, none of these mechanisms have been utilized with the goal of synthesizing a bulk conductive hydrogel in a single reaction vessel, let alone in application to neural electrode devices. Lastly, oxidants, such as APS, have been investigated for their ability to decompose photochemically, particularly in use as waste management or treatment processes, but these techniques require high energy

photons with wavelengths at or below 250nm and still require several hours for complete dissociation and reaction[89].

The methodology described herein therefore demonstrates novelty in two ways: 1) in its application as a rapid, solution processible polymerization method for conductive polymer synthesis that is expected to be generalizable across a wide range of conductive monomers susceptible to oxidative polymerization via persulfate initiators (and perhaps other oxidative initiators as well); and 2) in its application to the fabrication of methacrylate-based conductive hydrogels in a single step. The following sections will present and discuss results from the development, quantitative characterization, and tunability of a variety of materials produced via this methodology.

2.3.2.2 Applicability of the One-Pot Synthesis Method to Monomer vs. Macromer Systems

I had the distinct opportunity to travel to Australia to engage in an academic internship with Drs. Laura Poole-Warren and Penny Martens at the University of New South Wales to develop my novel one-pot conductive hydrogel synthesis method and investigate its applicability to the production of hydrogels from both monomeric an macromeric precursors. This section will discuss in detail the impact of this method on final gel properties when applied to these two distinct gel systems.

The PVA-based conductive hydrogel system introduced above was developed by Goding et al[30]. in the lab of Dr. Poole-Warren. The PVA macromer contained immobilized methacrylate groups for crosslinking and immobilized amino acid taurine residues to provide sulfonic acid moieties to serve as a dopant for PEDOT. Goding et al. demonstrated that this PVA system could be photopolymerized onto electrode contacts followed by electrochemical polymerization of PEDOT to form a highly conductive hydrogel coating on the electrode which improved its

electrochemical properties. Interestingly, an analogous conductive hydrogel system utilizing immobilized heparin methacrylate as a dopant demonstrated success in improving signal quality when applied to cochlear implants[90]. A key feature of this PVA system involved the distribution of immobilized anionic dopant moieties throughout the hydrogel network which promoted the growth of the PEDOT chains throughout the gel as opposed to concentrated locally on the electrode contact surface. The principle of immobilized dopant molecules throughout the hydrogel network was translated to the HEMA system via the inclusion of a small concentration of monomeric dopants which would be integrated throughout the hydrogel network upon polymerization.

Table 2 lists the four experimental groups that were fabricated and characterized in the following studies based on the monomeric HEMA and macromeric PVA systems introduced above. The nomenclature for the gel groups presented here and throughout this dissertation are based on the respective compositions of the pre-gel mixtures. For example, the monomeric PEDOT-free and PEDOT-containing HEMA groups were labeled H50C and H50C-2.5E, respectively, indicating the use of the HEMA hydrogel monomer, 50% monomer concentration, MA as an immobilized dopant (carboxylic acid, $-COO^-$ dopant moiety), and exclusion or inclusion of 2.5% (v/v) EDOT. The PVA system was adapted from Goding et al. (2017) and was synthesized at approximately 8% (w/v) macromer concentration with taurine as an immobilized dopant (sulfonic acid, $-SO_3^-$ dopant moiety), excluding or including EDOT and labeled as PVA or PVA-2.5E, respectively.

Table 2 Pre-gel compositions for experiments investigating impact of a monomer vs. macromer hydrogel system on materials produced via the one-pot synthesis method.

Gel Name	Hydrogel Concentration [v/v, %]	Dopant Selection	Dopant Concentration [mol/L]	EDOT Concentration [%]
H50C	50	AA ($-COO^-$)	0.25	0
H50C-2.5E	50	AA ($-COO^-$)	0.25	2.5
PVA	8	Taurine ($-SO_3^-$)	0.1	0
PVA-2.5E	8	Taurine ($-SO_3^-$)	0.1	2.5

2.3.2.2.a Morphological Analysis

Morphological analysis of the HEMA and PVA systems were carried out via SEM to investigate the impact of the one-pot synthesis method on gel microstructure. Figure 13 provides some insight into the possible growth mechanics of the hydrogel and conductive polymer components. Figures 13a and 13c depict cross sections of the H50C and PVA gels, respectively. The H50C gels showed a small degree of porosity on their surfaces but were otherwise considerably monolithic. Conversely, PVA gels were all extremely porous, which was expected due to the low gel density of the pre-gel solutions. Interestingly, the porous networks were both completely 'filled' for the H50C-2.5E and PVA-2.5E gels, as shown in Figures 13b and 13c, respectively, likely due to the growth of PEDOT throughout the porous networks. The large increase in porosity due to the low gel density of the PVA system likely enabled a significant increase in the interconnection of PEDOT chains and particles throughout the PVA-2.5E gels.

However, no significant macroscopic particle formation was observed throughout either of the gels, at least at the magnifications examined here. This suggests that the networks of PEDOT that formed were composed of small particles or that they were interacting with the PVA chains in some manner during polymerization to create a uniform distribution of interconnected PEDOT

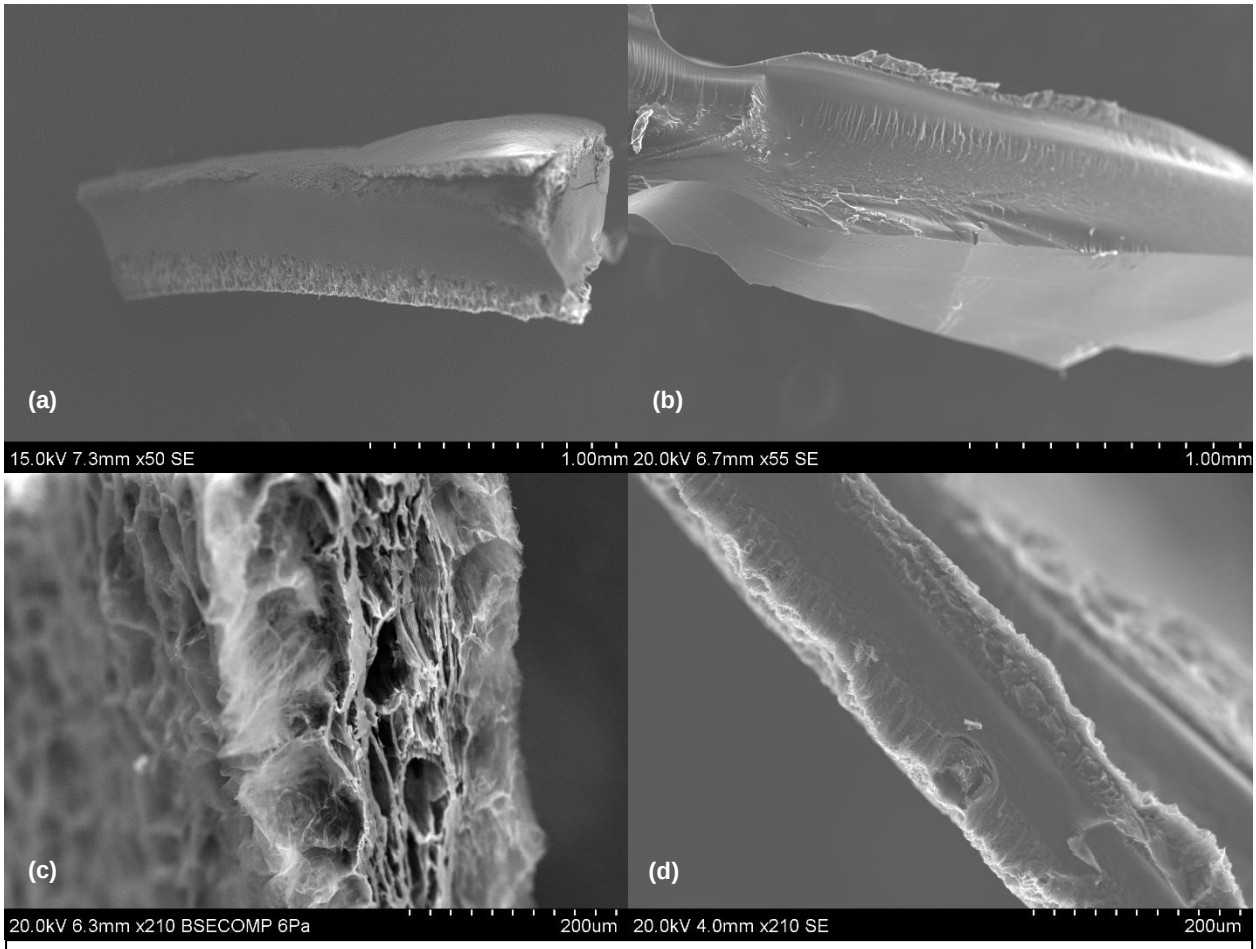

Figure 13: SEM images of H50C (a), H50C-2.5E (b), PVA (c), and PVA-2.5E (d). PVA gels are by far the least dense as can be seen by the large porous network throughout the gel cross section. H50C gels also show some porosity on the top and bottom surfaces. Both H50C-2.5E and PVA-2.5E gels are completely non-porous, but no PEDOT particles are observable at the magnifications used here.

chains. Future work utilizing higher resolution imaging techniques, such as tunneling electron microscopy, or ones that can distinguish between conductive and non-conductive regions within a polymer network, such as conductive atomic force microscopy, will provide deeper insight into the arrangement of these structures.

2.3.2.2.b Swelling Study

To assess the impact of the one-pot method on hydration properties a swelling study time course was conducted using PBS (pH 7.4) as a physiologically relevant hydration medium. Figure 14a illustrates the swelling ratio of the HEMA and PVA systems over the course of 7 days to determine the dynamics of solvent interaction. The first notable observation is in the drastic difference in swelling between the HEMA and the PVA systems. This difference was expected given the differences in gel density due to differences in hydrogel concentration and crosslinking density in the respective pre-gel solutions. The HEMA system had ~5-fold larger concentration of the hydrogel component and ~3-fold larger crosslinking density as compared to the PVA system which resulted in a ~4.7-fold reduction in swelling ratio. When exposed to the PBS wash medium, the PVA gels deswelled while the PVA-2.5E gels swelled as the alcohol-water mixture which served as the pre-gel cosolvent was exchanged over the 7-day incubation period. Conversely, both the H50C and H50C-2.5E gels swelled upon interaction with the PBS wash medium, though at different rates of solvent exchange. The equilibrium swelling ratios were recorded at 1172.5 ± 55.1% and 1088.3 ± 69.2% for PVA and PVA-2.5E, respectively, and 251.1 ± 9.4% and 204.9 ± 24.7% for H50C and H50C-2.5E, respectively.

The second notable observation is that, while the dynamics of how the gel systems approach their swelling equilibrium differ quite significantly across each system, the equilibrium swelling ratio of both conductive systems, H50C-2.5E and PVA-2.5E, demonstrated only minor reductions compared to their non-conductive controls, H50C and PVA, respectively. However, though minor this difference between conductive and non-conductive gels was statistically significant for all gels except on Day 0 for H50C vs. H50C-2.5E gels. This suggests that, unlike the two-pot system, the PEDOT chains grown in the one-pot system may be interacting more significantly with the hydrogel matrix to have a minor, though observable, impact on its interaction with the solvent. This may be a result of immobilizing the dopant molecules throughout the

hydrogel network, thus inducing closer association of the PEDOT chains to the hydrogel chains. This association could lower the overall hydrophilicity of the gel by neutralizing the highly hydrophilic anionic dopant moieties as they dope the PEDOT chains, and by bringing the more hydrophobic PEDOT molecules in proximity to the hydrogel matrix, thus impacting its ability to interact with the solvent.

That said, that these differences are minor provides an indication that, like the two-pot system, the hydration properties of gels produced via the one-pot synthesis method are primarily dictated by the hydrogel component. This is particularly noteworthy considering that the large weight percent of polyanionic dopant PSS, which may have contributed to the swelling in the two-pot system, was replaced with relatively smaller quantities of immobilized anionic dopants, MAA and Tau, for the one-pot systems. Furthermore, the relative concentration of PEDOT across the two-pot and one-pot systems was roughly equivalent. Therefore, it may be concluded that good control over gel equilibrium swelling is still enabled by tuning the hydration parameters of the hydrogel component such as selection of monomer/macromer chemistry, monomer/macromer concentration, and crosslinking density. Lastly, the large decrease in swelling ratio demonstrated by the non-conductive PVA system (solid orange line) suggests that the gel experienced significant deswelling after polymerization, which is counter to all other gels. This may be a result of changes in the PVA chains interaction with solvent once crosslinked. However, given the change is rather drastic, it is more likely that the 1-hour wash procedure in DI water that the gels experienced directly after synthesis disproportionately swelled PVA gels which then subsequently deswelled when incubated in PBS for the remainder of the study.

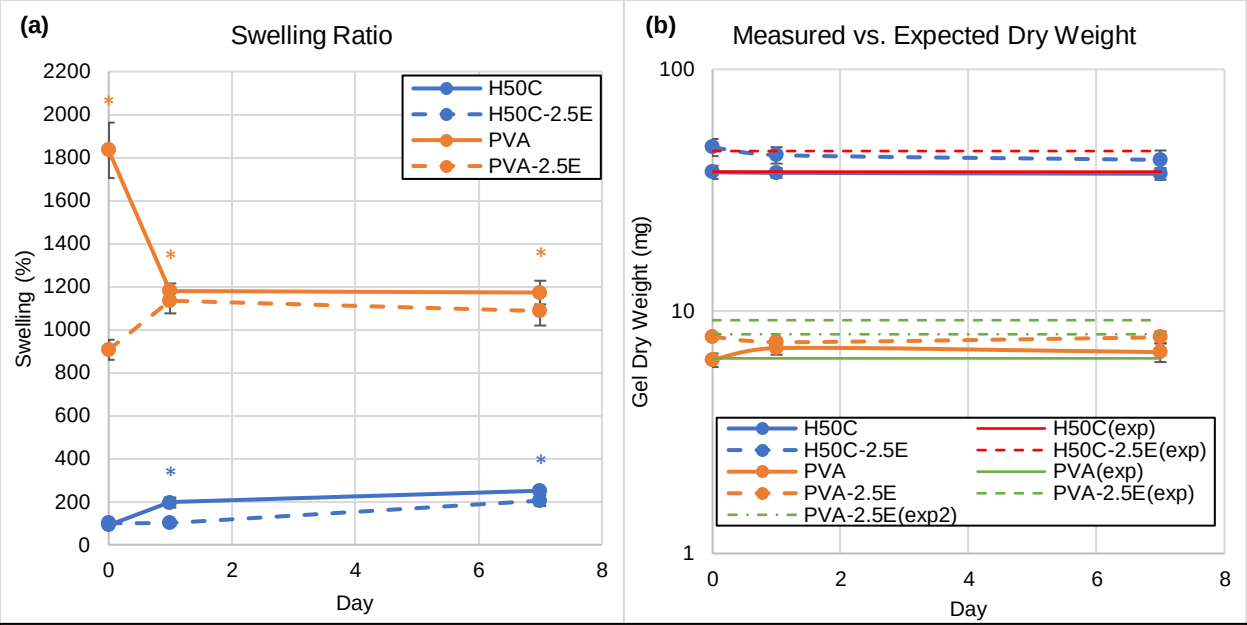

Figure 14: (a) Swelling ratio of H50C and PVA systems demonstrate a drastic increase in swelling of PVA gels compared to H50C gels. Both conductive gels, H50C-2.5E and PVA-2.5E, swelled slightly less than their non-conductive counterparts, H50C and PVA. Though minor, these differences were statistically significant for all gels (color coded asterisks) except on Day 0 for H50C vs. H50C-2.5E gels. (b) Measured dry mass for each gel was similar to calculated expected values ("exp") except for PVA-2.5E. Recalculation of PVA-2.5E expected mass [PVA-2.5E(exp2)] was carried out considering exclusion of small volume of pre-gel solution which remained in pipette tip – recalculated values matched observed dry mass more closely.

The dry weight of the gels was also measured across the same time points, plotted in Figure 14b. These measurements were in good agreement with the expected dry weights, calculated via Equation (3) using the nominal weight percent (w/v) of the expected solid content listed in Table 3. All gels demonstrated little to no mass loss over the course of the study as they reached their swelling equilibrium, indicative of a minimal sol fraction. One exception to the agreement with initially calculated expected dry weight was the PVA-2.5E gels which weighed ~15% less than expected (orange dotted line vs. green dotted line). The viscosity of the PVA-2.5E pre-gel solution was such that a small volume of the solution remained within the pipette tip when filling the mold. If this volume is accounted for by assuming a loss of ~10μL from the initial input volume, then the calculation produces an expected dry

Table 3

Gel	Wt%
H50C	54
H50C-2.5E	57.5
PVA	8.0
PVA-2.5E	11.5

mass value that is in closer agreement with the measured masses (orange dotted line vs. green dot-dash line).

Given that the measured dry mass values were stable over the course of the study duration and there was a known loss of volume input into the system, this seems the most likely cause for the observation. Furthermore, this reduction in expected mass loss is in agreement with the relative size of the PVA-2.5E gels observed in Figure 12c. If this size difference was a result of a significant change in hydration properties of the PVA-2.5E gel, these differences would be more readily observed in the swelling data. That the drastic difference in gel size did not produce an equally drastic change in equilibrium swelling properties provides further justification for the recalculation of expected dry mass for the PVA-2.5E gels and minimal sol fraction. Lastly, it should be noted that the viscosity of macromer systems like PVA-2.5E would make it difficult for sufficient infiltration into a sintered PMMA bead network and thus may not be well suited for STS fabrication or other solution processable methods requiring complex gel geometries.

2.3.2.2.c Mechanical Compression

To assess the impact of the one-pot synthesis methodology on gel mechanical properties, gel discs were subject to uniaxial compression and the compressive Young's modulus was calculated. Figure 15 plots the compression modulus of gels across the 7-day time course of the study. Here again there is a drastic difference in the modulus between the monomeric H50C and macromeric PVA systems in which the more dense and crosslinked monomeric system had a modulus roughly an order of magnitude larger than the macromer system. In terms of absolute comparisons, the PVA system outperformed the HEMA system in its proximity to the stiffness of brain tissue, which was expected given the differences in gel density.

However, in this case, the dynamics of the gel mechanical properties are relatively uniform across the two systems. Both the PVA and H50C gels experienced an initial drop in modulus after day 0 followed by an increase in modulus by day 7. This may have occurred as the gels initially moved toward their swelling equilibrium by day 1 and then experienced some degree of matrix restructuring, such as crystallization, upon prolonged interaction with the ions in solution. In the case of the PVA gels, the relatively high modulus on day 0 may also have been a result of the high degree of gel swelling placing strain on the matrix before deswelling in PBS. However, more fine-grained temporal analysis would need to be conducted in PBS and DI water to provide more information on the observed differences. However, in opposition to these mechanical dynamics, the conductive gels H50C-2.5E and PVA-2.5E experienced a much more regular decrease in modulus as they approached their swelling equilibrium.

Beyond the individual dynamics of the gel moduli, the comparison of the equilibrated compression modulus of the conductive and non-conductive gels provides some further insight into the potential internal structure of these one-pot gels. The equilibrium compression moduli were recorded at 63 ± 19 kPa and 135 ± 14 kPa for PVA and PVA-2.5E, respectively, and 689 ± 163 kPa and 958 ± 313 kPa for H50C and H50C-2.5E, respectively. The differences in equilibrium

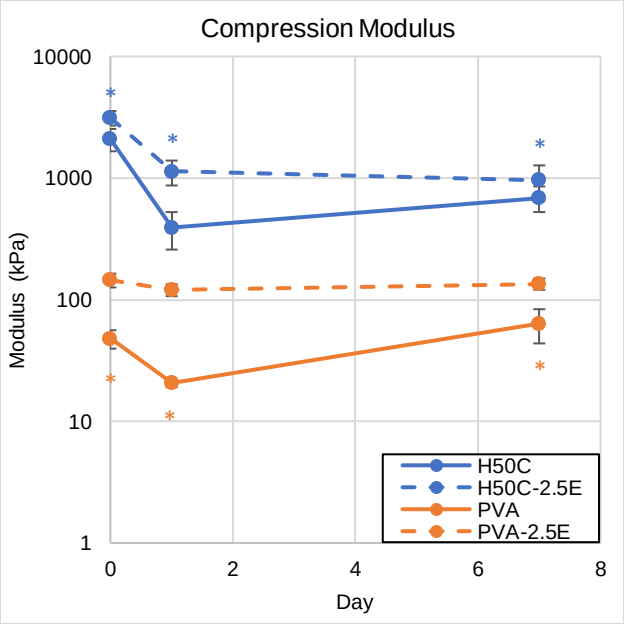

Figure 15: Mechanical properties of the PVA and H50C gel systems determined via uniaxial compression. Monomeric H50C systems were much stiffer than PVA systems given the significant difference in gel densities. Additionally, differences between conductive and non-conductive gels within both systems demonstrated statistically significant differences across all days (color coded asterisks). This suggests interactions of PEDOT and hydrogel networks upon experiencing compressive strain are analogous to the two-pot system.

moduli of H50C compared to H50C-2.5E and PVA compared to PVA-2.5E were statistically significantly across all days. Additionally, the magnitude of the difference in gel equilibrium moduli demonstrated a degree of correlation with the two-pot system. That is, the ratio of conductive to non-conductive (e.g. H50C-2.5E:H50C) moduli was 1.4:1 and 2.1:1 for the H50C and PVA systems, respectively, while it was 2.5:1, 2.3:1, and 2.0:1 for the H50, H50-C, and H50-GR systems, respectively. This indicates that the one-pot method may provide greater control over gel mechanical properties than the two-pot method for monomeric systems. However, this comes at the cost of gel electrical properties, discussed in depth below.

On the other hand, the ratio for the PVA system was much closer to that of the two-pot systems, suggesting that the structure of the PEDOT particle network may have been similar between these systems. Or, perhaps the crosslinking of the PVA network and polymerization of PEDOT in parallel caused the chains to grow/orient in such a way as to produce stress-inducing interactions upon compression that are similar to more phase-separated network structures expected by the two-pot method. Investigation of the nano-scale structure of gels produced via the two methods, such as with tunneling electron microscopy or conductive atomic force microscopy, would provide deeper insight in this regard. Furthermore, future work designed to extend these observations into gel systems with even softer initial mechanical properties will likely provide deeper insight into the relationship between gel density and mechanical properties for gels produced via the one-pot methodology. While it is encouraging that softer gel systems such as PVA-2.5E are capable of being applied to the one-pot synthesis method, continued work in testing softer gel systems will be necessary to produce devices matching the stiffness of human brain tissue (<10kPa).

2.3.2.2.d Electrical Impedance Spectroscopy

To characterize the electrochemical properties of gels produced via the one-pot methodology, hydrogel rods insulated in polyolefin were used, similar to gels produced via the two-pot method. Figure 16a plots the electrical impedance spectra for these gels with several notable observations that are in agreement with those above. Firstly, the conductive gels demonstrated a significant reduction in impedance across a broad range of frequencies as compared to the non-conductive gels. Figure 16b compares the impedance at 1kHz across the gels which were recorded at 35.2 ± 16.3kΩ and 7.5 ± 0.6kΩ for PVA and PVA-2.5E, respectively, and 88.6 ± 22.1kΩ and 54.9 ± 7.8kΩ for H50C and H50C-2.5E, respectively. Observed differences were statistically significant between gels of the same system (e.g. H50C vs. H50C-2.5E, asterisks) and between gels across both systems (e.g. H50C-2.5E vs. PVA-2.5E, double-hash). This provides a clear indication that the polymerization of PEDOT alongside the hydrogel component is producing a connected pathway for current to flow, thus increasing the conductivity of the gels and improving their overall impedance characteristics.

Secondly, similar to gels produced via the two-pot method, impedance magnitude for all gels demonstrated little to no frequency dependence which is indicative of capacitive charge transfer as the dominant charge transfer mechanism. Dedoping and redoping of PEDOT in the presence of an alternating electric field is thought to be a primary conduction mechanism that enables PEDOT to have high capacitive capabilities, which are congruent with our observations[91]. However, that this degree of frequency independence was observable across control samples lacking PEDOT indicates the size of the electrodes and surface area of the connection to the potentiostat also contributed to this effect. Thirdly, both PVA systems outperformed the H50C systems across all frequencies tested such that even the PVA gels demonstrated a lower

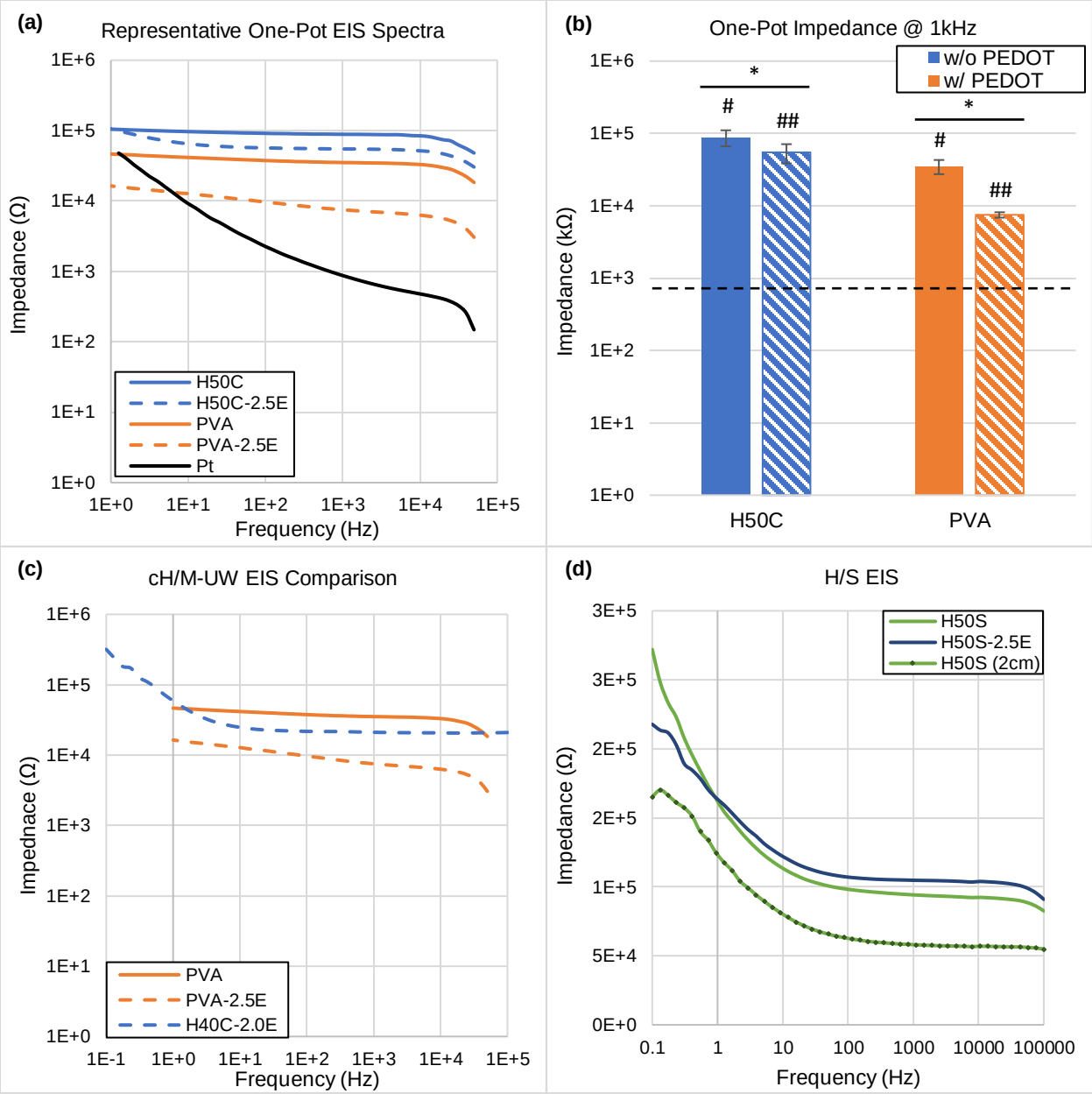

Figure 16: (a) Electrical impedance spectra of the one-pot H50C and PVA systems demonstrate a reduction in impedance occurs when PEDOT is incorporated into the system. Improvements in the impedance characteristics of PVA-2.5E are much greater than H50C-2.5E, indicating gel density is a major factor impacting gel electrical properties along with potential other factors such as dopant quality. (b) Differences in impedance magnitude at 1kHz are statistically significant when comparing conductive and non-conductive gels in the same system (asterisks), and between systems (H50C vs. PVA, solid bars, single hash; H50C-2.5E vs. PVA-2.5E, striped bars, double hash). The black dotted line is impedance of platinum control at 1kHz. (c) Reduction in gel density for the H40C-2.0E system demonstrated a further reduction in impedance, providing more evidence for the impact of gel density on gel electrical properties. (d) Modification of immobilized dopant to styrene sulfonate (SS) in H50S-2.5E gels showed an increase in impedance, possibly due to overoxidation of PEDOT due to a necessary change in the solvent system. However, H50S gels with 2cm length showed a reduction in impedance compared to H50S with 3cm length, indicating gel geometry is an important factor in gel conductivity. Note that the y-axis in (d) is linear, not logarithmic.

impedance than H50C-2.5E gels. This provides evidence for the impact that significant differences in gel density likely have on the resulting electrical properties of the gels. However, the degree of improvement in impedance characteristics is disproportionately larger between PVA and PVA-2.5E compared to H50C and H50C-2.5E, which suggests that other factors beyond gel density may be impacting the final electrical properties of the gels containing PEDOT. It is also worth noting that the PVA-2.5E gels preformed equally well from an impedance standpoint compared to the best performing two-pot conductive gels. This provides further evidence for the similarity in structure of the PEDOT networks between the two systems. This result is also very encouraging and further motivates optimization of this novel synthesis methodology in the context of neural microelectrode design.

The significant reduction in PVA-2.5E impedance naturally raises questions as into the factors which may be impacting the properties of gels produced via the one-pot method and if these factors can be elucidated to enable greater control over the design of these conductive hydrogel systems. Beyond gel density and crosslinking mechanism, other notable differences between the PVA and H50C systems include: 1) immobilized dopant chemistry and concentration, 2) vinyl concentration, 3) photoinitiator chemistry and concentration, 4) solvent selection, and 5) precipitate formation. The former 3 factors were deemed potentially important as they each lead to an increase in the free radical concentration within the solution during photopolymerization. Solvent considerations will be discussed in more depth below. Control over precipitate size/structure was not explored here but future investigation into the potential effect of this factor is warranted. The indiscriminate behavior of photoactivated free radicals could be attacking the growing PEDOT chains thus altering their structure and impacting their conductivity which may be protected if encapsulated within micelles.

Consideration of the factors discussed above led to a series of subsequent preliminary experiments aimed at teasing apart the independent impact that a selection of these factors may

be having on final gel conductivity. The first of these experiments involved the modification of the H50C-2.5E system to reduce the overall gel density to approximately 40% (w/v) by simply increasing the solvent volume by 1.5-fold. Figure 15c demonstrates that this adjustment in monomer concentration had a significant impact on the impedance characteristics of the resulting H40C-2.0E gels, bringing their impedance below that of the PVA gels. This result provides further evidence that gel density is a key factor for controlling gel electrical properties. However, these gels still did not perform as well as the PVA-2.5E gels.

While a simple alteration, modifying gel density by only increasing solvent volume necessarily reduces the concentration of all other species in solution, including EDOT and dopant. That this alteration still enabled a significant reduction in impedance provides more evidence that other factors are impacting gel conductivity. Related to the discussion above, key factors such as photoinitiator concentration, vinyl concentration, and immobilized dopant concentration were all modified along with the gel density in this manner. That said, for monomeric methacrylate-based hydrogel systems, modifying gel density without also modifying vinyl monomer and immobilized dopant (also vinylic species here) concentrations is virtually impossible. This suggests that the PVA system or another macromolecular system, such as low molecular weight PEGDA/PEGDMA could provide benefit for probing these differences. For example, these systems would offer simultaneous control over gel density and vinyl concentration by utilizing identical molar concentrations and crosslinks/chain of the macromer unit with a range of molecular weights.

To further probe the factors impacting gel conductivity, the H50C system was modified to replace the methacrylic acid (MAA) as immobilized dopant with styrene sulfonate (SS). SS was chosen as it is the vinylic monomer unit equivalent of the polyanionic PSS that has demonstrated much success to produce highly conductive PEDOT for a variety of applications. Additionally, the dopant moiety within the Taurine amino acid used in the PVA system was also contained a sulfonate moiety, which suggests that sulfonate is perhaps a better dopant than the carboxylic

acid moiety present in MAA. This may be due to the relative pKa values of the carboxylic (~4.8) and sulfonate (~1.0) moieties such that a larger portion of sulfonate moieties will be in their anionic, deprotonated state at physiological pH, thus providing for better doping capability for PEDOT. However, SS is sold as a sodium salt which is highly soluble in water but poorly miscible with alcohols. Therefore, to produce a uniform H50S system, the methanol used in the H50C system needed to be substituted for another solvent. A preliminary set of tests determined that a 50:50 mixture of ethylene glycol and glycerol, both highly polar solvents, could replace the same volume of alcohol to produce a uniform solution.

However, upon exposure to UV radiation for photopolymerization the resulting H50S-2.5E gels turned a brownish color, as opposed to the expected deep blue of highly doped PEDOT. Additionally, the gel demonstrated no improvement in impedance over the control H50S gel which contained no PEDOT, as demonstrated in Figure 16d. This change in color and lack of improvements in impedance suggests that the PEDOT chains are being overoxidized during the reaction, such as with the production of undesirable C=O bonds on the PEDOT backbone[92]. Such overoxidation limits the effective conjugation length of the polymers and thus drastically reduces their conductivity. The mechanism for this overoxidation in the one-pot system is currently unknown. However, it may be a result of the ~2-fold increase in hydroxyl groups present on the ethylene glycol and glycerol molecule compared to those present on methanol. Hydroxyl groups on these molecules, in addition to water, are known to be readily oxidized by APS to produce radicals which may be contributing to the attack on the growing PEDOT chains and/or otherwise consuming APS such that EDOT initiation/polymerization efficiency is greatly reduced. This increase in free radical concentration from the solvent could be acting together with those produced by photoinitiators and vinylic monomers to produce undesirable chemical species that limit control over final gel conductivity.

It is interesting to note that the PVA macromers used in the PVA-2.5E system have abundant hydroxyl groups, though the overall weight percent of PVA used still amounted to a ~3-fold decrease in hydroxyl groups present in solution compared to the monomeric system. Additionally, the PVA-2.5E system did not produce a uniform solution at the concentrations tested which may suggest that the production of micellular structures can offer some degree of protection of the growing PEDOT chains from radical attack. In order to elucidate the impact of these factors on gel conductivity, future studies will need to utilize a polymer system which provides independent control over these parameters.

A final experiment was conducted as a preliminary investigation into the impact of gel geometry on impedance characteristics. This provides a first look into understanding how the conductivity and charge transfer properties of these gel systems might change when applied to much smaller devices like microelectrodes. In this experiment, another set of H50S gel electrodes were fabricated with lengths of 2cm, as opposed to the standard 3cm length tested for all other gels, and their impedance characteristics evaluated, also shown in Figure 16d. The impedance of the 2cm long gel electrodes were ~2/3rds that of the 3cm electrodes (68.2%) suggesting a linear, resistive relationship between gel length and impedance. The gels used in this study contained no PEDOT but did have anionic SS immobilized throughout the network at the same concentration tested in H50S-2.5E samples.

Comparisons of the H50S system with H50 gels, both tested with gels of 3cm in length and similar relative gel densities, indicates that immobilized dopant molecules also act to reduce the gel impedance. However, addition of immobilized dopants does demonstrate a frequency-dependent impedance component, unlike the impact of changes to gel density alone which were observed between H50, H50-C, and H50-GR. Future work will need to evaluate differences in device geometry with PEDOT incorporated and with a reduction in electrode cross sectional area as both length and width of future devices will need to be reduced by 1-2 orders of magnitude to

be applicable to high channel count microelectrode fabrication. Additionally, application of these results to the generation of equivalent circuit models will provide insight into the relative contributions of each component on the gel electrochemical properties. Such models will also help to deepen understanding of the mechanisms behind each of these factors and how they might be tuned to further optimize gel conductivity.

2.3.2.2.e Cyclic Voltammetry

The cathodal charge storage capacity of H50C and PVA systems was also quantified and compared. Figure 17 demonstrates trends observed in charge storage were similar to those observed in impedance across these systems. Figure 17a demonstrates that the H50C-2.5E and PVA-2.5E gels with CSC_C at 8.4 ± 4.9mC/cm^2 and 69.6 ± 23.1mC/cm^2 outperformed H50C and PVA at 4.3 ± 2.6mC/cm^2 and 8.2 ± 2.2mC/cm^2, respectively, and all gel comparisons were statistically significant. Figure 17b shows an equivalent improvement in overall current density

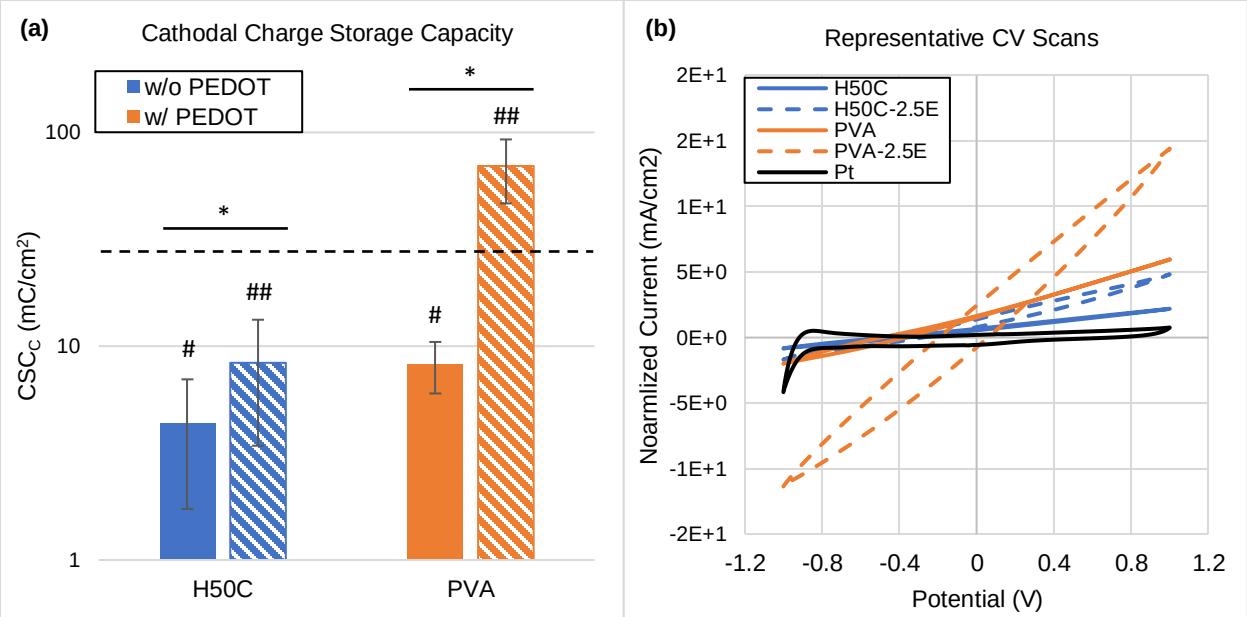

Figure 17: (a) Cathodal charge storage capacity of gels is significantly increased upon inclusion of PEDOT, though only the PVA-2.5E gel (orange bar, striped) outperformed the platinum control. All comparisons were statistically significant between gels within a system (asterisk), and between the different systems (H50C vs PVA, solid bars, single hash; H50C-2.5E vs PVA-2.5E, striped bars, double hash). (b) Representative CV scans from each of the gels fabricated via the one-pot method.

during CV scans. Furthermore, the large increase in performance of the PVA-2.5E gel's impedance characteristics was also observed in CSC_C and current density, indicating the factors discussed above also impact this gel property. Here again the PVA-2.5E system outperforms the highly conductive platinum control electrode and performs on par with the gels produced via the two-pot synthesis methodology.

2.3 Impact of Pre-Gel Monomer Concentration and Dopant Quality on Gels Produced via the One-Pot Synthesis Method

The results of the previous experiments provided strong evidence that both pre-gel monomer/macromer concentration and dopant chemistry had a significant impact on the final gel properties. Therefore, we sought to systematically probe the impact of these factors on materials produced via the one-pot synthesis methodology by utilizing a single gel system. A panel of gels were fabricated, shown in Table 4, using a monomeric gel system at two pre-gel monomer concentrations, 25% (v/v) and 50% (v/v), that incorporated immobilized dopants hosting either carboxylic acid ($-COO^-$) or sulfonic acid ($-SO_3^-$) moieties. Controls were fabricated with identical compositions without the incorporation of EDOT. For these experiments, a 4:1 mixture of HEMA and glycerol methacrylate (GMA) was used as the hydrogel component to enable the formation of gels at 25% gel density based on previous work conducted in our lab (data not shown). Each gel group had a uniform molar concentration of dopant, regardless of dopant chemistry or monomer concentration.

Table 4 Pre-Gel Composition for experiments investigating the impact of monomer concentration and dopant chemistry on final gel properties. The hydrogel component used for these experiments was comprised of an 4:1 mixture of HEMA:GMA.

Gel Name	Monomer Concentration [%, v/v]	Dopant Selection	Dopant Concentration [mol/L]	EDOT[a] [%, v/v]
HG50S	50	AMPS[b] ($-SO_3^-$)	0.1	0
HG50S-2.5E	50	AMPS ($-SO_3^-$)	0.1	2.5
HG25S	25	AMPS ($-SO_3^-$)	0.1	0
HG25S-2.5E	25	AMPS ($-SO_3^-$)	0.1	2.5
HG50C	50	AA[c] ($-COO^-$)	0.1	0
HG50C-2.5E	50	AA ($-COO^-$)	0.1	2.5
HG25C	25	AA $(-COO^-)^-$	0.1	0
HG25C-2.5E	25	AA $(-COO^-)^-$	0.1	2.5

[a] 3,4-ethylenedioxy thiophene; [b] 2-Acrylamido-2-methylpropane sulfonic acid; [c] acrylic acid

2.3.1 Swelling Study

The swelling ratio of gels, displayed in Figure 18, was measured at their swelling equilibrium in PBS (pH 7.4). As was observed previously, the incorporation of EDOT into the pre-gel mixture induced a reduction in the gels' final swelling ratio (orange bars) as compared to their respective controls (blue bars) across all groups tested. Groups with 50% pre-gel monomer concentration, HG50S and HG50C, exhibited similar swelling values to one another at 123.0 ± 2.7% and 122.4 ± 2.1%, respectively, with minor reductions in swelling for PEDOT-containing

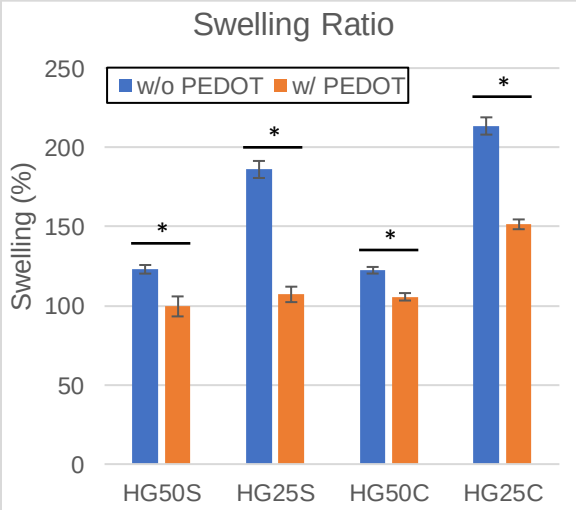

Figure 18: Pre-gel monomer concentration and dopant selection impact the swelling properties of gels produced via one-pot synthesis method.

samples HG50S-2.5E and HG50C-2.5E at 99.6 ± 6.3% and 105.6 ± 2.3%, respectively. This indicates the HEMA/GMA hydrogel component was the primary driver of hydration, similar to the H50C gels discussed above.

Conversely, groups with 25% pre-gel monomer concentration exhibited divergent swelling behavior based on composition, although they did show a general trend of increased swelling compared to groups with 50% pre-gel monomer concentration, as was expected due to greater free matrix volume. The HG25C gels exhibited the greatest swelling at 213.4 ± 5.5% with a reduction in swelling for the PEDOT-containing HG25C-2.5E at 151.4 ± 3.1%. The HG25S gels exhibited the next highest swelling value at 186.0 ± 5.4% while its PEDOT-containing counterpart, HG25S-2.5E, with a swelling value at 107.1 ± 4.9% demonstrated the greatest relative reduction in swelling. Comparison of the relative reduction in swelling between gels with PEDOT and their respective PEDOT-free controls showed an approximate 14%, 19%, 29%, and 42% reduction in swelling for HG50C-2.5E, HG50S-2.5E, HG25C-2.5E, and HG25S-2.5E, respectively.

Beyond the increase in hydrophobicity imparted to the gels with the inclusion of PEDOT, the differences in swelling also suggest a stronger interaction of the PEDOT chains with the hydrogel matrices containing immobilized sulfonic acid dopant as compared to those containing immobilized carboxylic acid dopant. Additionally, the larger free matrix volume in the lower density gels likely enabled the formation of larger PEDOT particles and subsequent enhancement of this PEDOT chain-hydrogel matrix interaction, thus leading to the drastic reductions in swelling observed for HG25S-2.5E. Taken together, these results indicate that the choice of immobilized anions impacts the gel swelling and that they impart a larger proportional impact on gel hydration properties at lower gel densities.

2.3.2 Mechanical Compression

Figure 19 displays the mechanical compression modulus of the gels, providing more information into matrix interactions. The inclusion of EDOT in the pre-gel solution of each group induced a reduction in the moduli of gels compared to their respective controls (orange vs. blue bars), except for the HG25S-2.5E group. The moduli of the groups with 50% pre-gel monomer concentration without PEDOT, HG50S and HG50C, were 487 ± 16 kPa and 487 ± 20 kPa, respectively, while their PEDOT-containing counterparts, HG50S-2.5E and HG50C-2.5E, were 308 ± 19 kPa and 293 ± 12 kPa, respectively. The trends observed between the moduli of these groups were nearly identical and correlated with their swelling values, providing additional evidence that the hydrogel component dominated their behavior. In contrast to results discussed in Section 2.2, the moduli for PEDOT-containing gels (orange bars) were lower than that of their respective controls (blue bars), possibly due to differences in the broad spectrum UV apparatus used to synthesize this set of materials leading to differences in polymerization kinetics.

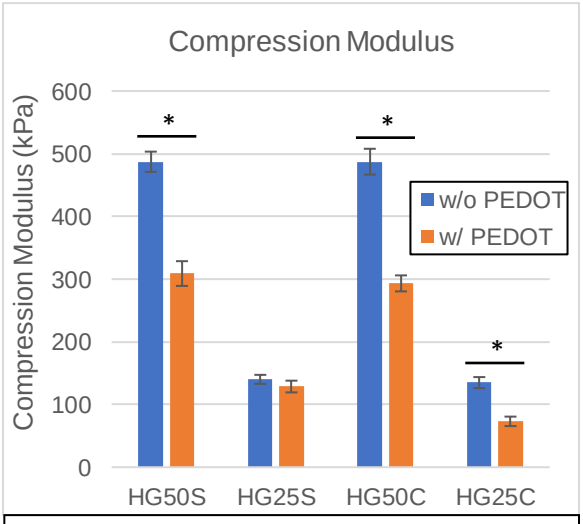

Figure 19: Pre-gel monomer concentration and dopant selection demonstrate a differential impact on gel mechanical properties.

Similar to results observed in hydration properties, the 25% gels demonstrated divergent behavior in their mechanical properties based on their respective compositions. The moduli of gels without PEDOT, HG25S and HG25C, were 140 ± 7 kPa and 135 ± 8 kPa, respectively, while their PEDOT-containing counterparts, HG25S-2.5E and HG25C-2.5E, were 128 ± 9 kPa and 73 ± 7 kPa, respectively. These differences correspond to a relative decrease in modulus by approximately 40%, 37%, 46%, and 8% for HG50C-2.5E, HG50S-2.5E, HG25C-2.5E, and HG25S-2.5E,

respectively, compared to their respective controls. All comparisons of compression moduli between PEDOT-containing gels and their respective controls represented statistically significant differences except for HG25S and HG25S-2.5E.

These results are in agreement with the correspondingly drastic reduction in swelling observed for HG25S-2.5E which is indicative of a lower free matrix volume and thus a more tightly packed gel leading to relatively stiffer mechanical properties. However, while the swelling ratio of HG25S-2.5E was similar to 50% gel group containing PEDOT, HG50S-2.5E, the compression modulus of HG25S-2.5E was still significantly lower, highlighting the impact of pre-gel monomer concentration on final gel mechanical properties.

2.3.3 Conductivity

The conductivity of the gels, shown in Figure 20 was measured via a two-probe method, subject to a DC voltage of 100mV, and read once a stable value had been reached. There were no significant differences in conductivity observed between PEDOT-containing (orange bars) and control gels (blue bars) in the 50% gel groups, but a significant increase in conductivity was observed for both sets of gels containing PEDOT in the 25% gel groups. The 50% gel groups without PEDOT, HG50S and HG50C, had conductivities of 8.7 ± 0.8E-4 S m^{-1} and 1.1 ± 0.1E-3 S m^{-1}, respectively, while their PEDOT-containing counterparts, HG50S-2.5E and HG50C-2.5E, were 8.2 ± 3.3E-4 S m^{-1} and 8.3 ± 4.0E-3 S m^{-1}, respectively.

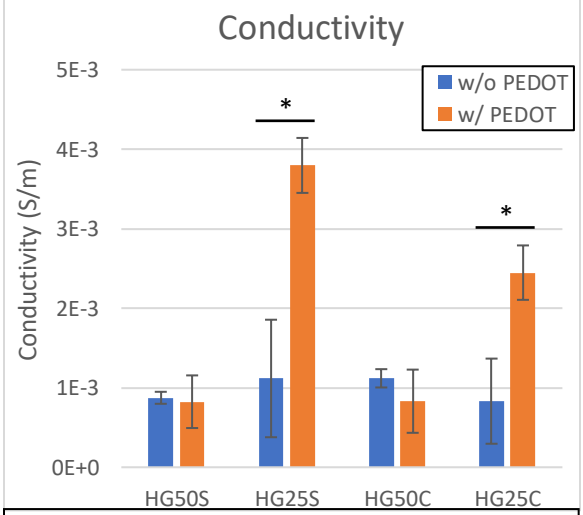

Figure 20: Dopant selection impacts the conductivity of one-pot gels, but only significantly in gels with low pre-gel monomer concentration.

The lack of significant difference in electrical activity of the 50% gel groups, HG50S-2.5E and HG50C-2.5E, compared to their respective controls agrees with trends observed in H50C-2.5E discussed in Section 2.2. The PEDOT chains/particles within these gels do not seem to be forming a coherent network to improve the electrical activity of the gels. The hydrogel phase may be too dense in these samples, causing the PEDOT network to be below the percolation threshold. PEDOT overoxidation may also be contributing to the lack of improvement in conductivity, regardless of the chemistry of the immobilized dopant moiety, discussed in more depth in Section 2.3.4 below.

Conversely, both PEDOT-containing gels in the 25% gel groups exhibited a significant increase in conductivity compared to their respective controls. The 25% gel samples without PEDOT, HG25S and HG25C, had conductivities of 1.1 ± 0.7E-3 S m^{-1} and 8.3 ± 5.4E-4 S m^{-1}, respectively, while their PEDOT-containing counterparts, HG25S-2.5E and HG25C-2.5E, were 3.8 ± 0.4E-4 S m^{-1} and 2.4 ± 0.3E-3 S m^{-1}, respectively. That HG25S-2.5E displayed the highest overall conductivity suggests that the sulfonic acid moiety served as a more efficient dopant for the PEDOT chains, thereby improving the bulk conductivity of the gel. The relative dissociation constants of the sulfonic acid (pKa ~1-2) and carboxylic acid (pKa ~4-5) moieties within these two materials may be contributing significantly to the efficiency of PEDOT doping, thereby impacting the conductivity of the gels. Alternatively, the relatively lower swelling ratio and higher compression modulus of HG25S-2.5E suggests that these gels are more compact which could effectively provide a tighter coupling between adjacent PEDOT chains/particles, thus increasing conductivity in this manner as well.

2.3.4 Vibrational Spectroscopy

In light of the conductivity measurements, Raman spectroscopy was carried out to gather more information on the doping state of the PEDOT network within the gels. Raman spectroscopy is a powerful tool to quantify the degree of doping in PEDOT by measuring the peak shift of the

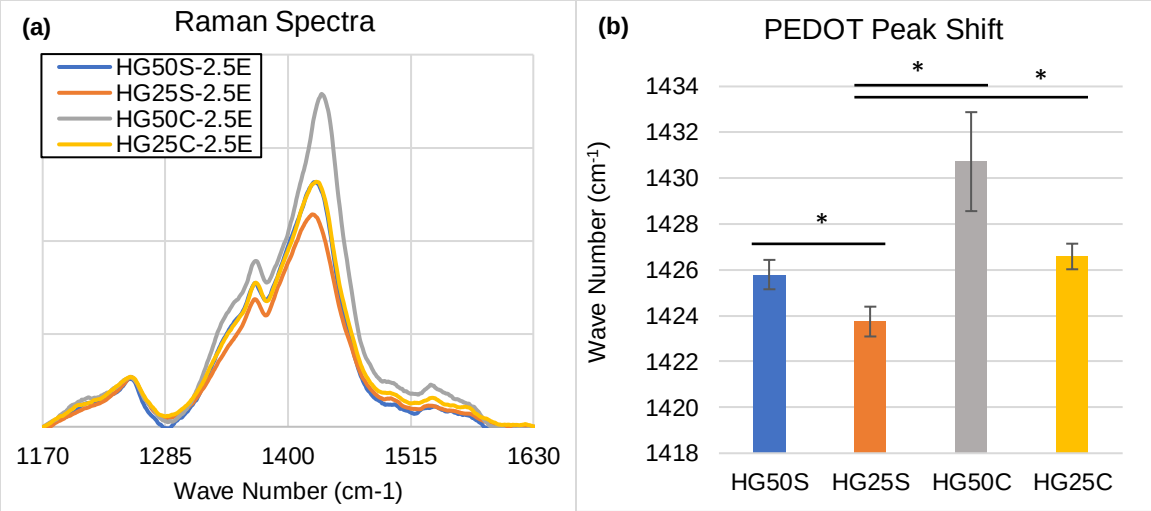

Figure 21: Raman vibrational spectroscopy indicates pre-gel monomer concentration and dopant selection both impact the doping level of PEDOT in the gels. (a) Representative spectra of PEDOT-containing gels. (b) Quantification of PEDOT peak shift indicates PEDOT in the HG25S gel is in the most doped state.

symmetrical C_α=C_β stretching vibration in the PEDOT thiophene ring with wavenumbers located between 1400-1450 cm^{-1}. Raman spectra were collected in the region between 1170 and 1630 cm^{-1} with a 785nm laser for PEDOT containing samples and representative spectra are shown in Figure 21a. Peak locations were in good agreement with previous reports for PEDOT. Figure 21b quantifies the peak shift in the PEDOT peak for HG50S-2.5E, HG25S-2.5E, HG50C-2.5E, HG25C-2.5E at 1425.8 ± 0.6 cm^{-1}, 1423.7 ± 0.7 cm^{-1}, 1430.7 ± 2.2 cm^{-1}, 1426.6 ± 0.6 cm^{-1}, respectively.

The Raman peak for PEDOT has been reported to exhibit a shift toward lower wavenumbers resulting from increases to doping which correlate to improvements to conductivity,[93] while a shift toward higher wave numbers resulting from decreases to doping correlated to reductions in conductivity.[94] The increases to doping are indicative of a structural change in the PEDOT backbone from a coiled benzoid conformation to a more linear quinoid conformation. Subsequent improvement to conductivity occurs due to a greater efficiency of transduction along individual chains and charge hopping between adjacent chains.

Both solvent interactions and over oxidation have been reported to have an effect on PEDOT doping and chain conformation. For example, Chiang et al. report a PEDOT peak shift toward lower wavenumbers which correlate with improvements to conductivity as a result of post-polymerization interactions with various polar organic solvents.[93] Conversely, Fan et al. report a PEDOT peak shift toward higher wavenumbers which correlate with decreases to PEDOT electronic conductivity as a result of overoxidation induced by exposure to the strong oxidizing agent, NaClO, in solution.[94] However, it should be noted that these measurements were carried out on thin films of PEDOT as opposed to macroscopic conductive hydrogel composite materials.

The observed trend in PEDOT peak shift values for these gels is therefore in agreement with the hypothesis that the sulfonic acid moiety enables a greater degree of doping within the gels and that these improvements may enable improvements to bulk conductivity. However, the discrepancies in PEDOT peak values and conductivity between HG50S-2.5E and HG25S-2.5E suggests that pre-gel monomer concentration has an impact on PEDOT doping in the final gel and that doping level does not correlate directly with bulk gel conductivity. Other factors that are likely impacting the doping level and conductivity of these gels include the density of the hydrogel phase, degree of overoxidation, and swelling which will each have disproportionate effects on the electronic and ionic conductivities of the gels.

For example, HG50S-2.5E had a significantly lower PEDOT peak wavenumber than HG50C-2.5E but did not exhibit significant differences in conductivity, which suggests that overoxidation or the density of the hydrogel phase may be inhibiting the formation of a conductive PEDOT network in the 50% gel samples. Furthermore, HG25C-2.5E exhibited a similar PEDOT peak wavenumber but a significantly higher conductivity compared to HG50S-2.5E which suggests an improvement in formation of a conductive PEDOT network. However, when considering their respective swelling values, a greater contribution of ionic conductivity may also be occurring in HG25C-2.5E. This also provides evidence that the degree of swelling in the

material may influence PEDOT doping, perhaps by modulating the interaction between PEDOT chains/particles and the dopant anions immobilized throughout the hydrogel network.

2.4 Impact of Pre-Gel EDOT Concentration on Gels Produced via the One-Pot Synthesis Method

The next factor that we sought to modify to continue optimizing the properties of conductive hydrogels produced via this one-pot methodology was the concentration of EDOT in the pre-gel mixture. The pre-gel EDOT concentration was increased from 2.5wt% to 5.0wt% and 7.5wt% for both the 50% and 25% gel groups. The compositions and naming convention of the gel groups tested are listed in Table 5.

Table 5 Pre-gel Compositions for experiments investigating the impact of pre-gel EDOT concentration on final gel properties. The hydrogel component used for these experiments was comprised of an 4:1 mixture of HEMA:GMA.

Gel Name	Gel Density [%, v/v]	Dopant Selection	Dopant Concentration [mol/L]	EDOT [%, v/v]
HG25SC-2.5E	25	AMPS & AA	0.2	2.5
HG25SC-5E	25	AMPS & AA	0.2	5.0
HG50SC-2.5E	50	AMPS & AA	0.2	2.5
HG50SC-5E	50	AMPS & AA	0.2	5.0
HG50SC-7.5E	50	AMPS & AA	0.2	7.5

The inclusion of PEDOT:PSS in various pre-gel mixtures followed by photopolymerization has demonstrated success in producing conductive hydrogels with interpenetrating network structure. However, the black/opaque nature of PEDOT:PSS reduces the photopolymerization efficiency of the pre-gel solution which limits the total amount of PEDOT:PSS that can be added

to the mixture while still enabling efficient photopolymerization and final gelation. Conversely, the EDOT monomer is virtually transparent when in solution which suggests a larger overall concentration may be incorporated within the pre-gel solution and thereby the final gel.

However, we observed that the impact of EDOT inclusion within the pre-gel solution discussed in Section 2.3 above were amplified with larger concentrations of EDOT. Upon increasing the EDOT concentration 2-3 fold, 50% gel samples were able to form gels but the 25% gel density groups were unable to form gels beyond 2.5wt% EDOT regardless of UV exposure duration and 7 days of incubation at 4°C. Additional tests were run that included both dopant molecules (sulfonic acid and carboxylic acid) into the pre-gel solutions – while 40 minutes of UV exposure alone was still unable to form gels in the 25% gel groups, complete gelation did occur after an additional 7 days of incubation at 4°C, but only for the 2.5wt% and 5wt% EDOT groups. Therefore, all compositions tested here contained both dopant molecules to make adequate comparisons between groups.

The above observation provides additional evidence that there is also significant interaction between EDOT and the radicals associated with the initiator and growing polymer chains which act to limit polymerization and/or crosslinking efficiency and lead to PEDOT overoxidation. Furthermore, that the HG25SC-5.0E group was able to form a gel after 7 days incubation at 4°C suggests a degree of physical crosslinking occurred as the PEDOT chains continued growing. Lastly, that the 25% gel density group with 7.5wt% EDOT (i.e. HG25SC-7.5E) was unable to form a gel suggests a hard limit to the pre-gel EDOT concentration for this composition given the interactions between the components, though further optimization of the pre-gel chemistry may yield better results.

2.4.1 Swelling Study

The integration of both dopants and the increase in PEDOT concentration within the pre-gel composition had only a minor effect on swelling for 50% gel groups, as shown in Figure 22. Their swelling ratios were measured at 134.0 ± 5.2%, 151.2 ± 3.1%, and 148.1 ± 7.8% for HG50SC-2.5E, HG50SC-5.0E, HG50SC-7.5E, respectively, indicating that increasing EDOT concentration did not have a significant impact gel hydration properties. In contrast to the 50% gel density, integration of dopants and EDOT concentration had a significant impact on the 25% gel density groups' swelling properties.

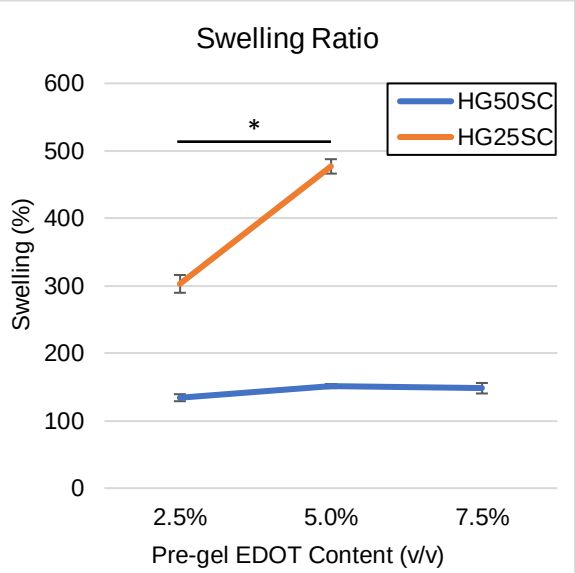

Figure 22: Pre-gel EDOT content only produces a significant difference in swelling in gels with low pre-gel monomer concentration.

The inclusion of both dopants caused the swelling of HG25SC-2.5E to be 302.7 ± 13.2%, a 250% increase compared to either HG25S-2.5E or HG25C-2.5E, likely due to an increase in ionic strength imparted by doubling the concentration of anionic monomers within the gel. Furthermore, the swelling of HG25SC-5.0E also exhibited a significant increase at 476.9 ± 10.7%, which was likely due to the combined effect of EDOT-radical interactions limiting polymerization efficiency and the secondary crosslinking mechanism that occur over the 7-day incubation period at 4°C after UV exposure.

2.4.2 Mechanical Compression

The mechanical properties of both 25% and 50% gel groups exhibited a consistent reduction in compression moduli as EDOT concentration increased, as shown in Figure 23. Interestingly however, the inclusion of both dopant monomers induced an initial 130% increase

followed a decrease in compression modulus for the 50% gel groups as compared to HG50S-2.5E and HG50C-2.5E. Compression moduli were recorded at 411 ± 16 kPa, 221 ± 21 kPa, and 64 ± 6 kPa for HG50SC-2.5E, HG50SC-5.0E, HG50SC-7.5E, respectively. Observed in conjunction with the minimal changes in swelling observed for these samples, these results suggest that the increase in ionic strength imparted to the gels by doubling the dopant concentration may have offset the reduction in modulus caused by an EDOT-induced reduction in photopolymerization efficiency. With higher ionic strength the gels would become more hydrophilic, thereby increasing in turgidity even as less overall monomer conversion was occurring as EDOT concentration increased.

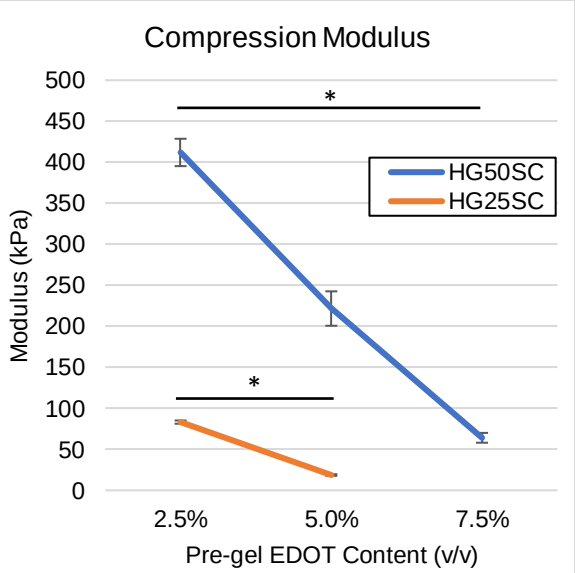

Figure 23: Compression modulus decreases proportionally to increases in pre-gel EDOT content.

In contrast to these trends, the 25% gel density groups exhibited an overall decrease in compression modulus to 83 ± 2 kPa and 18 ± 1 kPa for HG25SC-2.5E and HG25SC-5.0E, respectively. The inclusion of both dopants likely enabled a reduction in modulus for HG25SC-2.5E, given the larger free matrix volume than the 50% gel density groups, that enabled a greater degree of swelling. Furthermore, it is likely that both a reduction in monomer conversion and the unique gelation mechanism for the HG25SC-5.0E group provided for an additional reduction in modulus as a result of increased matrix free volume and swelling.

2.4.3 Conductivity

The conductivity of the samples, shown in Figure 24, followed trends in swelling ratio in a few ways. Firstly, no significant differences were observed between gels in the 50% gel group,

regardless of EDOT concentration, with conductivities measured at 1.88 ± 0.5E-3 S m^{-1}, 1.45 ± 0.5E-3 S m^{-1}, and 2.13 ± 1.6E-3 S m^{-1} for HG50SC-2.5E, HG50SC-5.0E, and HG50SC-7.5E, respectively. Secondly, an increase in conductivity was observed with increasing EDOT concentration for the 25% gel density groups, with conductivities measured at 4.89 ± 0.1E-3 S m^{-1} and 6.89 ± 0.1E-3 S m^{-1} for HG25SC-2.5E and HG25SC-5.0E, respectively.

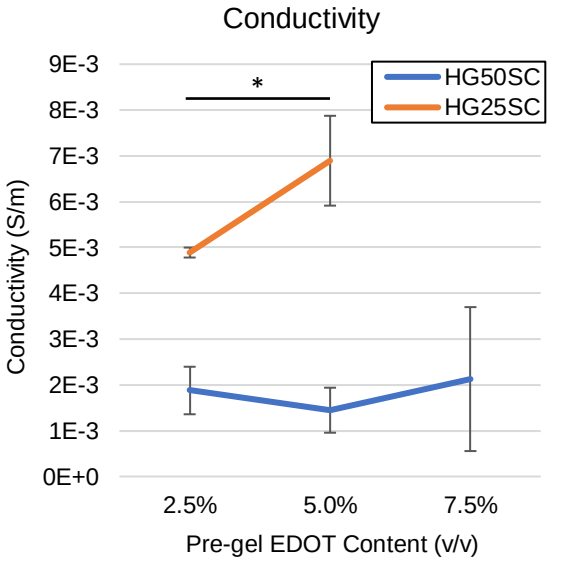

Figure 24: Conductivity of the is only significantly increased with increased pre-gel EDOT content in gels with low pre-gel monomer concentration.

Taken together, these results provide additional evidence that an overabundance of free radicals present in the reaction mixture may have deleterious effects on the formation of a highly conductive PEDOT network throughout the gel matrix. There may be a threshold monomer concentration at which PEDOT overoxidation will occur in a significant portion of the growing PEDOT chains and thereby inhibit any improvements in gel conductivity. Below this threshold, the impact of overoxidation may be minimal enough to enable further improvements in conductivity with increases in EDOT concentration. Lastly, the conductivities for the gel groups containing 2.5wt% EDOT, HG50SC-2.5E and HG25SC-2.5E, both exhibited minor increases in conductivity compared to gels with only a single immobilized dopant. The presence of additional anionic moieties within the hydrogel network likely served to increase the ionic conductivity of the gels and also perhaps provide additional doping to the PEDOT network.

2.4.4 Vibrational Spectroscopy

Raman spectroscopy was run once again to investigate the relationship between pre-gel EDOT concentration and PEDOT doping. The shift in PEDOT peaks were quantified and are displayed in Figure 25. Interestingly, trends between the two gel density systems were similar, showing decreases in wavenumber of the PEDOT peaks as EDOT concentration increased. The peak values for gels in the 50% gel density groups were recorded at 1429.8 ± 0.9 cm-1, 1423.4 ± 1.6 cm-1, 1423.8 ± 0.7cm-1 for HG50SC-2.5E, HG50SC-5.0E, and HG50SC-7.5E, respectively. Comparison of the PEDOT peak shift of HG50SC-2.5E to that of the single dopant gels HG50S-2.5E and HG50C-2.5E suggests that the vibrational characteristics of PEDOT within HG50SC-2.5E gels was dominated by the presence of the carboxylic acid moieties. This suggests that the minor increase in conductivity exhibited by HG50SC-2.5E was due primarily to increases ionic conductivity, as opposed to improvements in PEDOT doping or network structure.

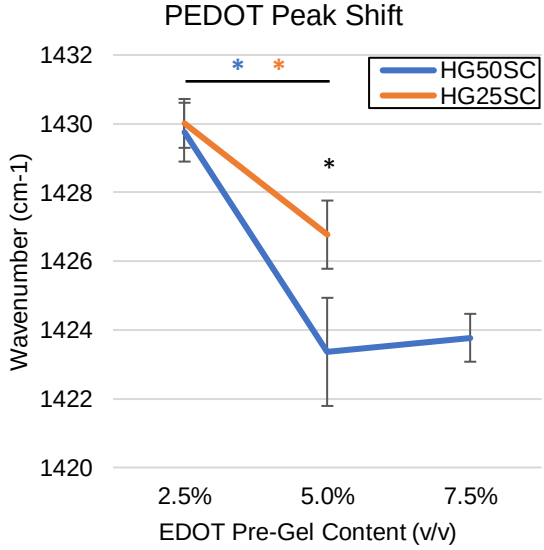

Figure 25: Increases in pre-gel EDOT content appear to increase the degree of doping up to 5% EDOT.

The subsequent shift in PEDOT peaks to lower wavenumbers for HG50SC-5.0E and HG50SC-7.5E are suggestive of an increase in PEDOT doping and chain linearity, per the discussion in Section 2.3.4. Interestingly, the wavenumbers exhibited by these samples are similar to the single dopant gel HG25S-2.5E, but the lack of any increase in conductivity exhibited by these samples indicates that the doped PEDOT chains/particles are not sufficiently interconnected. This provides additional evidence that, in addition to the negative impacting overoxidation may have on the PEDOT structure, the density of the hydrogel phase has the

propensity to produce a significant insulative barrier to the formation of a highly conductive PEDOT network. While the relative proportion of the PEDOT chains in a highly doped state may be increasing with increased EDOT content for these gels, the cumulative effect of overoxidation and increased inter-particle isolation may still be too large to enable the formation of a highly conductive PEDOT network.

The PEDOT peak wavenumbers for the 25% gel samples were measured at 1430.0 ± 0.7 cm-1 and 1426.8 ± 1.0 cm-1 for HG25SC-2.5E and HG25SC-5.0E, respectively. The large increase in wavenumber for HG25SC-2.5E compared to HG25S-2.5E was unexpected given the incorporation of an additional molar equivalent of anionic dopant. However, the greater degree of swelling exhibited by these samples compared to the single dopant gels may have had the effect of decoupling the interaction between PEDOT chains/particles and the immobilized anionic dopant moieties, i.e. de-doping the chains, thereby decreasing the interconnectivity of the conductive PEDOT network. The minor increase in conductivity exhibited by HG25SC-2.5E was therefore likely due to the combined effect of a large increase in ionic conductivity and a minor decrease in PEDOT network conductivity.

The subsequent peak shift to lower wavenumbers exhibited by HG25SC-5.0E is again suggestive of an increase in PEDOT doping, adoption of a more quinoidal structure, and subsequent increase in chain linearity compared to HG25SC-2.5E. However, the wavenumber of the peak is still relatively high compared to HG25S-2.5E which suggests the PEDOT network overall is still in a less doped state. It is worth noting the further increase in swelling exhibited by this sample and the effect it may have on decoupling the PEDOT chains from the immobilized anionic dopant molecules. The improvement in conductivity exhibited by HG25SC-2.5E is thus in agreement with previous observations in that significant increases in swelling may induce PEDOT de-doping but may still act in tandem with doped chains to improve material conductivity.

2.4.5 Electrical Impedance Spectroscopy

To further probe the impact of increasing EDOT concentration on the electrical properties of the materials, standalone macroelectrodes were fabricated and characterized with electrochemical impedance spectroscopy. Figure 26a displays representative impedance spectra for both the 50% gel samples (blue lines) and 25% gel samples (orange lines) with varying pre-gel EDOT content. Firstly, the relationship between HG50SC-2.5E and HG25SC-2.5E spectra (solid blue and orange lines, respectively) is in agreement with previous observations demonstrating that pre-gel monomer concentration impacts the electrical properties of the final material. Secondly, increasing pre-gel EDOT content appears to have opposing effects on the impedance properties of the two material sets with an increase in impedance magnitude observed for the 50% gel samples and reduction in impedance magnitude observed for 25% gel samples as EDOT content increases.

Figure 26b quantifies impedance magnitude at 1kHz stimulation frequency for the 50% gel samples, recorded at 206.5 ± 2.8 kΩ, 224.1 ± 17.8 kΩ, and 281.0 ± 34.7 kΩ for HG50SC-2.5E,

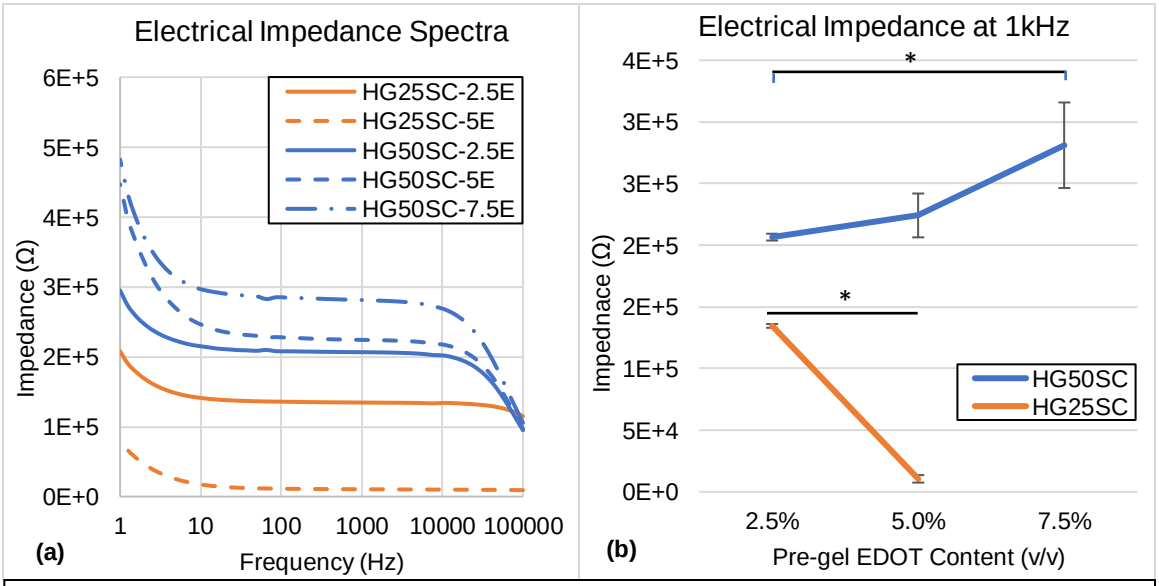

Figure 26: (a) Representative electrical impedance spectra of these gels demonstrate the effect of pre-gel EDOT content on impedance magnitude is highly dependent on pre-gel monomer concentration. (b) Quantification of impedance at 1kHz shows a reduction and increase in impedance magnitude for low and high pre-gel monomer concentrations with increasing pre-gel EDOT content.

HG50SC-5.0E, and HG50SC-7.5E, respectively. Given the observed shift to lower Raman wavenumbers with increasing EDOT content for these samples, the increasing impedance magnitude indicates that the doped PEDOT chains are becoming more insulated as EDOT content increases, perhaps by adjacent chains of overoxidized PEDOT on the periphery of growing PEDOT particles, thereby inhibiting charge transfer.

The impedance magnitude for the 25% gel samples was recorded at 134.6 ± 1.5 kΩ and 10.5 ± 3.0 kΩ for HG25SC-2.5E and HG25SC-5.0E, respectively. Firstly, it is interesting to note that the impedance magnitude for HG25SC-2.5E is larger than HG25S-2.5E which provides additional evidence that the increases to swelling ratio induced by an additional molar equivalent of anionic dopant negatively affected the overall charge transfer characteristics of the PEDOT network. Secondly, in contrast to the 50% gel samples, the decrease in Raman wavenumber exhibited by HG25SC-5.0E correlated with a significant decrease in impedance magnitude which indicates the doped PEDOT chains are producing a more coherent network for charge transfer throughout the material in spite of the drastic increase to its swelling ratio.

Taken together, these results support the indication that PEDOT overoxidation induced by free radical attack of EDOT monomers and growing PEDOT chains is occurring during this one-pot fabrication process and that the severity or probability increases with increased pre-gel monomer concentration.

2.5 Conclusion

Presented here is a novel conductive hydrogel photochemical fabrication process enabling *in situ* polymerization of conductive and hydrogel polymers in parallel within a single reaction vessel along with preliminary characterization of the resulting materials. Both pre-gel monomer concentration and dopant chemistry were shown to impact the material properties with low

monomer concentration and sulfonic acid dopant moieties producing the best results in terms of gel mechanical and electrical properties which are ideal for neural engineering applications. Furthermore, increasing pre-gel EDOT concentration also demonstrated improvements in material electrical properties although this improvement was offset by apparent overoxidation occurring within the PEDOT chains, the severity for which correlated with pre-gel monomer concentration, likely due to an increased probability of radical attack.

Manipulation of other features of the system have thus far been held constant such as conducting polymer and oxidative initiator selection and concentration and dopant concentration which are likely to also have a significant impact on final gel properties. Other conductive polymers may also be included, though PEDOT has consistently demonstrated superior electrical properties so inclusion of these other polymers may not improve the behavior of the system. Increasing oxidative initiator concentration may demonstrate a non-monotonic improvement in conductivity as some reports suggest a 2:1 molar ratio of APS:EDOT (as opposed to the 1:1 ratio used here) maximizes PEDOT conductivity.

However, significantly increasing APS concentration may increase the likelihood of overoxidation of PEDOT or off-target oxidation which may negatively impact gel properties. Replacing APS with another oxidative initiator may or may not improve the gel properties, but may have a significant impact on gel biocompatibility by either reducing it with initiators like Fe(III)-tosylate or perhaps improving it with sodium persulfate (NaPS). This is particularly of interest in the context of facile fabrication techniques for the manufacture of wholly organic microelectrode arrays which would benefit from usage of devices as-fabricated without requiring washing or other intermediate steps.

The PVA-2.5E and HG25SC-5.0E appear to have performed the equally well on the metrics of mechanical and electrical properties which is in agreement with the findings regarding pre-gel monomer concentration and dopant chemistry. It is also interesting to note the low vinyl

concentration of the PVA system, and associated crosslinking mechanism, which likely lessened the impact of PEDOT overoxidation in addition to enabling larger PEDOT particle formation. However, the synthesis procedure to produce the PVA macromer is relatively complex and time consuming and the viscosity would likely limit its application to the STS fabrication processes or other methods requiring arbitrarily complex gel geometries. Conversely, the HEMA monomer system utilizes commercially available monomeric components and is readily solution processable, although it does suffer from increased probability of overoxidation limiting the conductivity of the PEDOT network and limited gelation capability as a result of interactions between components in the pre-gel mixture during polymerization. Therefore, it is likely that some combination of a monomeric system with a PVA-based crosslinker, or another macromeric crosslinker that is not susceptible to oxidation-induced chain scission, will produce a gel system that outperforms the compositions tested here.

Considering this is a novel synthesis procedure, there is still a significant amount of research to be carried out to investigate the photochemical polymerization mechanism both from a basic chemistry standpoint and to further optimize the resulting conductive materials. Additionally, it will be interesting to investigate how broadly applicable this synthesis method is to the wide array of polymers and polymerization mechanisms that currently exist in the production of new composite conductive hydrogel materials. Lastly, the application of this synthesis method to micro- and nanofabrication techniques such as stereolithographic 3D printing and photolithography in the production of soft electronic devices is also worth investigating.

CHAPTER 3 – Optimizing the Property-Dependent Immunomodulation of Myeloid Cells Using Precision Porous Hydrogels as a Culture Model

3.1 Background

Past work in the Ratner lab with STS materials implanted into a wide range of peripheral tissue types has provided an interesting model for understanding the phenotypic heterogeneity of immune cells as they respond to the competing stimuli of implant associated tissue trauma and the precise microporosity of the biomaterial[51]. However, the *in vivo* environment is extremely complex, and many factors are at play simultaneously which make it difficult to tease apart the impact of these factors independently or on a mechanistic level. *In vitro* culturing of relevant cells within STS with various material properties instead provides an opportunity to investigate the processes which underly the inflammatory response and modulation thereof in a more controlled manner. Previous work in the Ratner lab has developed methods for seeding STS with cells of various lineages to answer specific questions about cell-material interactions[95]. In the context of neural tissue engineering, these experiments not only have the potential to provide insight into the impact that various material properties have on the inflammatory response of the cells which drive gliosis, but to also hone in on particular values for those properties that might translate well to minimizing gliosis and stimulating advantageous neural tissue integration *in vivo*.

As alluded to above, some key properties of interest to investigate which will be presented herein include material porosity, stiffness, electrical activity, and surface presentation of biomolecular ques. There has been considerable work investigating the immune response of inflammatory cells to each of these material properties *in vitro*. From the perspective of pore size, several groups have fabricated fibrous tissue engineered scaffolds via electrospinning[96] or 3D printing[97] technologies with various materials to investigate their impact on macrophage activation. Though the technologies utilized in these studies have relatively poor control over pore size, and produce pores up to 1mm in diameter, they still observed a distinct response with macrophages cultured in materials with larger pore sizes producing larger numbers of

proinflammatory cytokines. However, larger trends were observed based on material types used, whereby natural polymers, such as chitosan, caused the highest release of pro-inflammatory cytokines than synthetic polymers like poly(lactic acid) (PLA). It is worth mentioning here again that the STS fabrication process enables precise control over porous microstructure and thus has the potential to serve as a better model for determining the independent impact of pore size on the cellular response to inflammatory stimuli via controlled *in vitro* cell culturing experiments.

Previous work in the lab of Professor James Bryers at UW has utilized STS composed of PHEMA and PDMS as an in vitro culture model to investigate the pore-size dependent response of dendritic cells (DC)[98], another key peripheral immune cell involved in the innate immune response. Their findings demonstrate that pore size impacts the phenotypic expression of DC, even in the absence of explicit inflammatory stimulators, with smaller pores (20μm and 40μm diameter) inducing greater release of proinflammatory cytokines tumor necrosis factor-α (TNF- α) and interleukin 6 (IL-6). However, this study only seeded DC on top of the scaffolds with a culture duration of 24 hours.

More recent work conducted by Dr. Neal Beeman in the Bryers lab investigated the ability of precise STS porosity to tune macrophage activation in response to the inflammatory stimulator lipopolysaccharide (LPS, a bacterial cell wall component). This study utilized a capillary force seeding method to impregnate the STS with primary bone marrow derived macrophage (BMDM) cells followed by a 2-week culture period that concluded with LPS stimulation. They observed a distinct reduction in the release of pro-inflammatory cytokine interleukin 1β (IL-1β) for cells cultured in 40μm STS compared to 100μm STS, as shown in Figure 27a. Furthermore, similar, though more intense, responses were observed at the 2-week time point compared to the 1-week time point. To probe the mechanism of this response on a deeper level, the experiment was repeated with macrophages harvested from a transgenic MyD88 knock-out mouse in which a complete attenuation of this pore-size dependent M1 response was observed, as shown in Figure

27b. This result has led to the hypothesis proposed by Dr. Bryers and Dr. Beeman that the 40μm diameter pores are in effect altering the 'gain' of the macrophage TLR response to inflammatory stimuli. The different responses between immune cell types and across different time periods with the STS model illustrates the complexity of the immune response to implanted materials. Furthermore, it strongly indicates that an optimal tissue response *in vivo* will have to account for these differences in the design of regenerative biomaterials.

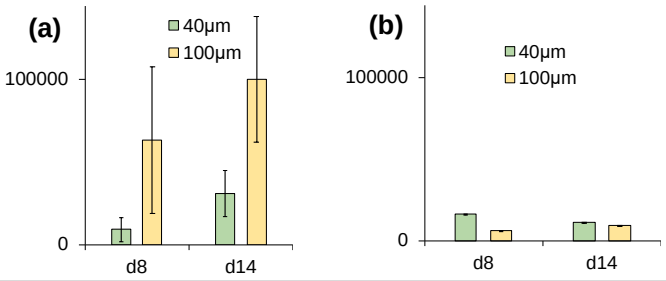

Figure 27: Previous work from the Bryers lab investigating the impact of STS pore size on macrophage polarization. (a) Pore size affects BMDM intracellular IL-1β. (b) Effect abolished with MyD88$^{-/-}$ BMDM. Y-axis = pg/mL IL-1β per mg total protein. X-axis = culture duration.

Beyond microporosity, material stiffness is an important factor affecting the phenotypic polarization of immune cells. The brain is of the softest of human tissues with a Young's Modulus ~2-10kPa[99]. Histological[100] and finite element modeling[101] studies indicate that the mechanical mismatch between hard silicon/metal electrodes (>10GPa) induces tissue strain and persistent trauma as brain micromotions occur during natural respiration and metabolism[102]. This stimulates continued inflammatory activation of immune cells, resulting in chronic gliosis. However, in addition to the prolonged mechanically induced tissue damage, the stiffness of the material substrate itself has been shown to drastically impact the response of immune effector cells.

Previous work demonstrates that substrate stiffness and structure provide a robust cue for macrophages to modulate their phenotype[103]. Several studies have been conducted in which BMDM were cultured on gels, such as poly(acrylamide) (PA) with stiffnesses varying from 1kPa to 150kPa[104]. Others have cultured macrophages on stiffer surfaces, like titanium, patterned with nanostructures such as grooves of varying widths to passively modulate their morphology[105]. Results from these studies demonstrate that topological cues can direct the phenotypic polarization of these cells by controlling cell morphology. It is interesting to note that macrophages

are also known to adopt different morphologies based on their activation state (i.e. M1 vs. M2) when presented with soluble factors[106] and that this relationship works in reverse as well. That is, structural cues alone are able to induce morphological changes in macrophages that subsequently induce changes in phenotypic polarization and release of soluble factors.

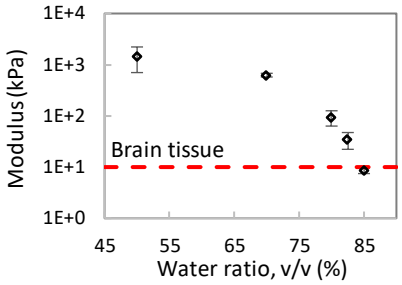

Figure 28: Tunable compressive modulus in poly(HEMA-co-GMA)

While these results provide strong evidence for the impact of material mechanical and topological properties on macrophage polarization, the vast majority of this work has been carried on gels in 2 dimensions which is a departure from the 3-dimensional tissue environment. Here again STS provide an opportunity to serve as a model which enables a reduction in complexity compared to the tissue response *in vivo* while also providing a more representative culture environment to investigate these crucial cell-material interactions. Furthermore, previous work in the Ratner lab by Dr. Le Zhen integrating glycerol methacrylate (GMA) with HEMA produced gels which exhibited a significant reduction in compressive modulus into the range of brain tissue by tuning pre-gel water content, as seen in Figure 28. These findings were applied in the production of materials in Chapter 2 (i.e. HG50C and related compositions) and in the following studies to fabricate a panel of materials with a range of moduli test the impact of STS mechanical properties on immune cell response.

The incorporation of electroactive components into biomaterial scaffolds has also demonstrated a significant impact in their functional integration with electrically active tissues, most notably muscle and nervous tissue[107]. Electroactive nanomaterials like metal nanoparticles, graphene, carbon nanotubes, and conductive polymers have been employed to this effect owing to their high conductivity and ease of incorporation into the biomaterial fabrication process[108]. Low levels of electrical current passed through electrically active biomaterials have been shown to increase progenitor cell recruitment and differentiation[109], axonal growth[110], and may even directly

modulate the phenotypic polarization of immune cells[111]. Therefore, the one-pot conductive hydrogel synthesis method is well suited to the fabrication of conductive STS to also investigate the impact of passive electrical activity of biomaterial scaffolds on immune cell phonotypic polarization.

The last point of consideration for *in vitro* investigation into material property-dependent immune cell modulation presented here involves surface immobilization of bioactive molecules. Many different bioactive molecules have been used as surface coatings on tissue engineered scaffolds. Two biomolecules of interest for investigation here include α-1 acid glycoprotein (AGP, also known as orosomucoid, ORM) and collagen VI (Col6). AGP has been shown to limit inflammatory reactivity and protect from TNFα toxicity[112]. *In vitro* experiments have shown AGP to upregulate CD163 (an M2 marker) when introduced to human monocytes in solution[113] and enhance neurite extensions of chick dorsal root ganglion cells[114,115]. AGP release from astrocytes has also been shown to increase in response to inflammatory stimuli in the brain and serves as a key mediator in the reduction of neuroinflammatory states of microglia[116]. Col6 is a naturally occurring extracellular matrix protein found in central and peripheral nervous tissue which has been associated with various neuroprotective[117] and neuroregenerative[118] effects. It serves as a key component of the basal lamina associated with brain blood vessels and dispersed in the brain parenchyma[119]. It has also been shown to serve as a cell adhesion molecule for neuronal and glial cell types via neural/glial antigen 2 (NG2) binding[120,121], and improve nerve regeneration by modulating macrophage recruitment and polarization toward M2[122]. Macrophages also secrete Col6 in the process of tissue stabilization and wound healing *in vivo*[123].

Previous work by Dr. Alex Chen in the Ratner lab demonstrated the capability of covalently immobilizing AGP and Col6 on 2 dimensional poly(HEMA-co-MAA) surface[124]. These surfaces were then used to investigate macrophage polarization and cytokine release upon inflammatory activation with LPS. Results demonstrated a synergistic effect of AGP and Col6 on macrophage

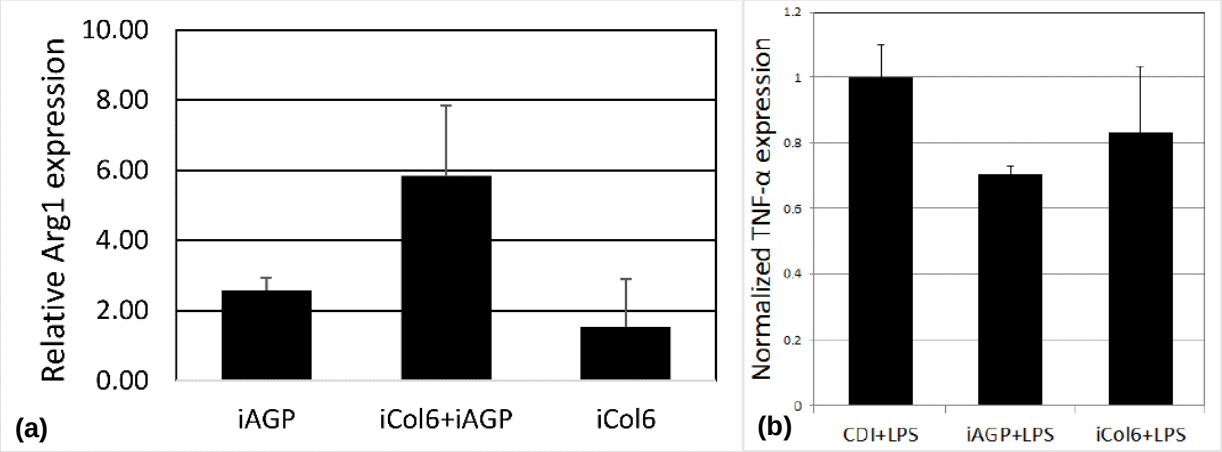

Figure 29: (a) AGP+Col6 co-immobilized on 2D H50 gels synergize to increase expression of macrophage M2 marker arginase-1 (Arg-1). (b) When immobilized on 2D H50 gels independently, AGP and Col6 both demonstrate a reduction in TNFa release in response to inflammatory stimulator LPS. Co-immobilization of AGP+Col6 was not tested under these culture conditions.

M2 activation, shown in Figure 29a. In this case, upregulation of arginase 1 (Arg1), an M2 marker, was observed when macrophages were cultured on surfaces co-immobilized with AGP and Col6 compared to either alone. Additionally, AGP and Col6 reduced the M1 response of macrophages as determined by a reduction in TNFα release, shown in Figure 29B. Based on these results, AGP and Col6 were investigated in the optimization of STS for neuroimmune modulation.

Before presenting results associated with this Chapter, it is worth reviewing the action of key cytokines which where were quantified in the culturing experiments, TNFα, IL10, and VEGF. TNFα is a critical early mediator of inflammatory reactivity in cells of myeloid origin, including microglia and macrophages[125,126] as well as from astrocytes and neurons[127]. This has been explicitly demonstrated by observing reduced inflammatory responses from microglia and peritoneal macrophages harvested from TNFα-knockout mice, in the form of reduced IL1b, IL6, IL10, and IL12 release from TNFα-null cells compared to wild-type cells[128]. Interestingly however, the same study observed no reduction in these secondary cytokines with wild-type mice inhibited with a TNFα-blocker prior to LPS stimulation, indicating that TNFα regulation is important during development but not directly necessary for the production of other inflammatory mediators in the context of LPS-induced TL4 activation. Observations of cytokine release in the context of brain

injury in animal studies indicates that TNFα cytokine and mRNA release are rapidly and robustly upregulated within 6-12 hours after initial insult to the brain, including implant trauma and hypoxia [129,130]. These studies also observed worse behavioral and recovery outcomes upon exogenous delivery of TNFα via systemic or local injections with increases to lesion size and disruptions to the blood brain barrier, demonstrating the deleterious effects of excess TNFα in these contexts.

Other studies investigating traumatic brain injury models also demonstrate a rapid increase in TNFα cytokine and mRNA bioactivity within 1 hour of trauma and with a peak at around 4 hours but that these increases were transient and with a return to basal levels by 24 hours post-injury[131,132]. The authors of these studies suggested that microglial cells were the primary producer of TNFα which contributed to microvascular damage and edema formation. Beyond its well documented involvement in the initiation of inflammatory response and perpetuation via secondary mediators, TNFα also mediates inflammation-resolving behaviors, such as inhibiting efferocytosis of neutrophils[133]. It has also been shown to inhibit mobility of astrocytes in response to a traumatic wound which may act to limit glial scar formation but also interfere with tissue repair mechanisms[134]. Aberrant TNFα release from macrophages and microglia has also been implicated in several peripheral and neurodegenerative diseases[135,136].

However, TNFα has also been implicated in various protective effects including cellular survival[137]. For example, pretreatment of mice with TNFα via intracisternal injection has been shown to increase cellular survival of neuronal cells exposed to significant levels of ischemia[138]. Other studies have demonstrated similar results indirectly by pretreating rats with LPS via intravenous injection prior to ischemia onset that resulted in a reduction in infarct volume compared to non-LPS treated rats that was nullified by coadministration of TNF binding protein, a potent TNFα inhibitor[139]. More recent studies have demonstrated that TNFα pretreatment of human fetus-derived neural progenitor cells (NPC) improved their survivability when exposed to an hypoxic-ischemic environment and that this neuroprotection translated to improvements in cell

survival upon transplantation[140]. Furthermore, application of TNFα-pretreated NPC conditioned media to BV2 cultures showed a significant decrease in release of proinflammatory cytokines including TNFα, IL1b, IL6, and iNOS after LPS stimulation which suggests significant crosstalk between neuronal and non-neuronal cells in regulation of inflammation associated with TNFα release. Lastly, it is also interesting to note that, from a clinical perspective, a significant portion of patients who have been prescribed anti-TNFα drugs for inflammatory conditions do not experience beneficial treatment outcomes from this treatment[135].

Taken together, these results indicate that TNFα plays a complex role in the inflammatory response, exhibiting deleterious effects when released in excess in the acute phase of injury and when ineffectively resolved in the subacute phases of injury but which may also serve as a cellular protectant via activation of an 'antideath' pathway to promote post-injury recovery[137]. Furthermore, the early presence of TNFα has been shown to induce apoptosis in fibro/adipogenic progenitor cells infiltrating a injury site, thereby limiting premature ECM deposition with the potential to lead to pathological fibrosis[141]. The complex intracellular and intercellular signaling that TNFα participates in, particularly in the context of nuclear factor kappa-B (NF-κB) signaling, indicate that improvement in disease or tissue regeneration outcomes are more likely to benefit from differential/controlled temporal modulation of TNFα release as opposed to simple suppression.

Other studies examining the dynamics of TNFα and IL10 release in the context of brain injury indicate that IL10 negatively modulates the production of TNFα in addition to a wide array of other proinflammatory signaling that it is produced by microglia and macrophages upon TLR stimulation[142]. IL10 is another important pleiotropic cytokine that induces macrophage and microglia polarization toward M2-like phenotypes and subsequent participation in anti-inflammatory signaling, resolution from inflammation, promotion of glial and neuronal cell survival, and modulation of vascular remodeling[143]. Microglial release of IL10 has also been shown to increase production of astrocyte-derived transforming growth factor (TGF)-B[144], and participate in

the regulation of adult neurogenesis[145,146]. In addition to IL10's potent anti-inflammatory effects on cells of myeloid origin, these observations demonstrate that IL10, like TNFα, is important for intercellular signaling between all cell types within the brain to contribute to tissue homeostasis.

Upon traumatic or ischemic brain injury, local IL10 expression is immediately upregulated and a significant increase in IL10 release is observable within 2 hours of injury onset that continues to increase past 24 hours[147] and remains elevated for days[148]. Interestingly, IL10-knockout mice show poorer motor and cognitive outcomes associated with larger lesion volumes, increased inflammation, and blood brain barrier-associated edema[149]. However, studies assessing the acute survival rate of humans who have experienced traumatic brain injury have observed a significant correlation between cerebrospinal fluid IL10 concentration upon admission and mortality[150]. These studies also observed that survivors typically had lower IL10 levels at admission that decreased during the initial 24 hour hospitalization period, while non-survivors had higher IL10 levels at admission that continued to rise during initial 24 hour hospitalization period. However, the mechanism behind these observations remained unclear. Additionally, prolonged exposure of IL10 has also been shown to limit the healthy inflammatory response associated with certain disease states, such as the reducing microglial phagocytosis and subsequent accumulation of amyloid-β deposits in a mouse model of Alzheimer's disease[151]. Taken together, these reports indicate that delicate control over the spatial and temporal release of IL10 are import for maximizing outcomes that are dependent on the pathophysiology of the target disease or injury.

VEGF is another extremely important pleiotropic cytokine that is produced by macrophages and microglia during injury and ischemia[152] and serves as a potent chemoattractant and proliferative stimulant for microglia and astrocytes[153]. VEGF has also been documented as a potent M2-polarizing factor for BV2 and primary microglial cells[154]. Release of VEGF after traumatic injury to the brain has been documented to begin at around 6 hours post-injury, peaks

around day 3-5, and persists for up to 2 weeks post-injury[155]. In this study blood brain barrier breakdown was observable within the first 10 minutes of injury onset, significantly before VEGF release, indicating that this breakdown was not associated with VEGF. In another study involving a cortical stab wound model, reactive astrocytes were also observed to express VEGF and VEGF receptors, indicating they may also participate in angiogenesis and/or blood brain barrier permeability in response to injury[156]. Indeed, other studies have demonstrated that stimulation of neurons and astrocytes with high doses of VEGF *in vitro* have a mitogenic effect which increased cellular density over the culture period[157]. Additionally, the delivery of VEGF has shown a protective effect on motor neurons with increased survival and reduction in apoptosis after exposure to TNFα, hypoxia, oxidative stress, serum deprivation, excitotoxicity[158].

However, similar to TNFα and IL10, VEGF has also demonstrated deleterious effects on neural recovery from injury, particularly in the case of post-ischemia reperfusion. For example, systemic delivery of VEGF within 1 hour of focal ischemia caused an increase in blood brain barrier leakage, edema, and hemorrhage[159]. However, systemic delivery of VEGF at 48 hours after focal ischemia instead improved neuronal recovery and halted the advance of the ischemic penumbra that was linked to an increase in angiogenesis[159]. The authors suggest that these divergent results may have been a function of the intravenous injection method that would deliver VEGF to the site of injury on the side of the vasculature as opposed to on the neural tissue. Indeed, other studies which delivered VEGF directly to neural tissue via topical application on the brain surface within 90 minutes of injury onset observed a reduction in lesion volume and increased neuronal survival after 24 hours[160].

Collating these reports from the literature, it is clear that TNFα, IL10, and VEGF serve as critical cytokines released and sensed by neural and non-neural cells of distinct lineages, including macrophages, microglia, astrocytes, and neurons. Furthermore, the precise timing, spatial distribution, and magnitude of release of these cytokines collectively play a significant role

in the initiation of and resolution from injury-induced neuroinflammation. Quantification of microglial and macrophage release of these cytokines after exposure to inflammatory LPS challenge will therefore provide insight into the modulatory capability of the range of STS material properties examined here.

The work presented below therefore sought to determine the impact of STS material properties, with respect to pore size, modulus, electrical activity, immobilized proteins, on macrophage and microglia polarization and optimization thereof *in vitro*. A panel of materials with a range of values across these properties were fabricated and seeded with BMDM and the microglial cell line BV2 and phenotypic polarization characterized. The ultimate goal of this work is to expand the neural microelectrode design toolbox with materials to modulate neuroinflammation and attenuate implantation-induced gliosis to maximize functional neural tissue regeneration as a means to pave the way for long-term clinical application of BCIs.

3.2 Materials and Methods

3.2.1 Materials

All materials were purchased from Sigma-Aldrich (St. Louis, MO) unless otherwise stated. Hydrogels used in the following culturing experiments consisted of monomers of HEMA (Polysciences), GMA (Polysciences), AA, and AMPS, and crosslinked with TEGDMA (Polysciences). Polymerization initiator species used was Irgacure 651. Bovine α_1-acid glycoprotein (AGP) and human collagen 6 (Col6, Rockland Antibodies and Assays) were immobilized to materials via the -COOH moiety on the AA units with *N*-(3-Dimethylaminopropyl)-*N′*-ethylcarbodiimide (EDC), *N*-Hydroxysulfosuccinimide sodium salt (NHS), and *N*-hydroxysulfosuccinimide sodium salt (sulfo-NHS), in 0.1M 2-morpholinoethanesulfonic acid (MES) buffer. Cellular release of proteins were quantified with enzyme linked immunosorbent assay (ELISA) kits for tumor necrosis factor-α (TNF-α; DY410, R&D Systems), interleukin 10

(IL10; DY 417, R&D Systems), and vascular endothelial growth factor (VEGF; MMV00, R&D Systems) to quantify the inflammatory response of myeloid cell types and normalized to total cell protein via the Bicinchoninic Acid (BCA) assay kit (R&D Systems). RIPA lysis buffer (Thermo Fischer Scientific) supplemented with a cOmplete protease inhibitor was used to lyse cells while inhibiting proteolysis of intracellular proteins for quantification of total cellular protein via the BCA assay.

3.2.2 STS Fabrication

Precision porous hydrogel scaffolds were fabricated via the methods described above to produce gels with 40μm and 100μm diameter pores and range of stiffnesses. Refer to the tables in the following sections for the exact compositions of the materials tested.

3.2.3 Protein Immobilization

A protocol was developed to immobilize Col6 and AGP to STS under sterile conditions in a biosafety hood for these culturing experiments. Briefly, porous gels were equilibrated in 0.1M MES buffer (pH 4.5) and then incubated in a solution containing 5M EDC, 0.1M of a 1:1 mixture of NHS:sulfo-NHS (this ratio was determined to enable protein immobilization while limiting other changes to material properties such as compression modulus) in 0.1M MES buffer (pH 4.5) for 1 hour. After 1 hour, gels were briefly washed in 0.1M MES buffer (pH 4.5) and placed on sterile kim wipes where ~50μL of protein solution (125μg/mL Col6 + 62.5μg/mL AGP in 0.1M MES, pH 4.5) was pipetted over the gels and allowed to be pulled through via capillary action. Gels were then placed into a closed, sterile container with the remaining protein solution and left to react in the fridge at 4C.

The following day gels were washed briefly in PBS (pH 8.5) to remove excess protein and then incubated in PBS (pH 8.5) over night to quench the unreacted NHS/EDC. The following days the gels were washed thoroughly in PBS (pH 7.4) and stored in sterile PBS (pH 7.4) at 4C in the fridge until initiation of the cell seeding experiment. To determine immobilization success, a set of reacted gels were frozen into blocks of OCT, cut into 10μm slices with a cryotome and mounted onto positively charged slides. Serial slices were then run through a brief immunohistochemical staining process involving a 1 hour block with 1% goat serum in PBS (pH 7.4), 1 hour treatment with primary antibodies for AGP (rabbit anti-AGP, ab134042, 1:250 dilution, Abcam, Cambridge UK) or Col6 (rabbit anti-Col6, ab6588, 1:250 dilution Abcam), a 1 hour treatment with fluorescent-tagged secondary antibodies (AlexaFluor 488 goat anti-rabbit IgG, A-11008, 1:250 dilution, ThermoFisher) with 4 rapid rinses in HBHS between each step. Stained slices were then visualized with a Nikon immunofluorescent microscope.

3.2.4 Cell Harvest

Primary bone marrow derived macrophages (BMDM) used in these studies were harvested from the femurs and tibia of adult mice via well-established methods[161]. Briefly, adult C57BL6 mice were sacrificed, and their hind limbs dissected and washed for 5 minutes in sterile 70% ethanol. After sterilization, excess tissue was removed from the bones and a pair of surgical scissors were used to gently clip both ends off the femur and tibia of both hind legs. A syringe filled with sterile RPMI 1640 supplemented with 20% fetal bovine serum (FBS) was used to flush the marrow containing myeloid precursor cells out of the bone cavity via a 26-gauge needle into a 10cm non-tissue treated poly(styrene) culture plate. Cells from both hind legs were flushed, strained through a sterile 40μm porous cell strainer and then returned to the plate with 10mL RPMI 1640 supplemented with 20% FBS, 0.1% penicillin/streptomycin (pen/strep), and 20ng/mL mouse macrophage colony stimulating factor (MCSF). The plate was then placed in an

environmentally-controlled incubator at 37C with 5% atmospheric CO_2. After 3 days another 10mL of RPMI 1640 supplemented with 20% FBS, 0.1% pen/strep, and 20ng/mL MCSF was added to the plate.

At day 7 or 8, the plates were removed from the incubator and washed semi-vigorously 3 times with Dulbecco's PBS (pH 7.4) lacking calcium or magnesium ions (DPBS-/-) to wash away any non-adherent cells. Macrophage progenitors and differentiated macrophages are known to remain strongly adhered to the untreated plate during such washes, while other cell types are washed away. In preparation for culturing experiments, adhered macrophage cells were incubated in DPBS-/- for 5 minutes to weaken their adhesion to the plate (as calcium is required to maintain adhesion to the plate) and then gently removed from the plate with a cell scraper, collected in RPMI 1640, and counted with a hemocytometer. Cell counts averaged around $8x10^6$ cells per mouse.

Microglial cells used were of the BV2 cell line as a gift from the Shain lab at UW and were expanded over several passage cycles as necessary. No cells past passage 20 were used in these experiments.

3.2.5 STS Cell Seeding and Culturing

To investigate the impact of various hydrogel scaffold properties on immune reactivity in 3 dimensions, STS of various material compositions and pore sizes were seeded with BMDM or BV2 cells via a capillary force seeding method previously established in our lab[95]. Briefly, STS sheets were punched into 6mm diameter discs using a sterile biopsy punch. STS discs were incubated in sterile complete Dulbeccos Modified Eagles Medium (DMEM), i.e. supplemented with 10% FBS, 1% pen/strep, and 1% L-glutamine (L-glut). Studies with BMDM also incorporated 10ng/mL MCSF into the complete DMEM for the duration of the culturing experiment. BMDM or

BV2 cell suspensions were brought to a concentration of 10^7 cells/mL, equilibrated STS discs were placed onto a stack of 5 sterile kim wipes, and 100µL of cell suspensions were slowly pipetted onto the top of the discs, allowing a total of 10^6 cells to be drawn into the pores of the disc. Seeded discs were then placed into sterile cell strainers within the wells of a 6-well plate (to enable ample diffusion on all sides of the disc) with 5mL complete DMEM. Control wells also contained either 10^6 BMDM cells or $5x10^5$ BV2 cells (given rapid replication of these cells) plated in 2 dimensions on the bottom of the well with 5mL complete DMEM.

BMDM cells were cultured for 7 days with 3mL complete DMEM replaced on days 2 and 4 to feed the cells while limiting serum shock. On day 4, discs were also transferred to new wells with new cell strainer supports with the transfer of 2mL from the old well and 3mL of fresh complete DMEM. This was to ensure that any cells which fell out of the scaffold during the initial culture duration were not included in the subsequent stimulation and collection. Control wells with cells cultured in 2D were not transferred to new wells. On day 6, 24-hours prior to harvesting conditioned media (CM) all wells besides a non-stim control were stimulated toward a classically inflammatory phenotype (M1) with 100ng/mL lipopolysaccharide (LPS). On day 7, CM and cells were collected for further analysis. In preparation for protein release analysis, seeded discs and cells plated in 2D were collected into DPBS (pH 7.4) and 1mL of CM from each of these wells was extracted off the top of each well. Cells and CM were flash frozen, and the stored in a -80C freezer until further analysis via ELISA/BCA. Other seeded scaffolds were collected and processed for morphological analysis.

BV2 cells were cultured for 4 days with no media replacement. On day 3, 24-hours prior to harvesting conditioned media discs were transferred to new wells with new cell strainer supports and 5ml of DMEM with 1% FBS and then stimulated with 100ng/mL LPS. On day 4, seeded discs and cells plated in 2D were collected and prepared for analysis as above.

3.2.6 Protein Release

To determine the release of key inflammatory cytokines as a measure of the inflammatory response to LPS and modulation thereof by the hydrogel scaffolds, CM was thawed to room temperature and then run through a set of ELISA kits following the manufacturer's instructions and compared to a standard curve of known concentrations to quantify protein release in pg/mL. Protein concentration values quantified via ELISA were normalized to total cell protein concentrations in µg/mL quantified via BCA assay by first washing the cells with several cycles of DPBS and then grinding the scaffolds in Eppendorf tubes with a plastic micropestle in 150µL RIPA lysis buffer supplemented with a cOmplete protease inhibitor to limit protein degradation. Protein release values (ELISA) were divided by total cellular protein values (BCA) for a final normalized value expressed as picograms released per microgram total cell protein (pg/µg) for comparison across treatment groups.

3.2.7 Mechanical Analysis

Compression modulus of discs fabricated in the second part of this chapter were measured via an Instron model 5543 as described in the previous chapter.

3.2.8 Morphological Analysis

Another set of discs were run through the same culturing procedure as above but at the end of the 7- day culture period were immediately placed into 4% paraformaldehyde (PFA) for fixation for 40 minutes followed by 30minutes in 0.4% osmium tetroxide (OsO_4) and then a series of washes in successively more concentrated ethanol up to 100% ethanol. Discs were then placed in a bath of liquid nitrogen-cooled ethanol until brittle and then cracked with a razor blade to expose cross sections. Disc fragments were placed back into 100% ethanol within a critical point

dryer (CPD) and dried. Dehydrated fragments were then sputter coated with a thin layer of metal (Au/Pd) and visualized via SEM at multiple magnifications.

3.2.9 Cytotoxicity Assessment

Prior to cell seeding, all gels were run through cytotoxicity and endotoxin tests. For the cytotoxicity assessment, gels were first incubated in cell culture medium at 6cm^2 surface area/mL for 24 hours following ISO standards. This conditioned medium was then used to culture NIH 3T3 cells following ISO Guidelines 10993-5 and graded for cytotoxicity at the 12-, 24-, and 48-hour time points according to Table 6. Grades were be averaged across 3 repeats to determine the cytotoxicity of each gel composition:

Table 6 ISO 10993-5 Guidelines for cytotoxicity assessment

Grade	Reactivity	Condition of Culture
0	None	No cells showing damage, intracellular granulation, no cell lysis.
1	Slight	< 25% damaged cells (these cells are round, without intracellular granulation) occasionally cell lysis
2	Mild	25-50% damaged cells (these cells are round, without intracellular granulation) cell lysis
3	Moderate	50-75% damaged cells (these cells are round, without intracellular granulation) wide cell lysis
4	Severe	75-100% damaged cells (these cells are round, without intracellular granulation) nearly complete destruction of the cell layers

3.2.10 Statistics

One-way ANOVA was used to compare across sample types followed Tukey's Honest Significant Difference post hoc test for pairwise comparison to calculate Q values using group means, mean square within, and number of samples per group. Statistically significant comparisons were determined by comparing Q values to lookup tables based on sample size and degrees of freedom and marked with an asterisk (*). All experiments were run in triplicate with at least 3 seeded scaffolds per experimental repeat and data are reported as mean ± standard deviation.

3.3 Results & Discussion

3.3.1 Initial Seeding and Culturing of Myeloid Cells within STS

Table 7 provides the names and compositions of the various materials tested in the following studies. A preliminary experiment was conducted to investigate the pore size-dependent response of STS on macrophage cells harvested and differentiated from the bone marrow of mice (BMDM). BMDM were seeded into H50 STS discs with 40μm and 100μm pores and onto a 2D polystyrene plate for 1 week followed by 24-hour stimulation with LPS before visualization and quantification of protein release, discussed below. Cell seeding was carried out via a capillary force method developed in the Ratner Lab. The STS discs used in this study were 8mm in diameter and composed of the H50 recipe with bulk modulus on the order of 1000kPa.

Table 7 Material composition of porous materials studied in preliminary cell seeding experiments.

Gel Name	Hydrogel Monomer	Hydrogel Conc. [%]	Dopant	Dopant Conc. [mol/L]	EDOT Conc. [%]	Pore Size [μm]
40-H50	HEMA	50	-	-	0	40
100-H50	HEMA	50	-	-	0	100
40-G15	GMA	15	-	-	0	40
40-G20	GMA	20	-	-	0	40
100-G25	GMA	25	-	-	0	100

The disc diameter was larger than the 6mm diameter discs used in previous studies in the Bryers lab, though the same absolute number of BMDM cells were seeded into each scaffold. As such the density of cells used here was ~$2x10^6$ cells/mL of scaffold compared to the ~$3.5x10^6$ cells/mL of scaffold used previously which is reflected in the density of cells/pore in the SEM images. However, the morphological trends between the two experiments are similar, as are the observed differences in protein release. Scaffolds were imaged via SEM to observe the morphological changes experienced by cells cultured in these materials.

Figure 30a and 30b depict low magnification images of 40μm and 100μm scaffolds, respectively. The number of visible cells is low given the low cell density but zooming in on specific regions/pores provides more insight into the morphology of the cells cultured within them. Figure 31 depicts a series of higher magnification images of BMDM in 100μm pores which were more frequently found isolated from other cells. These cells typically displayed elongated morphologies with end feet adhered to the pore walls, exemplified in Figures 31a and 31b. The fracturing of the fine structures of the cells in these images is likely a result of the critical point drying method used to prepare these samples for SEM. Besides these isolated cells, several groups of cells were observed together, and these cells frequently demonstrated more rounded or flattened morphologies, shown in Figures 31c and 31d.

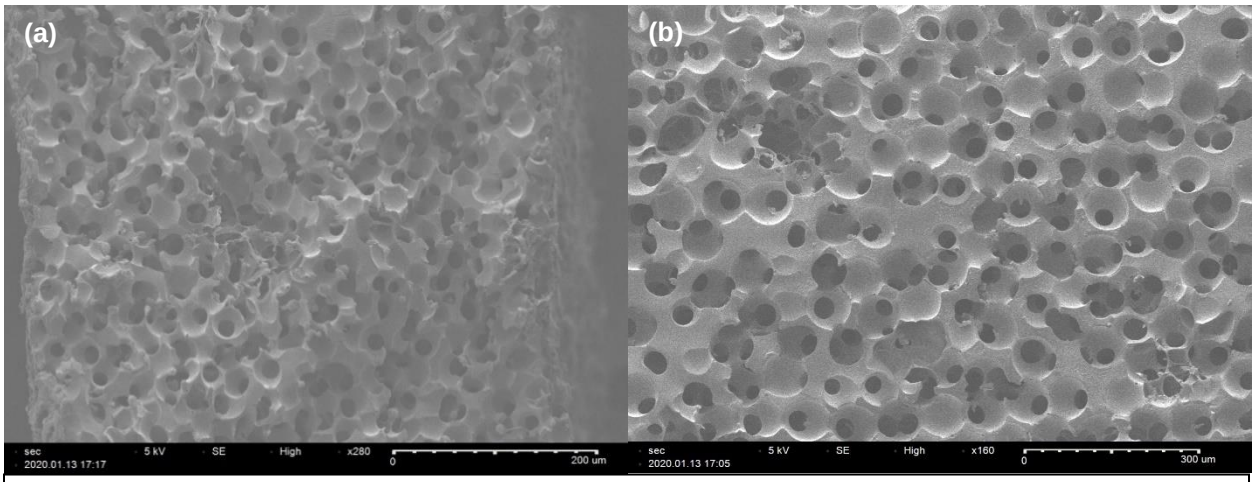

Figure 30: Low magnification SEM images of (a) 40μm and (b) 100μm STS seeded with BMDM.

Figure 32 depicts a series of high magnification images of BMDM cultured in 40μm pores which were more frequently found in clusters. Interestingly, the cells in these clusters displayed a range of morphologies, from rounded, to flattened on the pore surface, to elongated across the width of the pores. Taken together, there are several possible implications from these results. Firstly, this may suggest that the cells cultured within 40μm pores are exhibiting a range of phenotypes depending on their location in the pore and proximity to other cells. Indeed, immunohistochemical stains of explanted scaffolds demonstrate such heterogeneity of cell morphology and phenotypes within the porous network[52]. Additionally, fewer macrophages are found in STS with larger pore sizes *in vivo*, such that this low cell density culture model may be recapitulating some of these effects which are then driving the differences observed in the cytokine response as well. Interestingly, the elongated phenotype of macrophages has been correlated with M2 polarization and so cells demonstrating this morphology in these images may be polarized as such, even those within the 100μm scaffold. Indeed, the release of inflammatory cytokines by cells in 100μm scaffolds is lower than that released by cells cultured in 2D. As such, it is likely that some degree of immunomodulation is occurring in 100μm scaffolds which may be observable on the single-cell level via such cellular morphologies.

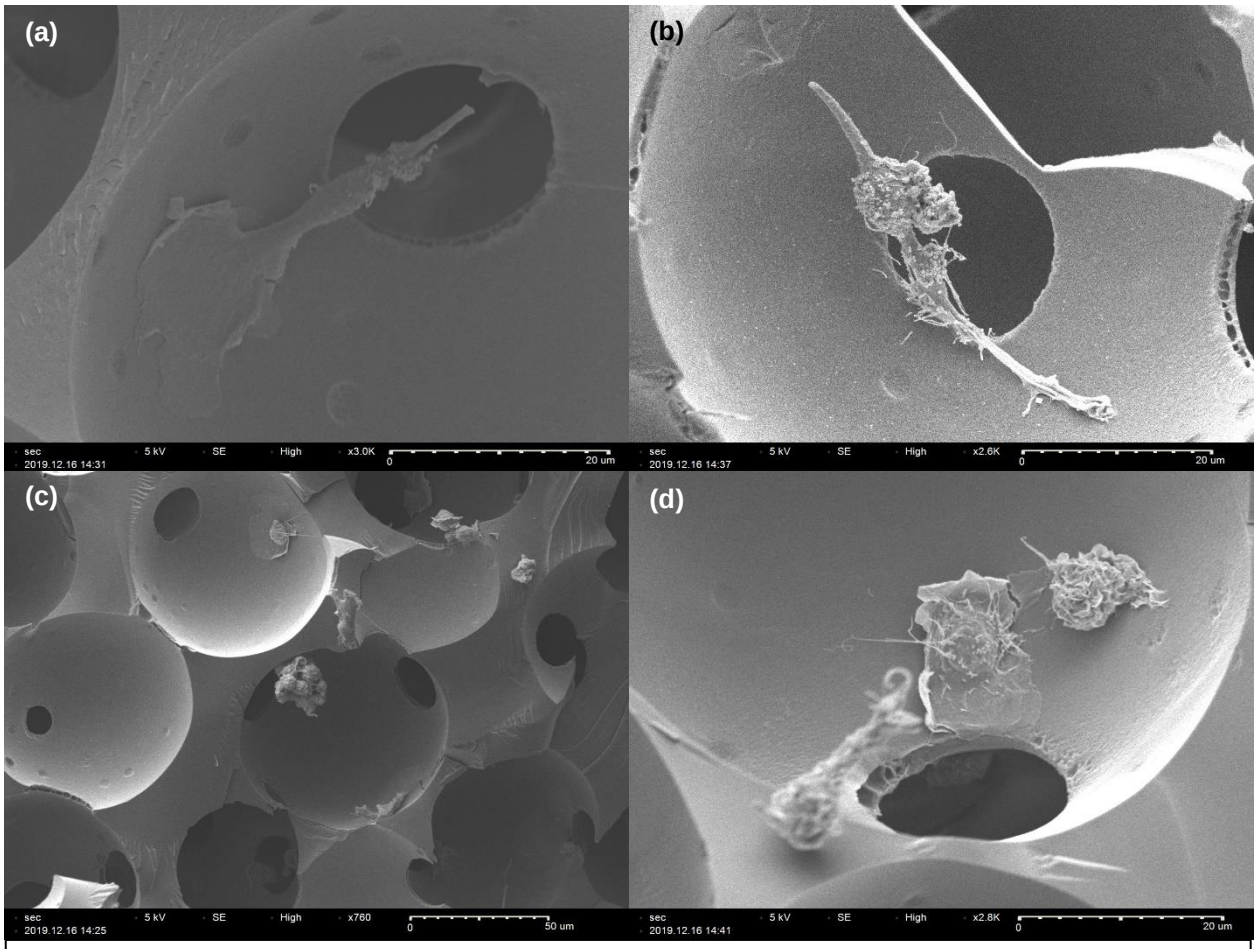

Figure 31: High magnification SEM images of 100µm STS seeded with BMDM. (a) and (b) demonstrate a fraction of isolated BMDM exhibiting elongated morphologies. (c) and (d) demonstrate more flattened or rounded morphologies when found in proximity within pores.

Another preliminary experiment was run to determine if cells derived from a microglial cell line, BV2, remained viable when cultured in STS of different material stiffnesses (10-1000kPa). These gels were fabricated by completely replacing HEMA with GMA and varying the water content in the pre-gel solution to produce a panel of GX gels (X = 50-15% monomer concentration). This experiment utilized 6mm disc sizes with $1x10^6$ cells/scaffold to increase the overall cell density which can clearly be seen in the SEM images in Figure 33. Cells in all scaffolds survived the full culture duration but were not stimulated with LPS. Figure 33a depicts a low magnification image of BV2 cells distributed throughout the porous network of a G20 gels with 40µm pores. Here you can see the cell density is much higher, the diameter of the cells is considerably larger, and the vast majority of cells are in a rounded morphology. Figures 33b depicts higher magnification

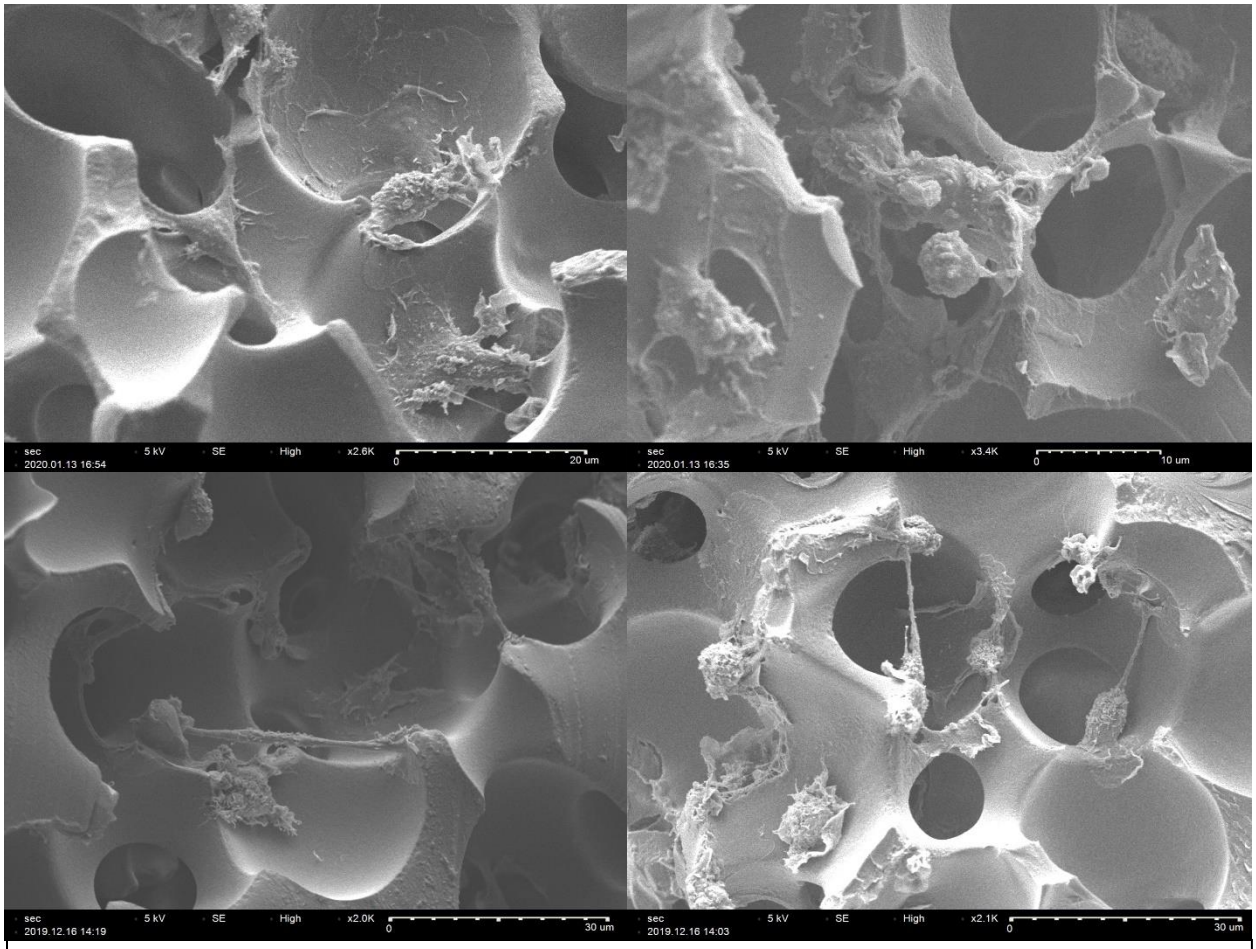

Figure 32: High magnification SEM images of 40µm STS seeded with BMDM. These cells demonstrated a wider range of morphologies and were more frequently found together.

images of cells cultured in G15 gels with 40µm pores. Here the rounded morphology of the cells can more clearly be seen. It is interesting to note that the surface of the pores in these high water content gels have microridges that may have an impact on cellular morphology, adherence, and migration, especially in the presence of inflammatory stimulators like LPS. However, these ridges may also simply be an artifact of the critical point drying method.

Figure 33c depicts a higher magnification image of cells cultured in G25 gels with 100µm pores. Unlike the 40µm scaffolds, single cells did not fill the pores of the 100µm scaffolds and thus were more likely to form clusters. Those that did not cluster together frequently extended adhesive filaments which can be seen in detail with the much higher magnification image in Figure 33d. The cellular adhesion demonstrated by these BV2 cells and BMDM cells above is particularly

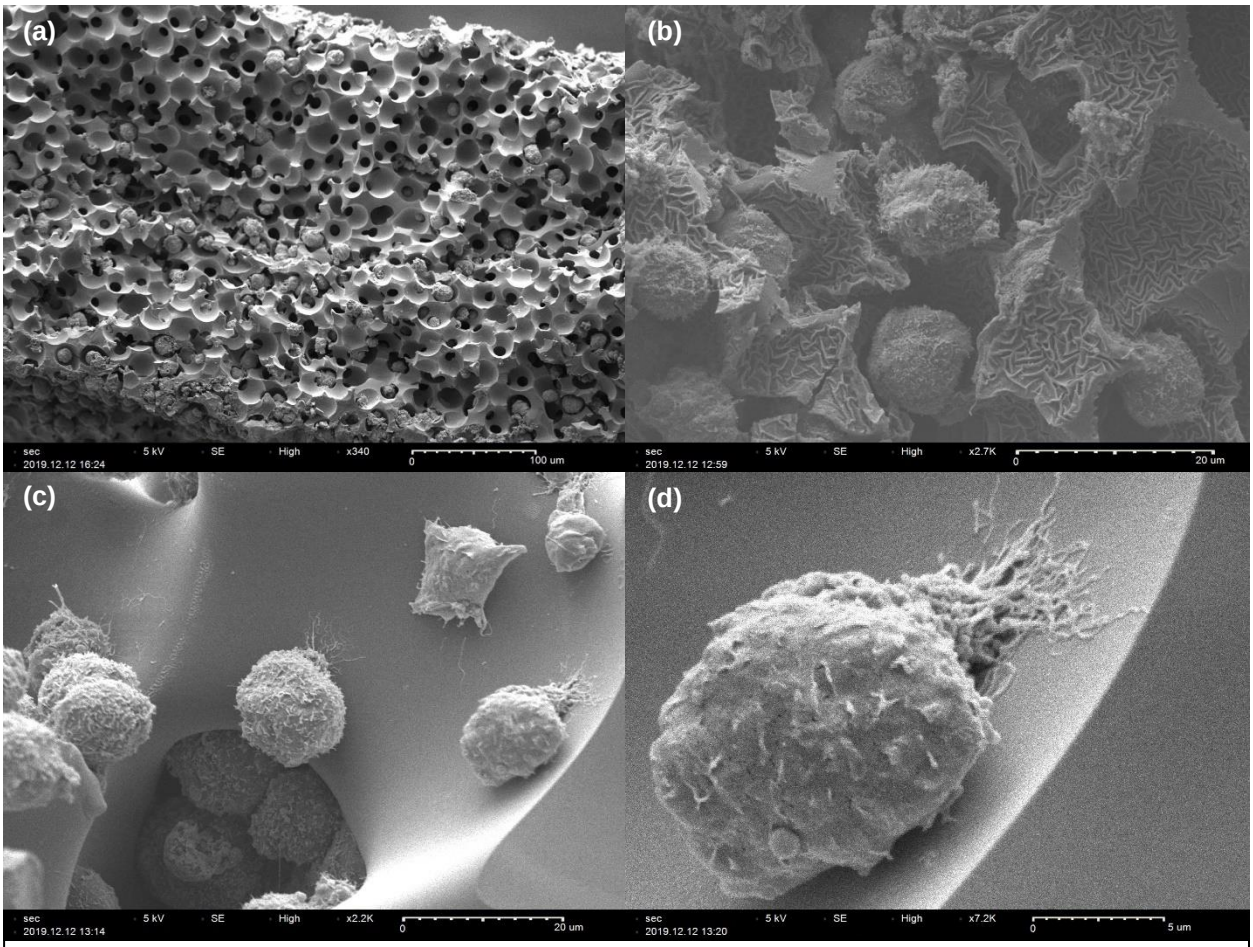

Figure 33: (a) Low magnification SEM image of BV2 cells seeded into G_0 STS with 40μm pores and ~10kPa compression modulus. (b) High magnification SEM image of BV2 seeded into G_0 STS with 40μm pores and <10kPa compression modulus. (c) High magnification SEM image of BV2 seeded into G_0 STS with 100μm pores and ~100kPa compression modulus. (d) Increased magnification of cell pictured in (c), highlighting the filamentous attachments of BV2 cells to the pore wall.

interesting given the materials' hydrophilicity and the lack of cellular adhesion domains present in the synthetic polymers used. That said, the cells were cultured in 10% fetal bovine serum, so some fraction of proteins from solution likely adsorbed onto the pore surface to provide adhesion points for the cells. In any case, this is an interesting result given discussion in the literature regarding the non-adhesive nature of synthetic polymer hydrogels.

3.3.2 Protein Release

The pore size dependent response of BMDM to inflammatory LPS stimulation was determined by quantifying the release of the classical inflammatory cytokine tumor necrosis TNF-

α via ELISA. Cytokine release profiles were normalized to the total protein content as a proxy for the number of cells in each scaffold to compare across treatment groups. Even though the cellular density was reduced as compared to work by the Bryers lab, the results are in good agreement with previously observed trends. Figure 34a demonstrates that BMDM cultured in the 40μm STS demonstrated a reduction in TNF-α release as compared to cells cultured in 100μm STS ($p = 0.08$), providing more evidence that pore size has a significant impact on the phenotypic polarization of BMDM. Cells cultured in both 40μm and 100μm STS demonstrated a significant reduction in TNF-α release as compared to cells cultured in 2D on tissue culture poly(styrene), indicating that the 3D culture environment itself also has a positive impact on modulating BMDM inflammatory reactivity.

However, it should also be noted that poly(styrene) culture plates are also much stiffer than the scaffolds tested here such that both pore size and mechanical stiffness were likely playing a role in the TNF-α release profile. However, the cells in the 40μm porous scaffolds do release more TNF-α than cells cultured in 2D which did not receive LPS stimulation. As TNF-α is

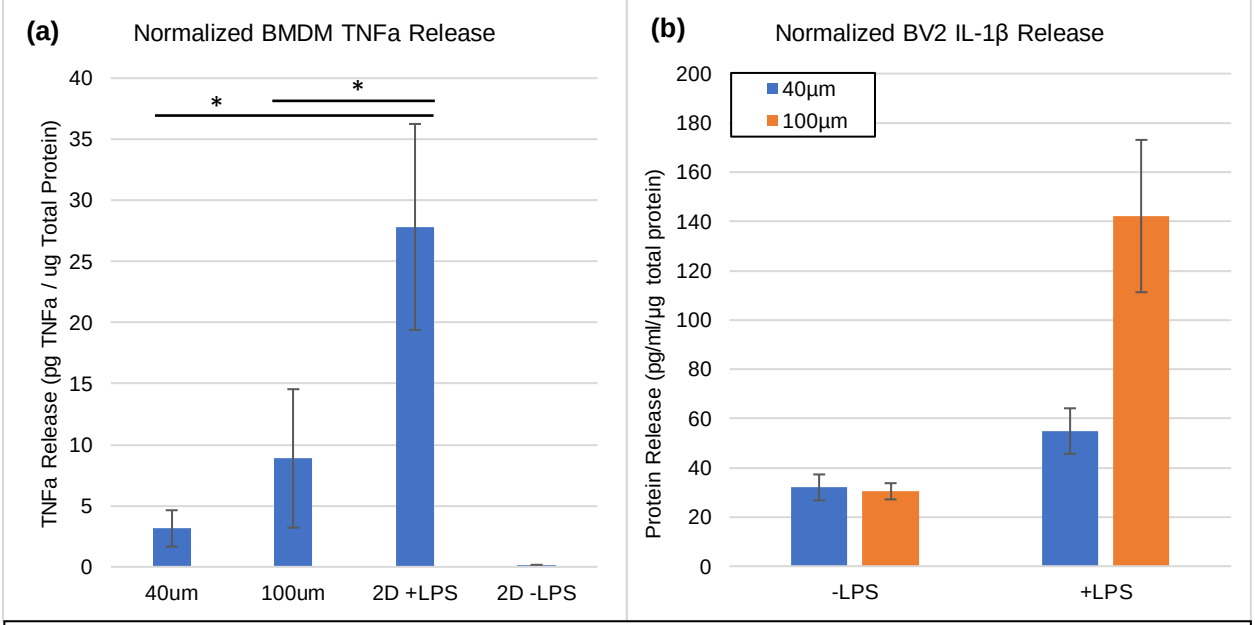

Figure 34: (a) Protein analysis of the proinflammatory cytokine TNFα released into the media by cells shown in Figures 24 and 25 demonstrates quantitatively the impact that pore size has on modulating BMDM phenotype. (b) BV2 cells also demonstrate pore size-dependent modulation of phenotype as determined by release of the pro-inflammatory cytokine IL-1β.

a key signaling molecule in the natural tissue response, it is likely that some degree of TNF-α is beneficial, or perhaps even necessary, for improving tissue integration *in vivo*. That said, this TNF-α release would likely be observed in conjunction with concurrent or sequential increases in pro-regenerative cytokines such as interleukin 10 (IL-10) or vascular endothelial growth factor (VEGF) in order to produce an optimal healing response. Additional modifications to the material properties of these scaffolds, such as stiffness, electrical activity, and immobilization of bioactive molecules were hypothesized to contribute additional immunomodulatory action to the scaffolds and thus were studied in greater detail in subsequent studies, discussed in the following section.

Other preliminary experiments carried out in collaboration with Dr. Neal Beeman from the Bryers lab also assessed the pore size dependent response of BV2 cells to LPS stimulation by measuring the release of interleukin 1-β (IL-1β) after being cultured in STS with 40μm and 100μm diameter pores. Figure 34b demonstrates that BV2 cell response to LPS stimulation is also modulated by pore size, with the 40μm pores minimizing IL-1β release, which provides support for the observations made from preliminary implant studies regarding the impact that precisely controlled porosity has on reducing gliosis severity[53] by modulating the phenotype of the key cells which drive this adverse neuroinflammatory response. While relatively simple, *in vitro* culturing experiments provide a powerful model for probing the impact that material properties have on these cellular responses in a controlled and independent manner. Furthermore, results from these *in vitro* experiments may then be directly applied to the tuning of material properties to design a biomaterial to perform in a desired manner when subject to the tissue environment.

However, questions remain as to the mechanisms which cause this pore size-dependent immunomodulation in these cells of myeloid origin. Particularly pertinent to this discussion is the concept of trained immunity. Trained immunity research to date has demonstrated that M1[162] and M2[163] activation of myeloid cells with soluble factors may serve to “train” these cells to strengthen or dampen subsequent responses. Results presented here corroborate and expand upon the trained immunity hypothesis by providing evidence for the impact of precise 3D structural features

(*i.e.,* scaffold porosity) as a passive, yet robust, initial training cue which modifies subsequent polarization of myeloid cells upon secondary exposure to inflammatory soluble factors, such as LPS. Taken together, these results suggest that pore size has an indirect effect on TLR4 response to inflammatory stimuli, possibly by modulating cell morphology (*e.g.* cytoskeletal remodeling) and thus affecting intracellular signaling dependent on these changes. Future studies designed to probe the impact of precise 3D structural cues presented by STS of varying pore sizes on cytoskeletal remodeling occurring in these cells and the downstream effect on cellular phenotype are therefore warranted.

3.4 Optimization of STS Properties for Immunomodulation of Cells of Myeloid Origin

Based on the results observed in the preliminary studies involving culturing of BMDM and BV2 in STS with varying pore sizes, a set of subsequent experiments was carried out to investigate the impact of other crucial material properties on immunomodulation to produce a more 'optimal' material for neural tissue regeneration and integration. A panel of materials were fabricated to investigate the impact of pore size, stiffness, electrical activity, and immobilization of bioactive molecules on the cellular response. Porous discs with a diameter of 6mm were fabricated and run through morphological analysis, mechanical compression analysis, and seeded with BMDM and BV2 cells as above to assess release of TNF-α, IL10, and VEGF. Table 8 the names and compositions of the materials tested in these studies.

Table 8 Pre-gel compositions for experiments investigating material-property dependent immunomodulation of myeloid cells.

Gel Name	Gel Group	Hydrogel Monomer	Hydrogel Conc. [%]	Dopant	Dopant Conc. [mol/L]	EDOT Conc. [%]	Pore Size [μm]
100-HG50	1	HEMA:GMA (80:20)	50	AA/AMPS	0.2	0	100
40-HG50	2	HEMA:GMA (80:20)	50	AA/AMPS	0.2	0	40
40-HG25	3	HEMA:GMA (80:20)	25	AA/AMPS	0.2	0	40
40-HG25-5.0E	4	HEMA:GMA (80:20)	25	AA/AMPS	0.2	5.0	40
40-HG25-5.0EP*	5	HEMA:GMA (80:20)	25	AA/AMPS	0.2	5.0	40

*P = AGP/Col6 proteins

3.4.1 Cytotoxicity Assessment

It is important to assess the degree of cytotoxicity and presence of bacterial endotoxins for materials designed to interface directly with cells and tissues to ensure that the chemical constituents used do not passively cause undue harm. PEDOT:PSS has already demonstrated remarkable cytocompability in a number of studies conducted both *in vitro* and *in vivo*, as have conductive hydrogels prepared with PEDOT[164,165]. However, the novelty of the hydrogel system necessitated that analogous cytocompatibility studies be conducted to determine the cytocompatibility of these materials specifically. Prior to initiation of culture experiments, all material groups were run through ISO 10993 standard for cytotoxicity assessment and a endotoxin kit. All materials passed both assessments with little to no observable cell death or presence of endotoxin, providing confidence that observations made regarding the modulation of cellular phenotype were the result of the various material properties tested as opposed to aberrant cell death or bacterial infection.

3.4.2 Material Morphological Analysis

Lyophilized cross sections of Groups 1-5 were imaged via SEM to examine the porous structure of each material, displayed in Figure 35, each of which demonstrate the success of the STS fabrication process to produce precision porous scaffolds. Figure 35a shows Group 1 with 100μm pore diameter and interconnected porous network. Figures 35b and 35c depict Group 2 and Group 3, respectively, with 40μm pore diameter and demonstrate that the reduction in monomer concentration associated with Group 3 did not significantly impact the pore size or network structure of the resulting STS material compared to Group 2. Figure 35d depicts Group 4 which has a porous network akin to Group 3 with smooth pore walls. This result was interesting considering the image presented in Figure 11b of the first successful application of the one-pot conductive hydrogel synthesis method to the STS fabrication process demonstrated pore walls with sub-micron surface roughness and porosity. However, the pre-gel material composition used here included isopropanol as a cosolvent instead of methanol, which may have improved the efficacy of polymerization or caused a reduction in deleterious gas formation during the polymerization reaction in these materials. Lastly, Figure 35e depicts Group 5 with a similar structure to Group 4, although some surface roughness was apparent in these samples. Figure 35f depicts a higher magnification of Group 5 which highlights this surface roughness along the pore walls. That the material itself does not show submicron porous features within the pore walls indicates that this material was also well formed and that the surface roughness was a result of significant AGP/Col6 surface immobilization throughout the material.

3.4.3 Material Mechanical Analysis

As mechanical stiffness was a key test parameter in the following cell culture studies, 6mm diameter discs of Groups 1-5 were run through uniaxial mechanical compression tests to determine how the inclusion of a porous network impacted the compressive moduli of the respective groups and to confirm differences were observable between the groups.

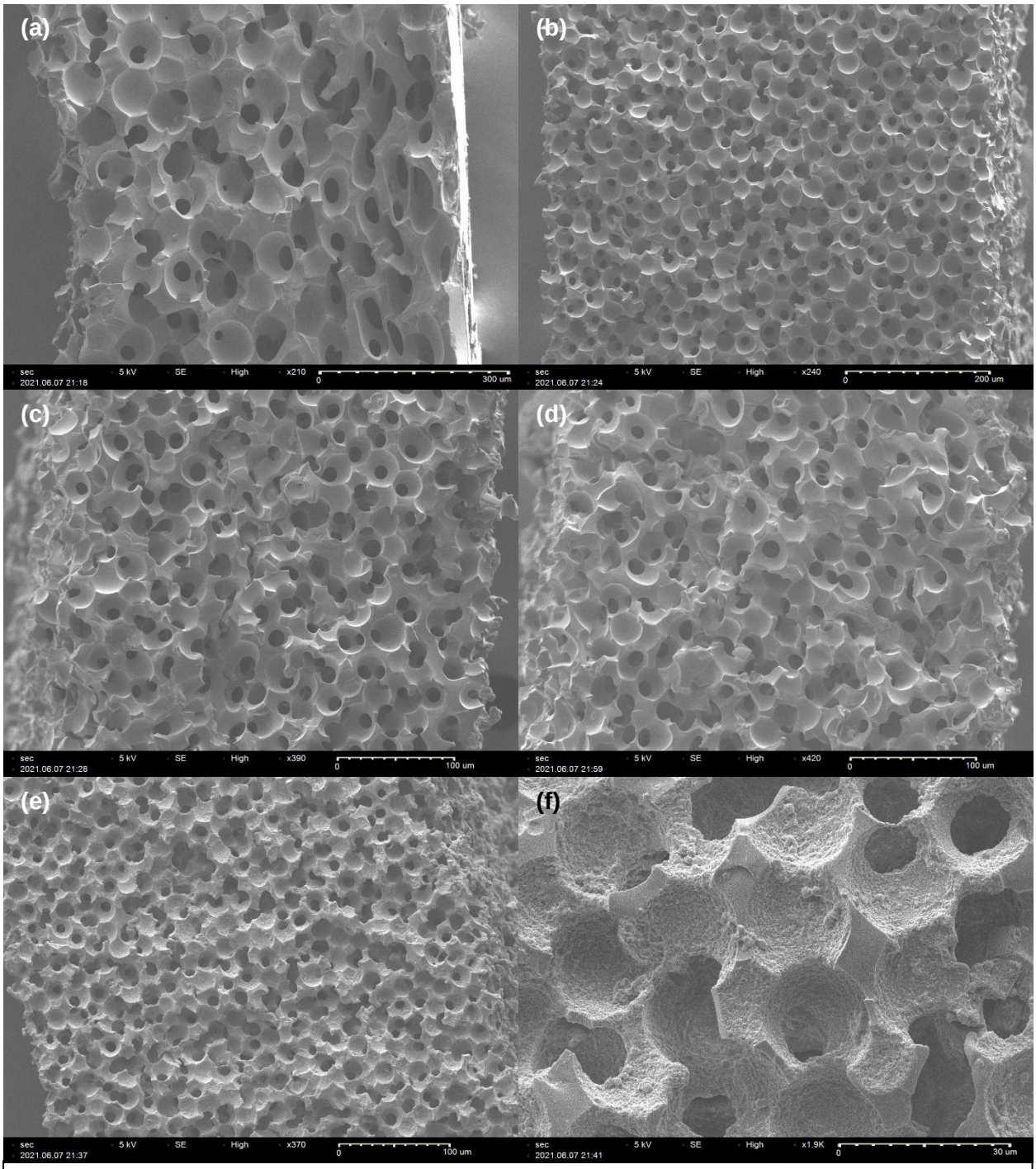

Figure 35: Scanning electron micrographs of the panel of porous materials seeded with BV2 and BMDM cells to investigate the immunomodulatory impact of various material properties on cell phenotype. (a) 100-HG50SC, (b) 40-HG50SC, (c) 40-HG25SC, (d) 40-HG25SC-5.0E, (e) & (f) 40-HG25SC-5.0E+P. Refer to Table 5 for material compositions.

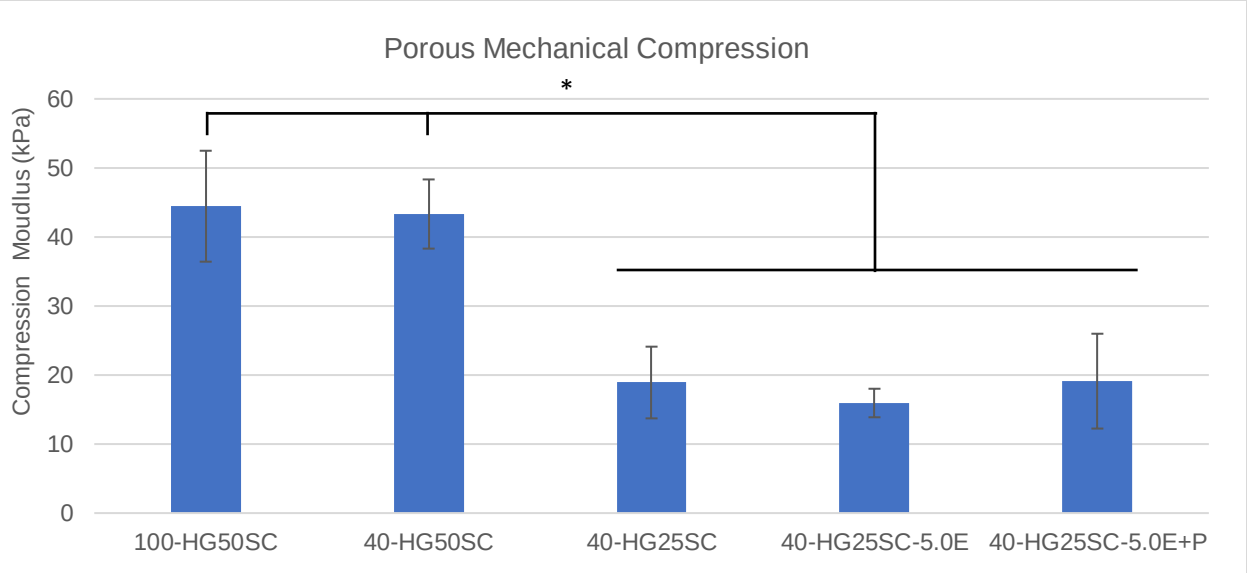

Figure 36: Mechanical compression of the panel of porous materials used in this study demonstrate that both imparting microporosity to these materials and a reduction in their pre-gel monomer concentration both result in a reduction in compression moduli.

Figure 36 shows the compression moduli of Groups 1-5 with compression moduli of 44 ± 8 kPa, 43 ± 5 kPa, 18 ± 5 kPa, 15 ± 2 kPa, 19 ± 6 kPa, respectively. The first notable result observed is that the moduli of these porous materials are all considerably low, even for Groups 1 and 2 with compositions involving 50% pre-gel monomer concentrations, though these values were still significantly larger than Groups 3-5. The incorporation of porosity clearly has an impact on the bulk mechanical properties of these materials in comparison to monolithic gels produced with an analogous material composition, i.e. 487 ± 16 kPa for HG50S (as shown in Figure 19).

No significant difference was observed in compression modulus between Groups 1 and 2, although this has been observed previously in our lab and is thought to be due to the fact that the void volume occupied by the porous network of tightly packed spheres is mathematically equivalent regardless of sphere/pore diameter. Bulk mechanical properties in these gels is therefore governed by the underlying material composition, as opposed to the pore size, which enabled the production of this panel of gels with independent control over gel mechanical properties. This is further confirmed by the observation that Groups 3-5, each of which was fabricated with 25% pre-gel monomer concentration all exhibited similar compression moduli.

That said, it is perhaps a bit striking that the moduli of Groups 3-5 are so similar considering the notable differences observed in the morphological properties between these groups as discussed above. However, the macroscopic measurement technique used to obtain these data may not have had high enough resolution to adequately detect the differences between these gels. Future studies which examine the micro- or nanoscale mechanical properties with an atomic force microscope in nanoindentation mode more provide more insight into subtler differences in the mechanical properties of these gels.

It is also interesting to note that the moduli of Groups 3-5 are similar to the modulus of the supposedly monolithic gel HG25SC-5.0E at 18 ± 1 kPa. However, this is likely due to the fact that HG25SC-5.0E gels were actually comprised of a porous network that simply lacked precise pore size or interconnect structure, which has been visualized previously via SEM (data not shown). Lastly, it is worth noting that Groups 4 and 5 did not show differences in compression moduli as an indication that the NHS/EDC process for protein immobilization in Group 5 did not significantly alter bulk mechanical properties.

3.4.4 Conductivity

As the composition of the materials tested here were analogous to those developed in Chapter 2, the conductivities of the materials used here were assumed to be the same. However, confirmation of the electrical properties of Group 5 was warranted to confirm that the additional chemical modification via NHS/EDC crosslinking of AGP/Col6 did not significantly affect the material's electrical properties as compared to Group 4. Figure 37 shows the conductivity of Groups 4 and 5 and confirms that the immobilization of AGP/Col6 did not significantly affect the materials conductivity.

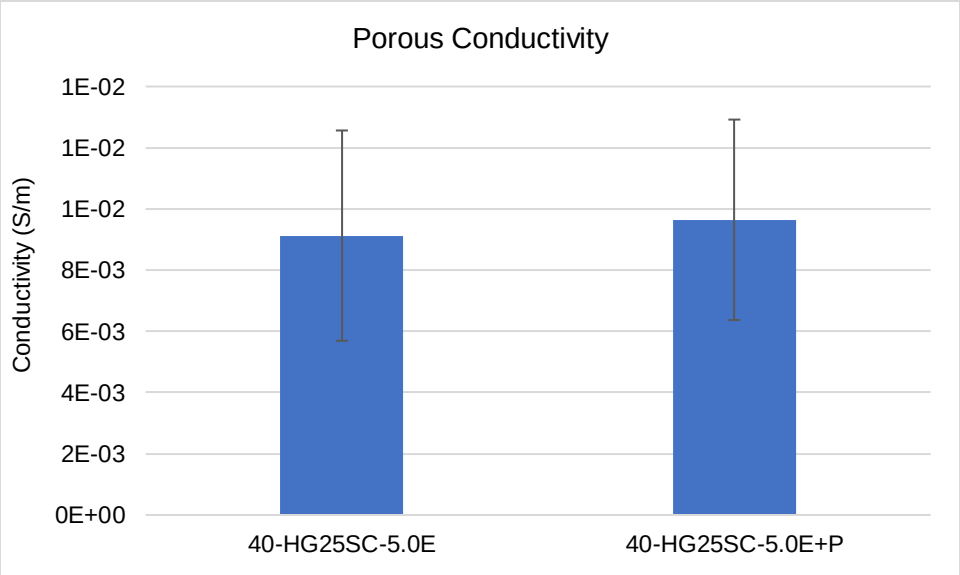

Figure 37: Immobilization of proteins via NHS/EDC chemistry does not significantly affect the electrical properties of the underlying material.

3.4.5 Protein Immobilization

The uniform and high-density co-immobilization of AGP and Col6 throughout the porous network turned out to be a non-trivial task. A great deal of experimentation was undertaken to maximize both the density and uniformity of both proteins throughout the gels. Figure X depicts the immunofluorescent staining of 10μm serial sections of Group 5 co-immobilized with AGP and Col6 via NHS/EDC crosslinking chemistry and the carboxylic acid moieties present on the AA subunits within the gels. Figure 38a was stained for AGP and Figure 38b was stained for Col6. These results were obtained by adapting the capillary seeding method used for cell seeding to this process improve the infiltration and immobilization of AGP/Col6 throughout the internal porous network.

The SEM figure depicted in Figure 35f suggests that the immobilization procedure was highly successful, but the immunofluorescent images shown in Figure 38a and 38b suggest that, while AGP/Col6 were immobilized successfully, the level of bioactivity of these molecules may not have been optimal. That said, no antigen retrieval techniques were used during the staining

procedure so what is visualized may not capture the full extent of surface bioactivity. Regardless, these images do indicate successful immobilization of some degree of bioactive AGP and Col6 which did result in effective modulation of cellular phenotype when seeded and cultured with microglia and macrophages, as discussed below. Future work will need to continue experimenting with parameters such as NHS/EDC concentration, MES buffer concentration and pH, incubation times, protein concentrations, and immunohistochemical analysis techniques to promote greater uniformity and density of bioactive protein immobilization throughout these STS materials.

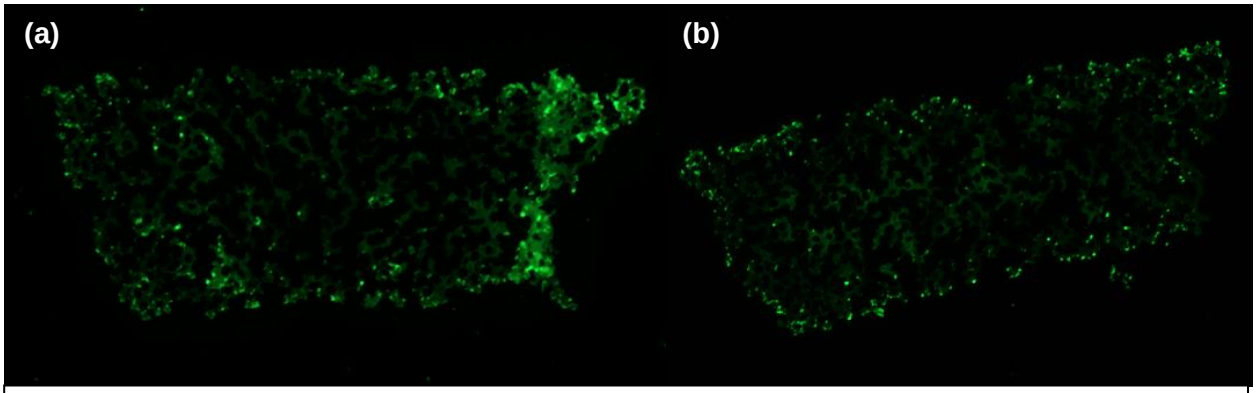

Figure 38: (a) Immunofluorescence of surface immobilized AGP and (b) Immunofluorescence of surface immobilized Col6 in serial slices of 40-HG25SC-5.0E+P

3.4.6 Protein Release

Microglia exhibit behavior analogous to peripheral macrophages with respect to polarization and function[12]. Broadly, M1-dominated microglia behave in a pro-inflammatory manner while M2-dominated microglia behave in a pro-healing manner[166,167]. Therefore, it was expected that microglia would demonstrate analogous responses to STS material properties *in vitro*, but the following results presented above suggest that these two cell populations may contribute heterogeneously to the neural tissue response to implanted STS.

Upon validation of the differences in the key material properties of interest, BV2 microglia and bone marrow derived macrophages (BMDM) were seeded into each of the 5 materials to

investigate the impact of these material properties on phenotypic polarization of the cells which are the primary drivers of gliosis in the context of neural electrode implantation. Figures 39 and 40 displays ELISA results quantifying the release of the pro-inflammatory cytokine tumor necrosis factor-α (TNFα), anti-inflammatory cytokine interleukin10 (IL10), and vascular endothelial growth factor (VEGF) from BV2 and BMDM cells, respectively, across the 5 material compositions after LPS stimulation as well as a set of and non-stimulated (C-) and LPS-stimulated (C+) controls cultured in 2D poly(styrene) wells. It is immediately apparent that the subpopulations of BV2 and BMDM cells cultured within each experimental test condition exhibited heterogenous phenotypic states as determined by their cytokine release profiles.

Compared to the heterogeneity among the BMDM subpopulations, the BV2 cells release profiles show a relatively more uniform set of phenotypic states, though with a few important differences. Firstly, Group 1 demonstrated a significantly higher release of TNFα as compared to Groups 2-5 which showed relatively uniform release of TNFα, as shown in Figure 39a. These observations corroborate results presented in Figure 27b which showed that BV2 cells cultured in STS with 100μm pores released a larger amount of the pro-inflammatory cytokine IL1β compared to those cultured in 40μm pores when challenged with LPS.

However, the previously conducted study did not incorporate a 2D control group, so the present comparison becomes increasingly noteworthy when considering Group 1 also exhibited a significant increase in TNFα release compared to the 2D control in this study. This suggests

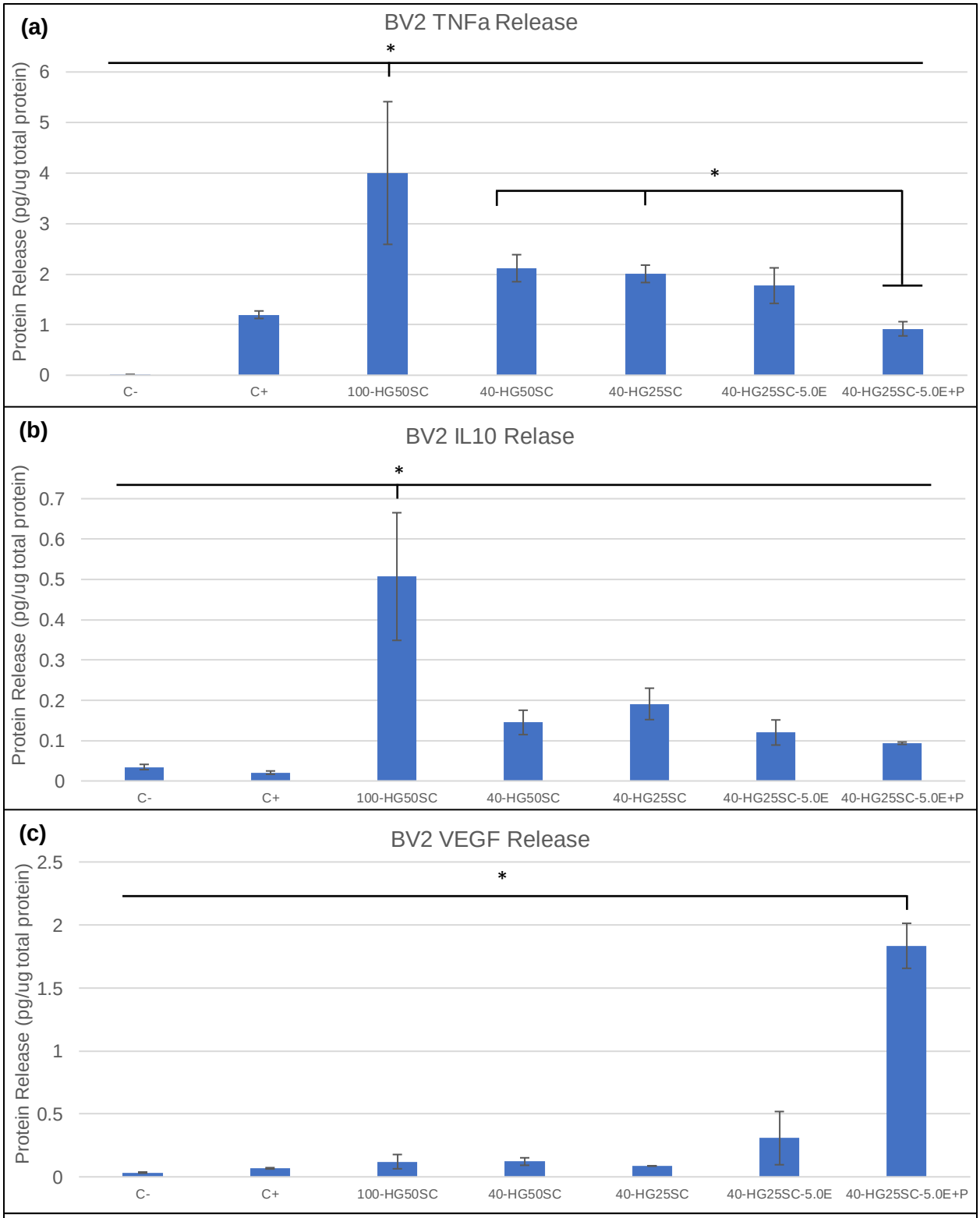

Figure 39: Normalized protein release from BV2 cells seeded in the panel of porous materials demonstrates a heterogenous population of cell phenotypes that is dependent on material properties. (a) TNFα release, (b) IL10 release, (c) VEGF release. All protein release values were normalized to total protein within each well, respectively, to improve accuracy of between-group comparisons. C- = non-stimulated 2D control; C+ = LPS-stimulated 2D control.

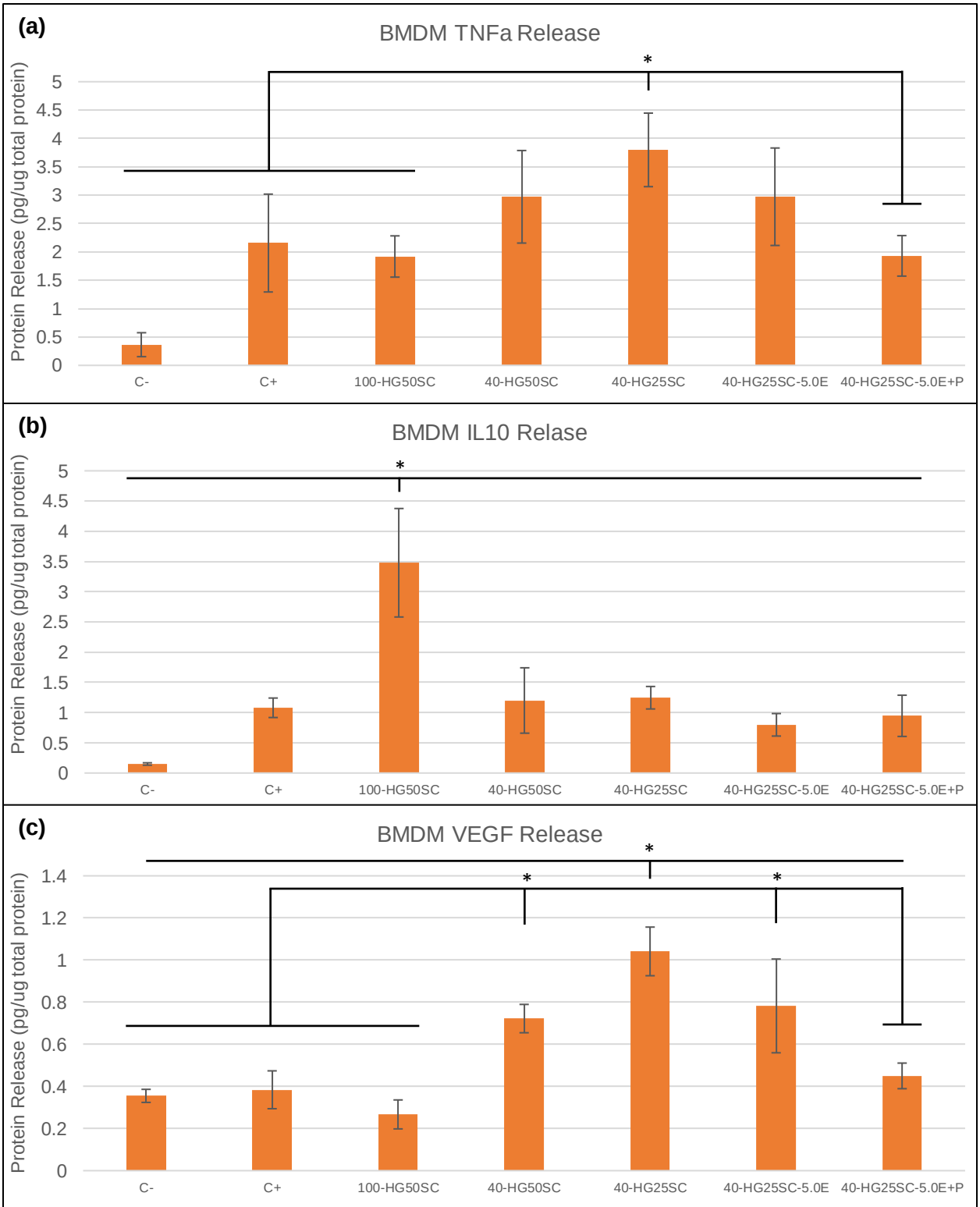

Figure 40: Normalized protein release from BMDM cells seeded in the panel of porous materials demonstrates a heterogenous population of cell phenotypes that is dependent on material properties. (a) TNFα release, (b) IL10 release, (c) VEGF release. All protein release values were normalized to total protein within each well, respectively, to improve accuracy of between-group comparisons. C- = non-stimulated 2D control; C+ = LPS-stimulated 2D control.

that the large, open, porous 3D culture environment had a significant impact on the reactivity of this cell population in response to LPS stimulation. The reason for this is difficult to discern but it may be a result of the different clustering enabled by the 3D culture environment and moderate curvature (compared to 40μm pores) which together had an impact on the intensity of intracellular signaling induced by LPS.

Compared to Group 1, Groups 2-5 showed significantly less TNFα release that was slightly higher than the 2D LPS control group, though these latter differences were not statistically significant. Interestingly, Group 5 showed the lowest TNFα release of all the groups stimulated with LPS though these differences were only statistically significant for comparisons between Group 1, 2, and 3. All groups released significantly more TNFα than the non-stimulated 2D control group, indicating they were responding as expected to the introduction of the inflammatory mediator LPS. Taken together, these data suggest that pore size played the largest role in modulating the phenotype and release of TNFα from the BV2 cells in this study, although immobilized AGP/Col6 also did demonstrate a modest impact on TNFα release.

BV2 release of IL10 showed a similar trend to TNFα release with Group 1 releasing a significantly larger amount of IL10 compared to all groups tested, as shown in Figure 39b. Groups 2-5 released a lower, and again relatively uniform, amount of IL10. In this case, all test groups released more IL10 than the 2D LPS-stimulated control group, though most of these differences were not statistically significant. Additionally, IL10 release by the LPS-stimulated 2D control was not significantly different from the non-stimulated 2D control group. Taken together, these data provide additional evidence that the 3D culture environment had a direct, though in most cases modest, impact on the phenotypic polarization of the BV2 cells tested here. The only other statistically significant differences in IL10 release for all other comparisons were between Group 3 and both the non-stimulated and LPS-stimulated 2D control groups. Lastly, it is worth noting that although Group 1 did demonstrate statistically significant increase in IL10 release compared

to all groups tested, the scale of the y-axis is relatively low in comparison to all others in Figure 39, indicating that absolute IL10 release was relatively low in the BV2 cells tested here.

BV2 release of VEGF showed highly divergent results compared to trends observed in TNFα and IL10 release with Group 5 exhibiting an order of magnitude increase in VEGF release compared to all other groups tested, as shown in Figure 39c. These data indicate that the co-immobilization of AGP/Col6, the key material property difference of Group 5 compared to all other groups, stimulated this significant release of VEGF from the BV2 cells. These results also suggest that the degree of AGP/Col6 bioactivity may not have been fully captured by the immunofluorescence images in shown in Figure 38. The active probing of the pore surfaces by BV2 cells may still have served as a sufficient stimulatory signal for the cells that was not captured by the immunofluorescent staining procedure.

In any case, these VEGF ELISA data demonstrate that even the modest bioactivity of this protein pair suggested by the immunofluorescent images could have a significant impact on BV2 phenotype. In light of this observation, it is likely that the AGP/Col6 immobilization also contributed a modest effect on the reduction of TNFα release from these BV2 cells. As discussed previously, AGP is a key anti-inflammatory mediator released by astrocytes in response to local trauma to brain tissue and has been shown to reduce TNFα and other inflammatory cytokine release from microglia[116]. However, to the best of my knowledge, no reports have demonstrated a connection between AGP stimulation and release of VEGF from microglia, so this may be a novel finding. As Col6 is a key ECM component of the basal lamina of brain vasculature, the immobilization of this molecule may also have served a stimulatory effect on VEGF release independently, or in combination with AGP stimulation.

Lastly it is interesting to note that Group 4 also demonstrated a modest, yet statistically significant, release of VEGF compared to both the non-stimulated and LPS-stimulated 2D controls which suggests that the presence of PEDOT in the gel also may have had a modest impact on

VEGF release. Microglia an astrocyte cells are known to be moderately electrically active via ion channels on their membranes, and so the electrical activity in the Group 4 materials may have contributed to the modulation of their phenotype. However, whether this observation was due to specifically to the passive electrical activity of the material or some other interaction is difficult to discern. These results will be discussed in greater detail together with BMDM results below.

The subpopulations of BMDM cultured in these experiments demonstrated a much greater degree of heterogeneity, although some trends were observed across the three cytokines tested here as shown in Figure 40. Firstly, like the BV2 cells, BMDM cells in all groups released significantly more TNFα than the non-stimulated 2D control, indicating a robust response to LPS challenge, as shown in Figure 40a. However, in this case, BMDM in Group 3 exhibited the highest TNFα release of all groups stimulated with LPS, though only comparisons between 1, 3, and the 2D control were statistically significant. Groups 2 and 4 exhibited an increase in TNFα released compared to all groups except Group 3, though none of these comparisons were statistically significant. Groups 1 and 5 exhibited TNFα release profiles that were essentially identical to the 2D LPS-stimulated control.

These results are counterintuitive as they present potentially conflicting information regarding the modulatory capability of the materials tested. That is, comparisons between Groups 1-3 suggest that smaller pores and softer material exacerbates the M1 response to LPS exposure in BMDM, which is counter to the proposed hypotheses and stands in contradiction to preliminary results presented in Figure 34a regarding pore size and previous results discussed in the literature regarding substrate stiffness. However, the composition of these gels was quite different than the pure HEMA gels in the studies associated with Figure 34a, as the gels tested here contained additional hydrophilic monomers in the form of GMA and strongly anionic AA ($-COO^-$) and AMPS ($-SO_3^-$). The incorporation of these additional chemical features may have served as another feature impacting cell-materials interactions and thereby contributed to the differences observed

between these results and those in Figure 34a, although additional studies explicitly investigating these differences are needed to form stronger conclusions in this regard.

However, consideration of Groups 4 and 5 in this light provide evidence that even slight chemical/molecular changes to the composition of the gels, i.e. the presence of PEDOT and immobilized AGP/Col6 in this case, may induce significant changes to the phenotypic expression of these cells. Furthermore, these data suggest that PEDOT and AGP/Col6 work together synergistically to limit the severity of the M1 response, observations which themselves are in agreement with the proposed hypotheses. Clearly, the various material properties are contributing to the phenotypic polarization of the BMDM cells cultured within them. These results will be discussed in greater detail below after presentation of BMDM IL10 and VEGF release data.

In contrast to the TNFα release profiles exhibited by BMDM cells in this study, IL10 release profiles were far more uniform and in good agreement with trends observed in BV2 IL10 release profiles, as shown in figure 40b. That is, Group 1 demonstrated a significant increase in IL10 release compared to all other groups, with Groups 2-5 demonstrating no differences compared to one another or the 2D LPS-stimulated control. All groups did release more IL10 than the non-stimulated 2D control, though only comparisons between Groups 2 and 3 were statistically significant. Taken together, these data indicate that LPS challenge induces an increase in IL10 release from BMDM regardless of the culture conditions tested, and that the relatively stiff, 100μm porous material in Group 1 modulated the BMDM cells towards an M2 phenotype, as determined solely by IL10 release, to the greatest degree.

Interestingly, the trends observed in VEGF released from BMDM cultured in this study follow those observed in BMDM release of TNFα, as shown in Figure 40c, though with a few key differences. Firstly, the VEGF release profile from the 2D non-stimulated control is elevated relative to the release profiles from the other culture conditions, indicating the degree of change from the background, non-LPS challenged state of these cells is different within the test

conditions. In light of this observation, Group 1 demonstrated an observable reduction in VEGF release compared to all other groups, including the control groups, though this effect was only statistically significant for comparisons between Group 2-4. Analogous to TNFα release profiles, Group 2 and 3 demonstrated sequentially elevated VEGF release profiles compared to Group 1, with subsequent reductions in VEGF release for Groups 4 and 5 back down to baseline levels, and only Groups 2-4 exhibited a significant increase in VEGF release compared to the control wells. That the non-stimulated and LPS-stimulated 2D controls showed no difference in VEGF release and that the material test conditions showed such dynamic responses provides another clear signal that the various material properties acted to differentially modulate BMDM phenotype in the context of LPS challenge.

Based on the results of BV2 cytokine release observed in this study, it is tempting to conclude that Group 5 outperformed all other groups in its ability to modulate or switch BV2 phenotype away from the classical M1 extreme induced by LPS toward a more M2-like, pro-regenerative phenotype considering it demonstrated the lowest TNFα release, highest VEGF release, and a modest increase in IL10 release compared to other the groups and the 2D controls examined in this study. The large increase in TNFα and IL10 release from BV2 in Group 1 is interesting but considering the relatively low absolute IL10 values suggests that these cells were exhibiting a more M1-like phenotype. However, conclusions regarding which of the groups seeded with BMDM performed the best from a M1 to M2 switching or polarization perspective are more difficult to make given the considerable heterogeneity of the responses. Furthermore, the degree of pleiotropy exhibited by these three important cytokines makes it difficult to resolutely extrapolate which of these materials might perform the best in the context of *in vivo* implantation as the different phenotypic states exhibited by these cells may have differential benefits on the tissue response depending on the tissue type and disease or injury model.

Reports on the classical and alternative activation of macrophages and microglia indicate that the M1 extreme, stimulated by inflammatory mediators like LPS, produce cellular phenotype with high TNFα release and low IL10 release[127]. Conversely, macrophages polarized to the M2 extreme, stimulated by anti-inflammatory cytokines like IL4, IL13, or prostaglandin E2 (PGE2), show a reversal in protein release with low TNFα and high IL10. From this perspective, Group 1, which exhibited moderate to low TNFα and high IL10 might be considered in an M2 state, while Groups 2-4 might be considered in an M1 state with high TNFα and low IL10. In this context, Group 5 would stand out for having only moderate TNFα and IL10.

However, upon taking the VEGF release profiles for these groups into consideration, the phenotypic state of these cells more nuanced. Wu et al. (2010)[168] have shown that the presence of IL10 in culture can have a significant effect on BMDM VEGF production that is dependent on the activation pathway. That is, high levels of IL10 were shown to repress the M1 polarization of BMDM as measured by pro-inflammatory IL6 and nitrite production, as expected, but that it also significantly suppressed the release of VEGF from these cells, but IL10 did not have the same effect on PGE2 stimulated cells. Interestingly, concomitant delivery of PGE2 and LPS also did not suppress VEGF release from BMDM, indicating myriad of phenotypes were induced by the combination of stimulatory molecules that exhibited differential impact on the cytokine release profiles. As a result, the authors even suggest the use of IL10 as a possible anti-angiogenic therapy for pathological angiogenesis.

In the context of these results, it is interesting to note the significant reduction in VEGF release from Group 1 considering this group demonstrated the highest IL10 response and a reduction in TNFα release. While at first glance this may seem like an optimal result, the suppression of VEGF would likely have serious consequences in the on the development of new blood vessels to support tissue regeneration. Furthermore, it is interesting to note these results in the context of *in vivo* data from STS implantation studies which report poorer tissue integration

as measured by fibrotic scar formation and neovascularization in and around STS implants with 160μm pores as compared to STS with 40μm pores[52]. These studies also observed a greater number of cells staining for M1 markers (or co-staining for M1 and M2 markers) within the pores of 40μm porous STS as compared to 160μm porous STS.

The release profiles from BMDMS cultured in Groups 2-4 are also interesting in this context as they had all had 40um pores and demonstrated relatively high TNFα, low IL10, and high VEGF, the combination of which may result in improved tissue regeneration outcomes *in vivo*. BMDM cultured in Group 5 exhibited perhaps the most interesting response in the lack of any observable difference from the LPS-stimulated 2D control might suggest that the material is not modulating the phenotype of these cells. However, in the context of the release profile of BV2 cells cultured in Group 5, the BMDM release profile may also suggest that significant changes may be occurring in the release of cytokines not measured in this study.

It should also be noted that that these observations were taken as a single time-point 24 hours after stimulation with an unresolving, highly inflammatory stimulus, so these studies were incapable of observing the dynamics of the release profiles exhibited by these cells. Future *in vitro* studies which examine the protein release profiles at a range of time points from a few hours to days after stimulation would provide greater insight into dynamical immunomodulatory capability of these STS materials. Additionally, conducting a multiplex analysis of a large number of cytokines would provide a greater breadth of information into the disparate phenotypes exhibited by these cells.

Lastly, the ultimate test of these materials is in their ability to modulate the neural tissue response upon implantation toward outcomes that would be beneficial for long-term recording applications in the context of a neural microelectrode composed of one or more of these materials. The next chapter will discuss these ideal outcomes and present results from a pilot implantation study of this nature.

3.4.7 Conclusion

The experiments presented above were designed to systematically explore the immunomodulatory capability of STS material properties on primary peripheral immune effector cells, macrophages, and the translation of these results into a model of CNS immune effector cells, BV2 microglia. The results presented indicate that STS of varying material properties have a direct impact on the phenotypic polarization of these cells in response to the inflammatory stimulator LPS. However, given the significant complexity of the signaling processes of the cytokines assessed here, it is difficult to concretely determine which of the materials preformed 'best' in terms of which will ultimately produce a better tissue response *in vivo* and what aspects of the cellular response might be governing the tissue response. However, that material-dependent phenotypic differences are observable indicate that a series of *in vitro* and *in vivo* experiments might be conducted in a feedback-feedforward manner to continue optimizing these materials to mitigate gliosis.

Future experiments might also dive deeper into this investigation by utilizing inhibitory molecules for the various cytokines tested here. These inhibitory molecules have been applied successfully in the literature to probe the impact of various treatment conditions on inflammatory signaling in response to mechanical and structural cues in the cellular microenvironment, but not to this particular array of materials. While there is still much work to be done to uncover the diverse phenotypic states of these cells of myeloid origin and the mechanisms by which various material properties impact their exact polarization state, the results presented here demonstrate that STS materials provide an excellent *in vitro* culture model for future studies to investigate these phenomena.

CHAPTER 4 – Application of Optimized Porous Scaffold to Neural Regeneration In Vivo

4.1 Background

While *in vitro* experiments serve as a meaningful supplement to biomaterial development and investigation, the final test for these materials is to determine how they interact with the tissue environment. As discussed above, a pro-regenerative response of CNS tissue to STS depends on both macrophage and microglial activation patterns as these are the primary immune cells driving gliosis[169]. Astrocytes are also known to play a major role in gliosis and the formation of glial scar tissue[18,170] and their phenotypic activation is closely linked to that of microglia[54,171]. Therefore, it was hypothesized that modulating microglial/macrophage activation in a material property-dependent manner would also have a direct impact astrocytic activation and distribution to reduce glial scaring and improve neuronal proximity to the implant surface. Together, these features are important not only for healthy regeneration of neural tissue but also in the context of a neural recording electrode which requires an intimate electrical connection with nearby, healthy neurons for appropriate function.

The neural tissue response to implanted microelectrodes has been studied in great deal as a means to understand the dynamics of gliosis, the properties of the electrodes or implant procedure that impact gliosis, and the deleterious effects of glial scar formation on neural recording and BCI outcomes[172]. Implantation of an electrode array first requires removal or penetration of the meninges (dura mater, arachnoid, pia mater), and penetration of the brain surface and parenchyma which damages extracellular matrix structure and neuron and glial cell bodies. Avoidance of large vasculature during this implantation procedure is critical to limiting the severity of tissue damage, however the neocortex has the greatest density of microvasculature within the brain, so some degree of rupture and mechanical deformation of vessels is unavoidable[173]. Rupture and deformation of blood vessels leads to infiltration of blood immune cells including macrophages, among others [10]. The presence of the device displaces tissue which

causes additional mechanical deformation and an increase in local pressure. The presence of blood-derived products (e.g. albumin), cellular debris, and other damage associated molecular patterns (DAMPS) cause an immediate activation of microglia and macrophages within the vicinity of the device which migrate to the device within 12-24 hours[174]. These cells release a host of inflammatory cytokines including TNFα, IL1, IL6 which induces astrocyte activation and induce release of reactive oxygen species and other deleterious species that create a neurotoxic environment that significantly reduces the neuronal density within ~50μm of the device interface[15,174,175].

The astrocyte response dynamics, including initiation of recruitment, upregulation of GFAP, and proliferation, are delayed in comparison to the macrophage and microglial response. However, the astrocyte population has been shown to be heterogenous in the vicinity around the implant, with at least three observable phenotypes, a subset of which extend processes toward and around the implant[176]. After about four weeks, a significant increase in astrocyte density is observed within ~100μm of the implant as they form a glial sheath around a core of microglial cells directly in contact with the device[175]. This microglial core/astrocyte sheath structure continues to develop and contract over the course of 12 weeks in the formation of a dense glial scar. While the above description is typical for the average response, significant variability has been observed in terms of the density of the scar formation which has been correlated with changes to electrode recording outcomes[175]. This is thought to be due to the degree of initial implant-induced vascular damage[177] and degree of mechanical mismatch between the device and tissue[178].

Quantification of changes to electrode impedance and signal quality provide information regarding the extent to which variability of glial scar severity affects neural recording outcomes[172]. Both the density of the glial scar and the proximity of neuronal cell bodies around the implanted electrode are thought to impact the degree to which charge can effectively flow from the neurons to the electrode during an action potential. However, there are conflicting reports on this matter.

For example, Cody et al. (2018)[179] report that a thicker and/or denser scar and a greater distance between neurons and electrode recording sites both contribute to an increase in electrical impedance and a reduction in signal quality. However, Malaga et al (2015)[180] report that scar formation itself does not have a significant impact on recording quality, rather that the displacement of neurons from the electrode recording sites plays a more significant role in increasing impedance and reducing recorded action potential amplitude. In any case, a gliosis-induced reduction in recording capability is certainly observed for implanted microelectrodes which can significantly affect the degree to which neural signals can be translated into output commands via a BCI. In this way, gliosis has a direct impact on the therapeutic potential of the entire BCI system and has been shown to account for roughly a quarter of BCI failures for silicon-based microelectrode arrays[11].

In light of these observations, various modifications have been made to the electrode properties to try to improve long-term recording outcomes. These include coating the electrode array with bioactive molecules, like the neural cell adhesion molecule L1[181], which have demonstrated improvements in neuronal proximity to recording sites and which correlated with reductions in electrical impedance magnitude and increased signal-to-noise ratio compared to non-coated controls. Inclusion of “smart” materials which have dynamic mechanical properties which are first rigid to enable penetration of the brain surface that then rapidly soften when hydrated have also demonstrated improvements to neural density around the device[178]. Alternatively, the recent development of a neurosurgery robot has allowed for the precision implantation of microelectrodes to avoid major blood vessels and limit interoperator error that occurs during manual implantation[34].

Coupling this automated implantation process with newer nanofabrication techniques that produce high channel count electrode arrays have shown limited glial scar formation and good recording outcomes out to 8 weeks post-implant. However, microelectrodes fabricated via these methods still use materials which are considerably stiffer than the brain and it is unknown how

this will impact tissue integration over the long term given the ability for macrophages and microglia to sense and react to the stiffness of the substrate. Therefore, there is still a need for new materials which aim to address each of these issues when applied to the fabrication of a high channel count microelectrode array to improve BCI performance for clinically relevant time scales.

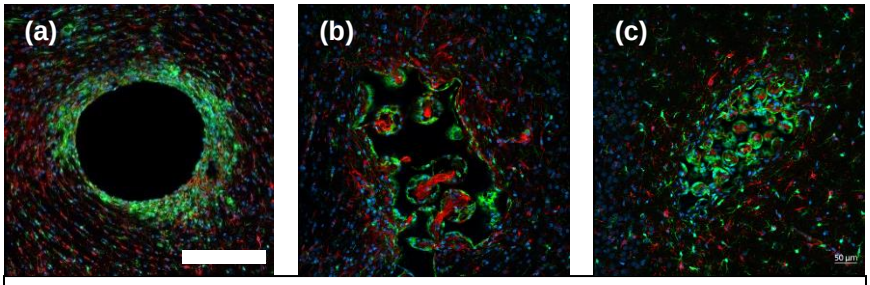

Figure 41: Immunohistochemistry of STS implanted into rat cerebral cortex; (a) non-porous; (b) 100µm STS; (c) 40µm STS. Hoechst (blue, nuclei), Iba-1 (green, mglia/mphage), GFAP (red, astrocytes). Bar = 200µm.

Previous work conducted in the Ratner lab by Dr. Ian Dryg[53] investigated the impact of STS on gliosis and neural tissue regeneration with rats implanted in cortex with 40µm and 100µm STS rods and a nonporous control rod[53]. The rods were punched out of larger STS sheets using a needle for a final diameter of ~300µm and ~3mm length. After 1 week, rats were sacrificed and prepared for immunohistochemical analysis. Figure 41 depicts a selection of cross-sectional immunofluorescent images of the nonporous H50 (Figure 41a), 100-H50 (Figure 41b), and 40-H50 (Figure 41c) materials produced from these studies. A significant reduction in astrocytic glial fibrillary acidic protein (GFAP, a glial scar marker) was observed around 40-H50 compared to the 100-H50 and H50 which is visualized by the degree of red fluorescent staining in Figure 41. The average GFAP signal across all samples was plotted as a function of distance from the center of the implant using the Radial Profile Angle plugin in FIJI (ImageJ, NIH), as shown in Figure 42. Both 40µm and 100µm STS enabled ingrowth of astrocytes (GFAP, red) and microglia (Iba-1, green). Nonporous rods stimulated the formation of a pronounced glial scar. The 40µm STS consistently showed the lowest GFAP signal in and around the porous structure. These results provide evidence suggesting that STS pore size has a significant impact on modulating gliosis and inducing neural tissue integration.

A follow up study conducted by Dr. Dryg investigated the impact of STS mechanical properties on the neural tissue response[53]. The results from this study confirmed that 40µm STS produce the lowest GFAP signal across all material stiffnesses tested, but that the softest material composed of poly(HEMA-co-GMA) with 85% water content produced the lowest GFAP signal out of all materials tested. However, glial scar formation around these samples was not completely abolished.

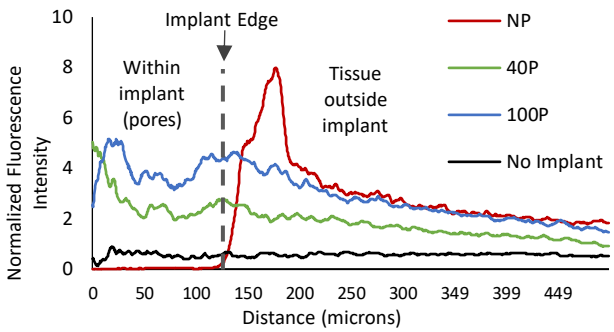

Figure 42: GFAP (astrocytes) signal vs. distance from implant center, 7 days post STS implant. 40P = 40µm; 100P = 100µm; NP = nonporous. STS with 40µm induce the lowest scarring response.

The following results were obtained from follow on *in vivo* studies which aimed to expand on the investigation into the neural tissue response to STS materials initiated by Dr. Dryg. The present studies sought to investigate the impact of PEDOT inclusion and a surface coating of AGP/Col6 in soft STS materials on the neural tissue response and to serve as a pilot study for the potential application of this material to the development of a wholly organic, immunomodulatory neuroelectronic interface. The main hypothesis tested here was:

Hypothesis: Soft, electrically active, 40µm porous STS co-immobilized with AGP+Col6 implanted into rat motor cortex will limit glial scar formation, as measured by astrocytic GFAP, and improve neuronal density in proximity to the implant compared to a stiff, monolithic control material.

4.2 Materials and Methods

4.2.1 Material Synthesis

The porous test material was fabricated via the STS fabrication process with 40um pore diameter and a pre-gel composition including 25% (v/v) of a 4:1 mixture of HEMA:GMA, 3.5% (v/v) EDOT, 0.25wt% Irgacure 651, 5wt% APS, and a 1:1 mixture of PBS:IPA as solvent. The

control material was composted of an identical pre-gel composition excluding EDOT. The materials were polymerized under a broad spectrum UV light for 24 minutes and then incubated for 1 week at 4C followed by significant serial washing in acetone, ethanol, and sterile PBS. Once completely washed, the porous test material was run through the protein immobilization protocol described in Chapter 3 to co-immobilize AGP and Col6 throughout the porous network and then incubated in sterile 15% gelatin for 24 hours at 37C. The infiltrated gelatin was incorporated to increase the mechanical stiffness of the soft porous test material upon dehydration to enable penetration of the brain surface during implantation. Hydrated sheets of the control material and protein immobilized, gelatin infiltrated porous test material were then cut into small pieces, approximately 200-300um in diameter and 2-3mm in length, with a sterile razor blade and left to dry in sterile tubes in preparation for implantation.

4.2.2 Surgical Implantation

All surgical intervention was carried out under approved IACUC protocols. Prior to material implantation, each animal received general anesthesia (isoflurane 2.5%). Once induced to a surgical plane, each animal received subcutaneous injections of antibiotics (Baytril, 10mg/kg), anti-inflammatories (meloxicam, 1mg/kg; dexamethasone, 0.5mg/kg) and fluids (Lactate Ringer's solution). A local anesthetic was injected intradermally at the incision site (lidocaine, 1%; bupivocaine, 0.25%). Each animal's temperature, heart rate, and breathing were continuously monitored during surgery using the SomnoSuite anesthesia monitoring system (Kent Scientific). Fluids were given as needed throughout the surgery.

Small craniotomies were opened in the skull of the animals bilaterally followed by removal of the dura and manual implantation of test and control materials into the motor cortex region of each rat, one implant per hemisphere, at 1.5mm anterior and 3mm lateral to bregma. Craniotomies were covered with gelfoam and exposed skull covered with a PMMA headcap

stabilized by bone screws. Immediately post-surgery, each animal received medicated water (Baytril, 0.2mg/mL) for up to 2 weeks and weighed periodically to ensure healthy weight gain. Otherwise, the rats received no other intervention prior to euthanization.

4.2.3 Brain Tissue Preparation for Immunohistochemistry

After 4 weeks of implantation, the animals were euthanized with a lethal dose of Beuthanasia-D and cardiac perfused with PBS (pH 7.4) followed by 4% PFA as fixative. Brains were gently removed from rat skulls, allowing implants to remain *in situ*, and post-fixed in 4% PFA overnight and then incubated serially in 15% and 30% sucrose solutions in Hank's Buffered HEPES Saline (HBHS). Brains were sectioned into 50µm thick slices with a vibratome and stored in 48-well plates with HBHS at 4C until staining.

4.2.4 Immunohistochemical Analysis

Table 10 provides information regarding the antibody stains used in this study. Protocol X in the Appendix was followed to stain and prepare the samples for imaging with a Nikon A1R HD25 confocal microscope using a Plan Apo 20x DIC M N2 objective with a 0.75 objective numerical aperture and pinhole size of 136.65µm. The emission and excitation wavelengths for the blue, green, and red channels were 450/405, 525/485.6, and 595/561.1, respectively. Each implant was imaged in a 3x3 array and then automatically stitched together with the Nikon NIS-Elements confocal software. All slices containing the same marker were imaged with the same settings and exported as .tiff files for processing and quantification with FIJI (ImageJ, NIH).

For astrocyte, neuron, and microglia quantification, each image was initially processed manually by drawing a region of interest around the edge of the material boundary and then a

custom python script was run to draw 10 sets of 25μm bands radiating outward from the implant edge (250 μm total breadth from implant edge) for band-wise quantification of immunofluorescence or cell counts. Astrocyte GFAP and microglial Iba-1 fluorescence intensity were averaged over the pixels within the material (0^{th} band) and over each band, averaged across slices from each animal, and then plotted for comparisons. Neuronal density was determined by manual counting of the cell bodies within each band, divided by band area (μm^2), and then normalized to neuronal density in healthy tissue at least 1mm away from implant location and plotted bin-wise for comparisons. Neurons that were observed within the outer pores of the porous test material were included as counts in the 1^{st} band (no 0^{th} band). At least 2 slices from each animal were quantified in this way for astrocyte intensity, microglia intensity, and neuron counts. For quantification of CD68, the number of CD68+ cells were counted in the interior and exterior of the test and control conditions for at least 1 slice per animal.

Table 10 Immunohistochemical Antibodies

Target	**Function**
Glial fibrillary acidic protein (GFAP)	Glial scar marker
Iba-1	Pan microglial marker
Neuronal Nuclei (NeuN)	Adult neuron marker
Hoechst	Nucleus marker
CD68	Macrophage/microglia M1 marker

4.3 Results and Discussion

The ultimate goal of the collection of studies presented throughout this dissertation was to develop and test a new conductive hydrogel-based biomaterial intended for application the design of a robust neuroelectronic interface. The previous chapters detailed the design and characterization of this novel material and an initial mechanistic investigation into its ability to

modulate the phenotype of the key cells which drive the neuroimmune response to implanted materials. The studies presented here represent the translation of this material into an *in vivo* context as an early pilot study to investigate the ability of the material to modulate the tissue response in ways that would be ideal for recording outcomes for future application of the material to a neural microelectrode device. In relation to the previous discussion, the main hypotheses that were tested with these *in vivo* experiments were that the combination of material properties including precise, 40μm pore diameter, soft mechanical properties, passive electroactivity via PEDOT, and presence of surface-immobilized AGP/Col6 would 1) reduce astrocytic scar formation and 2) improve neural density around the device compared to a stiff, monolithic control material. We sought to demonstrate that the combination of these features of the material, particularly the presence of PEDOT, composed into a form factor that emulated a penetrating microelectrode device would be capable of producing a tissue response that would be amenable to a neural microelectrode intended for long-term use in humans.

Compressive moduli, electrical activity, and protein immobilization for the test and control materials were quantified prior to implantation to confirm that significant differences were observable in each of the material properties tested and were in agreement with findings presented in Chapter 3. Figure 43a and 43c depict low magnification SEM images of the dehydrated control and test implants in their final form factor prior to implantation, both of which were gently cut from larger sheets of the underlying material with a razor. Figure 43b and 43d show higher magnification images of the monolithic control material and porous test material, respectively. The test material was infiltrated with a 15% gelatin prior to dehydration and implantation to temporarily increase the axial stiffness of the material to aid in the manual implantation process as the low modulus of the test material alone would not have enabled penetration of the brain surface. Figure 43d demonstrates that the gelatin was successfully infiltrated throughout the porous network, which can still be observed across the surface of the

material. The reader is referred to Figures 35e and 35f for a more detailed depiction of the porous network structure of the test material used in this study.

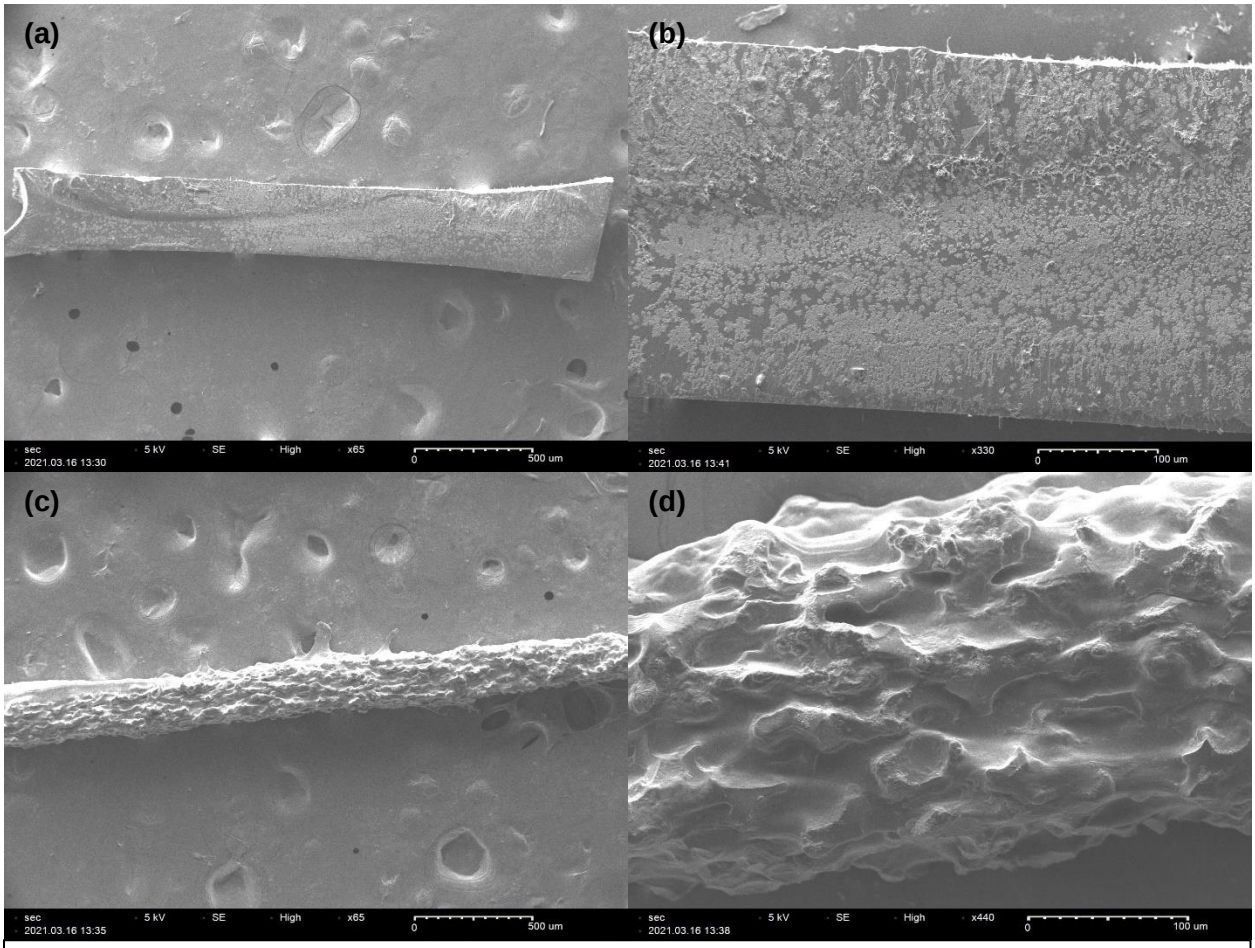

Figure 43: Scanning electron micrographs control and test materials prior to brain implantation. (a) and (b) depict the monolithic HG50SC control material. (c) and (d) depict the 40-HG25SC-5.0E+P test material infiltrated with 15% gelatin. Refer to Table 5 for material compositions.

The test and control materials in the form factors depicted in the SEM Figure 43 were then implanted bilaterally into the motor cortex (1.5mm anterior, 3.0mm lateral from bregma) of 6 adult Long-Evans rats, one implant per hemisphere. The location of test or control materials (i.e. left or right hemisphere) was randomized across the 6 rats. Only a single test and control material were implanted in each hemisphere as a means to limit the potential cross-talk between adjacent implants and also due to limited time and resources associated with this study. As discussed below in greater detail, future studies would benefit from increasing the number of animals tested and the number of test and control groups to better tease apart the independent impact of various

material properties on the tissue response. However, as indicated above, this pilot study was specifically designed as an initial test of the particular combination of material properties impact on the tissue response as an indication of their applicability to the design of a wholly organic, immunomodulatory neuroelectronic interface. Furthermore, the materials tested here were not connected to recording equipment of any kind, so future studies would also need to develop robust methods for connection to downstream hardware and examine the relationship between the tissue response and neural recording outcomes.

After 4 weeks of implantation, the rats were sacrificed and perfused with 4% paraformaldehyde (in PBS, pH 7.4) as fixative in preparation for immunohistochemical staining analysis of the tissue response. After fixation, the brains were sliced into 50μm slices with a vibratome with the implants remaining *in situ*, stained with a selection of antibodies listed in Table 7, and visualized with a Nikon A1R HD25 confocal microscope. Quantification of the resulting images was carried out with FIJI (ImageJ, NIH) to determine the extent of glial scarring and proximity of neural cell bodies to the implant surface as these values are known to correlate with recording outcomes, as discussed above. The response of microglia and macrophages was also examined as an indication of the response of the drivers of neuroinflammation.

Figure 44 depicts brightfield images of the test and control materials within the tissue environment. Figure 44a shows the monolithic test material within the tissue, the horizontal lines across the material were simply an artifact of the vibratome slicing action and not indicative of the material structure. Figure 44b shows the porous conductive hydrogel test material in the tissue environment which appears blue as a result of the presence of PEDOT throughout the material. The ingrowth of tissue into the porous network of the material is apparent in this brightfield image, demonstrating integration with the tissue environment.

Figure 45a and 45b depict representative fluorescent images of control and test materials, respectively, within the tissue environment stained for astrocytic glial fibrillary acidic protein (GFAP, red), neuronal cell bodies (NeuN, green), and cell nuclei (Hoechst, blue). A few noticeable differences are observable between the tissue response of the test and control images. Firstly, no staining was observed within the inner area of the control materials, which was expected given their monolithic structure, while a significant amount of staining is observable within the pores of the test material. Secondly, the pattern of GFAP staining indicates that a relatively large and

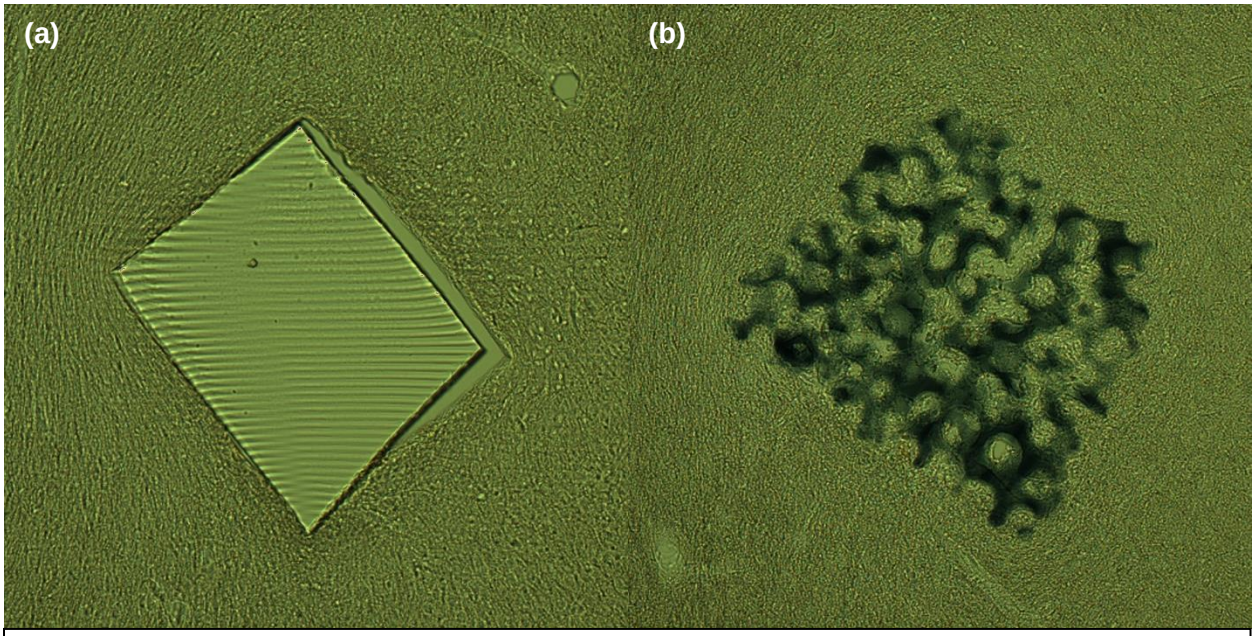

Figure 44: Brightfield images of the (a) control and (b) test materials cross-sectioned within the brain.

dense astrocytic response occurred around the edge of the test material, while a relatively more diffuse pattern of GFAP staining occurred around the test material with significant ingrowth of astrocytes, or their processes, throughout the porous network. Thirdly, staining of neuronal cell bodies in proximity to the implant surface is noticeably different between the control and test conditions, with an observable increase in neuronal density around the edge of the test implant as compared to the control implant. Together these data suggest that the test material encouraged a reduction in glial scarring and improvement in neuronal survival as compared to the test implant, quantification for which will be discussed below.

However, it is also worth noting the significant degree of variability observed across the animals in this study. Figure 46 depicts two examples of the control and test groups which demonstrated a divergence from the trends observed. The control material implanted into RAT L6 associated with Figure 46a showed little to no GFAP signal around the material which suggests a relatively mild glial response in this case. Interestingly however, the distance of neuronal cell bodies to the implant surface was still relatively high in this case. Conversely, the test material implanted to Rat L4 associated with Figure 46b showed a significant increase GFAP signal tightly around the edge of the device with little observable GFAP within the material. This also correlated with a reduction in neuronal cell count around the material, together indicating a relatively severe tissue response.

It is unclear why these implants demonstrated such divergence from the observed trends, but similar variability has been reported previously for implanted neural electrodes[10]. The L6 control implant and L4 test implant may simply have caused minor or major vascular damage upon implantation, respectively, which is known to contribute to variation in gliosis severity. Analysis of the structure of the L4 test implant across the implantation depth also indicate defects in the porous structure for this particular implant, which may also have contributed to the poor tissue integration observed. Furthermore, the lack of scar formation around the L6 control implant might also suggests that the material chemistry itself was well tolerated. The variability in the tissue response observed in these examples was also apparent in the quantification of the results across all implants which provides motivation for additional studies with larger number of animals to confirm the results observed in this study.

The quantification of astrocytic GFAP is a canonical method for examining the degree of glial scar formation in the context of neural microelectrode implantation. Here, glial scar severity was quantified by averaging the GFAP fluorescence intensity within discrete 25μm bins extending from the implant surface out to a total distance of 250μm for both test and control materials across

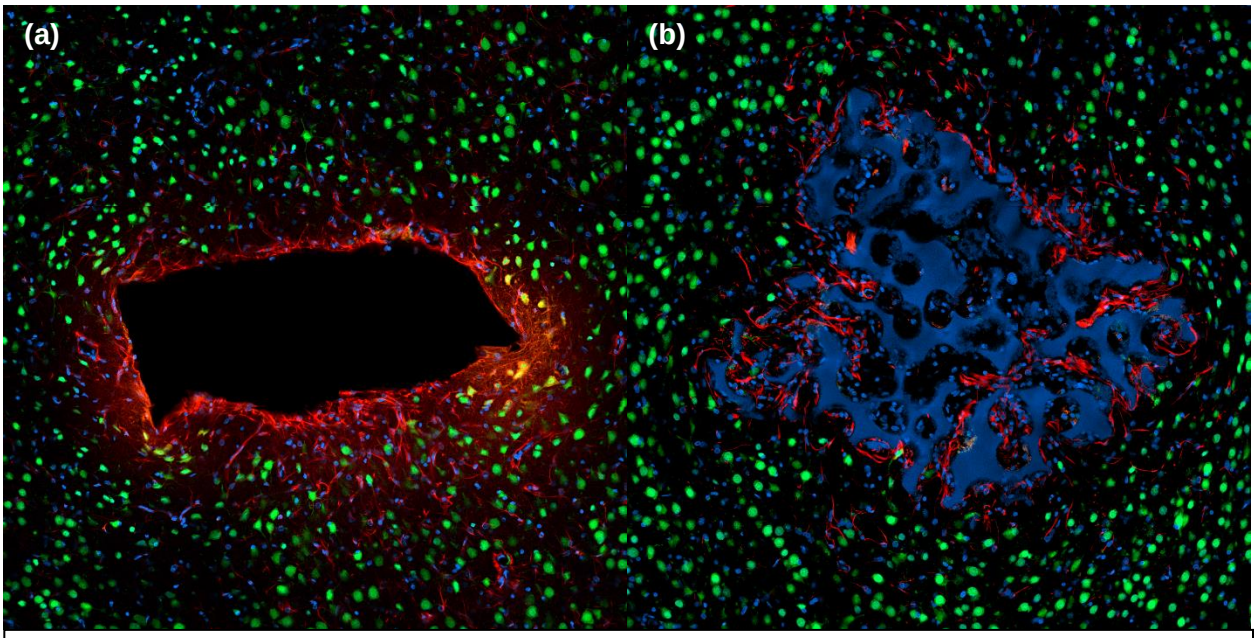

Figure 45: (a,b) Overlayed confocal images of the (a) control and (b) test material in the tissue environment. (c-h) Single red, green, and blue channels for control (c), (e), (g) control and test implants (d), (f), (h). Red = GFAP (astrocytic scar), green = NeuN (neurons), blue = Hoechst (cell nuclei).

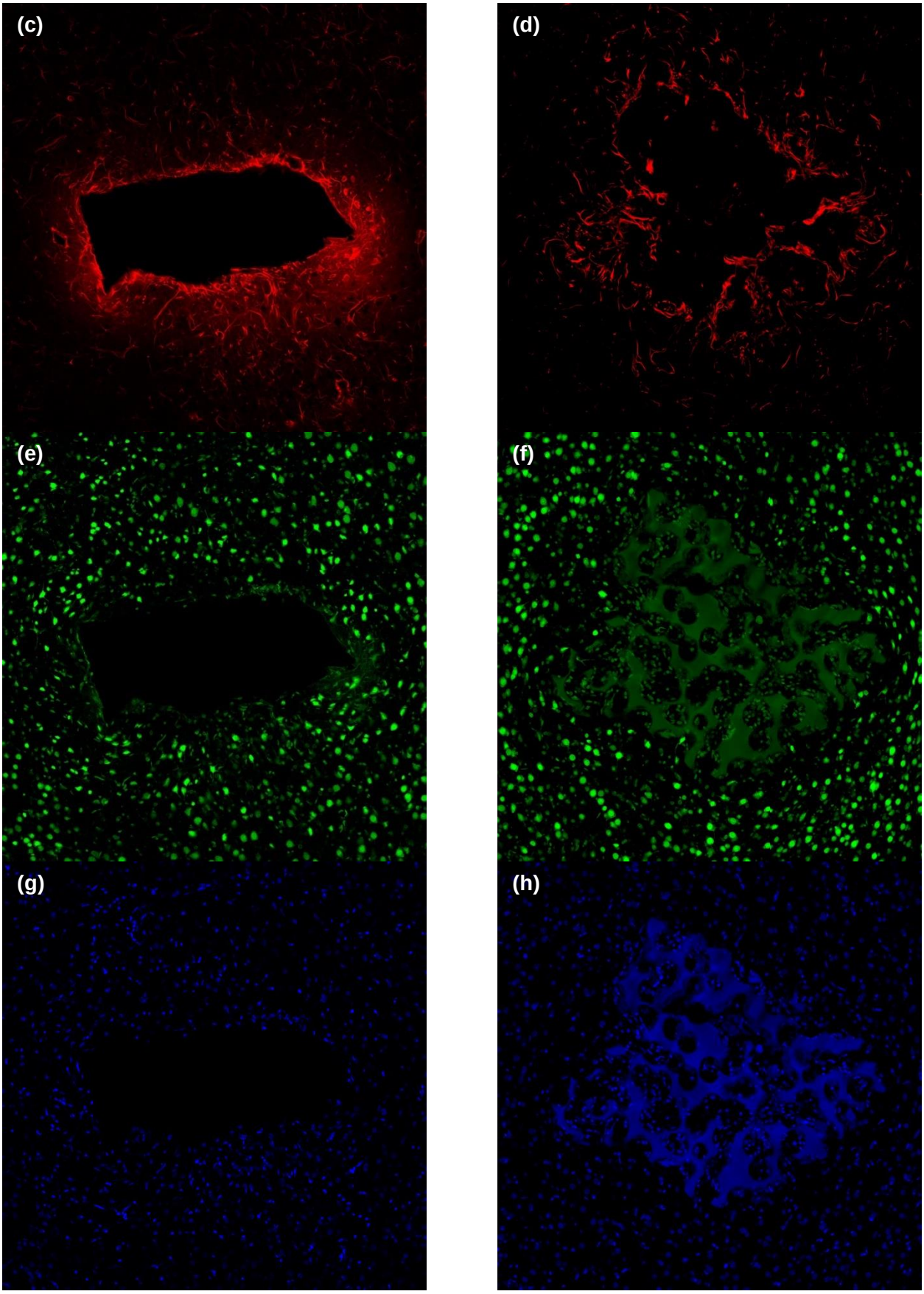
(c)
(d)
(e)
(f)
(g)
(h)

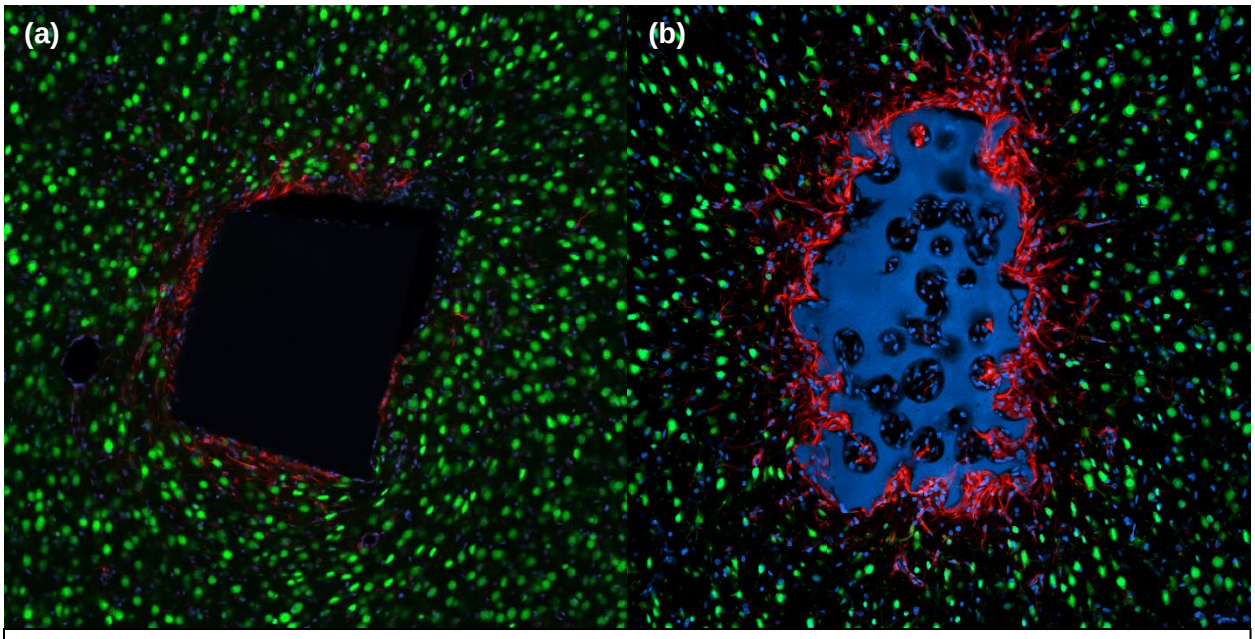

Figure 46: Overlayed confocal images of the (a) control and (b) test material in the tissue environment demonstrating the degree of variability in the tissue response.
Red = GFAP (astrocytic scar), green = NeuN (neurons), blue = Hoechst (cell nuclei).

all animals. An additional '0th' bin was included which averaged the GFAP fluorescence intensity within the perimeter of the material as an indication of astrocytic ingrowth into the material. Figure 47 plots the mean integrated density (i.e. average fluorescence intensity) for GFAP quantified in bins 0-10 for the control and test materials which demonstrates a few interesting results. Firstly, GFAP intensity within the material was significantly different for the test and control materials, as was expected given the porous and monolithic structure of these materials, respectively. Secondly, GFAP intensity within bin 1 was lower in the test condition than in the control condition, however these differences were not statistically significant ($p = 0.07$), which indicates a relatively large astrocytic scar was forming on the perimeter of both materials, on average.

However, that the degree of GFAP fluorescence in bins 0 and 1 for the test condition were not statistically different ($p = 0.27$) indicates that the porous network limited the severity of scar formation on the perimeter of the implant. While these differences observed between the test and control conditions are relatively minor, it may have significant implications for the ability of a neural microelectrode composed of this material to enable high-quality recording of neural activity over

chronic time frames given reports in the literature suggesting that long-term recording stability may not necessitate complete elimination of the glial scar[180]. Lastly, comparing the remaining bins 2-10 shows a gradual decline in GFAP intensity back toward baseline levels for both the test and control conditions. However, the test condition demonstrated a relatively higher signal in bins 3-10 compared to the control condition and with eventual return to baseline while the control condition exhibited a trend of reduced GFAP intensity compared to baseline for bins 6-10. Taken together, these results suggest a more diffuse scarring response induced by the test materials, with a greater number of astrocytes migrating to form a more compact scar directly on the perimeter of the control materials.

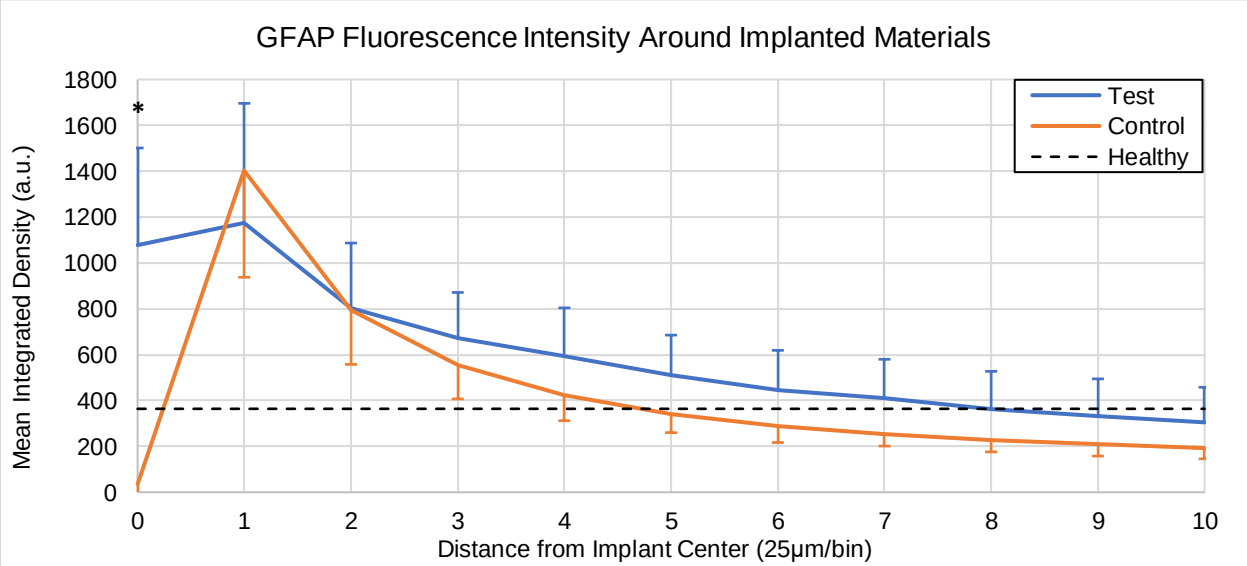

Figure 47: Bin-wise averaged GFAP intensity for the control (orange) and test (blue) materials compared to healthy tissue (black dotted) demonstrating a difference in astrocyte response to the tissue with a more compact aggregation of astrocytes around the control material and a more diffuse but upregulated astrocyte response with ingrowth into the porous network for the test material.

GFAP is normally expressed in low levels in the large filamentous processes of a majority of astrocytes throughout the healthy brain and has been shown to be critical for gliosis and glial scar formation[182,183]. Astrocytic GFAP is upregulated in response to tissue damage, driven primarily by release of inflammatory markers by microglia and macrophages, which likely accounts for the majority of the increases in GFAP staining observed here. Beyond their implications in scar formation, however, astrocytes are also primary mediators of

microvasculature as they play a significant role in the structure of the neurovascular unit and metabolic support of neuronal activity[182]. Some portion of GFAP staining in this context may therefore have been in response to neovascularization occurring within and around the material, as STS materials with 40μm pores are known to induce angiogenesis[51].

The significant release of VEGF observed upon seeding the test material with BV2 microglia *in vitro*, as shown in Figure 39c in Chapter 3, suggests an upregulation of VEGF release in response to these materials *in vivo* which may have contributed to an increase in vascular growth as well. Interestingly, an increase in astrocyte proliferation has been observed in proximity to blood vessels after traumatic injury[176], as well as specifically in response to VEGF exposure[157]. These results may account for the observations regarding the spatial dynamics of the GFAP signal around the test material in this study. Future implant studies with these materials therefore warrant quantifying the degree of new vessel growth in relation to astrocyte activation. However, a state of severe diffuse reactive astrogliosis with an upregulation and extension of GFAP positive astrocytic processes producing substantial overlap between neighboring astrocytes has also been reported in areas surrounding severe focal lesions[182] which may also account for the diffuse increase in GFAP staining observed here. Future studies staining for other markers which have been used to quantify astrocytic glial scar formation including vimentin and chondroitin sulfate proteoglycans may provide additional insight into the scar formation around these materials[182,184].

While the impact of glial scaring on long-term recording performance of implanted neural microelectrodes is still under debate, it is widely accepted that the proximity of neuronal cell bodies to recording sites on the surface of the electrode has a significant impact on signal quality. Therefore, neuronal density was quantified within each 25μm bin and normalized to neuronal density in healthy tissue at least 1 mm away from the implant site. Figure 48 plots the normalized

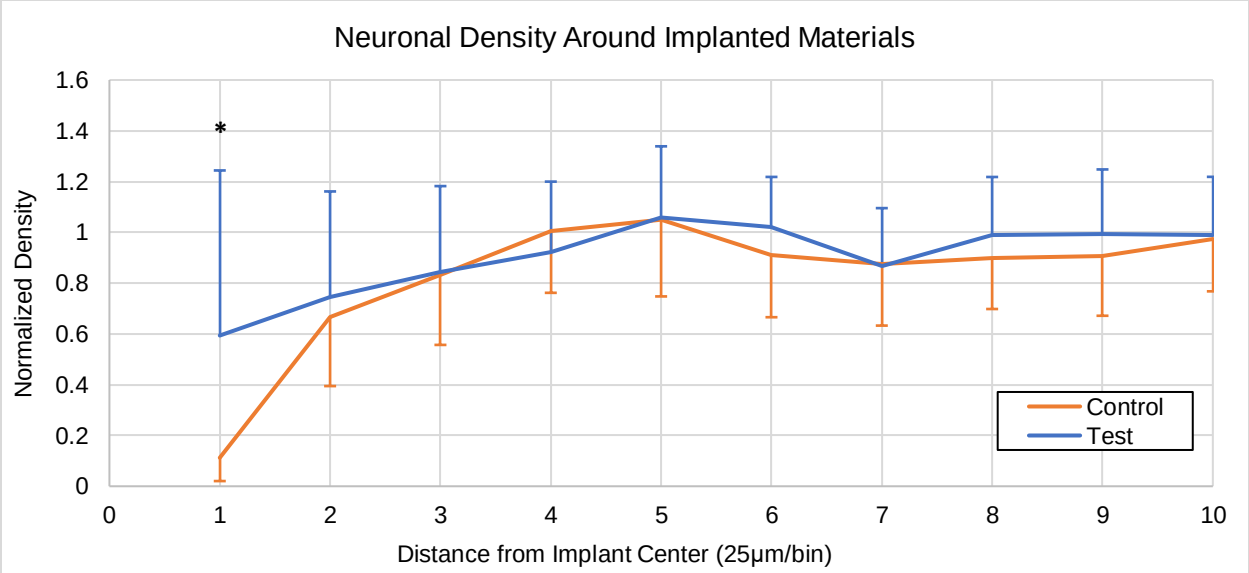

Figure 48: Bin-wise averaged neuronal density for the control (blue) and test (orange) materials compared to healthy tissue (black dotted) demonstrating a difference in astrocyte response to the tissue with a more compact aggregation of astrocytes around the control material and a more diffuse but upregulated astrocyte response with ingrowth into the porous network for the test material.

neuronal density in bins 1-10 averaged across all animals for the test and control conditions. While a few neurons were observed within the first layer of the porous network of the test material, no neurons were observed within the internal porous network, so these neurons were counted in bin 1 in these cases.

While the degree of variability in neuronal density observed in bin 1 for the test condition was quite large, comparison of the test and control conditions demonstrated a statistically significant difference ($p = 0.02$) in this bin. This indicates that, on average, the test material enabled an increase in neuronal survival around the implant in the test condition, although both the test and control conditions exhibited a trend of reduced neuronal density immediately around the materials compared to healthy tissue that gradually returned to baseline 100μm from the implant surfaces. However, these comparisons to healthy tissue were only statistically significant for bin 1 of the control condition, another indication of the significant variability observed in the tissue response in this study. As discussed previously, VEGF has also been reported to act as a neuroprotectant in the context of traumatic injuries to brain tissue and, in light of previous

discussion, may have contributed to the relative increase in neuronal cell density surrounding the test materials.

It is also interesting to note that the degree of cell loss around implanted control materials was both significant and showed little variation, regardless of the degree of glial scar formation as measured by GFAP intensity. These data suggest that implant-induced neuronal die-back was not entirely dependent on glial scar formation and that other factors, such as mechanical mismatch-induced tissue strain, may have contributed to neurodegeneration around the control material. Indeed, another signal of tissue health around implanted microelectrodes is the spherical regularity of neuronal cell bodies which can be seen to have significant deformation around the control material in Figure 46a. Reports have demonstrated that ellipsoid deformation of neuronal cell bodies induced by electrode implantation can stretch activate ion channels on the neuronal cell membrane, resulting in abnormal neural activity and gradual neurodegeneration[185,186]. Interestingly, Ravikumar et al. (2014)[187] have reported a correlation between the degree of CD68+ macrophage staining and neuronal cell loss around implanted microelectrodes which did not correlate with intensity of Iba1 (a pan microglia/macrophage marker) staining around the implants. Therefore, the authors suggested that inflammatory blood derived macrophages are the primary mediators of neurodegeneration following microelectrode implantation.

Immunohistochemical analysis of microglial distribution and infiltration of blood derived macrophages was also caried out in this study. Figure 49a and 49b shows representative confocal images of microglia (Iba1, green), infiltrating macrophages (CD68, red), and cell nuclei (Hoechst, blue) around the control and test materials, respectively. Ingrowth of microglia and macrophages into the porous network of the test material is clearly observable in these images, while the control materials exhibited a more compact population of these cells at the implant surface. However, as with the previous markers, there was considerable variability observed in the degree of microglial and macrophage staining between different samples in each of the test and control conditions.

Figure 50b depicts an image of the L4 test implant from above which exhibited a significant influx of CD68+ cells around the material, which appeared to correlate with the degree of scarring and neuronal dieback observed for this sample. Figure 50a depicts an image of the L4 control implant from above with little to no CD68+ staining.

The degree of microglial accumulation in and around the materials was quantified with mean Iba1 fluorescence intensity in a bin-wise manner, analogous to GFAP quantification. Figure 51 demonstrates that bin-wise Iba1 fluorescence intensity produced a similar curve shape to GFAP intensity for the test and control conditions with a few key differences. Firstly, the test condition showed an increased Iba1 intensity compared to the control condition for all bins, but only comparison between bin 0 was statistically significant. The test materials demonstrated a significant infiltration of microglia into the porous network that was essentially equivalent to the microglial density directly exterior to the material surface. These features of the curve together indicate microglial proliferation in and around the device for the test condition.

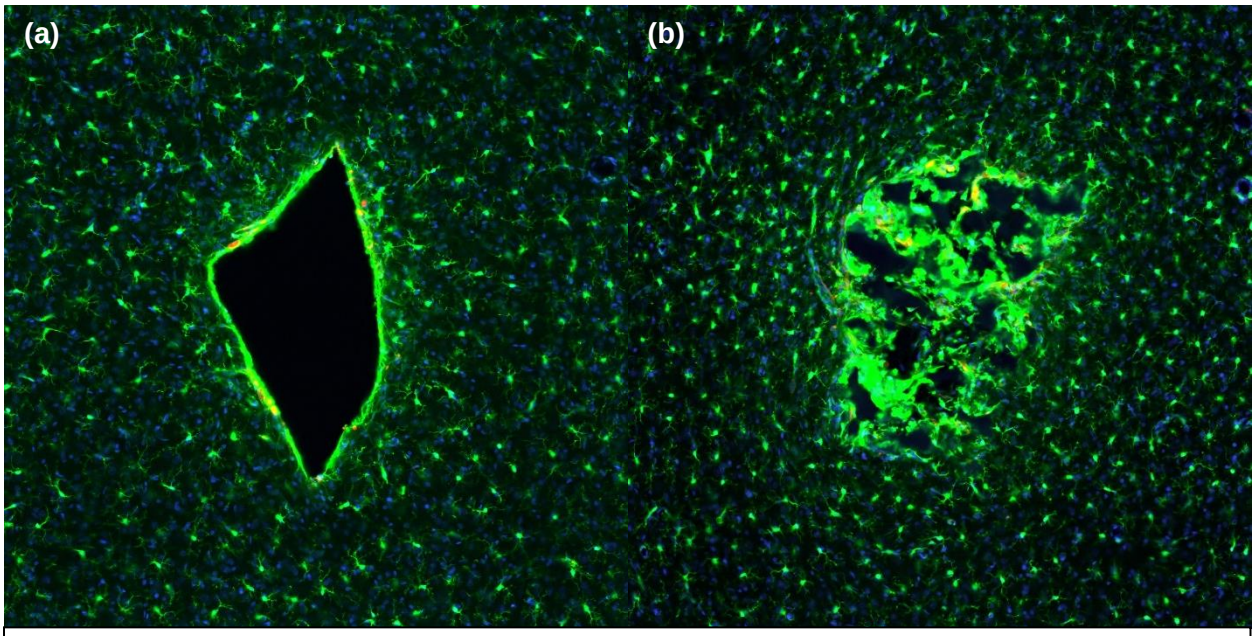

Figure 49: (a,b) Overlayed confocal images of the (a) control and (b) test material in the tissue environment. (c-h) Single red, green, and blue channels for control (c), (e), (g) control and test implants (d), (f), (h). Red = CD68 (M1 cell), green = Iba1 (microglia), blue = Hoechst (cell nuclei).

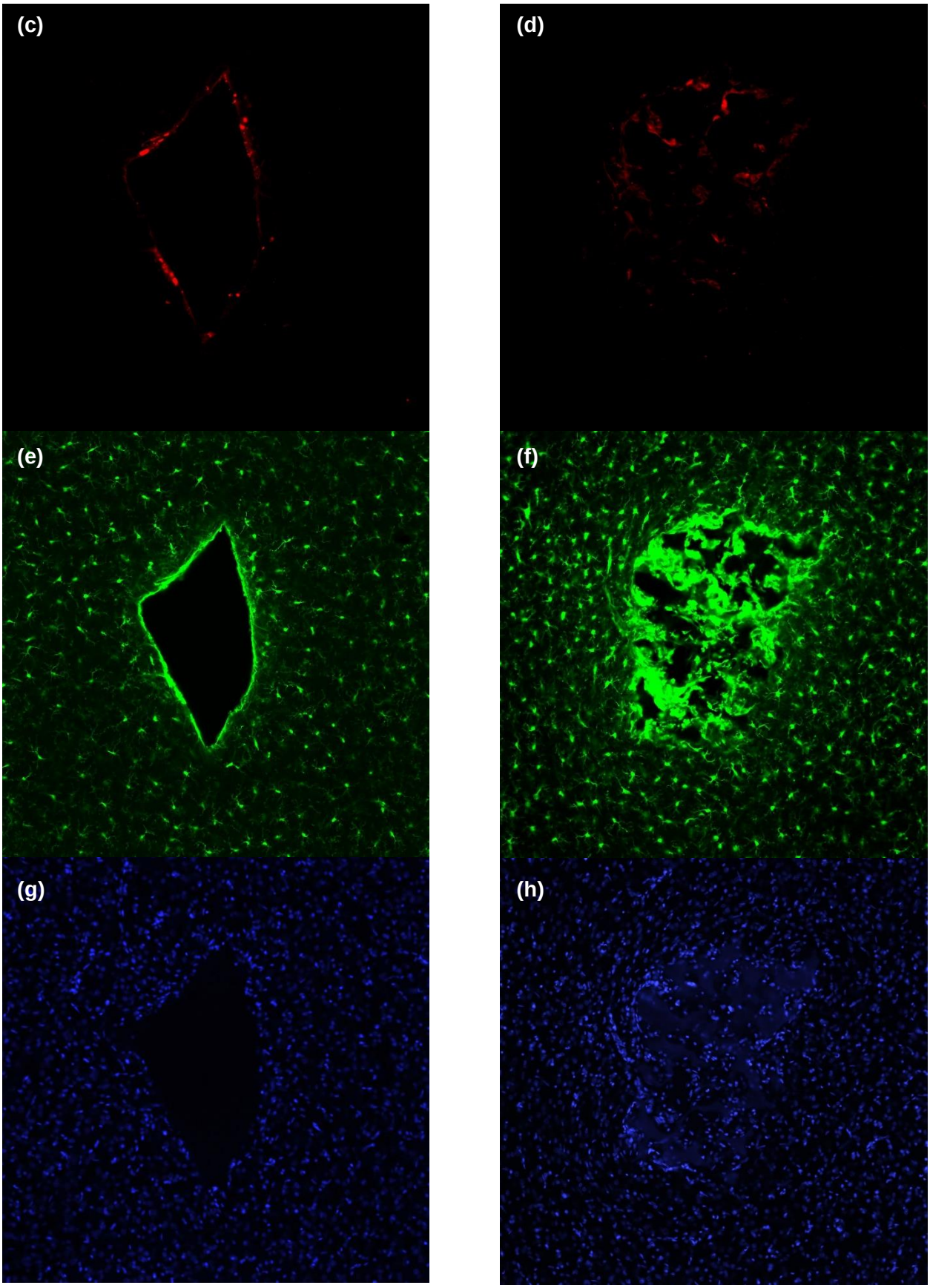
(c)
(d)
(e)
(f)
(g)
(h)

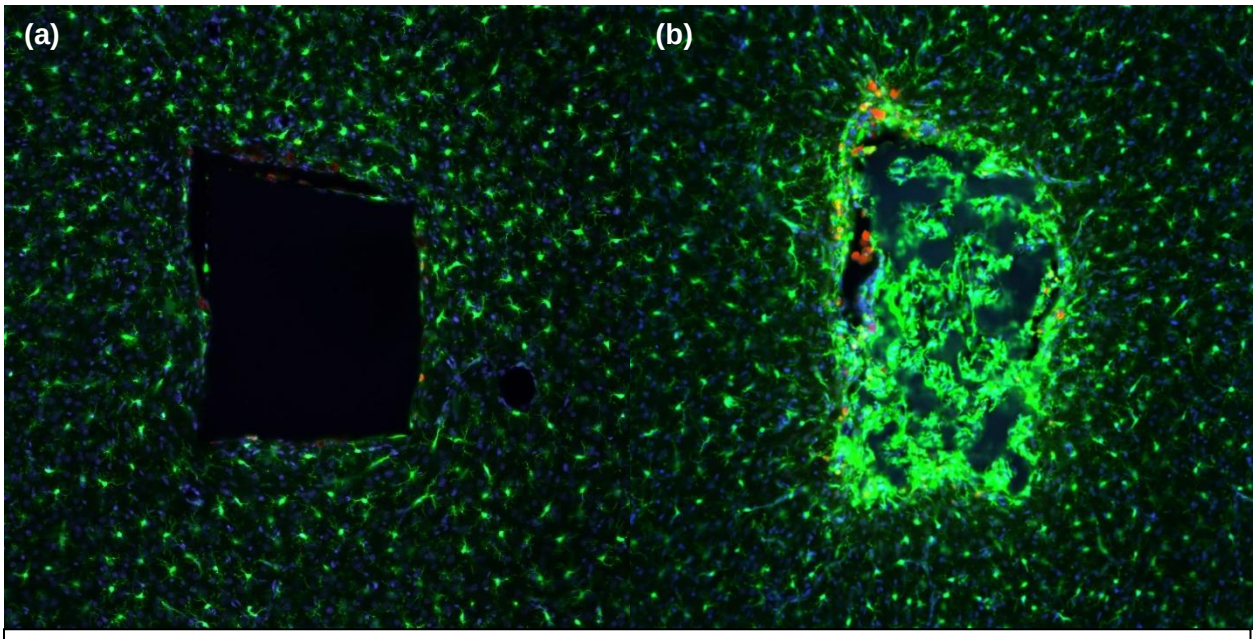

Figure 50: Overlayed confocal images of the (a) control and (b) test material in the tissue environment demonstrating the degree of variability in the tissue response.
Red = CD68 (M1 cells), green = Iba1 (microglia), blue = Hoechst (cell nuclei).

The large increase in VEGF released from BV2 cultured in these test materials discussed in Chapter 3 suggests that the microglial cells in contact with the material surface were stimulated by the surface-bound AGP/Col6. A similar stimulatory interaction with the material therefore likely occurred *in vivo* which may account for the increase in microglial density observed in the test condition. Soluble AGP is typically released from astrocytes in response to tissue damage which then mediates microglial activation, so it is interesting to note that the immobilization of AGP was still capable of inducing a significant stimulatory effect on microglia *in vitro*, as demonstrated in Chapter 3.

The crosstalk between microglia and astrocytes is well established, with microglia typically reacting faster to tissue damage to release inflammatory cytokines, like TNFα, and thereby inducing astrocyte activation and secretion of secondary inflammatory mediators[188]. In this way, astrocytes are also involved in both activating microglia and modulating their cellular functions. Therefore, preventing a preemptive astrocyte-derived anti-inflammatory signal may have

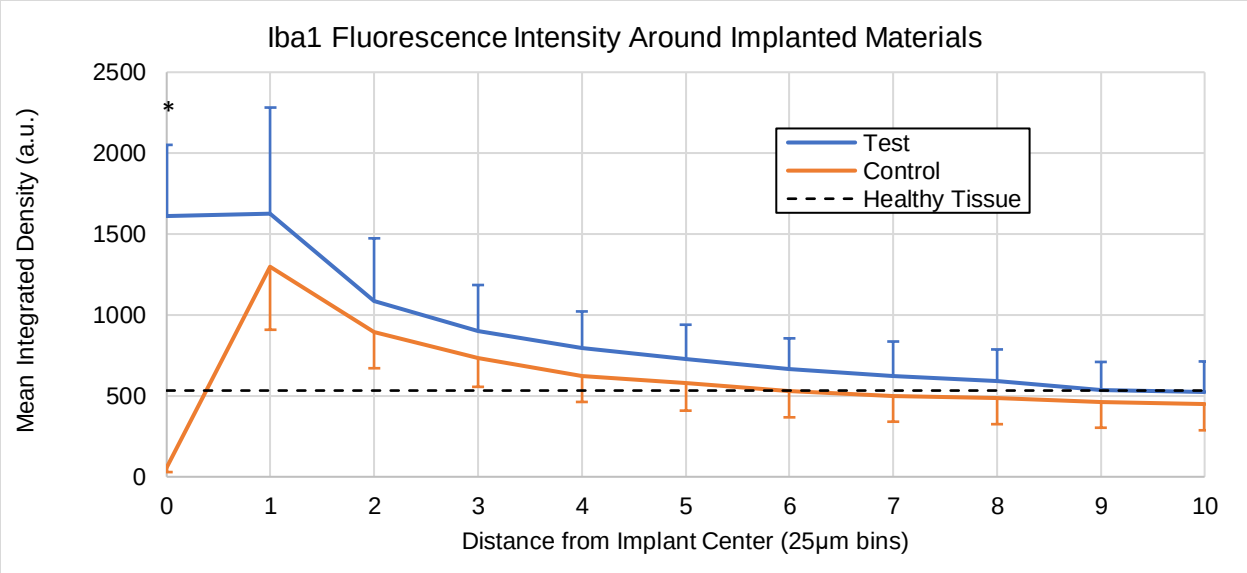

Figure 51: Bin-wise averaged Iba1 intensity for the control (orange) and test (blue) materials compared to healthy tissue (black dotted) demonstrating a difference in microglia response to the tissue with an increase in microglial density across all bins and significant ingrowth into the porous network for the test material.

contributed to the early modulation of microglial phenotype when in contact with the implanted test material to encourage pro-regenerative and/or neuroprotective outcomes. More specifically, these data suggest that a decrease in TNFα release and increase in VEGF release from microglial cells into the surrounding tissue may have contributed to neuronal survivability and distribution of astrocytic GFAP. Future work using these materials which stains specifically for VEGF will provide more information regarding its potential impact on the tissue response.

The number of CD68+ cells (M1-activated microglia and macrophages) was quantified by comparing cell counts on the interior and exterior of the materials in both the test and control conditions, data for which are plotted in Figure 52. Given the large variability between the samples, there were no statistically significant differences observed between CD68+ cell counts in the interior and exterior for the test conditions, or in the total CD68+ cell counts between the test and control conditions. However, a trend of increased CD68+ cell counts was observed for the test condition in comparison to the control condition. As discussed above, previous immunohistochemical analysis of *in vivo* implantation of STS has shown an increase in M1

staining within the pores of the material for STS with 40µm pores compared to larger porous materials. Interestingly, there appeared to be no difference between the number of CD68+ M1 macrophage cells inside and outside the material. However, the test material used here was significantly different than that used in the previous study, and the central nervous system response is also considerably different given the cell types involved.

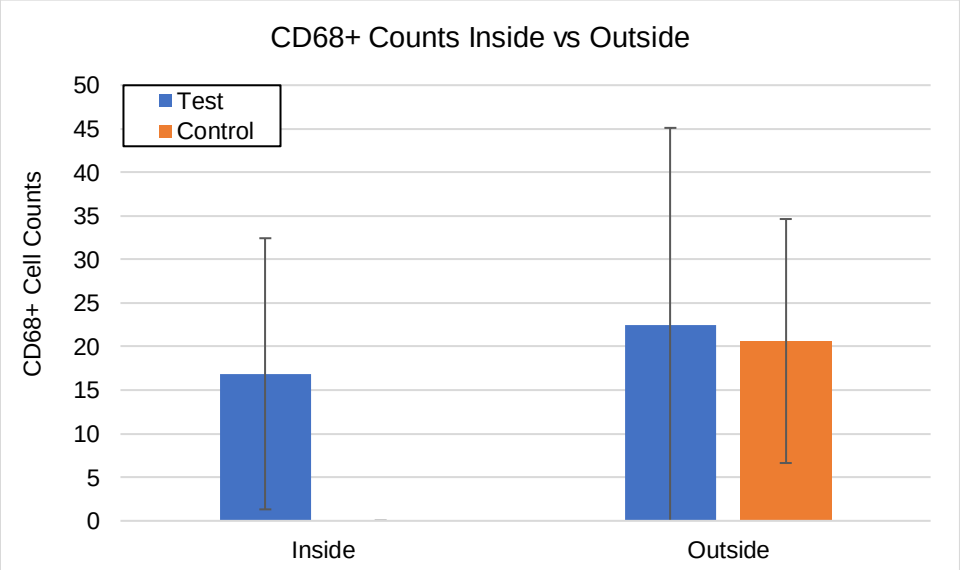

Figure 52: Counts of CD68+ cells inside and outside of the control and test material further demonstrate the variability in the tissue response between the animals.

In consideration of observations made by Ravikumar et al. (2014)[187] regarding a correlation between degree of CD68 macrophage infiltration and neuronal dieback, the data presented here do not appear to be in agreement with those previous findings. That is, the total number of CD68+ macrophages was greater for the test condition relative to the control condition, but the number of neurons and microglia in proximity to the material showed the opposite trend. However, the implants tested in Ravikumar's were single shank, 'Michigan-style' silicon dummy microelectrodes while the implants tested here were specifically designed for neural tissue engineering. The differences in the tissue response observed in this study are thus an indication of the immunomodulatory capability of these materials that warrant additional investigation into

vascular growth, additional M1 and M2 markers, and regulation of gene transcription around these novel neural tissue engineered materials.

CHAPTER 5 – Conclusion and Future Prospects

Taken together, the data presented throughout this dissertation provide a proof of concept that this novel conductive hydrogel material is amenable to the design and application of a wholly organic, immunomodulatory neuroelectronic interface. However, significant work still remains to apply the concepts presented here to generate a functional electrode with high channel density and robust connection to recording hardware and to validate its efficacy in BCI performance over clinically relevant time scales.

In light of the future work that still remains, a few design implementations are considered and discussed below, specifically in application of the material to solution processable photolithographic and 3D printing fabrication techniques. Figure 53 depicts an initial attempt at applying the one-pot photochemical polymerization process to the fabrication of electrode traces and recording sites. A liquid pre-gel composition of HG25SC-3.0E was deposited in a thin layer on a glass slide and covered with a custom-made mask followed by exposure to UV radiation with a broad-spectrum UV light for 5 minutes. Removal of the mask caused some tearing along the edge of top left traces indicating adherence to the glass substrate of the mask, but the structure of the electrode traces and recording sites was otherwise intact. The 5 minutes of UV exposure initiated the photochemical polymerization process described in Chapter 2 to produce crosslinked conductive hydrogel in a controlled manner. While the electrical properties of these materials were not characterized, this at least serves as a proof of concept that the one-pot photochemical polymerization method is applicable to photolithographic techniques. Future attempts will need to reduce the dimensions of the traces and recording sites and characterize the electrochemical

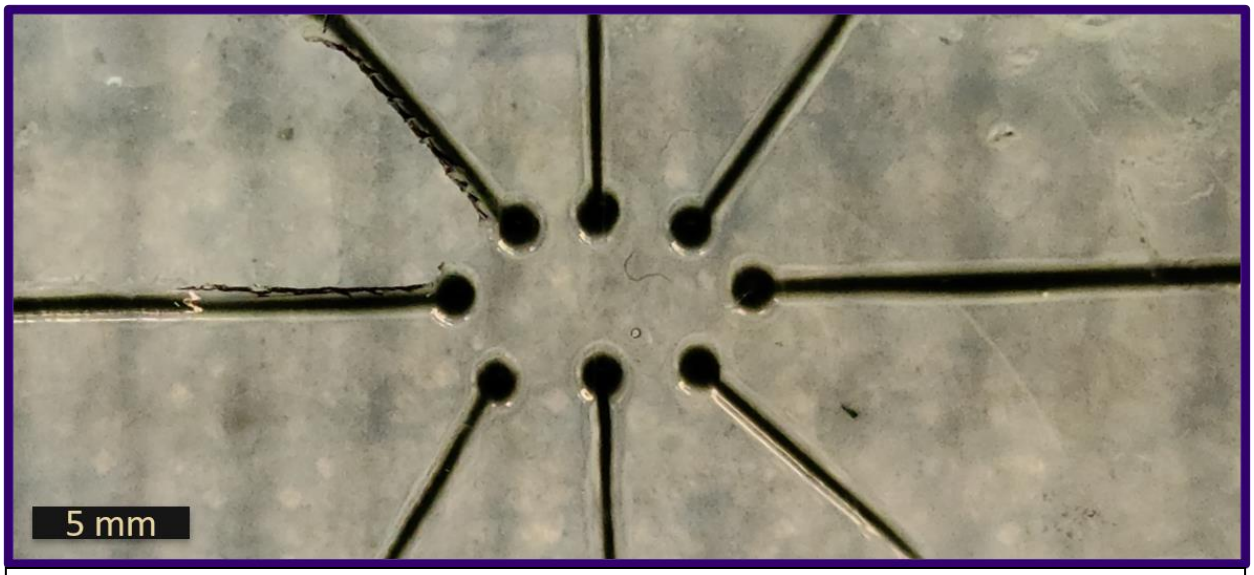

Figure 53: Proof-of-concept application of the one-pot photochemical synthesis method to photolithographic techniques.

properties of these electrodes to see how well they might serve as a wholly organic recording device.

Stereolithographic (SLA) 3D printing is another technique which operates via precision photopolymerization mechanisms and shows promise for producing micron-scale structures. The Ratner lab recently purchased a tabletop micro-stereolithography system, Dilase 3D, from Kloe (Saint-Mathieu-de-Tréviers, France) which operates by precisely directing a single-photon, 5μm laser beam up through a quartz window coated with a layer of poly(dimethyl siloxane) (PDMS) rubber into a bath containing a resin (i.e. pre-gel solution) of choice[189]. Suspended in the bath from above is an aluminum stage affixed with a removable glass slide onto which the laser bean is projected. The stage is lowered into the bath to just above the PDMS coating such that when the laser contacts the pre-gel solution it initiates a localized polymerization reaction that solidifies the solution and adheres it to the glass base with a thickness equivalent to the distance between the stage and the PDMS coating. The laser follows a raster scanning procedure along the *(x, y)* coordinates of the print geometry and then the stage elevates a fixed distance in the *(z)* direction before the raster scanning procedure is repeated with another layer of the print structure. This

process repeats, printing layer by layer, until the whole structure is printed, removed from the bath, and developed in ethanol in preparation for its intended application.

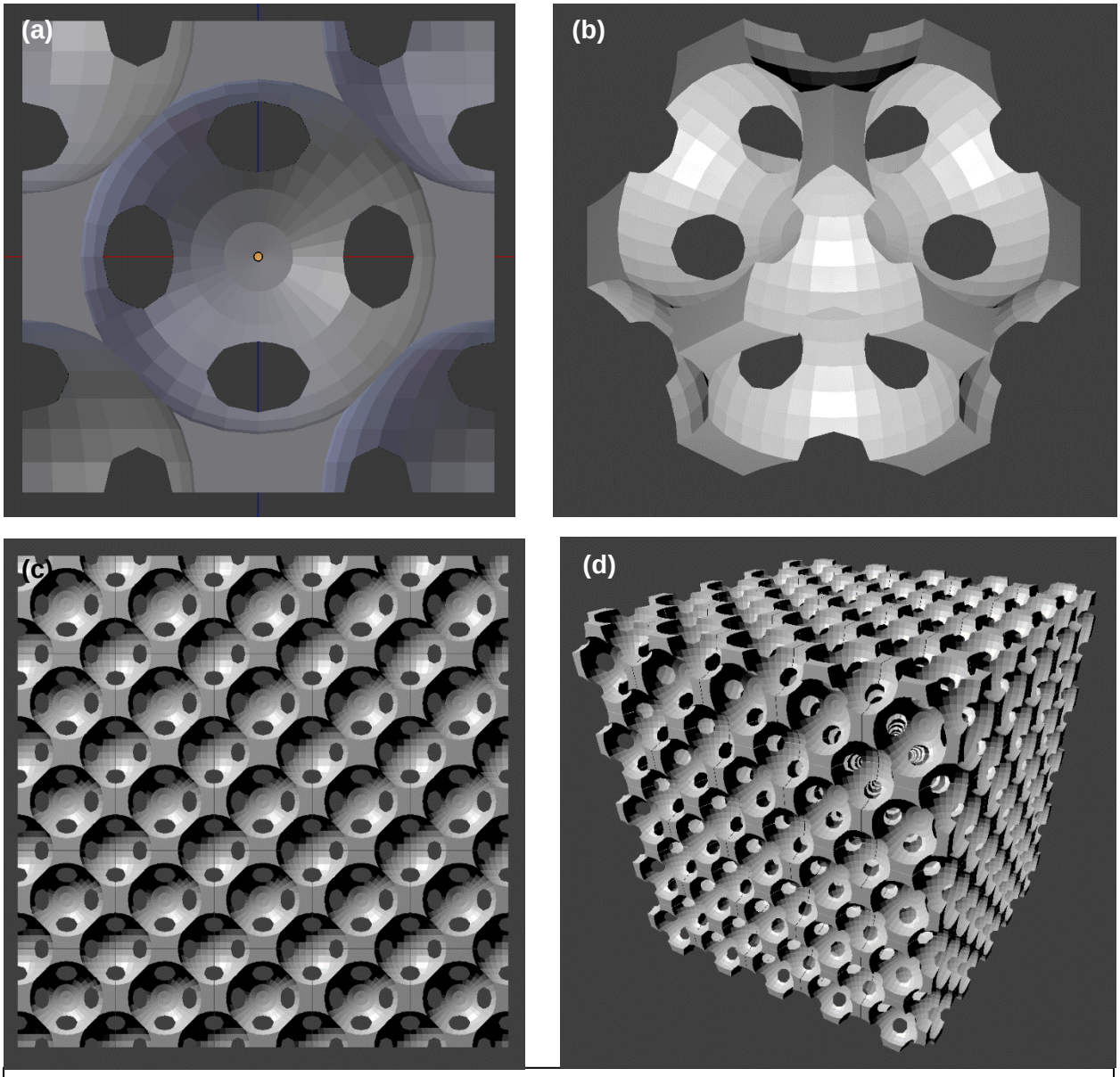

Figure 54: 3D rendering of the STS unit cell model visualized from a top-down (a) and side (b) view. The unit cell can be arranged into a lattice formation of arbitrary size to form larger structures with a precise porous network – (c) top-down and (d) side views of a 5x5 lattice of the STS unit cell.

Preliminary work has been carried out to translate the STS fabrication process to the 3D printing pipeline. This began with dissecting the STS network structure using a mathematical model of tightly packed spheres in a face-centered cubic arrangement to produce a unit cell of the STS material. The mathematical model, developed by Dr. Le Zhen in our lab, comprised 14

spheres with a small overlap at the sphere contacts to account for pore interconnects of approximately 1/3rd of the pore diameter. I then took this mathematical model and produced a 3D digital model of the STS unit cell using the open-source modeling software Blender, which is shown in Figures 54a (top-down view) and 54b (side view). The unit cell was designed such that it could be repeated in a cubic lattice formation to produce a 3D structure of arbitrary size and geometry composed of a precise, interconnected porous network. The pore size of the network can also be controlled by scaling the unit cell prior to lattice formation. An example of a 5x5 lattice of the STS unit cell is shown in Figure 54c and 54d.

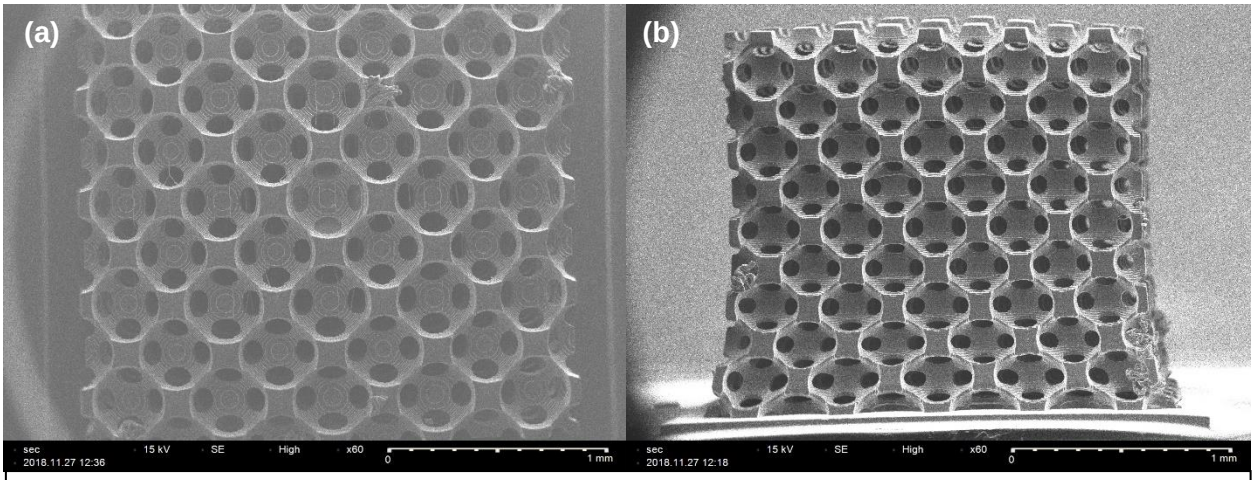

Figure 55: SEM images demonstrating a successful print of the 5x5 lattice of STS unit cells with the Dilase 3D stereolithographic system visualized via (a) top-down and (b) side views.

Once the digital design is complete, it can be exported as a .stl file which is a standard file type used by a wide range of 3D printers, including the Dilase 3D system. To produce a printable file, the Dilase software is first used to slice the .stl file into even slice thicknesses and determine the laser raster scanning path. These slices are then loaded into the Dilase 3D printer and printed. Figure 55 depicts an SEM image of the successful printing of the 5x5 lattice of the STS unit cell.

This successful demonstration of the translation of the core STS unit cell structure to a precise, micron-scale, 3D printable, porous object provides an interesting opportunity for the development of a novel penetrating microelectrode design which integrates the design features

explored throughout this dissertation. Before presenting this novel design, I have listed below a set of design features which an ideal intracortical neuroelectronic interface should incorporate:

1) Structural features (e.g. precise porosity) which promote the growth of healthy tissue (e.g. neurons and their processes) to recording sites.
2) Structural features (e.g. a handle) that make the design amenable to manipulation and implantation via precise, automated (i.e. robotic-assisted) surgical procedures.
3) Mechanical properties which are on the order of brain tissue (~10kPa) to limit mechanical mismatch-induced chronic tissue damage, AND robust to handling and insertion into the brain by an automated implantation system.
4) Electrical impedance in a low enough range (<100kΩ) to enable recording of extracellular neuronal electrical signals which are in the microvolt range.
5) A material chemistry amenable to immobilization of bioactive coatings or release mechanisms for bioactive molecules to improve the acute tissue response, AND which is stable and inert over chronic time scales within a biological environment.
6) A small cross-sectional footprint to limit implant-induced tissue damage.
7) Multiple recording channels to enable recording of neural circuit activity.
8) A thin, soft, flexible, and robustly adhered layer of insulation around the electrode traces.
9) A method for robustly connecting to downstream recording and signal processing hardware.

Several of the material compositions described throughout this dissertation have demonstrated an ability to directly address points 3), 4), and 5). Figure 56a (top-down view) and 56b (side view) visualize a rendering of a 3D model of a proposed novel “gelectrode” design which seeks to address a few of the remaining points listed above.

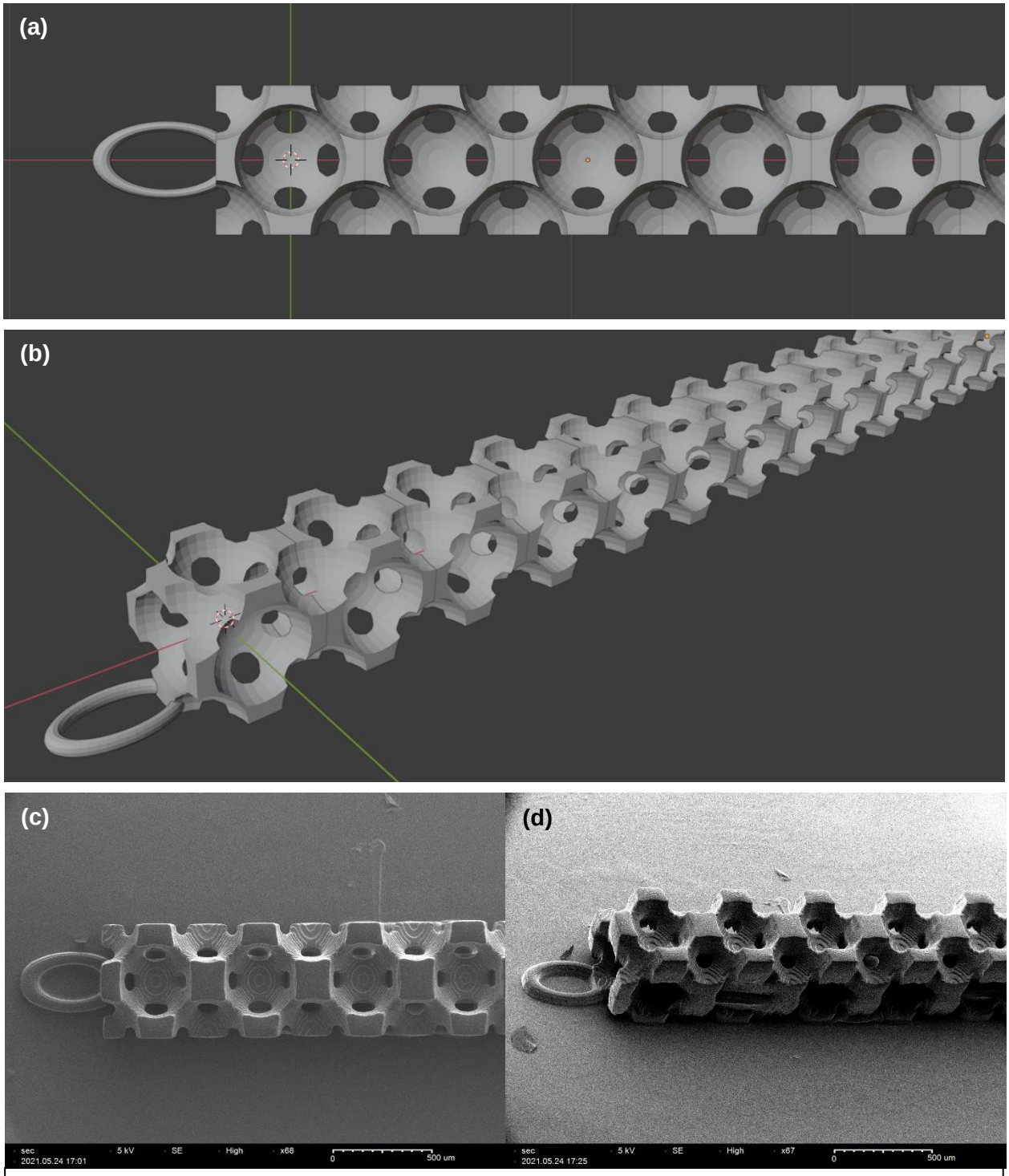

Figure 56: (a) Top-down and (b) side views of a 3D rendering of a proposed “gelectrode” design composed of a series of STS unit cells with a small handle at the distal end for robotic manipulation. (c) Top-down and (d) side views of a successful 3D print of the gelectrode prototype with the Dilase 3D sterolithographic system.

Figures 56c (top-down view) and 56d (side view) depict a proof-of-concept 3D print of the device using the Dilase 3D system. The model is comprised of a linear arrangement of STS unit cells that would represent the shaft of the electrode and would be composed of a combination of electrically active, insulative, and hydrophilic organic materials. This structural design incorporates the precise porous microstructure of the STS materials as a means to address point 1) and a handle at the distal tip of the electrode that could be grasped and manipulated by a robotic surgical system to address point 2). In order to adequately express the porous structure of the STS unit, the cross-sectional footprint of the design is relatively large compared to the most recent high channel count microelectrode designs which are beginning to surpass the submicron range[32,34]. While those electrode designs have subcellular dimensions, they are still composed of stiff underlying materials which may incite a gradual neuroinflammatory response that could compromise the device over chronic time frames.

That said, the cross-sectional area may still be made effectively small considering the microarchitecture of the design is such that most of the volume of the STS unit cell is void space. This is exemplified in Figure 57a which depicts axial cross sections of the first 9 slices of the device produced by the Dilase 3D slicing software. Figure 57b shows a zoomed in portion of one of these slices which highlights the travel path of the laser with the red line segments indicating the locations where the laser will be switched ON to initiate photopolymerization and the green line segments indicating the locations where the laser will be switched OFF but will still travel in order to to stabilize the raster scan pathway. Together, these aspects of the electrode structure may still adequately satisfy point 6).

Methods to address point 7) and 8) do not exist with the current set up of the Dilase 3D printing system as it has only a single resin bath which only enables printing of a single material composition. Modifications to the printer design for automated removal, development, and

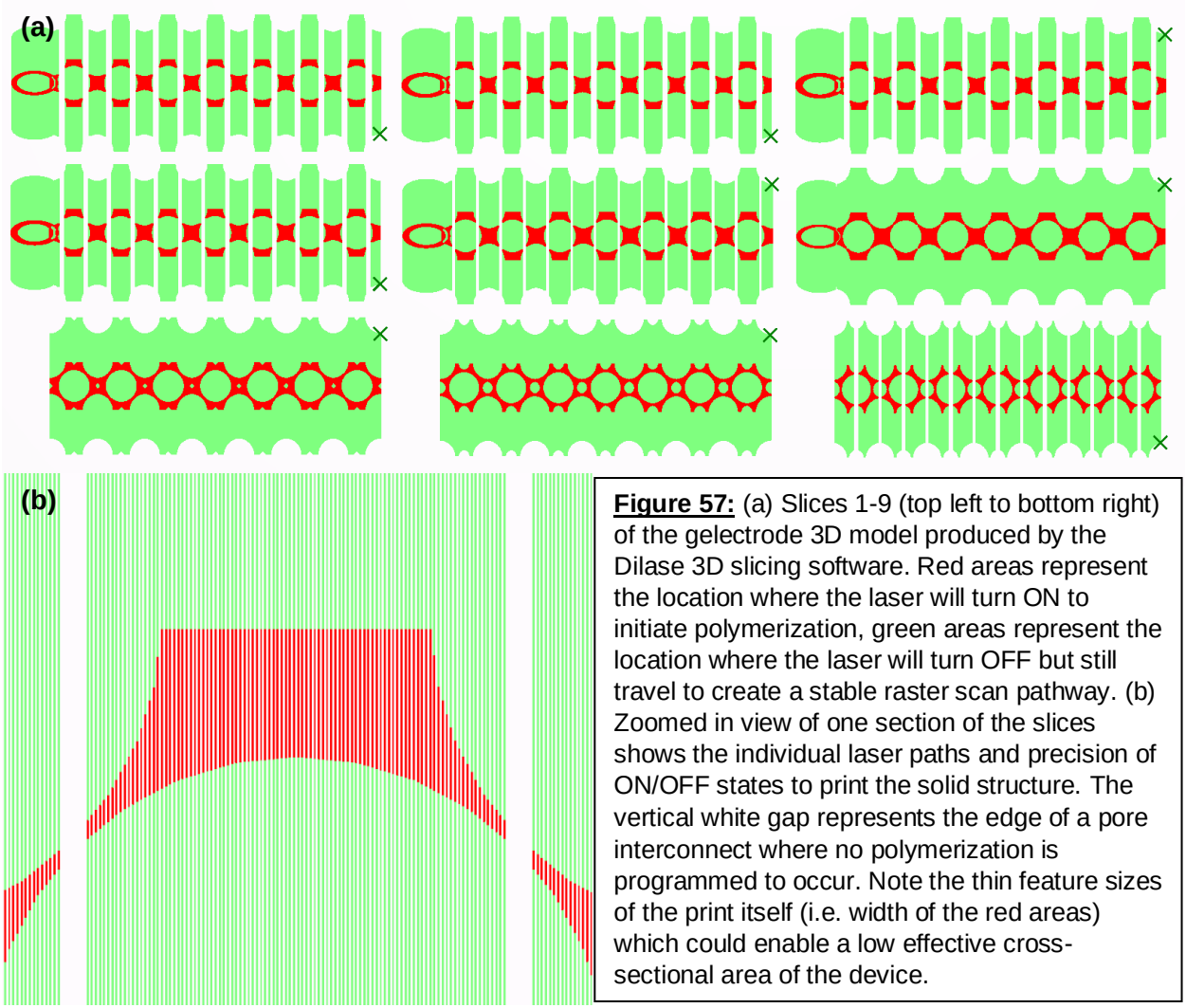

Figure 57: (a) Slices 1-9 (top left to bottom right) of the gelectrode 3D model produced by the Dilase 3D slicing software. Red areas represent the location where the laser will turn ON to initiate polymerization, green areas represent the location where the laser will turn OFF but still travel to create a stable raster scan pathway. (b) Zoomed in view of one section of the slices shows the individual laser paths and precision of ON/OFF states to print the solid structure. The vertical white gap represents the edge of a pore interconnect where no polymerization is programmed to occur. Note the thin feature sizes of the print itself (i.e. width of the red areas) which could enable a low effective cross-sectional area of the device.

placement into another resin bath would allow multiple material compositions to be printed on each layer such that conductive hydrogel electrode contacts and traces surrounded by high dielectric constant insulating segments could be embedded in a soft hydrogel substrate. Figure 58 provides a schematic example of the locations for the electrode contacts on the planar faces on the outer surface of each unit and electrode traces and insulation patterned along the interior of the material. Together, these features would allow for 6 or more recording channels per unit cell to enable a high channel count within a single shaft to address point 7). The use of a soft, elastic photopolymerizable insulator with a high dielectric constant, such as perfluoropoly(ether)-dimethacrylate (PFPEDMA; ~30kPa) developed by Liu (2019)[40] is highly suited for this application to address point 8).

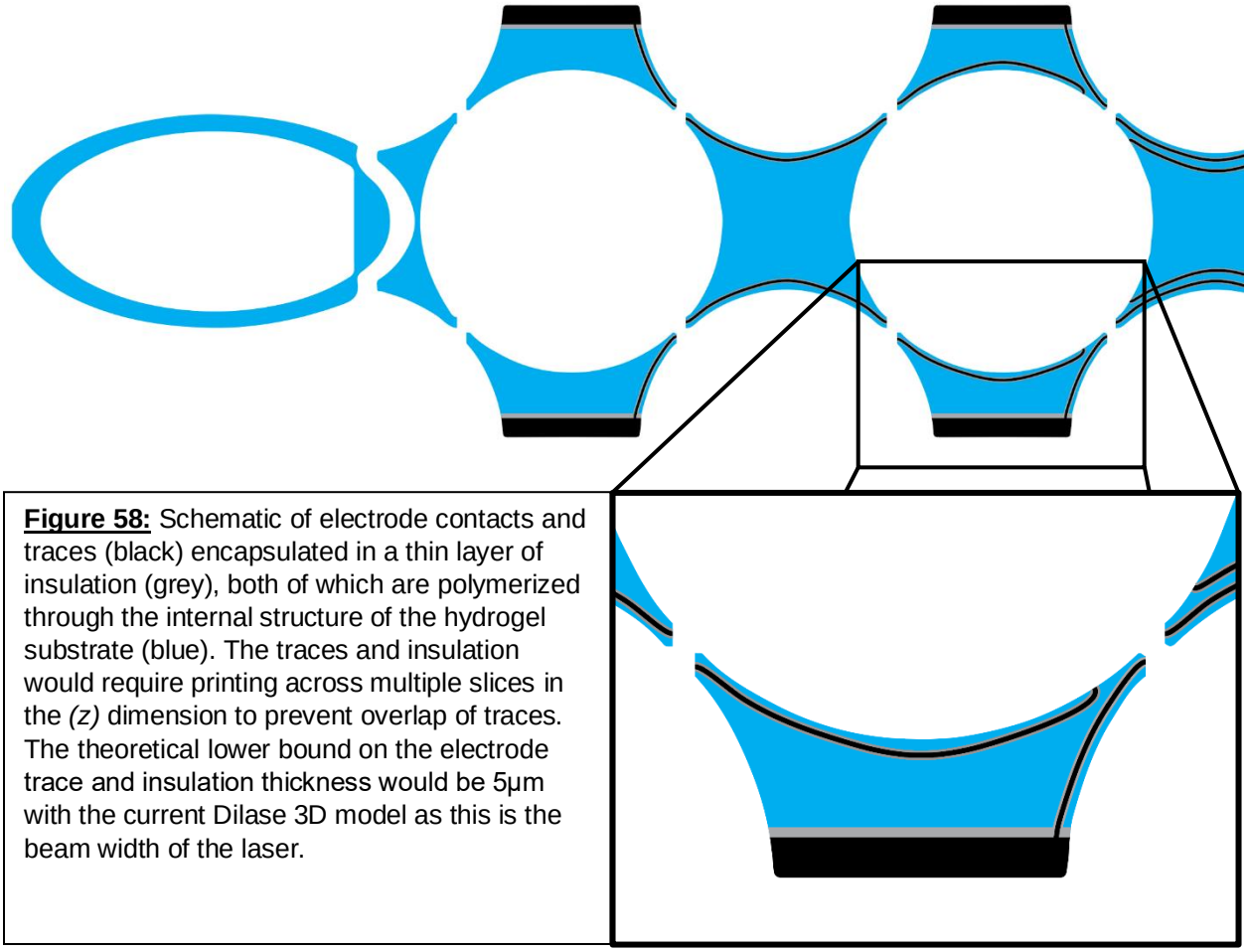

Figure 58: Schematic of electrode contacts and traces (black) encapsulated in a thin layer of insulation (grey), both of which are polymerized through the internal structure of the hydrogel substrate (blue). The traces and insulation would require printing across multiple slices in the *(z)* dimension to prevent overlap of traces. The theoretical lower bound on the electrode trace and insulation thickness would be 5μm with the current Dilase 3D model as this is the beam width of the laser.

Lastly, and perhaps most significant to the design of an intracortical electrode composed of entirely organic constituents, is the ability to robustly connect to downstream recording and signal processing hardware. Redesign of this hardware to also be composed of wholly organic parts is a much larger engineering challenge than developing a robust method for connecting soft, organic electronics to classical metallic electrical circuits. The best way that I can conceive of addressing this point at the present moment involves electrochemical deposition of PEDOT from the surface of the electrode connector while in contact with the proximal end of the gelectrode. The growth of PEDOT from the connector surface throughout the gelectrode would promote both a tight mechanical and electrochemical connection between the metallic connector and conductive traces of the electrode. If successful, this form of connection would be robust to

mechanical manipulation during implantation and enable high quality electrical signal acquisition from neural circuitry.

Clearly, the novel gelectrode design proposed and discussed above is still very much in a pre-proof-of-concept stage which will require a significant effort to develop and validate as a intracortical microelectrode. Still, both the gelectrode design, synthesis methodology, and material development and characterization of the resulting materials presented in this dissertation provide a meaningful conceptual contribution to the design toolbox toward the development of a wholly organic, immunomodulatory neuroelectronic interface for application to brain computer interface systems.

Bibliography

1. World Health Organization. *Neurological Disorders: Public Health Challenges*. (World Health Organization, 2006).
2. Whiteford, H. A., Ferrari, A. J., Degenhardt, L., Feigin, V. & Vos, T. The Global Burden of Mental, Neurological and Substance Use Disorders: An Analysis from the Global Burden of Disease Study 2010. *PLOS ONE* **10**, e0116820 (2015).
3. Pfurtscheller, G., Flotzinger, D., Mohl, W. & Peltoranta, M. Prediction of the side of hand movements from single-trial multi-channel EEG data using neural networks. *Electroencephalogr. Clin. Neurophysiol.* **82**, 313–315 (1992).
4. Maynard, E. M., Nordhausen, C. T. & Normann, R. A. The Utah Intracortical Electrode Array: A recording structure for potential brain-computer interfaces. *Electroencephalogr. Clin. Neurophysiol.* **102**, 228–239 (1997).
5. Kennedy, P. R. & Bakay, R. a. E. Restoration of neural output from a paralyzed patient by a direct brain connection. *NeuroReport* **9**, 1707–1711 (1998).
6. Taylor, D. M., Tillery, S. I. H. & Schwartz, A. B. Direct Cortical Control of 3D Neuroprosthetic Devices. *Science* **296**, 1829–1832 (2002).
7. Schwartz, A. B., Cui, X. T., Weber, D. J. & Moran, D. W. Brain-Controlled Interfaces: Movement Restoration with Neural Prosthetics. *Neuron* **52**, 205–220 (2006).
8. Leuthardt, E., Schalk, G., Moran, D. & Ojemann, J. The Emerging World of Motor Neuroprosthetics: A Neurosurgical Perspective. (2006).
9. Polanco, M., Yoon, H. & Bawab, S. Micromotion-induced dynamic effects from a neural probe and brain tissue interface. *J. MicroNanolithography MEMS MOEMS* **13**, 023009 (2014).
10. Polikov, V. S., Tresco, P. A. & Reichert, W. M. Response of brain tissue to chronically implanted neural electrodes. *J. Neurosci. Methods* **148**, 1–18 (2005).

11. Barrese, J. C. *et al.* Failure mode analysis of silicon-based intracortical microelectrode arrays in non-human primates. *J. Neural Eng.* **10**, 066014 (2013).
12. Hu, X. *et al.* Microglial and macrophage polarization—new prospects for brain repair. *Nat. Rev. Neurol.* **11**, nrneurol.2014.207 (2014).
13. Campbell, A. & Wu, C. ***(good electrode image) Chronically Implanted Intracranial Electrodes: Tissue Reaction and Electrical Changes. *Micromachines* **9**, 430 (2018).
14. Schendel, A. A. *et al.* The effect of micro-ECoG substrate footprint on the meningeal tissue response. *J. Neural Eng.* **11**, 046011 (2014).
15. Biran, R., Martin, D. C. & Tresco, P. A. Neuronal cell loss accompanies the brain tissue response to chronically implanted silicon microelectrode arrays. *Exp. Neurol.* **195**, 115–126 (2005).
16. McConnell, G. C. *et al.* Implanted neural electrodes cause chronic, local inflammation that is correlated with local neurodegeneration. *J. Neural Eng.* **6**, 056003 (2009).
17. Frampton, J. P., Hynd, M. R., Shuler, M. L. & Shain, W. Effects of Glial Cells on Electrode Impedance Recorded from Neural Prosthetic Devices In Vitro. *Ann. Biomed. Eng.* **38**, 1031–1047 (2010).
18. Turner, J. N. *et al.* Cerebral Astrocyte Response to Micromachined Silicon Implants. *Exp. Neurol.* **156**, 33–49 (1999).
19. Szarowski, D. H. *et al.* Brain responses to micro-machined silicon devices. *Brain Res.* **983**, 23–35 (2003).
20. Griffith, R. W. & Humphrey, D. R. Long-term gliosis around chronically implanted platinum electrodes in the Rhesus macaque motor cortex. *Neurosci. Lett.* **406**, 81–86 (2006).
21. Hatsopoulos, N. G. & Donoghue, J. P. The science of neural interface systems. *Annu. Rev. Neurosci.* **32**, 249–266 (2009).

22. Aregueta-Robles, U. A., Woolley, A. J., Poole-Warren, L. A., Lovell, N. H. & Green, R. A. Organic electrode coatings for next-generation neural interfaces. *Front. Neuroengineering* **7**, (2014).
23. Kim, D.-H., Abidian, M. & Martin, D. C. Conducting polymers grown in hydrogel scaffolds coated on neural prosthetic devices. *J. Biomed. Mater. Res. A* **71A**, 577–585 (2004).
24. Green, R. & Abidian, M. R. Conducting Polymers for Neural Prosthetic and Neural Interface Applications. *Adv. Mater.* **27**, 7620–7637 (2015).
25. Lecomte, A., Descamps, E. & Bergaud, C. A review on mechanical considerations for chronically-implanted neural probes. *J. Neural Eng.* (2017) doi:10.1088/1741-2552/aa8b4f.
26. Lacour, S. P. *et al.* Flexible and stretchable micro-electrodes for in vitro and in vivo neural interfaces. *Med. Biol. Eng. Comput.* **48**, 945–954 (2010).
27. Alba, N. A., Du, Z. J., Catt, K. A., Kozai, T. D. Y. & Cui, X. T. In Vivo Electrochemical Analysis of a PEDOT/MWCNT Neural Electrode Coating. *Biosensors* **5**, 618–646 (2015).
28. Chen, S. *et al.* PEDOT/MWCNT composite film coated microelectrode arrays for neural interface improvement. *Sens. Actuators Phys.* **193**, 141–148 (2013).
29. Luo, X., L. Weaver, C., Tan, S. & Tracy Cui, X. Pure graphene oxide doped conducting polymer nanocomposite for bio-interfacing. *J. Mater. Chem. B* **1**, 1340–1348 (2013).
30. Goding, J., Gilmour, A., Martens, P., Poole-Warren, L. & Green, R. Interpenetrating Conducting Hydrogel Materials for Neural Interfacing Electrodes. *Adv. Healthc. Mater.* **6**, n/a-n/a (2017).
31. Kim, Y. S. *et al.* Highly conductive and hydrated PEG-based hydrogels for the potential application of a tissue engineering scaffold. *React. Funct. Polym.* **109**, 15–22 (2016).
32. Luan, L. *et al.* Ultraflexible nanoelectronic probes form reliable, glial scar–free neural integration. *Sci. Adv.* **3**, e1601966 (2017).
33. Wei, X. *et al.* Nanofabricated Ultraflexible Electrode Arrays for High-Density Intracortical Recording. *Adv. Sci.* **5**, 1700625 (2018).

34. Musk, E. & Neuralink. An Integrated Brain-Machine Interface Platform With Thousands of Channels. *J. Med. Internet Res.* **21**, e16194 (2019).
35. Lewitus, D. Y., Smith, K. L., Landers, J., Neimark, A. V. & Kohn, J. Bioactive agarose carbon-nanotube composites are capable of manipulating brain–implant interface. *J. Appl. Polym. Sci.* **131**, n/a-n/a (2014).
36. Kozai, T. D. Y. *et al.* Ultrasmall implantable composite microelectrodes with bioactive surfaces for chronic neural interfaces. *Nat. Mater.* **11**, 1065–1073 (2012).
37. Lu, L. Soft carbon nanotube fiber electrodes for multimodal neural interfacing. (2019).
38. Minev, I. R. *et al.* Electronic dura mater for long-term multimodal neural interfaces. *Science* **347**, 159–163 (2015).
39. Khodagholy, D. *et al.* Highly Conformable Conducting Polymer Electrodes for In Vivo Recordings. *Adv. Mater.* **23**, H268–H272 (2011).
40. Liu, Y. *et al.* Soft and elastic hydrogel-based microelectronics for localized low-voltage neuromodulation. *Nat. Biomed. Eng.* **3**, 58 (2019).
41. Guilak, F., Butler, D. L., Goldstein, S. A. & Baaijens, F. P. T. Biomechanics and mechanobiology in functional tissue engineering. *J. Biomech.* **47**, 1933–1940 (2014).
42. Ai, J. *et al.* Polymeric Scaffolds in Neural Tissue Engineering: A Review. *Arch. Neurosci.* **1**, 15–20 (2014).
43. Subramanian, A., Krishnan, U. M. & Sethuraman, S. Development of biomaterial scaffold for nerve tissue engineering: Biomaterial mediated neural regeneration. *J. Biomed. Sci.* **16**, 108 (2009).
44. Winter, J. O., Cogan, S. F. & Rizzo, J. F. Neurotrophin-eluting hydrogel coatings for neural stimulating electrodes. *J. Biomed. Mater. Res. B Appl. Biomater.* **81B**, 551–563 (2007).
45. Kim, D.-H. & Martin, D. C. Sustained release of dexamethasone from hydrophilic matrices using PLGA nanoparticles for neural drug delivery. *Biomaterials* **27**, 3031–3037 (2006).

46. Addington, C. P., Dharmawaj, S., Heffernan, J. M., Sirianni, R. W. & Stabenfeldt, S. E. Hyaluronic acid-laminin hydrogels increase neural stem cell transplant retention and migratory response to SDF-1α. *Matrix Biol.* **60–61**, 206–216 (2017).

47. Plant, G., Chirila, T. & Harvey, A. Implantation of Collagen Iv/Poly(2-Hydroxyethyl Methacrylate) Hydrogels Containing Schwann Cells into the Lesioned Rat Optic Tract. *Cell Transplant.* **7**, 381–391 (1998).

48. Woerly, S., Marchand, R. & Lavallée, G. Intracerebral implantation of synthetic polymer/biopolymer matrix: a new perspective for brain repair. *Biomaterials* **11**, 97–107 (1990).

49. Annabi, N. *et al.* Controlling the Porosity and Microarchitecture of Hydrogels for Tissue Engineering. *Tissue Eng. Part B Rev.* **16**, 371–383 (2010).

50. Marshall, A. J. & Ratner, B. D. Quantitative characterization of sphere-templated porous biomaterials. *AIChE J.* **51**, 1221–1232 (2005).

51. Bryers, J. D., Giachelli, C. M. & Ratner, B. D. Engineering biomaterials to integrate and heal: The biocompatibility paradigm shifts. *Biotechnol. Bioeng.* **109**, 1898–1911 (2012).

52. Sussman, E. M., Halpin, M. C., Muster, J., Moon, R. T. & Ratner, B. D. Porous Implants Modulate Healing and Induce Shifts in Local Macrophage Polarization in the Foreign Body Reaction. *Ann. Biomed. Eng.* **42**, 1508–1516 (2014).

53. Dryg, I. Modulating Neuroinflammation with Porous Templated Scaffolds. (University of Washington, 2019).

54. Jha, M. K., Lee, W.-H. & Suk, K. Functional polarization of neuroglia: Implications in neuroinflammation and neurological disorders. *Biochem. Pharmacol.* **103**, 1–16 (2016).

55. Kumar, D. & Sharma, R. C. Advances in conductive polymers. *Eur. Polym. J.* **34**, 1053–1060 (1998).

56. Naficy, S., Razal, J. M., Spinks, G. M., Wallace, G. G. & Whitten, P. G. Electrically Conductive, Tough Hydrogels with pH Sensitivity. *Chem. Mater.* **24**, 3425–3433 (2012).

57. Cui, X. & Martin, D. C. Electrochemical deposition and characterization of poly(3,4-ethylenedioxythiophene) on neural microelectrode arrays. *Sens. Actuators B Chem.* **89**, 92–102 (2003).

58. Bakhshi, A. K. Electrically conducting polymers: from fundamental to applied research. *Bull. Mater. Sci.* **18**, 469–495 (1995).

59. Kivelson, S., Schrieffer, J. R., Su, W.-P. & Heeger, A. J. Solitons in conducting polymers. *Rev. Mod. Phys.* **60**, 781–850 (1988).

60. Tolbert, L. M. Solitons in a box: the organic chemistry of electrically conducting polyenes. *Acc. Chem. Res.* **25**, 561–568 (1992).

61. Groenendaal, L., Jonas, F., Freitag, D., Pielartzik, H. & Reynolds, J. R. Poly(3,4-ethylenedioxythiophene) and Its Derivatives: Past, Present, and Future. *Adv. Mater.* **12**, 481–494 (2000).

62. Venkatraman, S. *et al.* In Vitro and In Vivo Evaluation of PEDOT Microelectrodes for Neural Stimulation and Recording. *IEEE Trans. Neural Syst. Rehabil. Eng.* **19**, 307–316 (2011).

63. Starbird, R., García-González, C. A., Smirnova, I., Krautschneider, W. H. & Bauhofer, W. Synthesis of an organic conductive porous material using starch aerogels as template for chronic invasive electrodes. *Mater. Sci. Eng. C* **37**, 177–183 (2014).

64. Greco, F. *et al.* Ultra-thin conductive free-standing PEDOT/PSS nanofilms. *Soft Matter* **7**, 10642–10650 (2011).

65. Guiseppi-Elie, A. Electroconductive hydrogels: Synthesis, characterization and biomedical applications. *Biomaterials* **31**, 2701–2716 (2010).

66. Xu, C. *et al.* Biodegradable and electroconductive poly(3,4-ethylenedioxythiophene)/carboxymethyl chitosan hydrogels for neural tissue engineering. *Mater. Sci. Eng. C* **84**, 32–43 (2018).

67. Wang, S. *et al.* Hyaluronic acid doped-poly(3,4-ethylenedioxythiophene)/chitosan/gelatin (PEDOT-HA/Cs/Gel) porous conductive scaffold for nerve regeneration. *Mater. Sci. Eng. C Mater. Biol. Appl.* **71**, 308–316 (2017).

68. Green, R. A., Lovell, N. H. & Poole-Warren, L. A. Impact of co-incorporating laminin peptide dopants and neurotrophic growth factors on conducting polymer properties. *Acta Biomater.* **6**, 63–71 (2010).

69. Brahim, S. & Guiseppi-Elie, A. Electroconductive Hydrogels: Electrical and Electrochemical Properties of Polypyrrole-Poly(HEMA) Composites. *Electroanalysis* **17**, 556–570 (2005).

70. Chen, C., LaRue, J. C., Nelson, R. D., Kulinsky, L. & Madou, M. J. Electrical conductivity of polymer blends of poly(3,4-ethylenedioxythiophene): Poly(styrenesulfonate): N-methyl-2-pyrrolidinone and polyvinyl alcohol. *J. Appl. Polym. Sci.* **125**, 3134–3141 (2012).

71. Roh, E., Hwang, B.-U., Kim, D., Kim, B.-Y. & Lee, N.-E. Stretchable, Transparent, Ultrasensitive, and Patchable Strain Sensor for Human–Machine Interfaces Comprising a Nanohybrid of Carbon Nanotubes and Conductive Elastomers. *ACS Nano* **9**, 6252–6261 (2015).

72. Pattavarakorn, D., Youngta, P., Jaesrichai, S., Thongbor, S. & Chaimongkol, P. Electroactive Performances of Conductive Polythiophene/hydrogel Hybrid Artificial Muscle. *Energy Procedia* **34**, 673–681 (2013).

73. Fattahi, P., Yang, G., Kim, G. & Abidian, M. R. A Review of Organic and Inorganic Biomaterials for Neural Interfaces. *Adv. Mater.* **26**, 1846–1885 (2014).

74. Lim, B. C., Singu, B. S., Hong, S. E., Na, Y. H. & Yoon, K. R. Synthesis and characterization nanocomposite of polyacrylamide-rGO-Ag-PEDOT/PSS hydrogels by photo polymerization method. *Polym. Adv. Technol.* **27**, 366–373 (2016).

75. Heo, D. N. *et al.* Development of 3D printable conductive hydrogel with crystallized PEDOT:PSS for neural tissue engineering. *Mater. Sci. Eng. C* **99**, 582–590 (2019).

76. Yoon, K. R. Nanocomposite of polyacrylamide-rGO-Ag-PEDOT/PSS hydrogels by photo polymerization method. *J. Chem. Eng. Process Technol.* doi:10.4172/2157-7048-C1-008.

77. van Dommelen, J. A. W., van der Sande, T. P. J., Hrapko, M. & Peters, G. W. M. Mechanical properties of brain tissue by indentation: Interregional variation. *J. Mech. Behav. Biomed. Mater.* **3**, 158–166 (2010).

78. Cogan, S. F. Neural Stimulation and Recording Electrodes. *Annu. Rev. Biomed. Eng.* **10**, 275–309 (2008).

79. Hodge, R. M., Simon, G. P., Whittaker, M. R., Hill, D. J. T. & Whittaker, A. K. Free volume and water uptake in a copolymer hydrogel series. *J. Polym. Sci. Part B Polym. Phys.* **36**, 463–471 (1998).

80. Wen, Y. & Xu, J. Scientific Importance of Water-Processable PEDOT–PSS and Preparation, Challenge and New Application in Sensors of Its Film Electrode: A Review. *J. Polym. Sci. Part Polym. Chem.* **55**, 1121–1150 (2017).

81. Martin, D. C. *et al.* The Morphology of Poly(3,4-Ethylenedioxythiophene). *Polym. Rev.* **50**, 340–384 (2010).

82. Krongauz, V. V., Schmelzer, E. R. & Yohannan, R. M. Kinetics of anisotropic photopolymerization in polymer matrix. *Polymer* **32**, 1654–1662 (1991).

83. Paradee, N. & Sirivat, A. Synthesis of poly(3,4-ethylenedioxythiophene) nanoparticles via chemical oxidation polymerization. *Polym. Int.* **63**, 106–113 (2014).

84. Chen, S., Hu, T., Tian, Y., Chen, L. & Pojman, J. A. Facile synthesis of poly(hydroxyethyl acrylate) by frontal free-radical polymerization. *J. Polym. Sci. Part Polym. Chem.* **45**, 873–881 (2007).

85. Fujitsuka, M., Sato, T., Segawa, H. & Shimidzu, T. Photochemical polymerization of oligothiophene and dithienothiophene. *Synth. Met.* **69**, 309–310 (1995).

86. Piletsky, S. A. *et al.* Photochemical polymerization of thiophene derivatives in aqueous solution. *Chem. Commun.* 2222–2223 (2004) doi:10.1039/B408387C.

87. Iyoda, T., Kitano, M. & Shimidzu, T. New method for preparing poly(benzo[c]thiophene) thin films by photopolymerization. *J. Chem. Soc. Chem. Commun.* 1618 (1991) doi:10.1039/c39910001618.

88. Wochnowski, C. & Metev, S. UV-laser-assisted synthesis of iodine-doped electrical conductive polythiophene. *Appl. Surf. Sci.* **186**, 34–39 (2002).

89. Hori, H. *et al.* Efficient Decomposition of Environmentally Persistent Perfluorocarboxylic Acids by Use of Persulfate as a Photochemical Oxidant. *Environ. Sci. Technol.* **39**, 2383–2388 (2005).

90. Hassarati, R. T. *et al.* Improving Cochlear Implant Properties Through Conductive Hydrogel Coatings. *IEEE Trans. Neural Syst. Rehabil. Eng.* **22**, 411–418 (2014).

91. Proctor, C. M., Rivnay, J. & Malliaras, G. G. Understanding volumetric capacitance in conducting polymers. *J. Polym. Sci. Part B Polym. Phys.* **54**, 1433–1436 (2016).

92. Tehrani, P. *et al.* The effect of pH on the electrochemical over-oxidation in PEDOT:PSS films. *Solid State Ion.* **177**, 3521–3527 (2007).

93. Chiang, T.-Y., Huang, M.-C. & Tsai, C.-H. The effects of solvent on the electrochromic properties of poly(3,4-ethylenedioxythiophene). *RSC Adv.* **4**, 21201–21207 (2014).

94. Fan, J. *et al.* Tuning PEDOT:PSS conductivity to obtain complementary organic electrochemical transistor. *Org. Electron.* **66**, 148–155 (2019).

95. Long, T. J. Tissue-Engineered Prostate Cancer Xenografts: A Biomaterials-Based Approach to Study Tumorigenesis and Dormancy Escape. (2014).

96. Garg, K., Pullen, N. A., Oskeritzian, C. A., Ryan, J. J. & Bowlin, G. L. Macrophage functional polarization (M1/M2) in response to varying fiber and pore dimensions of electrospun scaffolds. *Biomaterials* **34**, 4439–4451 (2013).

97. Almeida, C. R. *et al.* Impact of 3-D printed PLA- and chitosan-based scaffolds on human monocyte/macrophage responses: Unraveling the effect of 3-D structures on inflammation. *Acta Biomater.* **10**, 613–622 (2014).

98. Chen, R., Ma, H., Zhang, L. & Bryers, J. D. Precision-porous templated scaffolds of varying pore size drive dendritic cell activation. *Biotechnol. Bioeng.* **115**, 1086–1095 (2018).

99. Lacour, S. P., Courtine, G. & Guck, J. Materials and technologies for soft implantable neuroprostheses. *Nat. Rev. Mater.* **1**, natrevmats201663 (2016).

100. Saxena, T. *et al.* The impact of chronic blood–brain barrier breach on intracortical electrode function. *Biomaterials* **34**, 4703–4713 (2013).

101. Lee, H., Bellamkonda, R. V., Sun, W. & Levenston, M. E. Biomechanical analysis of silicon microelectrode-induced strain in the brain. *J. Neural Eng.* **2**, 81 (2005).

102. Gilletti, A. & Muthuswamy, J. Brain micromotion around implants in the rodent somatosensory cortex. *J. Neural Eng.* **3**, 189 (2006).

103. Sridharan, R., Cavanagh, B., Cameron, A. R., Kelly, D. J. & O'Brien, F. J. Material stiffness influences the polarization state, function and migration mode of macrophages. *Acta Biomater.* **89**, 47–59 (2019).

104. Gruber, E., Heyward, C., Cameron, J. & Leifer, C. *Toll-like receptor signaling in macrophages is regulated by extracellular substrate stiffness and Rho-associated coiled-coil kinase (ROCK1/2). *Int. Immunol.* **30**, 267–278 (2018).

105. McWhorter, F. Y., Wang, T., Nguyen, P., Chung, T. & Liu, W. F. Modulation of macrophage phenotype by cell shape. *Proc. Natl. Acad. Sci.* **110**, 17253–17258 (2013).

106. Eligini, S. *et al.* Human monocyte-derived macrophages spontaneously differentiated in vitro show distinct phenotypes. *J. Cell. Physiol.* **228**, 1464–1472 (2013).

107. Qazi, T. H., Rai, R. & Boccaccini, A. R. Tissue engineering of electrically responsive tissues using polyaniline based polymers: A review. *Biomaterials* **35**, 9068–9086 (2014).

108. Khan, M. A. *et al.* A Review on Biomaterials for 3D Conductive Scaffolds for Stimulating and Monitoring Cellular Activities. *Appl. Sci.* **9**, 961 (2019).

109. Gelmi, A. & Schutt, C. E. Stimuli-Responsive Biomaterials: Scaffolds for Stem Cell Control. *Adv. Healthc. Mater.* **n/a**, 2001125.

110. Cangellaris, O. V. & Gillette, M. U. Biomaterials for Enhancing Neuronal Repair. *Front. Mater.* **5**, (2018).

111. Zhou, W. *et al.* Electrical stimulation ameliorates light-induced photoreceptor degeneration in vitro via suppressing the proinflammatory effect of microglia and enhancing the neurotrophic potential of Müller cells. *Exp. Neurol.* **238**, 192–208 (2012).

112. Libert, C., Brouckaert, P. & Fiers, W. Protection by alpha 1-acid glycoprotein against tumor necrosis factor-induced lethality. *J. Exp. Med.* **180**, 1571–1575 (1994).

113. Komori, H. *et al.* α1-acid glycoprotein up-regulates CD163 via TLR4/CD14 pathway: possible protection against hemolysis-induced oxidative stress. *J. Biol. Chem.* jbc.M112.353771 (2012) doi:10.1074/jbc.M112.353771.

114. Aebischer, P., Salessiotis, A. N. & Winn, S. R. Basic fibroblast growth factor released from synthetic guidance channels facilitates peripheral nerve regeneration across long nerve gaps. *J. Neurosci. Res.* **23**, 282–289 (1989).

115. Liu, H. M., Takagaki, K. & Schmid, K. In vitro nerve-growth-promoting activity of human plasma α1-acid glycoprotein. *J. Neurosci. Res.* **20**, 64–72 (1988).

116. Jo, M. *et al.* Astrocytic Orosomucoid-2 Modulates Microglial Activation and Neuroinflammation. *J. Neurosci.* **37**, 2878–2894 (2017).

117. Cheng, J. S. *et al.* Collagen VI protects neurons against Aβ toxicity. *Nat. Neurosci.* **12**, 119–121 (2009).

118. Lv, D., Zhou, L., Zheng, X. & Hu, Y. Sustained release of collagen VI potentiates sciatic nerve regeneration by modulating macrophage phenotype. *Eur. J. Neurosci.* **45**, 1258–1267 (2017).

119. Gregorio, I., Braghetta, P., Bonaldo, P. & Cescon, M. Collagen VI in healthy and diseased nervous system. *Dis. Model. Mech.* dmm032946 (2018) doi:10.1242/dmm.032946.

120. Tillet, E., Gential, B., Garrone, R. & Stallcup, W. B. NG2 proteoglycan mediates β1 integrin-independent cell adhesion and spreading on collagen VI. *J. Cell. Biochem.* **86**, 726–736 (2002).

121. Pfaff, M. *et al.* Integrin and Arg-Gly-Asp Dependence of Cell Adhesion to the Native and Unfolded Triple Helix of Collagen Type VI. *Exp. Cell Res.* **206**, 167–176 (1993).

122. Chen, P. *et al.* Collagen VI regulates peripheral nerve regeneration by modulating macrophage recruitment and polarization. *Acta Neuropathol. (Berl.)* **129**, 97–113 (2015).

123. Schnoor, M. *et al.* Production of Type VI Collagen by Human Macrophages: A New Dimension in Macrophage Functional Heterogeneity. *J. Immunol.* **180**, 5707–5719 (2008).

124. Chen, A. Modulation of macrophage polarization with surface immobilized bioactive molecules. (2017).

125. Pfeffer, K. *et al.* Mice deficient for the 55 kd tumor necrosis factor receptor are resistant to endotoxic shock, yet succumb to L. monocytogenes infection. *Cell* **73**, 457–467 (1993).

126. Flynn, J. L. *et al.* Tumor necrosis factor-α is required in the protective immune response against Mycobacterium tuberculosis in mice. *Immunity* **2**, 561–572 (1995).

127. Chio, C.-C., Lin, M.-T. & Chang, C.-P. Microglial activation as a compelling target for treating acute traumatic brain injury. *Curr. Med. Chem.* **22**, 759–770 (2015).

128. Harms, A. S. *et al.* **Regulation of microglia effector functions by tumor necrosis factor signaling. *Glia* **60**, 189–202 (2012).

129. Rostworowski, M., Balasingam, V., Chabot, S., Owens, T. & Yong, V. W. Astrogliosis in the neonatal and adult murine brain post-trauma: elevation of inflammatory cytokines and the lack of requirement for endogenous interferon-γ. *J. Neurosci.* **17**, 3664–3674 (1997).

130. Barone, F. C. *et al.* Tumor necrosis factor-α: a mediator of focal ischemic brain injury. *Stroke* **28**, 1233–1244 (1997).

131. Shohami, E., Gallily, R., Mechoulam, R., Bass, R. & Ben-Hur, T. Cytokine production in the brain following closed head injury: dexanabinol (HU-211) is a novel TNF-α inhibitor and an effective neuroprotectant. *J. Neuroimmunol.* **72**, 169–177 (1997).

132. Fan, L. *et al.* Experimental brain injury induces differential expression of tumor necrosis factor-α mRNA in the CNS. *Mol. Brain Res.* **36**, 287–291 (1996).

133. Michlewska, S., Dransfield, I., Megson, I. L. & Rossi, A. G. Macrophage phagocytosis of apoptotic neutrophils is critically regulated by the opposing actions of pro-inflammatory and anti-inflammatory agents: key role for TNF-α. *FASEB J.* **23**, 844–854 (2009).

134. Faber-Elman, A., Lavie, V., Schvartz, I., Shaltiel, S. & Schwartz, M. Vitronectin overrides a negative effect of TNF-alpha on astrocyte migration. *FASEB J.* **9**, 1605–1613 (1995).

135. Parameswaran, N. & Patial, S. Tumor Necrosis Factor-α Signaling in Macrophages. *Crit. Rev. Eukaryot. Gene Expr.* **20**, 87–103 (2010).

136. Hickman, S., Izzy, S., Sen, P., Morsett, L. & El Khoury, J. Microglia in neurodegeneration. *Nat. Neurosci.* **21**, 1359–1369 (2018).

137. Shohami, E., Ginis, I. & Hallenbeck, J. M. *Dual role of tumor necrosis factor alpha in brain injury. *Cytokine Growth Factor Rev.* **10**, 119–130 (1999).

138. Nawashiro, H., Tasaki, K., Ruetzler, C. A. & Hallenbeck, J. M. TNF-α pretreatment induces protective effects against focal cerebral ischemia in mice. *J. Cereb. Blood Flow Metab.* **17**, 483–490 (1997).

139. Tasaki, K. *et al.* Lipopolysaccharide pre-treatment induces resistance against subsequent focal cerebral ischemic damage in spontaneously hypertensive rats. *Brain Res.* **748**, 267–270 (1997).

140. Kim, M. *et al.* TNF-α Pretreatment Improves the Survival and Function of Transplanted Human Neural Progenitor Cells Following Hypoxic-Ischemic Brain Injury. *Cells* **9**, 1195 (2020).

141. Dondossola, E. *et al.* Examination of the foreign body response to biomaterials by nonlinear intravital microscopy. *Nat. Biomed. Eng.* **1**, 1–10 (2016).

142. Zhai, Q.-H., Futrell, N. & Chen, F.-J. Gene expression of IL-10 in relationship to TNF-α, IL-1β and IL-2 in the rat brain following middle cerebral artery occlusion. *J. Neurol. Sci.* **152**, 119–124 (1997).

143. Garcia, J. M. *et al.* *Role of Interleukin-10 in Acute Brain Injuries. *Front. Neurol.* **8**, (2017).

144. Norden, D. M., Fenn, A. M., Dugan, A. & Godbout, J. P. TGFβ produced by IL-10 redirected astrocytes attenuates microglial activation. *Glia* **62**, 881–895 (2014).

145. Pereira, L. *et al.* IL-10 regulates adult neurogenesis by modulating ERK and STAT3 activity. *Front. Cell. Neurosci.* **9**, 57 (2015).

146. Perez-Asensio, F. J., Perpiñá, U., Planas, A. M. & Pozas, E. Interleukin-10 regulates progenitor differentiation and modulates neurogenesis in adult brain. *J. Cell Sci.* **126**, 4208–4219 (2013).

147. Kamm, K., VanderKolk, W., Lawrence, C., Jonker, M. & Davis, A. T. The effect of traumatic brain injury upon the concentration and expression of interleukin-1β and interleukin-10 in the rat. *J. Trauma Acute Care Surg.* **60**, 152–157 (2006).

148. Csuka, E. *et al.* IL-10 levels in cerebrospinal fluid and serum of patients with severe traumatic brain injury: relationship to IL-6, TNF-α, TGF-β1 and blood–brain barrier function. *J. Neuroimmunol.* **101**, 211–221 (1999).

149. Chen, X. *et al.* Interleukin-10 mediates the neuroprotection of hyperbaric oxygen therapy against traumatic brain injury in mice. *Neuroscience* **266**, 235–243 (2014).

150. Kirchhoff, C. *et al.* Cerebrospinal IL-10 concentration is elevated in non-survivors as compared to survivors after severe traumatic brain injury. *Eur J Med Res* **13**, 464–468 (2008).

151. Chakrabarty, P. *et al.* IL-10 alters immunoproteostasis in APP mice, increasing plaque burden and worsening cognitive behavior. *Neuron* **85**, 519–533 (2015).

152. Cobbs, C. S., Chen, J., Greenberg, D. A. & Graham, S. H. Vascular endothelial growth factor expression in transient focal cerebral ischemia in the rat. *Neurosci. Lett.* **249**, 79–82 (1998).

153. Ruiz de Almodovar, C., Lambrechts, D., Mazzone, M. & Carmeliet, P. Role and Therapeutic Potential of VEGF in the Nervous System. *Physiol. Rev.* **89**, 607–648 (2009).

154. Ju, S., Xu, C., Wang, G. & Zhang, L. VEGF-C Induces Alternative Activation of Microglia to Promote Recovery from Traumatic Brain Injury. *J. Alzheimers Dis.* **68**, 1687–1697 (2019).

155. Nag, S., Takahashi, J. L. & Kilty, D. W. Role of vascular endothelial growth factor in blood-brain barrier breakdown and angiogenesis in brain trauma. *J. Neuropathol. Exp. Neurol.* **56**, 912–921 (1997).

156. Krum, J. M. & Rosenstein, J. M. VEGF mRNA and Its Receptorflt-1Are Expressed in Reactive Astrocytes Following Neural Grafting and Tumor Cell Implantation in the Adult CNS. *Exp. Neurol.* **154**, 57–65 (1998).

157. Silverman, W. F., Krum, J. M., Mani, N. & Rosenstein, J. M. Vascular, glial and neuronal effects of vascular endothelial growth factor in mesencephalic explant cultures. *Neuroscience* **90**, 1529–1541 (1999).

158. Matsuzaki, H. *et al.* Vascular endothelial growth factor rescues hippocampal neurons from glutamate-induced toxicity: signal transduction cascades. *FASEB J.* **15**, 1218–1220 (2001).

159. Zhang, Z. G. *et al.* VEGF enhances angiogenesis and promotes blood-brain barrier leakage in the ischemic brain. *J. Clin. Invest.* **106**, 829–838 (2000).

160. Hayashi, T., Abe, K. & Itoyama, Y. Reduction of Ischemic Damage by Application of Vascular Endothelial Growth Factor in Rat Brain after Transient Ischemia. *J. Cereb. Blood Flow Metab.* **18**, 887–895 (1998).

161. Weischenfeldt, J. & Porse, B. Bone Marrow-Derived Macrophages (BMM): Isolation and Applications. *Cold Spring Harb. Protoc.* **2008**, pdb.prot5080 (2008).

162. Netea, M. G. *et al.* Trained immunity: a program of innate immune memory in health and disease. *Science* **352**, aaf1098 (2016).

163. Piccolo, V. *et al.* Opposing macrophage polarization programs show extensive epigenomic and transcriptional cross-talk. *Nat. Immunol.* **18**, 530–540 (2017).

164. Pires, F., Ferreira, Q., Rodrigues, C. A. V., Morgado, J. & Ferreira, F. C. Neural stem cell differentiation by electrical stimulation using a cross-linked PEDOT substrate: Expanding the use of biocompatible conjugated conductive polymers for neural tissue engineering. *Biochim. Biophys. Acta BBA - Gen. Subj.* **1850**, 1158–1168 (2015).

165. Castagnola, E. *et al.* pHEMA Encapsulated PEDOT-PSS-CNT Microsphere Microelectrodes for Recording Single Unit Activity in the Brain. *Front. Neurosci.* **10**, (2016).

166. Cherry, J. D., Olschowka, J. A. & O'Banion, M. K. Neuroinflammation and M2 microglia: the good, the bad, and the inflamed. *J. Neuroinflammation* **11**, 98 (2014).

167. Boche, D., Perry, V. H. & Nicoll, J. a. R. Review: Activation patterns of microglia and their identification in the human brain. *Neuropathol. Appl. Neurobiol.* **39**, 3–18 (2013).

168. Wu, W.-K., Llewellyn, O. P. C., Bates, D. O., Nicholson, L. B. & Dick, A. D. IL-10 regulation of macrophage VEGF production is dependent on macrophage polarisation and hypoxia. *Immunobiology* **215**, 796–803 (2010).

169. Eric Thomas, W. Brain macrophages: evaluation of microglia and their functions. *Brain Res. Rev.* **17**, 61–74 (1992).

170. Karve, I. P., Taylor, J. M. & Crack, P. J. The contribution of astrocytes and microglia to traumatic brain injury. *Br. J. Pharmacol.* **173**, 692–702 (2016).

171. Lian, H. *et al.* Astrocyte-Microglia Cross Talk through Complement Activation Modulates Amyloid Pathology in Mouse Models of Alzheimer's Disease. *J. Neurosci. Off. J. Soc. Neurosci.* **36**, 577–589 (2016).

172. Campbell, A. & Wu, C. Chronically Implanted Intracranial Electrodes: Tissue Reaction and Electrical Changes. *Micromachines* **9**, 430 (2018).

173. He, W. & Bellamkonda, R. V. A molecular perspective on understanding and modulating the performance of chronic central nervous system (CNS) recording electrodes. (2011).
174. Kozai, T. D., Jaquins-Gerstl, A. S., Vazquez, A. L., Michael, A. C. & Cui, X. T. Brain tissue responses to neural implants impact signal sensitivity and intervention strategies. *ACS Chem. Neurosci.* **6**, 48–67 (2015).
175. Winslow, B. D. & Tresco, P. A. Quantitative analysis of the tissue response to chronically implanted microwire electrodes in rat cortex. *Biomaterials* **31**, 1558–1567 (2010).
176. Bardehle, S. *et al.* Live imaging of astrocyte responses to acute injury reveals selective juxtavascular proliferation. *Nat. Neurosci.* **16**, 580–586 (2013).
177. Nolta, N. F., Christensen, M. B., Crane, P. D., Skousen, J. L. & Tresco, P. A. BBB leakage, astrogliosis, and tissue loss correlate with silicon microelectrode array recording performance. *Biomaterials* **53**, 753–762 (2015).
178. Capadona, J. R., Tyler, D. J., Zorman, C. A., Rowan, S. J. & Weder, C. Mechanically adaptive nanocomposites for neural interfacing. *MRS Bull.* **37**, 581–589 (2012).
179. Cody, P. A., Eles, J. R., Lagenaur, C. F., Kozai, T. D. Y. & Cui, X. T. Unique electrophysiological and impedance signatures between encapsulation types: An analysis of biological Utah array failure and benefit of a biomimetic coating in a rat model. *Biomaterials* **161**, 117–128 (2018).
180. Malaga, K. A. *et al.* Data-driven model comparing the effects of glial scarring and interface interactions on chronic neural recordings in non-human primates. *J. Neural Eng.* **13**, 016010 (2015).
181. Eles, J. R. *et al.* Neuroadhesive L1 coating attenuates acute microglial attachment to neural electrodes as revealed by live two-photon microscopy. *Biomaterials* **113**, 279–292 (2017).
182. Sofroniew, M. V. & Vinters, H. V. Astrocytes: biology and pathology. *Acta Neuropathol. (Berl.)* **119**, 7–35 (2010).

183. Herrmann, J. E. *et al.* STAT3 is a Critical Regulator of Astrogliosis and Scar Formation after Spinal Cord Injury. *J. Neurosci.* **28**, 7231–7243 (2008).
184. Silver, J. & Miller, J. H. Regeneration beyond the glial scar. *Nat. Rev. Neurosci.* **5**, 146–156 (2004).
185. Sohal, H. S., Clowry, G. J., Jackson, A., O'Neill, A. & Baker, S. N. Mechanical Flexibility Reduces the Foreign Body Response to Long-Term Implanted Microelectrodes in Rabbit Cortex. *PLOS ONE* **11**, e0165606 (2016).
186. Eles, J. R., Vazquez, A. L., Kozai, T. D. Y. & Cui, X. T. In vivo imaging of neuronal calcium during electrode implantation: Spatial and temporal mapping of damage and recovery. *Biomaterials* **174**, 79–94 (2018).
187. Ravikumar, M. *et al.* The effect of residual endotoxin contamination on the neuroinflammatory response to sterilized intracortical microelectrodes. *J. Mater. Chem. B* **2**, 2517–2529 (2014).
188. Jha, M. K., Jo, M., Kim, J.-H. & Suk, K. Microglia-Astrocyte Crosstalk: An Intimate Molecular Conversation. *The Neuroscientist* **25**, 227–240 (2019).
189. Accardo, A., Courson, R., Riesco, R., Raimbault, V. & Malaquin, L. Direct laser fabrication of meso-scale 2D and 3D architectures with micrometric feature resolution. *Addit. Manuf.* **22**, 440–446 (2018).

Appendix

A.1 Protocols

A.1.1 One Pot Photochemical Synthesis of Conductive Hydrogels Protocol

The following protocol will prepare ~2mL of composition HG25SC-5E from Table 5, results for which are discussed in Section 2.4. Various parameters of this solution may be modified to test

specific hypotheses, e.g. monomer concentration, monomer selection, EDOT concentration, APS concentration etc.

1. Prepare molds
    - Glass slides clamped together with teflon spacer of desired width
    - 800um glass capillary tubes open on both ends
2. Obtain a 10mL septa vial (V1) and a 20mL scintillation vial (V2)
3. V1 - septa vial
    - Weigh out add to V1
        - 40mg AMPS (dopant component)
        - 5mg Irgacure 651 (photoinitiator component)
4. V2 - scintillation vial
    - Weigh out add to V2
        - 100mg APS (oxidative initiator component)
5. V1 - septa vial
    - Pipette into V1
        - 400uL HEMA (hydrogel component)
        - 100uL GMA (hydrogel component)
        - 40uL AA (dopant component)
        - 50uL TEGDMA (crosslinking component)
        - 100uL EDOT (conductive polymer component)
    - Sonicate V1 for 5 minutes to dissolve the Irgacure 651 and disperse the AMPS - the solution should be cloudy at this point
    - Pipette into V1
        - 750uL isopropyl alcohol and swirl/shake gently to mix
        - Solution should still be cloudy here

6. PV2 - scint vial
    - Pipette into V2
        - 750uL PBS (pH 7.4) and swirl/shake until dissolved, ~1 minute - solution will be clear
7. Pipette contents of V2 to V1 dropwise
    - Swirl/shake relatively firmly to mix - solution should shift from cloudy white to clear, continue mixing for ~30 seconds
    - Sparge septa vial with N2 for 2-3 minutes
8. Pipette solution from V1 into molds
    - Open ends of capillary tubes should be sealed with parafilm wrapping
9. Polymerize under broad spectrum UV light for 24 minutes, 12 mins/side
    - After 24 mins, the solutions within the molds should be dark blue/black but will likely still not have gelled
10. Gently wrap molds with parafilm to seal from ambient environment without spilling contents
    - DO NOT remove gels/solutions from molds
11. Place wrapped molds into 4C fridge, positioned upright so liquid contents may not spill out
    - Incubate at 4C for 1 week
12. After 1 week, remove samples from fridge, and remove parafilm wrap - solutions should have gelled at this point
    - Capillary tubes may either be gently broken by striking with tweezer or left as is for wash step
13. Place gels into PBS (pH 7.4) for washing
    - Replace with fresh PBS several times a day for 1 week

- Gels within capillary tubes may be removed by exposing 1 end of glass tube to positive pressure via air valve in fume hood to gently eject gel into wash medium

14. Prepare gels for characterization
    - Biopsy punch produces highly uniform discs for mechanical, swelling, etc. analysis
    - Gel rods (from capillary tubes) may be inserted into shrink wrap polyolefin tubing and exposed to heat to shrink firmly around gel to serve as insulation, exposing only the tips of the gel for charge transfer in electrochemical analysis setup

A.1.2 Capillary Cell Seeding, BCA Assay, ELISA

The following protocol contain values for concentrations that will need to be updated/modified according to the needs of particular experimental questions/designs and according to updates to the manufacturer's guidelines (e.g. ELISA Kit reagent concentrations).

1. **Prepare** - 6 well plates (one disc/well)
    0. Plate 1: test samples
    1. Plate 2: control samples
    2. Obtain cell strainers (40um pores) and cut to size to fit into each well to place seeded disc onto
    3. Punch 6mm porous discs for seeding, incubate in sterile PBS or complete DMEM for ~1hr prior to seeding
    4. Obtain and count cells, bring cell suspension to concentration of $1x10^7$ cells/mL in complete DMEM
5. **Seed** - 100uL of $1x10^7$ cells/mL into 6mm discs for a total of $1x10^6$ cells/disc

a. Obtain a 6mm disc and place on 5-6 sterile folded kimwipes (for extremely soft materials, wet the kim wipes first with complete DMEM prior to placing the disc to limit initial drying/suction of the disc)
b. Slowly pipette 100uL cell suspension ($1x10^7$ cells/mL) onto the disc allowing fluid and cells to flow through - be prepared to lift the disc off the kim wipe relatively quickly after finishing pipetting
c. Place seeded disc into well on top of cell strainer 5mL complete DMEM
    i. Complete DMEM: 10% FBS, 1% L-Glutamine, 1% Pen/strep
    ii. Non-seeded control well should have total $1x10^6$ cells in the 5mL media

6. **Culture** - 1 week
    a. Exchange 2mL media off the top every 2 days to feed while avoiding serum shock
        i. Replace medium carefully, slowly from outside the cell strainer to not disturb the seeded disc
    b. 72 hours before sample collection transfer discs to new wells/plates with new cell strainers to exclude cells that have fallen out of the scaffold, replace 2mL media, begin serum starvation (no feeding)

4. LPS stimulation (Time -24h)

a. 24 hours before sample collection, deliver LPS
    i. 100ng/mL final LPS concentration in each well, 500ng/well (@ 5mL medium/well)
        1. Dilute LPS to 1mg/mL (=1ug/uL) in PBS
        2. Calculate total amount of LPS needed
            a. 100ng/mL * 5mL/well * Xwells = 500X ng total LPS
            b. Example: 10 wells
                0. 100ng/mL * 5mL/well * 10wells = 5000ng (5ug) total LPS
                1. 5ug LPS = 5uL LPS stock solution (@ 1ug/uL)
    ii. Dilute LPS into 100uL PBS, transfer 500ng to wells

1. Example: 5ug LPS in 5uL stock solution diluted into 100uL PBS = 50ng/uL LPS
2. 10uL of 50ng/uL LPS into each well (for 500ng total LPS/well; 100ng/mL in each well)

5. **Sample collection (Time 0h)**

a. Conditioned media (CM) collection

i. Obtain microcentrifuge tubes and label for each test group

1. In each tube add 1mL of CM from each of the wells
2. Flash freeze and store samples until ELISA

b. Seeded scaffold collection

i. Obtain microcentrifuge tubes and label for each test group

1. In each tube add 1mL of DPBS
2. Transfer scaffolds from each well into these tubes (this is WASH #1)
3. Flash freeze these samples and store in -80 until BCA assay

c. Control cell collection

i. Obtain microcentrifuge tubes and label for each test group

ii. Vacuum remaining media from wells, and wash 2x with warm DPBS to remove non-adherent cells

iii. Add 1mL RT DPBS (or trypsin/EDTA) to begin cell detachment, then scrape completely and transfer cell suspension to relevant tubes

iv. Spin cells down at 500g for 5 minutes (replace trypsin/EDTA with DPBS here if used)

v. Flash freeze these samples and store in -80 until BCA assay

6. BCA Assay (Total Protein)

a. Lysis Prep

i. Scaffolds

1. Obtain ice bucket + ice
2. Obtain frozen scaffolds, place on ice to defrost (currently on WASH #1)
3. WASH (5x total)
    a. Place tubes in centrifuge, spin 500g for 5 minutes at 4C
    b. Decant, replace 1mL DPBS, spin + decant
    c. Repeat 3x more times (5x total)
4. LYSE
    a. Prepare RIPA + cOmplete lysis buffer
        i. Add 1mL 10x RIPA buffer to 9mL DI H2O, mix well
        ii. Add 1 cOmplete tablet to solution and mix well
        iii. Store 1x RIPA+cOmplete Lysis Buffer 2-8C (before aliquoting)
    b. Obtain 2.0mL lysis buffer (RIPA+cOmplete)
        i. X samples x 150uL/sample
    c. Transfer 150uL lysis buffer to each tube
    d. Sonicate on ice for 1 hour (add more ice every 15-30 mins to ensure cold)
    e. Grind discs with micropestle
        i. Same micropestle can be used across tubes if necessary - wash well with 70% EtOH and dry between tubes
    f. Sonicate on ice for 30 minutes (add more ice 15 mins to ensure cold)
    g. Spin tubes at MAX SPEED at 4C for ~45 minutes

h. Transfer top of solution to new tubes

i. Same labeling scheme

i. Shear DNA with 30G needle 12x times

j. Store samples on ice until BCA assay

ii. Cells (6 samples)

1. Obtain frozen cells, place on ice to defrost

2. WASH (1x)

a. Place tubes in centrifuge, spin 500g for 5 minutes at 4C

b. Decant in prep for lysis.

3. LYSE

a. Obtain 1.0mL lysis buffer (RIPA+cOmplete)

i. X samples x 150uL/sample

b. Transfer 150uL lysis buffer to each tube

c. Sonicate on ice for 1 hour (add more ice every 15-30 mins to ensure cold)

d. Spin tubes at MAX SPEED at 4C for ~45 minutes

e. Transfer top of solution to new tubes

i. Same labeling scheme

f. Shear DNA with 30G needle 12x times

g. Store samples on ice until BCA assay

b. <u>BCA Assay</u>

i. PLATES - obtain 1x 96 well Assay Plates

1. BCA Assay Plate (BA)

ii. Standards - Obtain 1 closed BSA ampule (1mL @ 2mg/mL)

1. Obtain 9 microcentrifuge tubes and label with Groups A-I

2. Obtain 5mL sterile filtered PBS as diluent

3. Follow table below for generating pre-assay standard solutions in each tube

Group	Volume Diluent (uL)	Volume/Source BSA (uL)	Final BSA Conc (ug/mL)
A	0	300 of stock	2000
B	125	375 of stock	1500
C	325	325 of stock	1000
D	175	175 of B	750
E	325	325 of C	500
F	325	325 of E	250
G	325	325 of F	125
H	400	100 of G	25
I	400	0	0

iii. Working Reagent (WR)

1. 9 standards + X unknowns x 2 replicates x 200uL = Total WR Volume Needed

    a. Recipe calls for 25uL sample + 200uL WR for each plate well (1:8 ratio of S:WR)

2. Obtain a conical tube capable of holding Total WR Volume Needed

    a. Add Y_1 mL Reagent A

    b. Add Y_2 uL Reagent B, mix well

        i. Y_1 mL Reagent A x 1/50 ratio A:B = Y_2 uL Reagent B

        ii. $Y_1 + Y_2 \geq$ Total WR Volume Needed

iv. Sample Prep + Analysis

1.Obtain cell lysate samples + 9 standards (0-2000ug/mL)

2.Using a single pipette, transfer 25uL of each sample to the appropriate labeled well -->

3.Using a multi pipette, transfer 200uL of WR to each sample

a. Mix thoroughly on plate genie for 30 seconds

4.Cover plate and incubate at 37C for 30 minutes

5.Cool plate to RT and measure absorbance at 562nm on plate reader

6.Subtract absorbance of BLANK wells from each sample and then compare test samples to standard curve (quadratic best-fit curve) to find protein concentration in ug/mL

7. <u>TNFa ELISA</u>

a. <u>Plate Prep</u>

i. PLATES

1. TNFa ELISA Plate (TEP)

ii. CAPTURE (Time -24h)

1. Obtain **5mL** of TNFa Capture Antibody at RT in an ELISA boat

a. TNFa + LPS DRC prep

i. 96 wells x 50uL/well = 4,800uL (**5mL**) of 800ng/mL (working concentration)

ii. 5mL x 800ng/mL = 4,000ng (4ug) total capture antibody needed

b. Dilution Prep - **5mL** of 800ng/mL target

i. Reconstitute 50ug into 0.5mL PBS - 100ug/mL stock concentration

ii. Add 4.96mL PBS to a 15mL conical

iii. Transfer 40uL of 100ug/mL reconstituted stock into the 15mL conical + mix

iv. Pour 5mL of 800ng/mL capture antibody solution into a ELISA boat

2. Add 50uL of TNFa Capture Antibody to each of the TEP wells
3. Seal plates with adhesive strip and incubate **overnight at RT**

iii. WASH (Time 0h)

1. Prepare bucket to forcefully discard liquid followed by blotting onto paper towel
2. Obtain **90mL** of Wash Buffer in an ELISA boat
3. Wash each well with 285uL 1x Wash Buffer 3x times
    a. 96 wells x 285uL x 3 washes = 82.08mL (**90mL**) 1x Wash Buffer
    b. 10 seconds Plate Genie each Wash cycle

iv. BLOCK (Time 0h)

1. Obtain **10mL** of RD in an ELISA boat
2. Block each well with 100uL Reagent Diluent (1% BSA in PBS) at for **1 hour at RT**
    a. 96 wells x 100uL = 9.6mL (**10mL**) RD

v. WASH (Time +1h)

1. Prepare bucket to forcefully discard liquid followed by blotting onto paper towel
2. Obtain **90mL** of Wash Buffer in an ELISA boat
3. Wash each well with 285uL 1x Wash Buffer 3x times
    a. 96 wells x 285uL x 3 washes = 82.08mL (**90mL**) 1x Wash Buffer
    b. 10 seconds Plate Genie each Wash cycle

b. Assay Procedure

i. PLATES

1. **ELISA Prep Plate (EPP)**
2. **TNFa ELISA Plate (TEP)**

ii. SAMPLE (Time +1h)

1. Prep Plate **(EPP)**
    a. TNFa Standard
        i. Prepare 110uL RD in **EPP 1B-G**
        ii. Add 220uL of 2000pg/mL TNFa standard in prep well 1A
        iii. Transfer 110uL from well **1A** to **1B**, mix well
            a. Repeat for **1B-1C; 1C-1D; 1D-1E; 1E-1F; 1F-1G**
    b. Samples
        i. Obtain frozen CM samples and place on ice to thaw
        ii. Place 55uL of each CM sample into the appropriate **EPP** wells
            a. Take care to duplicate samples correctly as shown in the plate map
2. ELISA Plate **(TEP)**
    a. TNFa Standard
        i. Using a multipipette, transfer 50uL from wells **1A-G** from **EPP** to ***BOTH*** wells **1A-G *AND* 12A-G** on **TEP**
    b. Samples
        i. Using a multipipette, transfer 50uL from wells **2-11A-G** from **EPP** to **TEP**
    c. Seal TEP with adhesive strip and Incubate for **2 hours at RT**

iii. WASH (Time +3h)

1. Prepare bucket to forcefully discard liquid followed by blotting onto paper towel

2. Obtain **90mL** of Wash Buffer in an ELISA boat
3. Wash each well with 285uL 1x Wash Buffer 3x times
    a. 96 wells x 285uL x 3 washes = 82.08mL (**90mL**) 1x Wash Buffer
    b. 10 seconds Plate Genie each Wash cycle

iv. DETECTION (Time +3h)

1. Obtain **5mL** of TNFa Detection Antibody at RT in an ELISA boat
    a. TNFa + LPS DRC prep
        i. 96 wells x 50uL/well = 4,800uL (**5mL**) of 75ng/mL (working concentration)
        ii. 5mL x 75ng/mL = 375ng total detection antibody needed
    b. Dilution Prep - **5mL** of 75ng/mL target
        i. Reconstitute 4.5ug into 1.0mL RD - 4.5ug/mL stock concentration
        ii. Add 4.916L RD to a 15mL conical
        iii. Transfer 83.3uL of 4.5ug/mL reconstituted stock into the 15mL conical + mix
        iv. Pour 5mL of 75ng/mL detection antibody solution into a ELISA boat
2. Add 50uL of TNFa Detection Antibody to each of the **TEP** wells
3. Seal plates with adhesive strip and incubate for **2 hours at RT**

v. WASH (Time +5h)

1. Prepare bucket to forcefully discard liquid followed by blotting onto paper towel
2. Obtain **90mL** of Wash Buffer in an ELISA boat
3. Wash each well with 285uL 1x Wash Buffer 3x times

a. 96 wells x 285uL x 3 washes = 82.08mL (**90mL**) 1x Wash Buffer

b. 10 seconds Plate Genie each Wash cycle

vi. STREP-HRP (Time +5h)

1. Obtain **5mL** of Strepavidin-HRP RT in an ELISA boat

a. TNFa + LPS DRC prep

i. 96 wells x 50uL/well = 4,800uL (**5mL**) of 40x dilution (working concentration)

b. Dilution Prep - **5mL** of 40x dilution target

i. Add 4.875mL RD to a 15mL conical

ii. Transfer 125uL of 1x Strep-HRP into the 15mL conical + mix

iii. Pour 5mL of 40x dilution Strep-HRP solution into a ELISA boat

2. Add 50uL of Strepavidin-HRP solution to each of the **TEP** wells shown **-->**

3. Seal plates with adhesive strip and incubate for **<u>20 minutes at RT *IN THE DARK*</u>**

a. Begin Substrate Solution preparation (1:1 of Reagent A + B)

vii. WASH (Time +5h 20m)

1. Prepare bucket to forcefully discard liquid followed by blotting onto paper towel

2. Obtain **90mL** of Wash Buffer in an ELISA boat

3. Wash each well with 285uL 1x Wash Buffer 3x times

0. 96 wells x 285uL x 3 washes = 82.08mL (**90mL**) 1x Wash Buffer

1. 10 seconds Plate Genie each Wash cycle

viii. SUBSTRATE (Time + 5h 20m)

1. Obtain **10mL** of Substrate Solution at RT in an ELISA boat

a. TNFa + LPS DRC prep

i. 96 wells x 100 uL/well = 9,600uL (**10mL**) of Substrate Solution

b. Dilution Prep - **10mL** of Substrate Solution

i. Add 5mL of Reagent A to a 15 mL conical

ii. Add 5mL of Reagent B to the 15 mL conical

iii. Mix Reagent A + B well to produce Substrate Solution

iv. Pour **10mL** of Substrate Solution into a ELISA boat

2. Add 100uL of Substrate Solution to each of the **TEP** wells shown **-->**

3. Seal plates with adhesive strip and incubate for **20 minutes at RT *IN THE DARK***

ix. STOP (Time +5h 40m)

1. Obtain **5mL** of Stop Solution at RT in an ELISA boat

a. TNFa + LPS DRC prep

i. 96 wells x 50uL/well = 4,800uL (**5mL**) of Stop Solution

2. Add 50uL of Stop Solution to each of the **TEP** wells

a. 10 second plate genie

x. READ

1. Set the plate reader to 450nm as the primary reading wavelength

2. Use 540nm and/or 570nm as secondary wave lengths for wavelength correction

a. Subtract readings at 540/570nm from readings at 450nm

A.1.3 Immunohistochemistry for Floating Sections (Shain/Dryg)

***Brains should be sectioned at 50um/slice with a vibratome (speed 5, amplitude 3 usually works well) and stored in 500uL of HBHS w/ NaN_3 in 24well plates at 4C until ready for IHC

- See right for HBHS solution prep -->
- All following mentions of HBHS should have NaN_3

HEPES Buffered Hanks Solution (HBHS) SOP

- 10x Stock Salt Solutions

	Salt	**Grams/1L**

Monovalent Salts 10x Stock	NaCl	75.4
	KCl	3.0
(NOTICE where the subscript numbers are)	Na_2HPO_4	1.4
(NOTICE where the subscript numbers are)	KH_2PO_4	0.7
Divalent Salts 10x Stock	$CaCl_2$	1.2
	$MgCl_2$	0.3
	$MgSO_4$ x $7H_2O$	0.5

- HBHS Working Solution

	Amount/L
Monovalent Salts 10x Stock	100mL
Divalent Salts 10x Stock	100mL
HEPES	2.4g
Glucose (dextrose/D-glucose)	2.0g
Sodium Azide (NaN_3, preservative)	90mg

- HBHS Preparation Directions
    - Add half of ddH_2O to container before adding stock solutions (otherwise divalent salts will precipitate)
    - Add stock salt solutions

- Add HEPES and Glucose
- Add Sodium Azide
- Bring volume to 100% with ddH_2O
- pH to 7.4

Day 1

1. Wash 3x in HBHS, rapid rinses
    a. HEPES in HBHS replaces bicarbonate of Hanks, HEPES is very physiological at a wide temperature range (maintains osmolarity to +/- 0.1 mosm). Osmolarity greatly influences cells because of pressure/shrinking
    b. ***BE SURE TO HOLD THE SLICE OUT OF THE WAY WHILE SUCTIONING TO PREVENT DAMAGE OR LOSS OF SLICE
2. Incubate in 5mg/mL $NaBH_4$ in HBHS for 30mins
    a. Exposes antigens post PFA crosslinking
    b. Make just enough for (#wells x 500uL)
3. Wash 3x in HBHS, rapid rinses
4. Incubate in 0.2% Triton-X-100 in HBHS for 30mins
    a. Triton-X-100 is a detergent which lyses cell membranes
    b. Useful to make stock of 1% Triton-X-100 in HBHS
5. Wash 3x in HBHS, rapid rinses
6. Incubate in 3% serum in 0.2% Triton-X-100 in HBHS
    a. Blocks non-specific protein adsorption
    b. Use serum from same species as 2ndary antibody
7. Wash 3x in HBHS, rapid rinses
8. Incubate in Image-iT FX for 30mins at room temperature

    a. Blocks background staining from non-specific and dye interactions
    b. 4-5 drops per well (24well plate)
9. Wash 3x in HBHS, rapid rinses
10. Incubate overnight in diluted primary antibodies in 0.2% Triton-X-100 in HBHS at room temperature

Day 2

1. Wash 4x for 30mins each in HBHS
    a. ***WASH SPATULA BETWEEN SLICES TO PREVENT CROSS CONTAMINATION OF PRIMARY ANTIBODIES
2. Incubate overnight in secondary antibodies in 0.2% Triton-X-100 in HBHS at room temperature
    a. ***COVER WITH FOIL TO PROTECT CONJUGATED ANTIBODIES FROM LIGHT

Day 3

1. Wash 4x for 30mins each in 0.5% Tween 20 in HBHS
    a. Reduces non-specific and protein-protein interactions
    b. *On 3rd wash, use 1/1000 dilution Hoechst in 0.5% Tween 20 in HBHS to stain nuclei
    c. Do not suction on final wash, to keep slices hydrated while mounting onto slides
    d. ***WASH SPATULA BETWEEN SLICES IF USING MORE THAN 2 SECONDARY ANTIBODIES ACROSS SLICES
2. Mount slices onto slides with Fluoromount-G or Prolong Gold
    a. Wet slide with wash liquid (create a small puddle)

b. Transfer slice to slide with paint brush (flipping brush once slice is picked up to lay opposite side down helps with getting the slice flat on the glass surface)
c. Tap/drag slice to open/spread, wetting as needed
d. Once slice is open and oriented, spread puddle out to help suction removal
e. Try to remove unnecessary bulbs on slice and bubbles to help prevent fold over of slice
f. Suck remaining puddle away from tissue on slide (CAREFUL not to damage the slice)
g. Place 1 drop of Fluoromount-G on middle of slice and a thin line along the top edge of the slide
h. Place cover slip onto slide by Fluromount-G line and wet the edge of the cover slip
    i. Here cover slip should be connected to slide via Fluromount-G like a door on a hinge
i. Slowly lay down cover slip over the slice to allow line of Fluoromount-G to meet droplet on the slice
j. Once line and droplet meet, gently let go of cover slip to allow fluoromount-G to fully connect cover slip to slide
k. Gently press on any bubbles that form under coverslip to move them out to the edge and suction away along with excess Fluoromount-G that oozes out between coverslip and slide
l. Allow Fluoromount-G to set overnight IN THE DARK

Day 4

1. Paint clear nail polish around the edge of the cover slip to seal in moisture
2. At this point, slice + slide are ready for fluorescent or confocal imaging
3. Store slides at room temperature in the dark